Downloaded from orbit.dtu.dk on: Apr 25, 2024

DTU Library

Superconducting Wind Turbine Generators

Mijatovic, Nenad

Publication date:
2012

Document Version
Publisher's PDF, also known as Version of record

Link back to DTU Orbit

Citation (APA):
Mijatovic, N. (2012). *Superconducting Wind Turbine Generators*. Technical University of Denmark.

General rights
Copyright and moral rights for the publications made accessible in the public portal are retained by the authors and/or other copyright owners and it is a condition of accessing publications that users recognise and abide by the legal requirements associated with these rights.

- Users may download and print one copy of any publication from the public portal for the purpose of private study or research.
- You may not further distribute the material or use it for any profit-making activity or commercial gain
- You may freely distribute the URL identifying the publication in the public portal

If you believe that this document breaches copyright please contact us providing details, and we will remove access to the work immediately and investigate your claim.

Superconducting Wind Turbine Generators

Nenad Mijatovic

Center for Electric Technologies

Technical University of Denmark

A thesis submitted for the degree of

PhilosophiæDoctor (PhD)

January 2012

1. Reviewer:
Henk Polinder, Ph.D

2. Reviewer:
Philippe J. Masson, Ph.D

3. Reviewer:
Arne Hejde Nielsen, MSc

Day of the defense: January 2012
Signature from head of PhD committee:

_____

Primary Supervision:
Bogi B. Jensen, Ph.D.

Co – Supervision:
Chresten Træhold, Ph.D.

Co – Supervision:
Asger B. Abrahamsen, Ph.D.

Abstract

A HTS machine could be a way to address some of the technical barriers offshore wind energy is about to face. Due to the superior power density of HTS machines, this technology could become a milestone on which many, including the wind industry, will rely in the future. The work presented in this thesis is a part of a larger endeavor, the Superwind project that focused on identifying the potentials that HTS machines could offer to the wind industry and addressing some of the challenges in the process. In order to identify these challenges, I have design and constructed a HTS machine experimental setup which is made to serve as precursor, leading towards an optimized HTS machine concept proposed for wind turbines.

In part, the work presented in this thesis will focus on the description of the experimental setup and reasoning behind the choices made during the design. The setup comprises from a HTS synchronous machine where a revolving armature winding spins around an open bath liquid nitrogen cryostat, which contains the HTS coils cooled down to 77 K. A significant part of the thesis is allocated to the description of the setup, particularly the torque transfer element and the compact cryostat design, where a concept with ∼20 W of heat transfer is achieved.

Following the setup description, the focus turns to the electromagnetic design consideration of the HTS machine. Particularly, an approach to increase the performance of HTS coils and the influence of the armature reaction to the HTS field winding will be discussed.

Two design strategies are proposed, novel in a machine design, in order to reduce the amount of HTS required in a machine whereby the merits of both have been experimentally verified. The first employs a multiple HTS types in the machine design, since each type of the HTS tape has a specific

magnetic characteristic with respect to the critical current. I have showed that the potential for the reduction of HTS conductor can be significant, if the coils are placed strategically, whereby the coils wound with BSCCO performed 40% better depending on the placement in the field winding. The 2G coils were less sensitive to the placement which made them particularly useful for high magnetic field regions in the field winding. The second design approach proposed and tested was to use multiple current supplies which allowed each coil to operate close to its critical current. I have demonstrated that by introducing one additional power supply, an order of 12% higher MMF was generated (or equivalent HTS savings achieved). Increasing in the number of additional power supplies did not show the same potential for HTS reduction.

The implications of an armature reaction impact on the HTS field winding performance were examined and verified throughout a series of Locked Armature experiments. The interaction have been defined in the terms of two (direct and quadrature) axis machine theory (Park transformation), where significant reduction of $\sim 20\%$ was observed for the rated armature reaction in the q axis. Building on this observation, a control strategy for the excitation current to improve a partial load efficiency of a HTS machine is proposed.

Thus, this work has shown that a significant savings of a the costly HTS tape could be realized indicating that the HTS machine design can still be optimized towards more competitive alternative to conventional machines. Additionally, by constructing the HTS machine setup we went through most of the issues related to the HTS machine design which we managed to address in rather simple manner using everyday materials and therefore proving that HTS machines are close to commercialization.

Resumé

Høj temperatur superledende (HTS) maskiner kan komme til at adressere nogle af de tekniske barrierer som havvindmølle sektoren står over for på grund af deres overlegne effekt tæthed. Arbejdet præsenteret i denne afhandling er del af en større indsats i Superwind projektet, som er fokuseret på at identificere mulighederne HTS maskinerne kan bidrage til vindmølleindustrien og diskutere udfordringerne forbundet med dette. For at identificere udfordringerne, har jeg designet og konstrueret en HTS eksperimentel maskine opstilling, som skal danne grundlaget for optimeringen af et HTS maskine koncept til vind møller.

Arbejdet præsenteret i denne afhandling vil fokusere på en beskrivelse af den eksperimentelle opstilling og på tankerne bag de valg som blev truffet i design fasen. Opstillingen består af en HTS synkron maskine, hvor ankeret roteres omkring en åben bad flydende kvælstof kryostat, som indeholder HTS spolerne nedkølet til T = 77 K. En stor del af afhandlingen er dedikeret til beskrivelsen af opstillingen, specielt kraft moment overførsels elementet og det kompakte kryostat design, hvor et koncept med 20 W varme overførsel til den kolde rotor blev opnået.

Efter beskrivelsen af den eksperimentelle opstilling bliver fokus rettet mod de elektromagnetiske design overvejelser af HTS maskinen. Specielt bliver en måde at øge ydeevnen af HTS spoler og indflydelsen af anker vekselvirkningen på HTS felt viklingen diskuteret. To nye design strategier bliver foreslået med formålet at reducere mængden af HTS leder som er nødvendigt i en maskine og fordelen ved disse bliver eftervist eksperimentelt. Den første strategi omfatter brugen af forskellige typer af HTS tapes i en maskine, fordi de har forskellige karakteristika med hensyn til den kritiske strøm de kan bære. Jeg har vist, at potentialet for at reduceret HTS tape

forbruget er betydeligt, hvis forskellige spoler placeres strategisk og i tilfældet af spoler viklet med BSCCO tape kan ydeevnen forøges med 40 %. Spolerne baseret på 2G tape var mindre følsomme over for magnet felt og gjorde dem specielt anvendelige i regioner af felt viklingerne med høje magnet felter. Den anden design strategi er at benytte flere strømforsyninger, som tillader at hver spole kan forsynes med en strøm tæt på den kritiske strøm af spolen. Jeg har demonstreret, at man kan øge MMF af rotor viklingen med omkring 12 % ved at introducere en ekstra strømforsyning (hvilket svarer til en mulig 12 % reduktion af forbrug af tape). Der blev ikke observeret yderligere forbedringer ved at introducere flere forsyninger.

Indvirkningen af anker vekselvirkningen på HTS felt viklingen er blevet undersøgt og eftervist i en række låste anker eksperimenter. Vekselvirkningen er blevet defineret i termer af to-akse maskine teori (Park transformationen) og en signifikant reduktion på 20 % blev observeret med nominal anker vekselvirkning i q-aksen. Disse observationer er blevet benyttet til at foreslå en kontrol strategi for magnetiserings strømmen for at forbedre effektiviteten af en HTS maskine ved dellastning.

Dette arbejde har vist at en signifikant besparelse på den dyre HTS tape kan opnås og dermed indikerer, at designet af HTS maskiner kan optimeres mod et konkurrence dygtigt alternativ til konventionelle maskiner. Desuden har konstruktionen af test opstillingen bragt Superwind teamet igennem de fleste design overvejelser for en HTS maskine, og da det er lykkedes at løse disse med brug af simple materialer er det bevist at HTS maskiner er tæt på en kommercialisering.

To Andrijana

Preface

This thesis was written at Center for Electric Technology (CET) which is a part of Department of Electrical Engineering at Technical University of Denmark (DTU) in partial filament of the requirements for acquiring the Ph.D. degree. The Ph.D. project is supported by the DTU globalization funds in the frame of the Superwind project. The main focus of the study is a design and performance evaluation of a HTS machine with reference to the wind turbine application.

At the beginning of my project, the aim was to design a 50 kW demonstration HTS machine as a prototype for the future wind turbine generator. Since a HTS machine research is a costly venture, ambitions had to be revised. Instead, creating a versatile experimental HTS machine setup in order to build a solid base knowledge that will ultimately lead towards an optimized machine prototype was considered a better choice.

In the first year of my work, I have spent significant time learning about superconductivity and its applications since my background was in design, analysis and control of conventional electrical machine. At the same time, the effort was made to strengthen the competence in the machine design at CET by employing a senior specialist in the field. The situation changed when Dr. Bogi B. Jensen started in 2010 as Associate Professor teaching electrical machines and stepped in as my primary supervisor since my previous supervisor Professor Niels F. Pedersen retired. Parallel to the learning process, I have worked on the HTS machine design starting out with the main design issues and considerations. The design and construction process spanned over two and a half years where most of the parts were designed and built from the scratch.

My most sincere gratitude, I would like to extend to people at CET and Risøwho gave me the opportunity to carry out this research and welcomed me to the Superwind team. From the very beginning I have felt as part of the team and a valued member and for that I am very grateful to everyone in Superwind. I would like to express special thanks to Bogi B. Jensen , Chresten Træhold (co- supervisor), Asger B. Abrahamsen (co-supervisor) and Niels F. Pedersen for all support and guidance without which my research would be impossible. Many thanks to Freddie Fahnøe and the staff in the workshop for help provided with all practical issues. Furthermore, I would like to express my thanks to CET management, Jacob Østergaard and Morten Sadolin, where in the time of challenging conditions during the reconstruction of laboratories, I could rely on your support and understanding. Last but not least, without the support and encouragement from my Andrijana, family and friends to whom I owe so much, none of my dreams could be realized; thank you!

Declaration

I herewith declare that I have produced this paper without the prohibited assistance of third parties and without making use of aids other than those specified; notions taken over directly or indirectly from other sources have been identified as such. This paper has not previously been presented in identical or similar form to any other Danish or foreign examination board.

The thesis work was conducted from 1. May 2008 to 31. December 2011 under the supervision of Prof. em. Niels Falsig Pedersen in period from 1. May 2008 until 30. May 2010 and Dr. Bogi Bech Jensen from 1. Jun 2010 until 31. December 2011 at Department of Electric Engineering, Technical University of Denmark .

Lyngby, December 2011

Nenad Mijatovic

Contents

List of Figures

LIST OF FIGURES

List of Tables

Glossary

LN_2	Liquid Nitrogen
MgB_2	Magnesium Diborate, a superconducting compound with moderate transition temperature of 39 K
1G	First generation of High Temperature Superconductor tape or BSCOO or Bi–2223
2G	Second generation of High Temperature Superconductor tape or YBCO or Coated Conductor
AMS344	YBCO 344 coated conductor from American Superconductor
AMSC	American Superconductor Inc.
Arr1	Configuration of the HTS field winding with four HTS coils
Arr2	Configuration of the HTS field winding with six HTS coils
Bi–2223	$Bi_2Sr_2Ca_2Cu_3O_{10}$ High Temperature Superconductor
BSCOO	$Bi_2Sr_2Ca_2Cu_3O_{10}$ High Temperature Superconductor
CC	Coated Conductors
DD	Direct Drive wind turbine
DDPMSM	Direct Drive Permanent Magnet Synchronous Machine
EC	European Commission
EU	European Union
EU–27	European Union member states
EWEA	European Wind Energy Association
GM	Gifford–McMahon refrigerator or cryocooler
HP	Hewlett–Packard
HTS	High Temperature Superconductors
IBAD	Ion Beam Assisted Deposition
ICPP	Intergovernmental Panel on Climate Change

GLOSSARY

IV curve	Relation between current and voltage of superconductor.
LTS	Low Temperature Superconductor
MMF	Magneto motive force
MOCVD	Metal Organic Chemical Vapor Deposition
MOD	Metal Organic Deposition
MTOE	Million Tons of Oil Equivalent
p	number of pair of poles
p.u.	per unit
PIT	Powder In Tube wire manufacturing technology
PM	Permanent Magnet
PMSM	Permanent Magnet Synchronous Machine
PT	Pulse Tube refrigerator or cryocooler
RABITS	Rolling Assisted Bi-axial Textured Substrate
RE	Rare Earth element
SC	Superconductor
SM	Synchronous Machine
SS	Stainless steel
TTE	Torque Transfer Element
USD	US dollar
USD/kAm	US dollar per meter for 1000 A conductor
YBCO	$YBa_2Cu_3O_6$ High Temperature Superconductor

Chapter 1

Introduction

"Happy is he who gets to know the reasons for things." **by Virgil**.

1.1 Motivation and challenges - An HTS direct drive wind turbines

An offshore wind energy sector is expected to expand in the next decade. However, the speed of the development of the offshore wind is impeded by the market cost as at the moment it is twice as costly as onshore wind energy. As a way to decrease a cost of wind energy, the trend towards large wind turbines can be observed where the size of 10 MW is expected. A broader discussion about the trends, state of the renewable energy and the incentives for the offshore wind development is presented in the Appendix.A. The increase in the size of the turbines is followed by the number of challenges where the size and the weight of a direct drive generator are significant contributors.

On the other hand, one of the prominent characteristics of superconducting machines is superior power density compared to a conventional machine, which is expected to be $1.5 - 3$ times higher(3, 4, 5). Therefore, if the superconducting machine is employed as a wind turbine generator, scaling of gearless drive train becomes technically easier and potentially commercial superior (which depends on the cost and maturity an HTS technology). In addition, the HTS technology is several times less susceptible

to the cost fluctuations of the Rare Earth elements. This stems from the fact that an HTS machine would use three orders of magnitude less of the Rare Earth elements than a permanent magnet alternative (which is highly attractive for wind application). Comparison between 10 MW High Temperature Superconductor and Permanent Magnet direct drive generator with respect to the usage of Rare Earth elements is included in the A.4, where an estimated requirements for RE if the future turbines are PM machines would be higher than the world's annual production of RE.

To investigate the potential of High Temperature Superconductor machines in the wind energy, it is vital to examine the superconducting machine as a whole, where all aspects are considered, such as: cooling efficiency, complexity and reliability; an HTS performance, cost and availability; auxiliary systems like protection system and power electronic control units; a machine performance and maintenance and etc.

Since an HTS technology is still in the phase of development, the design and construction of the specific prototype would involve too many unknowns. As an alternative approach, the experimental setup where a number of superconducting materials could be employed and machine concepts could be examined had an obvious advantage and it was deemed to be more valuable at this stage. The design of the experimental setup has involved the same (or similar) challenges a specific HTS machine would have and thereby prove to be highly educational endeavor. Therefore, this work (as a part of Superwind) presents a valuable contribution to the global knowledge pool regarding an HTS machines and it represents the initial step towards an optimized design machine design intended for large wind turbines.

1.2 Layout of the thesis

Chapter-2 – The thesis will start by introducing the superconductivity which is intended for readers new to the field, underling the physical differences between types of High Temperature Superconductors and their physical properties. Manufacturing and cost projection based on the raw material content is carried out, and prospect of HTS candidates for large scale application are indentified.

Chapter-3 – In Ch.3, the concept of HTS machines are explained and the overview of demonstration projects to the date is given. The concepts of an HTS machines

with a high torque density are identified as the candidates for the future wind turbines. Specific aspects of an HTS machine design such as cooling systems and torque transfer from a low temperature to a room temperature are identified as crucial in the design and general recommendations with respect to the design of these are presented. Furthermore, I will briefly reflect on the nature of HTS machine parameters and the implications of these for a wind turbine application. This is done with the help of an analytic model of an HTS machine where in addition a magnetic interaction between an HTS winding and armature winding is identified as one of the important aspects for the performance of the HTS. The interaction is afterwards examined experimentally. Finally, the chapter will conclude by proposing two design strategies for improving the performance of an HTS field winding.

Chapter-4 - The design details and choices made in the Sperwind project during the design and construction of the HTS machine setup are presented in Ch.4.The flexibility of the design and value of such a concept are emphasized.

Chapter-5 - Experimental results are presented and discussed in Ch.5. The HTS coils are characterized at the beginning of the chapter. The hypothesis presented in the Ch.3 are verified where versatility of the experimental setup will prove to be highly usefully.

The impact of the armature reaction on the performance of the HTS winding is examined throughout a series of experiments, after which this interaction is quantified and defined in the terms of two (quadrature) axis machine theory (Park model). Consequently, the control strategy for an HTS machine excitation current is proposed aimed to improve the performance of an HTS machine at partial load. In addition, the design approach concepts proposed in Ch.3 to improve the performance of an HTS field winding are put to the test where obtained results are presented and their implication discussed. Finally, the Superwind HTS machine is characterized by the No Load and Short Circuit experiments where combination of these have been used to derive the machines parameters which are compare to the machine parameters derived from the FE model.

Chapter-6 The chapter provides a summary of the thesis and outlines its main contributions, achievements, but also its boundaries and limitations. Furthermore, possible future work is discussed since this thesis represents only a part of what is intended to be a longer strategic research related to an HTS machine design.

Chapter 2

Superconductivity

"The experiment left no doubt that, as far as accuracy of measurement went, the resistance disappeared. At the same time, however, something unexpected occurred. The disappearance did not take place gradually but abruptly. From 1/500 the resistance at 4.2 K, it could be established that the resistance had become less than a thousand-millionth part of that at normal temperature. Thus the mercury at 4.2K has entered a new state, which, owing to its particular electrical properties, can be called the state of superconductivity." **by Heike Kamerlingh Onnes**.

Superconductivity has played an essential role in the development of both science and technology. This chapter will give a short retrospective of the history of superconductivity. The difference between normal conductivity and two types of superconductivity is reviewed and physical properties of High Temperature Superconductors (HTS) used in the Superwind project are presented. Production process will be described together with the electromagnetic performance of each of the conductor. The Chapter2 will conclude with a review of published work on production scale up and cost forecasting of HTS intended for large scale applications.

2.1 Brief history of Superconductivity

Superconductivity as a phenomena was discovered a century ago, by Heike Kamerlingh Onnes in 1911 in Leiden during his experiments with mercury at liquid helium temperatures (6). In those experiments he observed an abrupt transition and absence of electrical resistance of Hg at $4.2K$. In coming decades, superconductivity was observed in several other materials, mostly metals and metal alloys. Chronology of discovery of superconductivity in various materials is presented in the Fig.2.1.

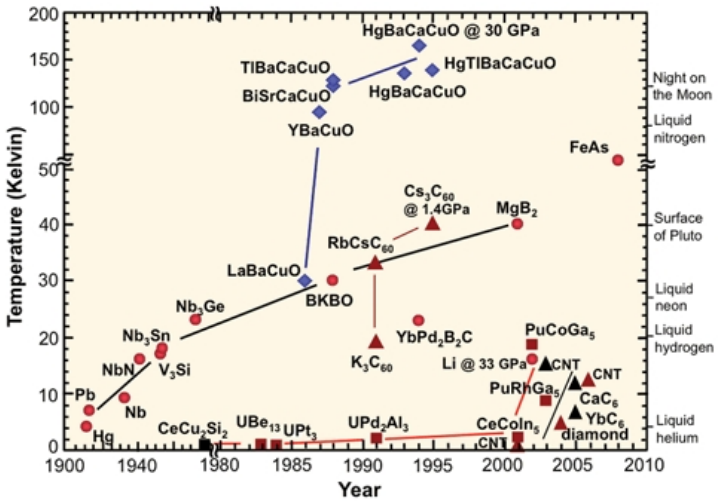

Figure 2.1: Discovery of superconductivity in various materials during a century of research - The metals and metal alloys are presented with red markers, while HTS ceramics are blue. Source: Reprinted from(7)

The breakthrough in the field came in 1986, when Bednorz and Mueller discovered superconductivity in a lanthanum-based material (8) (for which they were awarded the Nobel prize(9)). The $La_2 - BaCuO_4$ had a transition temperature of 35K which was believed to be impossible at that time(10). This discovery was followed by the discovery of $YBa_2Cu_3O_{6+x}$ (11) in 1987 with a transition temperature of 93 K. The quest for materials with even higher values of T_c was on the way, where room temperature superconductivity was predicted as an ultimate and yet unfulfilled goal (12). The most recent developments in material science have led to the discoveries of superconductivity in MgB_2 (13) and $FeAs$ (14) which caused a debate about their unique physical properties.

Thus with a discovery of new superconductors, the understanding of physical mechanisms behind superconductivity increased over the years. A brief explanation on basic differences between normal conduction and superconducting phenomena is presented in the following section.

2.2 Physics of superconductivity

Superconductivity is a complex phenomena occurring in some materials under certain conditions. Electric current in normal material (metals) constitutes the motion of electrons. As moving electrons collide with the lattice, part of the kinetic energy is converted into heat which constitutes a partial loss of the electrons energy (15). Macroscopically speaking, this energy dissipation gives rise to the notion of resistance. With the discovery of superconductivity, the apparent resistance vanished, thus allowing lossless flow of electric current (6).

On the other hand, superconductivity is caused by pairing of conduction electrons in metals into an electron pair, a so called Cooper pair. The flow of Cooper pairs constitutes a 'super-current', ie. a current in a material flowing without any resistance (electron pair lattice, collision free interaction) (16). Coupling of electrons into Cooper pairs is caused by the interaction of electrons and crystal lattice vibration of a material. One of the moving electrons will attract the positive ions of the crystal lattice, which will contract after the electron has moved on (17). The contracted region of the lattice will appear slightly more positive and thereby attract anther electron. Thus, an attractive interaction is established via the lattice vibration. The electron - phonon mediated superconductivity was described theoretically by Bardeen, Cooper and Schrieffer in the famous BCS theory (18, 19).

The prediction of 30 K (28 K calculated for Nb_3Sn)(10) as the highest theoretical temperature above which superconductivity could not exist, derived from BSC theory, was based on the general material parameters of metals and alloys. However, the report of $T_c = 35$ K in 1986 in the ceramic compound La_2BaCuO_4 and later $T_c = 93$ K in $YBa_2Cu_3O_6$ (10) was in contradiction with what was at that time the understanding of electron pairing mechanisms. This was a birth of a new class of materials, called High Temperature Superconductors (HTS) due to a widely accepted belief that T_c could not surpass 30 K.

2.2.1 Classification of superconductors

Superconductors can be classified into type 1 and type 2 superconductors (10). Type 1 are usually pure metals characterized by the Meissner state where superconductivity vanishes when an applied magnetic field becomes higher than the critical magnetic field (20). Type 2 superconductors are bi-metals and ceramic materials characterized by the Meissner state for magnetic fields lower than the first critical magnetic field, H_{c1}. However, for magnetic fields above the first critical value superconductivity does not disappear. Instead, the material enters into a mixed state where the magnetic field gradually penetrates into the superconductor in non-superconducting tube shaped regions called flux lines. If the applied magnetic field becomes larger than the upper critical magnetic field, H_{c2}, the superconductivity will vanish and the superconductor will enter into a "normal state"(20). All practical applications of superconductivity are based on type 2 superconductors.

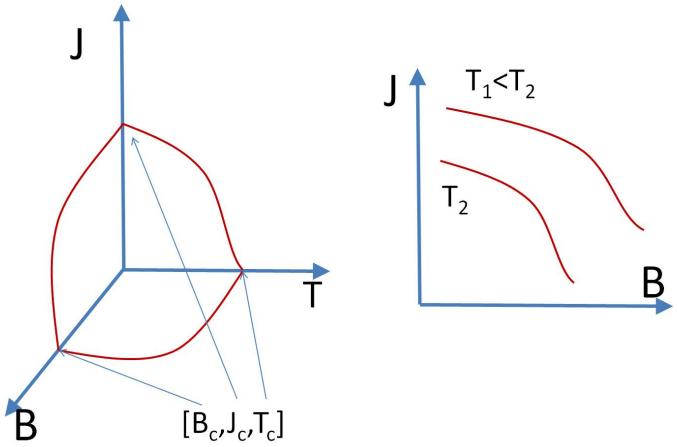

Figure 2.2: $J - B - T$ **critical surface** - Illustration of critical surface defined by the critical current (or critical current density), magnetic flux density (or magnetic field) and temperature, i.e. $J - B - T$.

2.2.2 Critical parameters of superconductor

A superconducting state of material is described by three parameters, the critical magnetic field (or flux density), the critical current density and the critical temperature. If presented in a 3D Cartesian coordinate system, these parameters will define a so

called critical surface. A typical critical surface of a superconductor is illustrated in the Fig.2.2 and presents a boundary between superconducting and normal conducting state.

The definition of critical current of superconducting (HTS) material is related to the measure of pinning sites (crystal defects and incorporated nano–particles), which will prevent the flux lines from moving due to the force acting on them caused by a current flowing in material. Yet, macroscopically, the current - voltage relation of superconductors, where voltage increases due to the motion of flux vortexes, can be described with a power law, as expressed in 2.1

$$E = E_0 \left(\frac{I}{I_c(B,T)} \right)^{n(B,T)} \tag{2.1}$$

where I_c is the critical current of the superconductor and the n value is an exponent which defines how abruptly the transition between superconducting and normal state occurs. These are parameters of material and are dependent on the magnetic field and temperature. The criteria used to define critical electric field (electric field in a superconductor when the critical current is running) is E_0=1 μV/cm=10^{-4} V/m.

The expression 2.1 can be used as one of the ways to experimentally determine I_c of a superconductor. The so called 'Short sample' experiment (21) is experiment where a short piece of superconductor is cooled to the desired temperature after which a transport current is passed through the sample and the voltage drop across the superconductor is measured. By increasing the transport current, the critical current is reached when the voltage drop becomes equal to the critical electric field E_0 =1 μV/cm=10^{-4}V/m. Repeating this, for several temperatures and values of external magnetic field, a family of so called 'IV' curves is collected. Further post processing of IV data with the help of 2.1 will result in a critical surface (illustrated in the Fig.2.2) for that particular HTS conductor.

2.3 HTS conductors

HTS produced as commercial conductors which are used in superconducting applications, are $Bi_2Sr_2Ca_2Cu_3O_{10}$ (Bi–2223) and $YBa_2Cu_3O_6$(YBCO). In recent years MgB_2 has gained high attention and looks very promising for number of applications. Since this project is limited to T= 77 K, MgB_2 was not considered as an option. The

Bi–2223 was first to be commercially produced as HTS tapes from the early 1990's (22). Thus, the name 'first generation of HTS' or 1G is often used and will be used in this thesis too. The YBCO came some years later and therefore is known as a 'second generation of HTS or 2G conductor.

Both HTS materials are ceramic oxides where superconductivity takes place in CuO_2 planes of the material lattice (20). The prevailing belief is that with an increase of CuO_2 planes in the unit cell of the lattice, the critical temperatures of superconductors will increase. Yet, this trend is absent for more than 3 layers (23) since compounds with higher number of planes are not chemically stable. Thus, alignment of the CuO_2 planes of the grains of the material is of crucial importance. Achieving a high level of superconductor grain aliment is one of the inhibiting factors in an HTS wire manufacturing, downgrading the performance of HTS wires. To understand the limitation and potentials of these HTS conductors first it is necessary to understand how difficult is to produce an HTS wire (tapes).

2.3.1 Manufacturing of Bi–2223

The 1G HTS tapes are made by the Powder In a Tube (PIT) wire technology. The PIT production process, illustrated in Fig.2.3, starts by loading a pressed powder pellet into a silver tube, which is further on drawn into thinner diameter wires. Thin wires of Bi–2223 immersed in a silver matrix are packed into a silver tube and drawn again. This is continued until the target wire diameter is obtained (24). The final step of extrusion is rolling the multi–filament wire into the tape with rectangular cross section, where ∼4 mm wide and ∼0.3 mm thick tape is most common. Multi–filament wires are reacted in an atmosphere of oxygen, which can diffuse through silver at high temperatures. As mentioned before, good alignment of the Bi–2223 grains is a crucial element which determines critical current density of the final conductor. As a final conductor, a BSCCO conductor comprise 70%-30% share of silver to HTS ratio which can vary but not more then 20%.

One of the leading companies of 1G HTS today is Sumitomo Electric Industries (25). American Superconductor Inc. started its HTS program with 1G but have recently declared development of only 2G HTS (1). Several manufactures, somewhat smaller, such as Bruker Energy(26), Zenergy Power(27) and others also have 1G in its product portfolio.

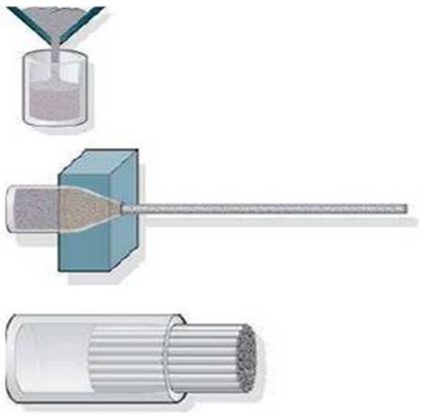

Figure 2.3: Powder In a Tube production steps - PIT wire technology is based on basic production steps illustrated in this figure. The loading of a pressed powder pellet into a metal tube is the first step which is followed by an extrusion. Last step illustrates packing and extrusion of several wires into a multi–filament wire. The last step is repeated until desired size of the filament is achieved.

2.3.2 J–B–T characteristics of 1G HTS

One of the tapes used in the Superwind project is 1G HTS. Thus, the nature of BSCCO characteristic critical current - magnetic field interaction will be discussed on the example of critical current of the DI-BSCCO from Sumitomo(25). The critical current will be a function of an external magnetic field applied either parallel or perpendicular to the wide side of the tape. Presented in the Fig.2.4, the $I_c(B)$ dependence is shown for several temperatures. For T= 77 K and magnetic flux density B $\leq$0.5 T applied perpendicular to the wide side of the HTS tape, the critical current reduction is large. For the parallel direction of magnetic flux that is not the case. Magnetic anisotropy of 1G HTS is strongest at high temperature ($\geq$70 K) where at lower temperatures ($\leq$30 K), 1G tape will exhibit both lower sensitivity to magnetic field and lesser difference between parallel and perpendicular directions of external magnetic field.

At low temperatures (20 K – 30 K) an increase in I_c of 1G tape can be tenfold where a lower magnetic sensitivity and anisotropy of the conductor are observed. Thus, it may be concluded that the Bi–2223 superconductor is suitable for low magnetic field applications at high temperatures where the performance of a tape is substantially improved at lower temperature.

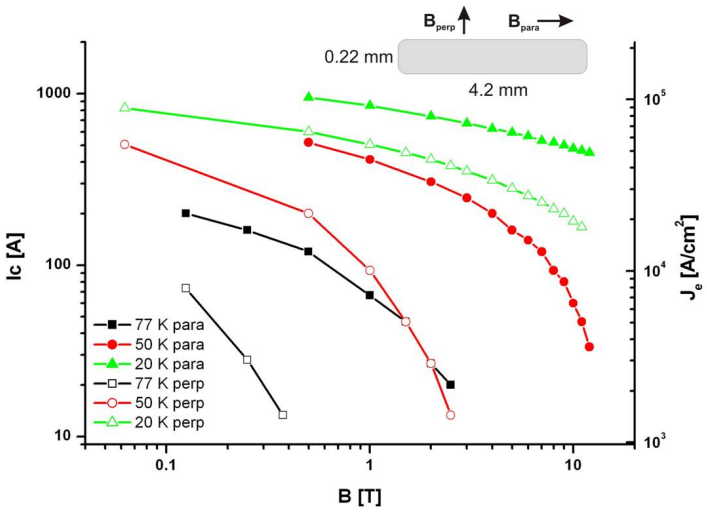

Figure 2.4: Critical current of DI-BSCCO - The figure illustrates the critical current I_c and engineering critical current density J_e (defined as the critical current divided by the wire area of a 4.2 mm wide and 0.22 mm thick Bi–2223 wire from Sumitomo) at different temperatures and as a function of applied field either parallel (B_{para}) or perpendicular (B_{perp}) to the HTS tape. Reproduced from:(28).

2.3.3 Manufacturing of YBCO

Several attempts were reported of YBCO wire production with PIT wire technology, but the obtained critical current densities reported were orders of magnitude lower compared to Bi–2223 (28, 29, 30). Insufficient alignment and connectivity of the grains are the main causes for the low values of critical current. Therefore, even though the YBCO wires produced with PIT technology have superconducting properties, the values are too low to make this production practical. One of the ways to obtain a bi-axial alignment of the CuO_2 planes of the YBCO grains in a conductor is to grow the YBCO as a thin film on the top of a bi-axially textured substrate(31). Such wires are called coated conductors (CC) and are based on either bi-axial textured metal substrates or bi-axial deposition of buffer layers on non-textured metal substrate(31).

Several ceramic buffer layers may be deposited on the metal in order to achieve a better match between the material lattice of the buffer and the lattice of the YBCO. The illustration of the general architecture of coated conductors produced commercially today is presented in Fig.2.5. American Superconductor as a primary manufacturer of CC is using the Rolling Assisted Bi-axial Textured Substrates (RABITS) (32, 33),

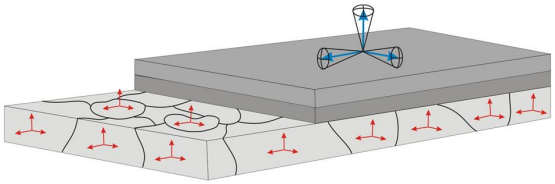

Figure 2.5: YBCO Coated Conductor (CC) - Architecture of coated conductor consisting of a metal substrate (light gray), one or more ceramic buffer layers (darker gray) and on top a $(RE)Ba_2Cu_3O_6$ layer (dark gray). Orientation of $(RE)Ba_2Cu_3O_6$ grains is induced by the texture of substrate and buffer layers. Reproduced from:(28).

sputtering of buffer layers and Metal Organic Deposition (MOD) of the YBCO layer (1), which is subsequently sealed by a metal layer on top. SuperPower is using non–textured metal substrates and obtain a bi-axial textured buffer layer by Ion Beam Assisted Deposition (IBAD) (34) followed by Metal Organic Chemical Vapor Deposition (MOCVD) of the YBCO layer (2).

2.3.4 J–B–T characteristics of 2G HTS

Critical current of a CC from American Superconductor is shown in Fig.2.6 for 75 K and 64 K. It is obvious that the J_e anisotropy is smaller for CC compared to the 1G tape at magnetic fields larger than 1 Tesla and at temperatures above 64 K.

It should be noted that the active superconductor layer (YBCO) of the CC is only $\sim$1 μm thick compared to the total tape thickness of 0.2 mm. Thus the critical current density of the superconductor by itself is $J_c = 2{\cdot}10^6 \mathrm{A/cm}^2$ at T= 77 K and in zero field. Given that YBCO CC are a relatively new technology and $R\&D$ is ongoing, substantial improvement of J_e of CC could be achieved either by improving the HTS properties of the thin layer of YBCO (improved pinning, alignment...), increasing the layer thickness where J_c is maintained, or by reducing the substrate thickness (35, 36, 37). Some of the listed methods may sound simple enough but a number of challenges must be addressed first.

One of the major challenges in further development of the coated conductors is to increase the superconducting fraction of the tape cross section area by growing thicker layers while maintaining J_c. The present technology is limited to a YBCO layer thickness of $\leq$2 μm, since further increase in thickness is not improving J_e (33, 38).

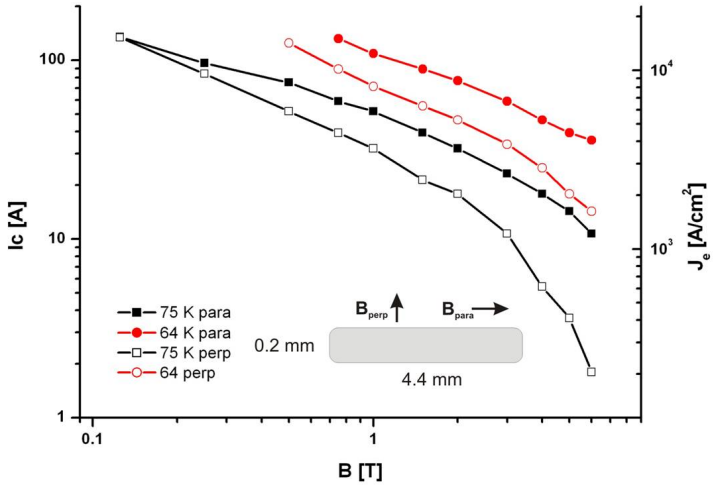

Figure 2.6: Critical current of YBCO, AMS344 - Critical current, I_c, and engineering critical current density, J_e, of 344 coated conductor from American Superconductor as function of the field parallel or along the tape for two temperatures. The cross section area of the tape is shown by the insert and the critical current in self field and at T= 77 K is I_c= 140 A (1).Reproduced from:(28).

It should be said that progress with respect to YBCO layer thickness is reported (39) without loss of J_c which is highly encouraging.

2.4 Production of HTS: scale consideration

Production capacity of HTS (both 1G and 2G) worldwide is estimated to be 1000 km annually in 2009 (40) which is only a fraction of the production capacity required to maintain large-scale application such as HTS machines or HTS cables (∼3% (41)). The maximum length of HTS conductors in continues pieces needs to be increased. For 1G conductor, lengths above 1000 m for a single tape have become a standard (42), while 2G tape is still produced in only a few hundred meters lengths (43, 44), even though a slow increase in lengths is noticeable (45). Issues with increasing the length of single tape in part stems from variations of critical parameters over the length of the tape, where a section with low I_c downgrades the whole batch.

An important aspect to consider before choosing which HTS technology to use in large scale application is growth potential. As a good point of reference with respect to the cost - performance evaluation, a low temperature superconductor (LTS) could

be used. A cost - performance factor is compared among superconductors through the cost of conductor in USD (US Dollars) versus current capacity per length in kAm. $NbTi$ and $NbSn_3$ conductors have a cost of 1 USD/kAm and 8 USD/kAm at 4.2 K, respectively. Breakdown of material content for both 1G and 2G tapes can provide better insight in scaling implications with respect to the cost - performance evaluation.

A BSCCO HTS tape is comprised of 70%–30% share of silver to superconductor ratio (46). The cost of 1G HTS will never become lower than cost of raw material used. Due to high content of silver, even if the cost of HTS is neglected, the cost of 1G tape will be 70% of the value of silver, i.e $0.7C_{Ag}$, where C_{Ag} is the cost of silver. If the 0.3 USD/gram (47) is adopted for a price of silver, the resulting cost for 1G tape taking only that into the account would be ∼20 USD/kAm. The price in 2011 for 1G HTS tape was ∼200 USD/kAm, which implies that the cost reduction is possible, assuming production and cost of BSCCO are lower than silver. However, the lowest cost 1G HTS could ever reach would be closely correlated to the price of silver.

On the other hand, 2G HTS is comprised of a 1–2 micron thick superconducting layer deposited on a substrate (such as stainless steel) resulting in HTS tape which is 0.2 mm–0.3 mm thick (1, 2). The HTS content (YBCO) in 2G conductor is 0.5% – 1.5% of conductor thickness. Thus, the cost of YBCO will be added to other costs. Other cost contributors such as cost of substrate, buffer layers and laminates will be minor contributors to a total cost. It should be noted that capital investment and production cost can be significant (44). Nevertheless, these initial costs will be subjected to a learning curve and as the production optimization level increases, so will the reduction of cost, all driven by the increase in volume of production.

Yttrium is one of the rare earth (RE) elements in the periodic table with the cost of 56 USD/kg for yttrium oxide in 2010 (48). Since the required amount of yttrium is very small, ∼ 30 mg per meter for 4 mm wide tape with 1.2 micron thick YBCO layer, the cost of active raw material in 2G HTS tape would be ≤1 USD/kAm. Cost of substrate and thin coating of silver were included as well while the deposition efficiency of YBCO layer was not included. The cost of 2G HTS in 2010 was 200–400 USD/kAm.

This simple analysis shows that the cost of 2G HTS stems from its complex production process and thus holds the potential for great reduction with production optimization. It is also important to stress that 2G technology harbors higher potential of increasing J_e, a parameter not explicitly quantified by USD/kAm criteria. Several

approaches have been proposed and promising results were reported such as improved pining(49) and increased HTS layer thickness as mentioned before.

Chapter 3

HTS machines

"The rotating armatures of every generator and motor in this age of electricity are steadily proclaiming the truth of the relativity theory to all who have ears to hear." **by Leigh Page**.

The motivation for superconducting machines was known from as early as 1960 when the first demonstrations of superconducting machines took place (50). Hence, the idea to improve the conventional design of electric machines has been tried before with low temperature superconductors (niobium titanium and triniobium tin) in several demonstration projects(50). Most of the initiated demonstrations were successful and proved merits and technical feasibility of superconducting machines. However, in the first ambitious effort to demonstrate a fully superconducting synchronous machine, where both stator and rotor winding were superconducting(51), that was not the case. A 50 kW machine failed during testing, yet it was the very first evidence of the importance that ac losses have in application of superconductivity and complexity involved in the design of superconducting machines.

After initial successful demonstrations, an aim of further LTS machine development focused on utility generators where the number of designs and demonstrations ranging from 20 MW up to 1200 MW was carried out. All of these have confirmed over and over that the concept of a superconducting machine is promising, but have also identified various issues where the difficulty of the refrigeration to 4 K was by far the largest(50).

With the discovery of HTS and the possibility of higher operation temperatures, superconducting machines have become again interesting to researchers. A main difference between LTS and HTS application is not only that the temperature range is substantially higher, but the temperature operational window of HTS material is much wider. Hence, a refrigeration system and thermal insulation can be simpler and more efficient compared to LTS systems. A number of designs have been suggested over the course of two decades to enhance electric machines with usage of HTS. Among the proposed machines which could benefit by employing HTS were synchronous, induction, switched reluctance, trapped field and dc homopolar machines. Improvements and design challenges of the most promising HTS machine concepts will be reviewed in coming sections where the concept most suitable for lightweight machines is identified.

It is interesting to notice that even from early on in the history of application of superconductivity, very few novel concepts of superconducting machines have been proposed (a Meissner motor, Trapped field motor). Instead, superconductivity was used to enhance conventional designs by increasing either magnetic field or electric loading in a machine.

3.1 Superconducting machine - motivation

Regardless of if it is a dc or an ac machine, machine operation is based on the interaction of two magnetic fields, one from the rotor and one from the stator. It is possible to express the power and torque output of an electrical machine in terms of these fields and the machine dimensions, as 3.1

$$P = \frac{\pi^2}{\sqrt{2}} k_w B_r A_s D^2 L n_s \Longrightarrow \frac{P}{n_s} = T = (2\sqrt{2}\pi k_w) B_r A_s V \tag{3.1}$$

where B_r, A_s and V=(D/2)$^2\pi$L are flux density at an air gap produced by the rotor, electrical loading of an armature winding and the volume of a machine (air gap), respectively. k_w is the winding coefficient for armature winding.

For a conventional electrical machine, the product $B_r A_s$ is limited by material properties. Maximum values of peak air gap flux densities in all machine designs are limited to values 1 T due to saturation of the magnetic circuit. Any increase in the flux density would call for substantial magneto-motive (MMF) force to drive it, which means higher current in the copper turns of the rotor winding (or thicker permanent magnets

if a PM machine is in question). Consequently, one can come to the conclusion that excessive cooling must be used to manage temperature increase in the rotor winding (caused by high current densities), and that only a small increase of the air gap flux density could be obtained due to the low magnetic permeability of saturated steel.

Electric loading of a conventional machine produced by the stator (armature winding) is bound by the maximum temperature of electric insulation (usually 120°C – 150°C) to 50 kA/m – 200 kA/m depending on cooling (52, 53). An additional, but less prominent constraint to armature loading is the maximum force (radial in faults). Thus, a closer look at the torque expression, 3.1, by taking into account that $B_r A_s$ product has its maximum, reveals that the size of a conventional electric machine is related to the torque T that the machine can develop. In order to increase the torque density of machine, according to 3.1, only an increase of $B_r A_s$ will give results.

Superconductor, with practically lossless magneto-motive force (MMF) can provide a significant increase of MMF available in a machine design. Consequently, the product $B_r A_s$ could be improved by increasing the value of the air gap flux density to $\geq$2 T or even further by increasing both the air gap flux and the electric loading, depending on where the superconductors are employed. Accordingly, superconducting machines can be made smaller than conventional machines and the degree of volume and weight reduction can be adjusted by choice of the $B_r A_s$ value.

3.2 Design concepts of an HTS machines and practical experience

The description of design concepts for HTS machines proposed and demonstrated to date is presented in the following section. The most frequent design used for an HTS application is a synchronous machine (SM), where the dc application of HTS offers the most of advantages(54). Several other HTS machines such as induction, switch reluctance, trapped field machines, dc homopolar machines and others are described as well.

3.2.1 Synchronous machines (SM)

The majority of the designs proposed and demonstrated have been radial flux SM, but the same configurations with a little modification are applicable for axial flux machine

as well. Moreover, it is possible to make a distinction between two concepts: HTS SM where only field winding is superconducting and HTS machine where both field and armature windings are superconducting, which will be referred to as a full HTS SM in order to avoid confusion.

3.2.1.1 An HTS–SM with warm rotor

An HTS machine with a conventional armature winding (slotted stator), warm rotor iron and an HTS rotor coil, illustrated in Fig.3.1, is the HTS machine design closest to a conventional machine where only a conventional field winding is replaced by an HTS field winding. The motivation for this concept was based on improved efficiency of large machines, since with HTS field winding excitation loss can be significantly reduced which would in turn make the machine more efficient. An advantage of this

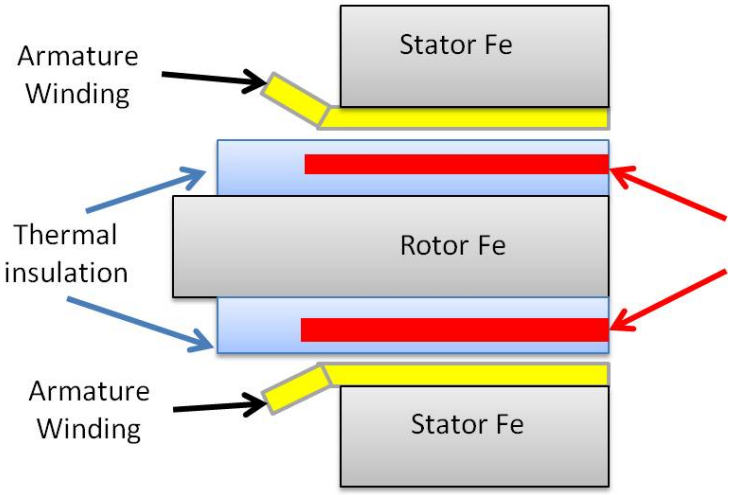

Figure 3.1: An illustration of HTS-SM design with warm rotor iron - The field winding is made of number of HTS coils (red) which are thermally insulated (blue) from the rest of the rotor. Thus, the rotor steel (gray) is at room temperature, same as are the armature winding (yellow) and stator steel (gray).

concept compared to the other HTS SM designs can be a simpler torque transfer since most of the developed torque acts on the warm steel and not on the HTS coils.

Demonstrations: An HTS SM with warm rotor In 2003, a 1.5 MVA HTS generator has been designed, built and successfully tested by General Electric as an engineering prototype for a 100 MVA turbo generator(55). The HTS coils in the 1.5

MVA demonstrators, wound with BSCCO HTS were designed to operate at 20K–40K (55, 56). A closed cycle helium refrigeration system was employed using GM cryocoolers (56, 57). The refrigeration unit and the helium transfer coupling used was a full size model needed for a 100 MVA generator (55, 57). Consequently, the design of the full 100MVA generator based on the constructed prototype is being finalized (55, 58).

In Europe, Converteam had undergone a construction of a 1.79 MW, 28 poles, 214 rpm hydroelectric generator(59, 60) which was actually a retrofit of old hydroelectric generator. The HYDROGENIE HTS generator is excited from a 1G HTS field winding cooled to about 30 K using high pressure helium gas(61) which is transferred from static cryocoolers (GM) to the rotor via a bespoke rotating coupling (62). The rotor steel in the machine is kept at room temperature while the armature winding is left unchanged, i.e. conventional slotted stator(61).

3.2.1.2 An HTS SM with cold rotor

An HTS SM machine design where the entire rotor is cooled down to operating temperatures of HTS is illustrated in Fig.3.2 and Fig.3.3. The difference between these two is the presence of ferromagnetic steel in the cold rotor. In the first design, an HTS field winding is wrapped around cold steel, while in the second an HTS field winding is mounted on a nonmagnetic support structure. In both concepts, a thermal insulation encloses the whole rotor. The latter is often called an air core HTS machine since the rotor holds no ferromagnetic material. The air core concept of HTS SM requires the highest amount of HTS (large MMF is necessary in absence of steel) but it is also the concept with highest power density (large weight reduction due to lack of rotor steel).

As a consequence of thermal insulation an HTS machine with a cold rotor will have a much large effective air gap (10 mm - 200 mm), compared to an HTS SM with warm rotor or a conventional machine. Consequently, the amount of MMF required to achieve considerable values of magnetic flux density at armature winding ($\geq$1 T) needs to be much larger than for the conventional machines. With such high values of MMF at rotor and dominant air nature of machines, electromagnetic parameters will differ considerably from what is found in the conventional machines.

In addition, for both designs where the entire rotor is cold, a few additional design specific elements have to be introduced. A Torque Transfer Element (TTE) is the structural element which is required to transfer rated torque from a cold rotor to a warm

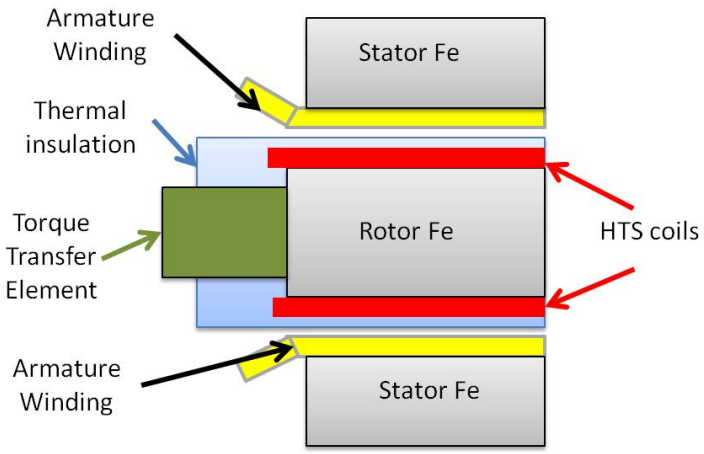

Figure 3.2: An illustrations of HTS SM design with cold (ferromagnetic) rotor - The field winding is made of a number of HTS coils (red) which are at the same temperature as the rest of the rotor. Armature winding (yellow) and stator steel (gray) are at room temperature. Additional element in the design is the Torque Transfer Element (dark green). The armature winding (yellow) can be either an air-gap winding or conventional slotted design.

shaft. The developed electromagnetic torque needs to be transferred to a warm shaft (to either primary mover in a case of generator or mechanical load in a case of motor) this element will need to provide both mechanical strength and thermal insulation, objectives which are in contradiction for most structural materials. A torque transfer element design and concepts will be discussed in details later on, but it should be stated that its necessity in the design can significantly increase complexity of an HTS machine design.

An additional consideration for HTS SM with cold rotor is loss in the cold steel. Although a field winding and rotor steel are exposed to a main dc flux, in a machine operation some ac flux will be present. Any load change or spatial and time harmonics of flux linkage in a machine will cause some loss in the rotor steel (not a big loss and often neglected for conventional machines). Yet, due to a poor cooling efficiency, any (even small) loss dissipated at low temperature can become a significant load for a cooling system, and thus not negligible anymore. Several HTS machine designs(63, 64), particularly where high power density is an objective (65), have employed an air gap armature winding instead of a conventional winding placed in slots of stator steel laminates. In the following section advantages and issues tied to air gap winding are

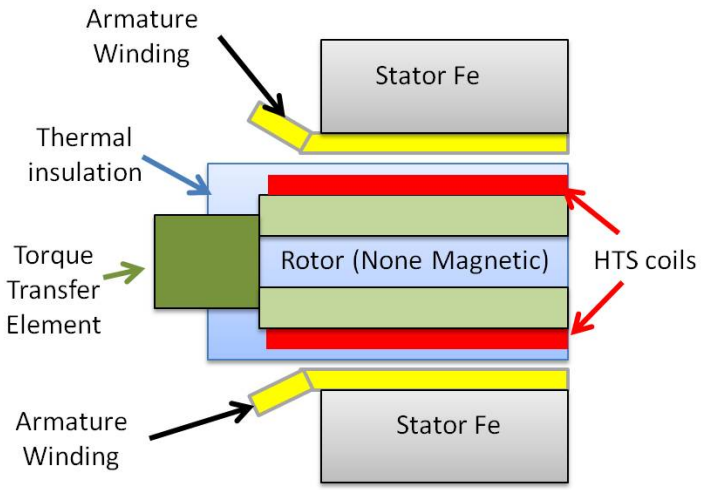

Figure 3.3: An illustrations of the "air core" HTS SM design - The field winding is made of a number of HTS coils (red) which are at the same temperature as rest of the rotor. A mechanical support for HTS coils (light green) is made from nonmagnetic material (stainless steel or composite material). An armature winding (yellow) and stator steel (gray) are at room temperature and Torque Transfer Element (dark green) is a mechanical interface between low temperature and room temperature. An armature winding (yellow) can be either an air gap winding or conventional slotted design.

presented.

Demonstrations: An HTS SM with cold rotor Reliance Electric (Rockwell Automation) was the first company to start development of HTS motors in US(58).DOE funded projects for a 150 kW motor built and tested in 1996(66) and for a larger 750 kW motor tested in 2000(67). Both motors were 4 poles, 60 Hz machines using conventional slotted armature winding (54) (water cooled) with HTS field coils fabricated by AMSC (68) using BSCCO HTS conductor cooled by helium gas down to 20 K – 27 K.

Two HTS SM with cold rotor steel have been designed and constructed by Siemens (69). The first machine was 400 kW (64), 1500 rpm with HTS field winding made from BSCCO coils, with an air gap armature winding. The machine was operated at 25K and cooled with GM cryocooler placed outside of machine where liquid neon served as a coolant media(65). The second machine, had a rating of 4 MW with an identical design concept also employing 1G HTS in the field winding (70, 71). Both motors were developed for ship propulsion as the primary application field and are being certified

by Germanischer Lloyd (70).

Several machines were constructed in projects led by American Superconductor (AMSC). Among the first was a synchronous condenser, built to improve the power factor of power system (72). Rated at 12 MVAR, the machine had a 1G HTS field winding and an air-gap armature (73). AMSC also designed, built, and tested a 3.5 MW four pole, 1800 rpm machine (63). In this design, the whole rotor including coils wound with BSCCO HTS conductor was cooled down to 35 K using a closed cycle neon heat pipe concept (72). Under contract with the Office of Naval Research AMSC built two prototype motors (5 MW, 230 rpm motor (74) and 36.5 MW, 120 rpm motor (75)) as a power compact ship propulsion alternatives to existing ship propulsion concepts (74).The armature is liquid cooled with dielectric insulating oil. Both motors employed 1G (BSCCO) field windings cooled with GM cryocoolers and operated at 30 K.

The objective of the HTS 36.5 MW motor was the development of a full - scale, high power density, lightweight, advanced propulsion motor suitable for future naval applications. It employs many of the technologies developed for the 5 MW motor, including the HTS field winding, a high current density liquid - cooled stator, and the refrigeration, mechanical support, and excitation systems. This machine presents the highest torque HTS machine constructed up to date with an output shaft speed of 120 rpm, and over 2.9 MNm of torque and weight estimate of 75 tons which is proof of how difficult it is (but not impossible) to build compact high torque machines(54).

At University of Southampton a 2 pole, 100 kVA HTS SM with a cold rotor generator was designed and constructed in 2004 (76, 77). The HTS rotor is designed to operate in the range of 64 K – 77 K using either liquid nitrogen or air where coolant was introduced through a hollow shaft and rotating coupling (77). The field winding was assembled from a number of coils wound from BSCCO HTS conductor. The innovative approach in this design was handling a perpendicular magnetic field which would at higher operation temperatures constrain the current capacity of BSCCO coils to a high degree(78). The same generator was retrofitted into an air core configuration by omitting a ferromagnetic core(79) where also BSCCO coils were used and cooled by sub-cooled nitrogen(80).

The 1 MW, two pole HTS machine employing the BSCCO coils in air core configuration and air gap armature winding was designed and constructed at KERI (81, 82). The rotating HTS field coils were cooled below 30 K (83) by the cryogenic rotating

cooling system which consisted of GM cryocooler and thermosyphon via neon circulated cooling system. Issues with ensuring desired degree of concentric alignment were reported (83).

Several plans have been put forward to design and construct a 10 MW wind turbine generator from the time the Superwind project started (2007). Converteam came first with an air core HTS SM machine using 1G HTS tape(84). AMSC has also announced intention to construct a wind turbine DD generator under the brand name SeaTitan(85). Construction of the proposed wind generator has not begun to date, as far as the author is aware.

3.2.1.3 Fully HTS-SM

There were several suggestions towards large utility fully superconducting generators using LTS (86, 87) and a very limited number of laboratory scale projects of fully superconducting machines using HTS conductors (88). The obvious advantage of fully HTS SM is higher electric loading of HTS armature (89). In addition, if an armature and field winding operate at the same temperature, the air gap can be made much smaller and thus the whole magnetic design of the machine becomes more efficient. Nevertheless, the largest issue in this concept is the ac loss generated by HTS armature. Since the HTS in the armature will be in the path of full flux (alternating with revolution of rotor), and will also carry ac current, the ac loss will be the dominant loss in the machine. At the moment, the amount of ac loss in high field ac application is regarded as prohibitive (54) due to a poor cooling efficiency. Several approaches are investigated in order to decrease the ac loss of HTS conductors (90, 91). A proposal for fully superconducting wind turbine generators (class of 10MW) has been put forth by AML using a Double-Helix technology and MgB_2 superconductor (92). Yet, no HTS full superconducting machine has been developed by industrial partners.

3.2.2 Other types of HTS machines

Several other HTS machines such as induction, switch reluctance, trapped field machines, dc homopolar machines and others suited for high power applications were demonstrated as well. Intended application for these was more focused on improvement or modification of machine operation characteristic (torque – speed, overload characteristic, etc.) than on to increase of torque density of such machines. A brief,

overview of demonstrated projects of induction, switched reluctance, trapped field and dc homopolar machines are presented in the following section.

Induction machines with HTS conductors Induction machine designs published so far had only a HTS rotor squirrel cage (93, 94). In this way, a torque characteristic of an induction machine would have a different trend compared to a conventional machine, due to the ac loss in HTS bars, which is a function of slip (higher the slip, larger the rotor resistance) (95). Consequently, start and maximum torque of induction machine will become much higher (93) and due to very stiff characteristic (very small slip) the energy loss in the rotor can be very small (96, 97). However, the dominant ac nature of induction machines (even at slip frequencies for rotor currents) requires improved HTS conductor with respect to ac operation.

Switched reluctance machines If an HTS bulk material is introduced in a rotor, due to the flux screening effect of HTS material, flux path permence of d axis and q axis of a machine will differ, hence reluctance effect will be enhanced. Several demonstration projects were carried out where the latest one was a 400 kW motor with $NdFeB$ magnets and bulk HTS (YBCO) in four pole rotor topology which was successfully constructed and tested (98) where the rotor was cooled via liquid nitrogen at 77 K (99).

Trapped field machines HTS material can be regarded as a particular type of permanent magnet. If the magnetic field is trapped inside of HTS material, the HTS bulk would sustain the field for very long time. Maximal trapped flux density for bulk material would correspond to 1T – 2T at 77 K and 7 T – 8 T at 20 K (99). Thus, in principle this would be a very convenient way of designing an electrical machine, since these machines are very similar to conventional permanent magnet machines. However a number of issues need to be addressed such as magnetization techniques, stability of trapped field, ac loss and etc.

DC homopolar machines DC homopolar machines are based on Faradays disk machine (100, 101). It is a relatively simple machine design comprised of a dc magnetic field winding (usually simple solenoid) which creates an excitation field in axial direction. A conducting disk which presents a rotor is placed in such a way so both axial

axis are aligned, thus the excitation field is perpendicular to the disk (54). Current will flow from the center of disk towards the outer radius where current collectors are placed at the edge of a disk and at the center of a disk. In this way current and magnetic flux are perpendicular; hence a torque is proportional to the product of current, flux and radius. Limiting issues in the design of dc homopolar machines (as well as for conventional dc machine) is the design of current collector, here even more so as the currents of the rotor are very large. With higher magnetic flux, rotor current becomes lower for the same torque; hence a collector has a simpler design. The first successful demonstration came with LTS in (102) a field winding wound by LTS. A 3.7 MW machine was designed and constructed as a prototype, where a preliminary design of a 36.5 MW generator is being developed for U.S Navy application by General Atomics (103).

3.3 HTS SM design considerations

A torque transfer element, an HTS winding and cooling system are the most essential aspects of an HTS machine design. Considerations with respect to the mentioned design aspects will be presented in the following sections. A state of the art low temperature refrigeration systems is reviewed where advantages and drawbacks with respect to potential wind turbine generator application for offshore wind turbines are discussed. Afterwards, a torque transfer element and its unique requirements are identified. The general guidelines are derived for geometry of this element regardless of material choice, which allows an optimized design to be applied for the design of an experimental setup. Finally, HTS coil topologies are discussed and magnetic anisotropy of an HTS coil is acknowledged.

3.3.1 Low temperature cooling system overview and thermal insulation

Refrigeration at low temperatures is an inefficient process. It is well known that the ideal Carnot efficiency can never be attained in practice. Since all practical cryocoolers work on the bases of compression and expansion of gases (usually helium), present cryocoolers are still a long way from Carnot ideal limit (104). A typical ratio for input work /output work for the temperature range 300 K to 30 K is approximately 100 to

1. This means that in order to obtain a 100 W of cooling power at 30 K, an electrical input power needs to be about 10 kW (50).

Several concepts of refrigeration can be used depending on the HTS machine concept and operating temperature. Often applied configuration is cooling in a closed cycle of helium with one or several cryocoolers where a coolant which can be either a gas or a liquid (nitrogen, oxygen, neon, hydrogen) is circulated between heat exchanger (cold head) and HTS coils. Since gas or liquid is possible to be transferred via rotating coupling between stationary cold head and rotating HTS coils, where either a thermosiphon or forced circulation of fluid is employed, this configuration has particular benefits for HTS SM machines and is by far the most readily used (58, 63, 82, 105). Instead of convection cooling, where fluid is the heat transport media, it is also possible to employ a conduction cooling where HTS coils are in a good thermal contact with heat exchanger (cold head) (106). Hence, a cyrocooler needs to rotate with an HTS winding. Presented concepts are considered as a standard solution where "off the shelf" cryocooler is employed. As an alternative to this concept, it is possible to use a boiling of some of the gaseous with appropriate boiling temperature (T_{He} ∼4 K, T_{H_2} ∼20 K, T_{Ne} ∼27 K and T_{N_2} ∼77 K) where fluid absorbs the heat by phase transition (107). If the system is closed, a liquefier would be necessary in the cooling loop, otherwise an inflow of cooling fluid must be ensured (constant inflow of LN_2 for example). Gifford-McMahon (GM) refrigerator is the by far most often used cyrocooler used for low temperature cooling, while Pulse Tube refrigerators are looking very promising.

A Gifford-McMahon refrigerator Gifford-McMahon (GM) refrigerators are used in cooling thermal shields of low temperature superconductor MRI systems (cooled ≤ 4.2 K). Hence, it is considered to be a well established technology (65, 108). The refrigeration power of available models is limited to ∼100 W at ∼20 K, which suggest that for higher cooling requirements several cryocooler in parallel will be necessary. Efficiency of a cryocooler is relatively good, where for example AL325 GM from CryoMech has 100 W at 25 K for 11.2 kW input power (109) which gives a factor of ∼112 for cooling penalty. A GM cryocoolers have couple of drawbacks with respect to machine application. From the HTS machine application perspective oil-lubricated compressors and cold head moving displacers are considered weak links, both of which have high maintenance requirements (once annually). Also dependence of the orientation with

respect to gravity can become an issue (65). Thus, GM cryocoolers are available and are not costly, yet they do require maintenance which is an issue for future offshore application.

A Pulse Tube refrigerator Pulse Tube refrigerators (PTR), developed as an alternative to GM, have no moving displacer in the cold head. Cost of PTR is considerably higher compared to a GM. In addition, the cooling efficiency is lower (e.g.the PT63 available cooling power at 30 K is 11.5 W for input power of 4.2KW (110)). Consequently, a cooling penalty becomes ∼356 which is substantially higher than GM. However, if an oil free linear compressor is employed (which is also a possibility in GM refrigerator systems), a cooling system with PTR could have a lower maintenance (once every 2 – 3 years) and longer lifetime (111). In addition, PT refrigerates can be highly susceptible to orientation (111) where operation with cold end down is a requirement (110). However, a development of Stirling type co-axial PT cryocoolers is encouraging since these are able to be incorporated on-board in rotating equipment (112). Substantial efforts are invested in development of PTR in order to make them more efficient and less costly (111, 113).

Thermal insulation Regardless of which refrigeration cycle is used, HTS coils have to be well insulated in order to decrease a parasitic heat inflow and minimize effects of poor cooling efficiency on the whole system efficiency. Consequently, a cryostat for HTS needs to be designed. For temperatures between 20 K – 80 K, a cryostat will probably need to have a vacuum insulation in order to minimize convection and conduction heat transfer. Depending on the HTS SM design concept, an additional requirement for cryostat and vacuum insulation is to be as thin as possible (an air gap is vital for machine design). To prevent radiation heat transfer, a Multi Layer Insulation (MLI) in the form of thin aluminum foils can be used as an efficient way to reduce radiation to an acceptable level.

The necessity of a low temperature cooling system is certainly one of the most prominent inhibiting factors for development of HTS machines and reluctance of industry to employ this technology. Thus, mastering and improving a low temperature refrigeration and thermal insulation technology is as important for HTS application as development of the HTS.

3.3.2 Torque Transfer Element (TTE)

The main candidate for achieving significant improvement of torque density is an air core HTS SM. This design needs to have an element that can transfer the full electromagnetic torque (both rated and fault conditions) from the cold rotor to the warm shaft of the primary mover. Hence, the heat transfer through the torque transfer elements needs to be minimized. A suitable name for this element could be Torque Transfer Element (TTE) which will be used through out this thesis. Torque tube is also a commonly used name in publications.

The mechanical strength and thermal conductivity are objectives, standing in contradiction for such an element. Although a TTE represents one of the essential elements in a design of a HTS SM with a cold rotor, surprisingly little has been published on this subject and the challenges it involves. It should be stated that the heat transfer through the TTE is a large contributor to the base load of the refrigeration system next to the current leads and radiation heat; hence its optimization is critical.

In LTS application for large turbo generators, two solutions have used stainless steel torque tubes, where the heat transfer is minimized with a flow of cold gas in the return path from the HTS coils towards the heat exchanger (114, 115, 116, 117). A TTE for HTS machines at Southampton, Siemens and AMSC was based on complex composite material elements. An obvious advantage of composite materials is a rather low heat conduction with strength comparable to that of steel. The fiberglass G10 TTE in the design of the 100 kW (∼320 Nm of rated torque) air core machine developed in Southampton consist of multiple parts, eight 180 mm long "dog−bone−shaped" arms tapered by fiberglass bracing cone (105), where the total heat input (including current leads and heat transfer through the cryostat and TTE) was estimated to be 60 W (105, 118) at 77 K. A G-FRP (glass-fiber reinforced plastics) monolithic TTE was developed by CrossLink Faserverbundtechnik GmbH for Siemens for the 400 kW ship propulsion machine with ∼2500 Nm for rated torque and only 22 W of total cooling power requirements (119) at ∼30 K. An even more impressive accomplishment for the 400 kW machined design is the fact that the torque tube was able to sustain torques up to 37 kNm, which is ∼15 times higher than rated torque. This was required since the machine had very low synchronous reactance $x_d = 0.15$ p.u. which would cause large fault currents and forces. AMSC holds several patents regarding TTE, HTS

rotor construction and design(120, 121), yet little information is available on details of solutions used in HTS machine demonstration projects AMSC led.

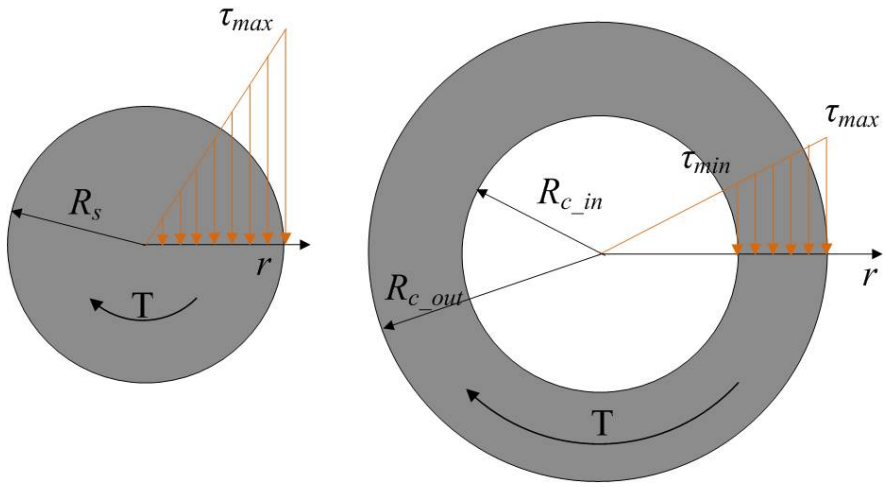

Figure 3.4: The stress distribution in the material - The stress distribution in the TTE for the case that the TTE is the shaft and cylinder. The maximal stress will occur at the largest radius.

Thus, from this short overview one may get the impression that relatively little recommendation on general guidelines toward TTE design are available. With regards to material candidates for TTE, the composite materials (G10 and GFRP) showed advantages over structural stainless steel. However, the design of TTE is far from trivial and its importance in the design of high torque machines (with rated torque of 1 MNm) requires an even higher degree of optimization in order to minimize the cost of refrigeration.

3.3.2.1 Mechanical and thermal consideration for TTE

Regardless of which material is used, the guidelines for optimal TTE are necessary, such that will minimize the heat inflow while providing good torsion transfer capabilities. Let us assume that we need to design a simple TTE. As no complex shapes are of interest (only 2D analytical analysis will be used), a simple shaft and cylinder could be candidates for optimal TTE.

When exposed to the torsion torque, T, the stress distribution in the material is a linear function of distance from the axial axes around which the torsion acts. The

highest sheer stress will always be at the largest radius (122). This is illustrated in Fig.3.4 for a shaft and a cylinder, two simple candidates for TTE. The relation between the torsion torque, T and maximal sheer stress in the material τ_{max} is expressed as

$$T = \int rdF = \int r\tau dA = \int r \underbrace{\frac{r}{R}\tau_{max}}_{\tau} dA = \frac{\tau_{max}}{R}\int r^2 dA \longrightarrow J\frac{\tau_{max}}{R} \tag{3.2}$$

were dF is elementary force, dA is elementary surface of the cross section, r is the distance from the center of the torsion and $J = \int r^2 dA$ is a polar moment of inertia for the particular shape of the TTE. R is the largest distance of material from the axis of torsion, hence $R = R_s$ in the case of shaft or $R = R_{c\_out}$ in the case of the cylinder. The relation $\tau/\tau_{max} = r/R$ was used in 3.2. To compare these two with R_s for a shaft radius and R_{c_out} and R_{c_in} for an outer and inner cylinder radius, respectively, both TTE will need to have same torsion capability. Using 3.2, the equal torque condition can be expressed as 3.3 where $J_s = 0.5\pi R_s^4$ and $J_c = 0.5\pi(R_{c\_out}^4 - R_{c\_in}^4)$.

$$T_{shaft} = T_{cylinder} \rightarrow J_s\frac{\tau_{max}}{R_s} = J_c\frac{\tau_{max}}{R_{c\_out}} \tag{3.3}$$

From 3.3, it is possible to express the shaft's radius as a function of the outer radius of the cylinder and the wall thickness, $\delta_{wall} = R_{c\_out} - R_{c\_in}$, as 3.4.

$$R_s^3 = \frac{R_{c\_out}^4 - R_{c\_in}^4}{R_{c\_out}} = \frac{R_{c\_out}^4 - (R_{c\_out} - \delta_{wall})^4}{R_{c\_out}} \tag{3.4}$$

From 3.4, by defining the ratio $R_s/R_{c\_out}^4$ as a function of δ_{wall}, we can identify "mechanically equivalent" candidates for TTE. If the wall thickness is normalized to the outer radius of the cylinder, equation 3.4 now expressed with 3.5 will become more general.

$$\delta_{wall\%} = \frac{\delta_{wall}}{R_{c\_out}} \rightarrow \frac{R_s}{R_{c\_out}} = \sqrt[3]{1 - (1 - \delta_{wall\%})^4} \tag{3.5}$$

The next step is to define a ratio of cross sections, expressed by 3.6.

$$\frac{A_s}{A_c} = \frac{\pi R_s^2}{\pi(R_{c\_out}^2 - (R_{c\_out} - \delta_{wall})^2)} = \frac{(\frac{R_{c\_out}^4 - (R_{c\_out} - \delta_{wall})^4}{R_{c\_out}})^{2/3}}{R_{c\_out}^2 - (R_{c\_out} - \delta_{wall})^2} \tag{3.6}$$

This ratio using the relation between shaft and cylinder radii defined by 3.4 can be used to estimate which of the candidates, equal in maximum torque rating, will have

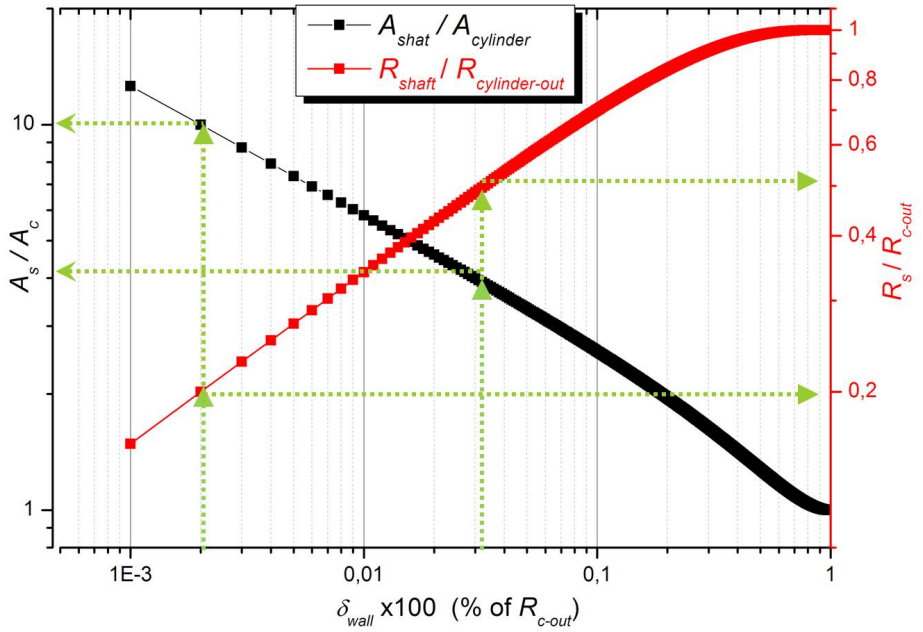

Figure 3.5: Comparison of the cross section area of a shaft and a cylinder with same torque transfer capabilities. - The derived ratio of the cross sections of a shaft and a cylinder with the same maximum sheer stress in the material when exposed to the same torque, as a function of the wall thickness of the cylinder normalized to the outer radius of the cylinder is presented with the black trace. The red trace defines the ratio of the radii of the shaft over the cylinder as a function of the wall thickness of the cylinder normalized to the outer radius when both are equally strong (same torque capability). Thus, the shaft with the same mechanical capability to transfer the torque as for example the cylinder with the radius (outer) of 1 m and wall thickness of 3 cm (which is 3% of the outer radius) would need to have radius of 0.5 m. This is indicated with the green dashed line going from 3% for the horizontal axis and reading the value for the red trace on the right axis. To compare now the heat conduction of these two, the value of the black trace for the 0.03 is found on the left axis for the black trace. The conclusion is that the shaft would have ≈4 time higher heat conduction. In the case of the TTE integrated in the Superwind cryostat design, the wall thickness is 2%.

lower heat conduction. Similar to the previous case, with the same normalization here, the 3.6 can be reduced to

$$\frac{A_s}{A_c} = \frac{\sqrt[3]{1-(1-\delta_{wall\%})^4}}{1-(1-\delta_{wall\%})^2} \tag{3.7}$$

Fig.3.5 illustrates the ratio of the cross section surface of the TTE as a function of

$\delta_{wall\%}$. Looking at Fig.3.5 it is obvious that for the same torque capability (the same maximal torque), a shaft will have larger cross section area compared to a cylinder. Fig.3.5 would imply that the largest possible radius for the cylinder as TTE would result in the lowest heat transfer regardless which material is used. In addition to heat transfer, the cylinder would make a lighter option too, since less material is used. In reality it would mean that the TTE should practically be at the same radii as the air gap.

3.3.3 An HTS field winding

The HTS field winding consists of number of HTS coils. Therefore it is important to understand the limitations of the HTS coils and see which configuration could be optimal for a HTS machine application.

3.3.3.1 HTS Coil design concepts

It is well known (from Ch.2) that both $1G$ and $2G$ HTS conductors are manufactured as a thin tape (0.1 mm – 0.4 mm thick) of different widths from 2 mm – 15 mm (where 4.2 mm is the most common) (1, 2). HTS tapes have specific mechanical constraints, which are necessary in order to preserve the superconducting properties of the brittle ceramic material. These constrains are usually specified in terms of maximal pitch angle an HTS tape can be exposed to, minimal bending radius and maximal strain (stress) after which degradation of the current capacity will occur. Due to all these mechanical limitations, the only practical coil design for winding HTS tape is a racetrack coil.

This is one of the reasons why it is, although not impossible, rather difficult to design a multi phase armature winding with racetrack coils for an all-superconducting machine where the armature is superconducting as well. Insulated tape is wound into racetrack coils which are usually paired into so–called double pancake, thus creating a compact winding assembly. A HTS field winding comprises a number of racetrack coils, stacked together and connected in series.

HTS coils need to be designed and constructed in such a way as to ensure good cooling conduction for the HTS turns, and good mechanical support in both nominal and fault conditions. Finally, HTS field winding also needs to maximize the performance of the HTS tapes, and hence the field winding design should minimize the exposure of HTS turns to the magnetic field (particularly perpendicular to the turns).

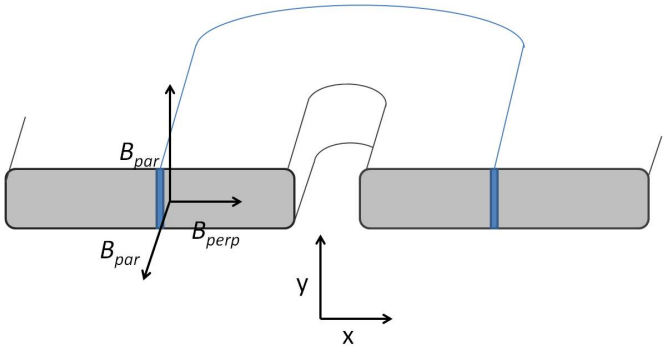

Figure 3.6: An illustration of HTS racetrack coil cross section - One turn of HTS tape is identified in the racetrack coil where prevailing perpendicular direction and parallel direction of flux are indicated with the local coordinate system

3.3.3.2 Magnetic sensitivity of an HTS coil

It has been demonstrated in Ch.2, that the performance of the HTS conductor is sensitive to a magnetic field. It was also shown that 1G will exhibit a higher degree of magnetic anisotropy at higher temperatures compared to 2G HTS conductors.

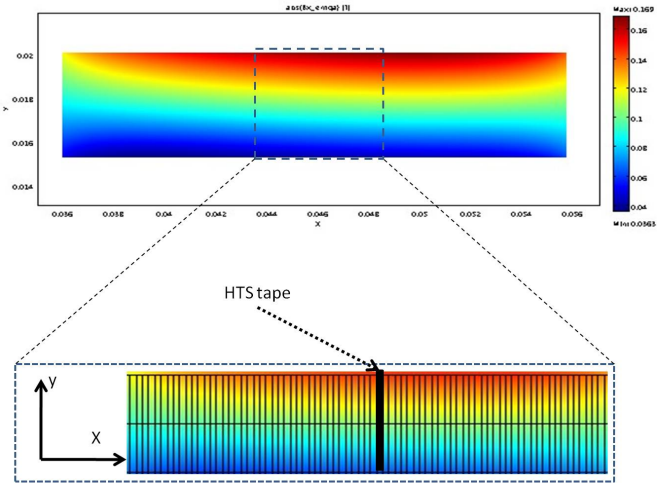

Figure 3.7: A 2D FE simulation of the flux density distribution of the HTS coil - An HTS coil carrying current will be exposed to either self generated and/or external magnetic flux (generated by other coils). The distribution of flux density will differ between turns.

If an HTS coil carries a current, magnetic field will have a certain distribution in space. Nevertheless, it is almost certain that the magnetic field will not be the same

at each turn of a HTS coil. Thus, the turns will exhibit different critical currents. Depending on the particular case, some turns in the coil will be exposed to very large flux while others will be in no field. The critical current of a coil will be limited by the section of the coil with the lowest critical current, expressed as

$$I_{Coil} = MIN(I_c(L)) \tag{3.8}$$

where $0 \leq L \leq L_{Coil}$ and L_{Coil} is length of the HTS tape in the coil. Otherwise, some sections could carry currents above the critical value, which could put them in risk of quench. The same thinking applies for a stack of coils where the coil with minimal critical current will set the current of a coil stack. Therefore, in a good design of HTS field winding there is an effort to minimize the exposure of HTS coils to the perpendicular flux and thus increase available MMF of the field winding. Instead of 3.8, in practice the coil current is derived from the coil voltage which is composed of multiple turns. More on the effects of non uniform flux distribution will be discussed in Ch.5 where the experimental results are presented.

3.4 Electromagnetic model of HTS SM

The difference between a conventional and an HTS machine concept was clarified in the previous section. The next step is to understand the difference between electromagnetic parameters of conventional and HTS machines as well. The cold rotor HTS SM represents the concept of HTS machine with the highest potential for torque density increase and thus could also be a potential concept for a DD wind turbine generator.

Due to the absence of iron in an air core HTS SM or a large air gap caused by a thermal shield, the traditional approach of magnetic permenace of magnetic circuit of an electric machine is inapplicable (52, 53). The flux across the air gap in an air core machine is not only radial, as assumed for a conventional machine. Consequently, the distribution of magnetic flux density cannot be assumed constant in the air gap but rather a function of the radial distance. To evaluate the radial distribution of flux density, analytical formulation of magnetic flux distribution generated by the current sheet approximation of windings (both armature and field winding) is used. A derivation of the current sheet approximation for HTS field winding is presented in Appendix.C.2 and discussed in more details in (4). The discussion on the nature of inductances of

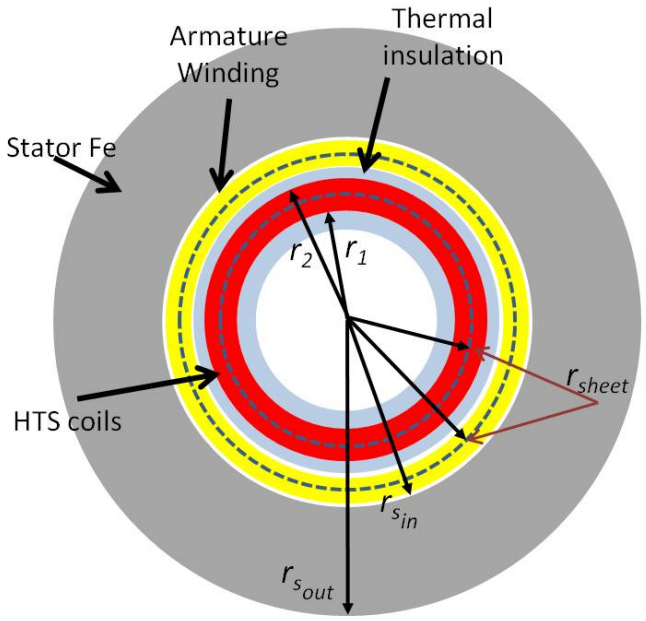

Figure 3.8: Illustration of the generic cross section of the HTS SM - The air core HTS SM machine with the armature winding (the yellow ring) and HTS filed winding (the red ring) enclosed by the thermal insulation (the blue rings) is presented. The stator back steel is presented by the gray ring with radii $r_{s_{out}}$ and $r_{s_{in}}$. Each winding can be approximated by the infinitely thin current sheet at radii r_{sheet}.

an air core HTS SM is presented next, followed by analysis of the impact an armature reaction has on the HTS is recognized which will be the base for the experimental verification of this effect. The flux density distribution expression assumes the geometry of an air core HTS SM illustrated in the Fig.3.8.

3.4.1 Flux density distribution

Vector potential formulation A_z of Maxwell equations is a convenient way to derive analytical expressions for spatial flux distribution in a machine. The method was presented in (52) and adopted here. In the formulation, the authors have assumed an infinitely thin current sheet at radius r_{sheet} with harmonic current distribution along the circumference $A_{(\theta)} = A_{sheet} sin(p\theta)$. The method presented in (52) is extended with the derived current sheet approximation for HTS winding representation.

The radial magnetic flux density distribution of the current sheet enclosed by the stator back iron is presented in 3.9. Saturation and "end effects" are not included in this

approach even though iterative procedures were proposed by other authors where the saturation could be included (123). For $r_{sheet} < r < r_{s_{in}}$, the radial flux distribution can be expressed as

$$B^{\nu}_{(r,\theta)} = \frac{\mu_0}{2} A^{\nu}_{sheet} \cdot \underbrace{\left[\frac{r_{sheet}}{r}\right]^{(\nu p+1)} \left(1 + \eta_s \lambda_s \left[\frac{r_{sheet}}{r_{s_{in}}}\right]^{2p\nu}\right)}_{K^{\nu}_{(r,p)}} \cdot cos\left(\nu p \theta\right) \tag{3.9}$$

or as

$$B^{\nu}_{(r,\theta)} = \frac{\mu_0}{2} A^{\nu}_{sheet} K^{\nu}_{(r,p)} \cdot cos\left(\nu p \theta\right) \tag{3.10}$$

where μ_0 is the permeability of vacuum. The ν is the harmonic order and p is the number of pairs of poles. A_{sheet} is the electrical loading of the current sheet at radius r_{sheet}. If the radial flux density distribution of the armature winding is to be investigated, the current sheet approximation at armature radius should be used (dashed line in yellow ring in Fig.3.8). The radii $r_{s_{in}}$ and $r_{s_{out}}$ are inner and outer radius of the stator back iron. The tangential component of flux density has the same expression as 3.9, where *sin* is used instead of *cos*. The influence of the stator back iron on the flux density of an current sheet is seen throughout parameters λ_s and η_s, defined by the 3.12 and 3.11 respectively, where μ_s is the relative permeability of the stator back iron.

$$\eta_s = \left[1 - \left(\frac{r_{s_{in}}}{r_{s_{out}}}\right)^{2p\nu}\right] / \left[1 - \lambda_s^2 \left(\frac{r_{s_{in}}}{r_{s_{out}}}\right)^{2p\nu}\right] \tag{3.11}$$

$$\lambda_s = \frac{\mu_s - 1}{\mu_s + 1} \tag{3.12}$$

The distribution of the flux density for the $r < r_{sheet}$ will be the same as 3.10 with one difference in $K^{\nu}_{(r,p)}$, which is expressed as 3.13

$$K^{\nu}_{(r,p)} = \left[\frac{r_{sheet}}{r}\right]^{(\nu p-1)} \left(1 + \eta_s \lambda_s \left[\frac{r_{sheet}}{r_{s_{in}}}\right]^{2p\nu}\right) \tag{3.13}$$

3.4.2 Nature of inductance of an air core HTS SM

The air core HTS SM is considered to be the main candidate for lightweight machines, hence interesting for wind turbine generators. Due to the lack of iron and air-gap

armature, the synchronous reactance of an air core HTS machine will be lower than the inductance in conventional machines. Therefore, it is interesting to make a comparison between machine concepts and the nature of the synchronous inductances. The value of synchronous inductance (in p.u.) can be expressed as a function of the magnetic field that the armature current sheet would create at the radius of the armature current sheet (52, 53). For an air core machine, if the armature winding is presented as a current sheet (same as above), the expression for synchronous inductance in p.u. would be (52)

$$L_{(air-core)} = \frac{\mu_0 k_w}{\sqrt{2}} \frac{A_{sheet}}{B_{sheet}} (1 + (\frac{r_{sheet}}{r_{s_{in}}})^2) \tag{3.14}$$

while for the conventional machine where g would stand for the air gap, the synchronous inductance can be expressed as (52)

$$L_{(conv)} = \frac{\mu_0 k_w}{\sqrt{2}} \frac{A_{sheet}}{B_{sheet}} (\frac{2r_{s_{in}}}{g}) \tag{3.15}$$

For example, the values for L_d for SM in MW class can be between 1.5 p.u. – 3 p.u. (124). In MW class conventional machines, the air gap is much smaller than the radius of armature winding. Thus, it is clear what kind of effect a small air gap has on L_d from 3.15 where for 2% air gap, $2r_{s_{in}}/g$ would be 100. In the contrast to a conventional machine, there is no air gap in the air core machine. The amplification factor $(1 + (r_{sheet}/r_{s_{in}})^2)$ would be 2 at most when the armature winding is placed closest to stator back steel, i.e. $r_{sheet} = r_{s_{in}}$. Consequently, it is obvious that air core machines will have an order of magnitude lower inductance than conventional machines. This certainly presents the largest difference between a conventional and an air cored HTS SM.

It is essential to understand that an increase in power density of a machine will go hand in hand with the decrease of the inductance. Thus, if future wind turbine generators are required to be compact machines, the expected value of inductance would be much lower than conventional machines have. However, this is only true if the air gap flux density is increased while electric loading is either kept constant or decreased. In the case of a full HTS SM, the electric loading can be significantly increased. The effect of increase of the electric loading on the inductance is opposite. Hence, if the ratio A_s/B_r is maintained constant or increased, the power density of

the machine can be increased while the values of inductance can be adjusted to more acceptable values.

Note: Consequences of low synchronous inductances for machines can be seen in outstanding transient and overload capabilities and better voltage and power control due to inherently low load angle value (70, 74, 75, 77). Yet, it is important to say that low values of synchronous inductances would cause large short circuit currents. For example, if $x_d = 0.1$p.u., the protection system (breakers) would need to be rated for an order of magnitude higher than the rated value. In other words, having the increase of torque density of a machine will result in smaller a machine but at the same time will require an elaborated protection system which will need to be greatly oversized. Thus, for real world application the whole system needs to be considered and not only machine size and cost.

Additional complications in the design phase of HTS machine will arise from the large values of transient forces and heat dissipation, which will in turn call for more structural reinforcement in the design (75, 119). Therefore it is important to look at the HTS SM machines not as a substitute for conventional machines but rather as a unique component with a list of specific requirements.

3.4.3 Armature reaction effect on an HTS field winding

Due to the magnetic sensitivity of the HTS tape, the field winding critical current will be reduced. Thus, the field winding will be characterized by the magnetic conditions in the machine. However, since an interaction of two magnetic fields of the rotor and the stator is the grounds for operation of the electric machine, the effects the armature winding will have on HTS performance must be evaluated as well.

Operation of the machine (air core HTS SM) is accessible by the analytic model presented above. If two current sheets are at the HTS field radius and at the armature radius, operation of the machine depend on the amplitude of the magnetic flux density generated by the field winding current sheet, electric loading of the current sheet the armature winding has and angular displacement between these. Hence the torque developed by the interaction between the rotor and stator magnetic field can be estimated by 3.16.

$$T(\theta) \sim B_r cos(p\theta) A_s sin(p\theta + p\gamma) \rightarrow T(\gamma) \sim B_r A_s sin(p\gamma) \tag{3.16}$$

The impact an armature has on the HTS field winding will depend on the ability of the armature reaction to alter magnetic conditions the HTS field winding is in. Thus, the flux density generated by the armature current sheet at the field winding can be used to quantify this change (for flux distribution expression consult (52)).

Two aspects the armature reaction has on HTS field winding can be recognized. The first is the intensity of armature reaction, where the stronger it is the larger effect it will have on the flux distribution and thus on HTS operation. The second is angular displacement, $p\gamma$, as this will disrupt the flux distribution at HTS field winding. The latter is the consequence of magnetic anisotropy of the HTS field winding.

Fig.3.9 illustrates the effect of the number of pair of poles on the angle between an armature reaction and perpendicular direction of flux to HTS turns. As this angle will scale as $\sim (p\pi)/2$, the impact of armature reaction is expected to be most severe for the two pole machines.

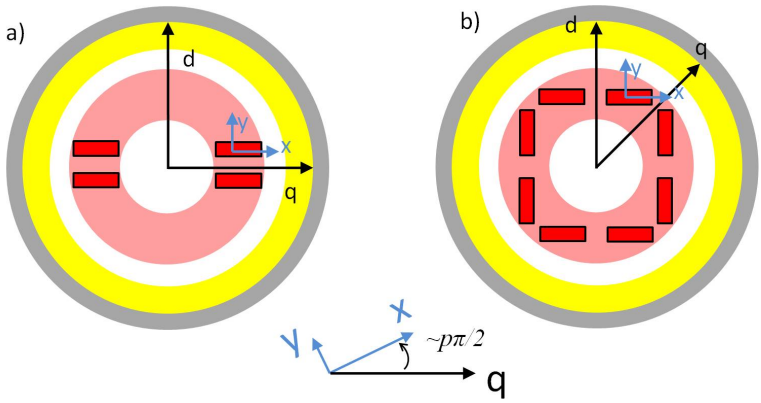

Figure 3.9: Difference between two pole and multipole machines - The air core HTS SM machine with the armature winding (the yellow ring) and HTS filed winding (the red ring) for (a) p= 1 and (b) p= 2. The HTS coils, the d and q axises and local x and y coordinate of HTS turns are presented. The figure illustrate that the angle between the x axis (perpendicular flux direction) of an HTS coil and the q axis will depend from number of poles, i.e it will scale $\sim p\frac{\pi}{2}$.

The effects of armature reaction on HTS field winding have not been discussed in published material in a systematic manner. An exception to this is the excellent work done in (77) where the authors do investigate the angular dependence of armature reaction on HTS field winding, but since the machine design took advantage of flux diverters placed between coils, the conclusions derived in this work cannot be used

as a general statement true for all cold rotor HTS SM machines. In work reported by (56, 64, 70), aspects of armature reaction in fault conditions and with respect to quenching of HTS field winding have been reported.

As an effort to address this important aspect of an HTS machine, this thesis will experimentally investigate the effect that armature reaction has on the HTS field winding in normal operation which includes both intensity of the armature reaction and the load angle γ between these. The experimental setup is designed and constructed with the specific purpose to investigate this interaction, where description of the setup and experiments is presented in Ch.4 while results are presented in Ch.5.

3.5 Suggested methods for increasing an HTS winding performance

HTS tapes are costly and any means to minimize the usage will be appreciated in an application where large amounts of HTS are required. Two design strategies have been proposed and investigated as an approach to better utilize the HTS tapes and ultimately to increase the MMF of HTS field winding. The first proposed approach is to employ multiple types of HTS tapes assuming that the optimal composition of different types of HTS exists. The second approach investigates improvements due to multiple current supplies to the field winding. Both approaches will be discussed in coming sections while quantification of potential improvements of each approach will be deduced experimentally. The experimental results for the proposed concepts and degree of improvements achieved in the experimental setup will be presented in the following chapters.

3.5.1 An HTS field winding with 1G and 2G coils

Combining different superconductors as an idea comes from magnet technology where hybrid high field magnet design (125, 126) take advantage of LTS and HTS coils working together. A number of inset coils (one or two) are usually placed in the bore of a larger magnet which provides a background field on which the inset coils will build on. Since an HTS is sensitive to magnetic field, the performance of inset coils is adapted to the magnetic conditions inside of the magnet bore.

The same approach can be used for electric machines where an objective could be to minimize the cost of machine which is in tight connection with amount of HTS used. Fig.3.10 illustrates a simple case of a field winding formed from a stack of HTS coils. Coils on the left are wound with only one type of HTS tape and the coils on the right are wound with multiple types of HTS conductor. Cumulative HTS machine experience and demonstration projects reported so far have employed either 1G or 2G HTS or a bulk material. As far as the author is aware, no systematic analysis of combination of HTS types used in HTS machines is performed so far. This thesis will investigate the potential benefits of combining 1G and 2G coils in the field winding. In principle, this approach next to HTS could be extended to include also MgB_2 (due to cost and availability) as a viable candidate for systems where operation temperature allows it.

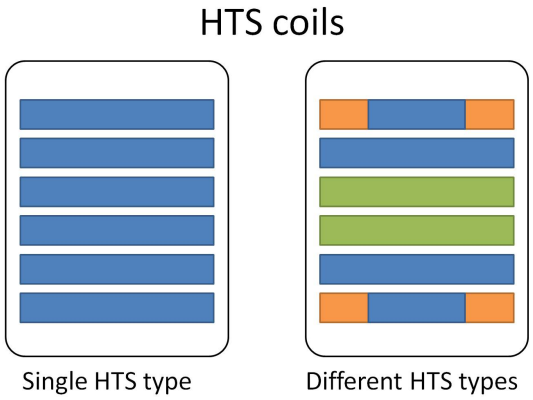

Figure 3.10: An HTS field winding comprising single and multiple types of HTS - Illustration of an HTS field winding where the possibility of using multiple HTS types are investigated. The single HTS tape (one color) winding presented at left is the conventional approach, while the concept at the right presents the hybrid concept employing multiple types of HTS tape where each color stands for types of different HTS.

Tape manufacturers are investing efforts to create HTS conductor which is less sensitive to magnetic field (improved pinning) and at the same time has higher uniformity with respect to the angle of the external magnetic field (127, 128). However, tapes highly sensitive to magnetic field (like 1G) produced at low cost used in combination with HTS tapes less susceptible to magnetic field could result with lower overall cost of the system (field winding).

The most convenient way to include multiple types of HTS in a field winding is to

differentiate between different coils. Thus, inner coils would be wound with one type while the next layer can be another type of HTS. With a higher degree of complexity, benefits to MMF could be achieved if the coils could have inset coils from different tapes or if they are simply wound with two types of HTS, one continuing on the next one. Connection points of two HTS types need to be carefully engineered as superconductivity is interrupted and a resistive joint is introduced (129). By taking advantage of magnetic sensitivity and anisotropy of different types of superconductors and a degree to which they differ, an optimal composition of superconductors could lead to significant savings in HTS material. Thus, less costly 1G tapes which are highly sensitive to a magnetic field could be used in the field winding where the flux is low, while less sensitive and more expensive 2G tape could be placed in high flux conditions.

An additional parameter to consider on the path toward optimal field winding is the electric insulation of the HTS tapes. Electric insulation could have a prevailing effect on the design of HTS coils and engineering current of the coils and it can be used to adjust MMF distribution of the field winding. Compact coils can employ an insulating coating adhered to the HTS tape (only 0.05 mm – 0.1 mm thick) which would allow the highest values of engineering current density.

3.5.2 An HTS field winding with multiple power supplies

By allowing a number of power supplies to supply currents to the field winding, the critical current of each coil could be reached and thus the full capabilities of the HTS tapes can be utilized. This scheme for the excitation system of an HTS machine represents adaptation of practice found in magnet technology where for inset coils separate supplies are usually employed (126, 130). Proposed concepts are presented in Fig.3.11.

This method, suggested as a means to boost the performance of magnets (131), where 30% improvements in MMF was observer, is not seen as an applied practice for a supply scheme of an HTS field winding.

Next to providing an increase in MMF of the field winding, additional power supplies will present additional cost and complexity. Although the power rating of excitation system is not increased, a one multi terminal dc source or several single output sources are required which cause the increase in the cost of auxiliary systems of HTS machine.

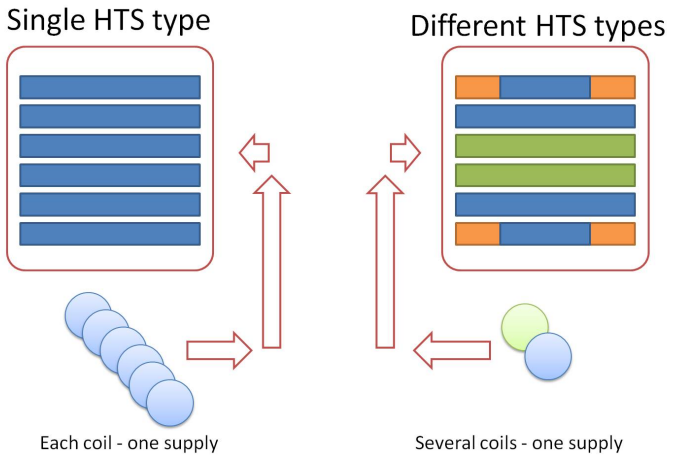

Figure 3.11: Supply schemes for an HTS field winding - Most flexibility and thus an increase in performance of HTS winding is achievable by assigning one power supply to one coil (left). By optimizing the number of power supplies improvements can be achieved as the increase of the performance will not scale linearly with the increase in number of power supplies.

However, reliability of the HTS excitation system will increase together with introducing additional power supplies. If a fault happens in one of the coils depending on how much power supplies are present in the excitation system the machine could still operate with partial output.

3.5.3 Proposed optimization approach

The concept of topology optimization was applied to an HTS machine (implemented and carried out in 2D FE) in order to maximize the effectiveness of the HTS current capacity. Here, instead of optimization of each coil geometry and afterwards a coil stack (shape optimization), which is the traditional way optimization is carried out in magnet technology (132) on MRI and high field magnets, the optimization algorithm controls the material distribution. An illustration of the concept is presented in Fig.3.12, comparing the traditional optimization approach and topology optimization.

Thus, if an optimization variable is defined in an optimization domain which is corresponding to the space allocated for HTS coils, the value of that variable could correspond to the material distribution. If the value of the variable is 1, the HTS conductor is present and carries current, while a 0 would correspond to an empty space (inactive

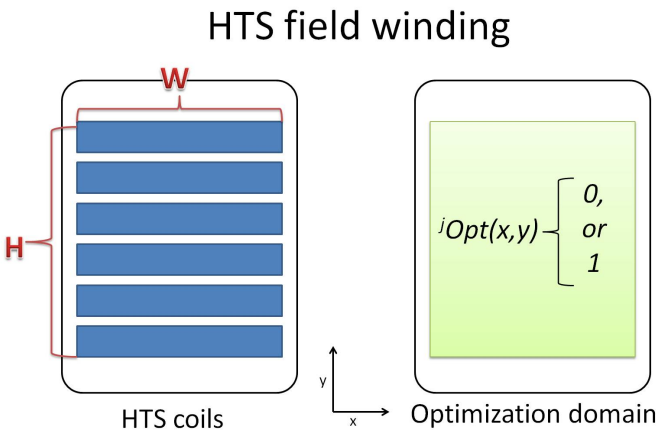

Figure 3.12: Optimization approach - The shape optimization, presented at the left, is conventionally used in various optimization problems including HTS magnets. As an alternative in the topology optimization approach, presented at the right, the algorithm is in charge of the material distribution.

material). The optimization algorithm needs to evaluate the objective function which contains all boundary conditions for the optimization problem and determine what distribution of HTS material would be the best. The amount of HTS can be included in the objective function and thus minimization will result in the lowest amount of HTS where defined constrains, which could be air gap flux density, electromagnetic torque or similar, are kept in defined bounds. Since two values for optimization variable are of interest, 0 and 1, the problem could be constrained to only binary variables.

Proposed optimization, described in (133) (included in the Appendix.G.4), was implemented in a 2D model of multi pole (16 pole) HTS SM in Comsol Multiphysics (134) presented in Fig.3.13a. The paper presents formulation of topology optimization in Comsol Multiphysics for several types of HTS and multiple current supplies which will not be presented here. The results for three different HTS types, presented in Fig.3.13b with different costs and $J_c(B)$ have been obtained where the tape with lowest cost produced the cheapest solution but also had largest volume of the coil.

The highest possible reduction of HTS for infinite number of power supplies (each turn has different current) for presented model 2D model was reported in (133) to be 50% for 2G and 30% for 1G HTS at 20 K. These values should be taken as indication to how much of HTS conductor is not fully utilized in field winding and hence the

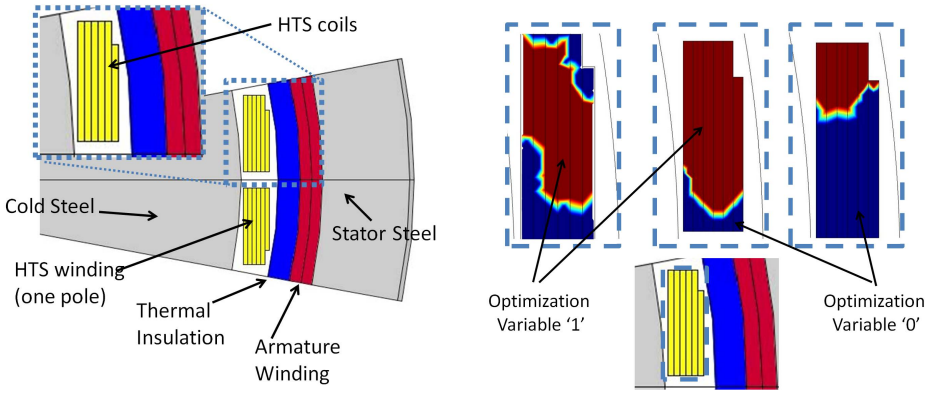

(a) The 2D model of 16 pole HTS generator

(b) Results of optimization

Figure 3.13: Implementation of topology optimization of HTS coils in Comsol MultiPhysics - (a) Only one pole of the 16 pole generator is modeled. **(b)** Optimization returned proposed distribution for an HTS conductor where the dark red is where the conductor is present while the dark blue the area where conductor is absent. The figure includes three different cases for three different HTS types.

potential of multiple power supplies approach.

However, presented optimization approach and results are only initial step. The built–in optimization algorithm in Comsol was unable to handle a binary values of optimization variables. Thus, this had to be addressed throughout the contributions to the global objective function, where number of contributions have been defined in order to force the optimization variables to either 0 or 1. Unfortunately, this have interfered with optimization process (evaluation of sensitivity based on gradient of objective function) and proved to be a limiting factor of described implementation. However, if an optimization engine capable of handling binary variables (like Branch and Bound) is employed, the presented optimization can become valuable mean for achieving an optimal layout of HTS machine.

Chapter 4

Superwind–HTS machine setup

"If at first the idea is not absurd, then there is no hope for it." **by Albert Einstein**.

4.1 Introduction

As a part of the effort to assess the state of the HTS technology and its application challenges in the wind industry, we have designed and constructed a small scale experimental HTS machine test platform. The focus during the design process was on creating the setup where various HTS tapes, coils, their performance and handling as a part of an electrical machine could be evaluated.

The coils wound from HTS tapes produced by several manufacturers, both 1G and 2G technology, have been tested as a part of an HTS field winding in the HTS machine. A modular approach during platform development was of crucial importance. It was important to design a versatile HTS machine platform where modification to the HTS field winding like interchanging the HTS coils, trying out different connections strategies of the coils, etc. is a straightforward task completed in a couple of hours.

The setup, illustrated in Fig.4.1, is comprised of a three phase armature winding rotating around a stationary HTS field winding operated at 77 K. The HTS field winding is immersed into a LN_2 chamber of the custom made cryostat which in this stage is operated as an open LN_2 bath. The setup is also equipped with the custom angular

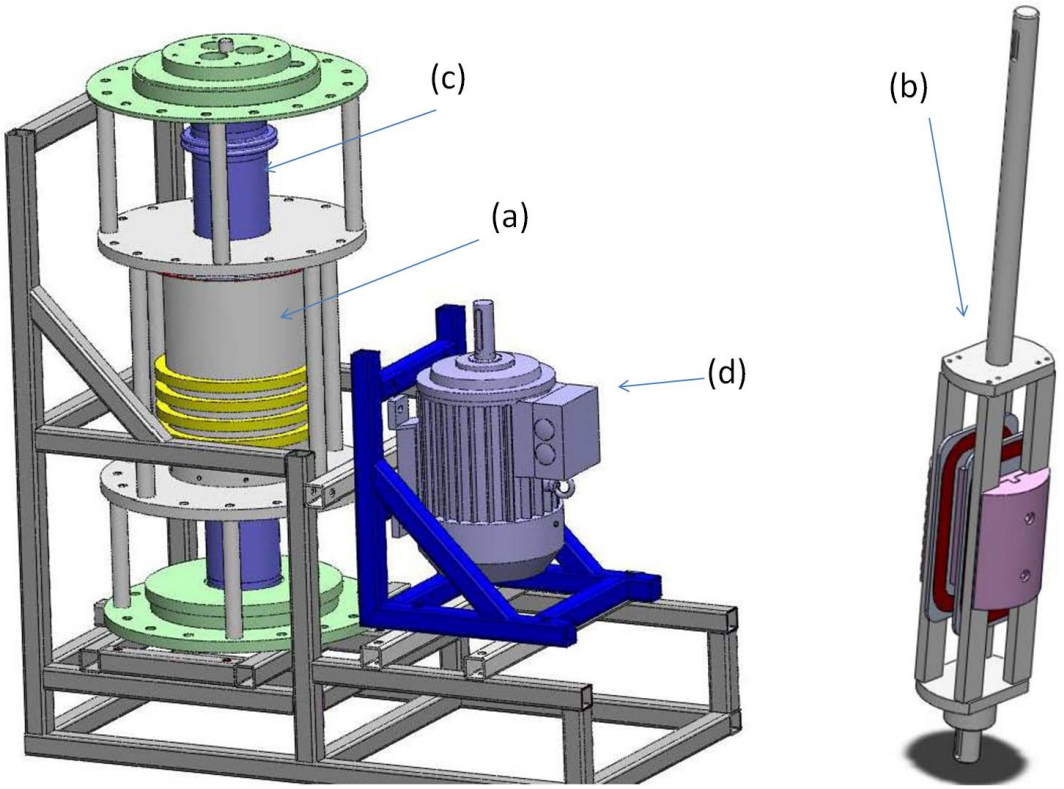

Figure 4.1: 3D CAD model of the Superwind setup and HTS field winding. - The armature winding, (a), is rotating around the HTS field winding (b) which is enclosed inside an open top LN_2 cryostat, (c). The armature is driven by the belt coupled induction motor, (d), controlled by a frequency converter. The belt connection is not shown. The assembled HTS field winding, (b), is lowered to the LN_2 chamber from the top of the cryostat.

position and speed measurement of the rotating armature as well as the stationary torque measurement. The armature position can be locked with respect to the HTS field winding and the angle relative to the armature can be adjusted in the 360° span.

The speed of the armature winding is controlled by the frequency converter driving the induction machine (it is an open loop U/f control of the induction machine). The induction machine is coupled to the armature winding by a belt. The speed reference is set manually by entering the desired value of the speed into the frequency converter control panel.

Data acquisition and control of the HTS field winding, supplied with six HP power supplies, is controlled by the LabVIEW software. The schematic illustration of the data

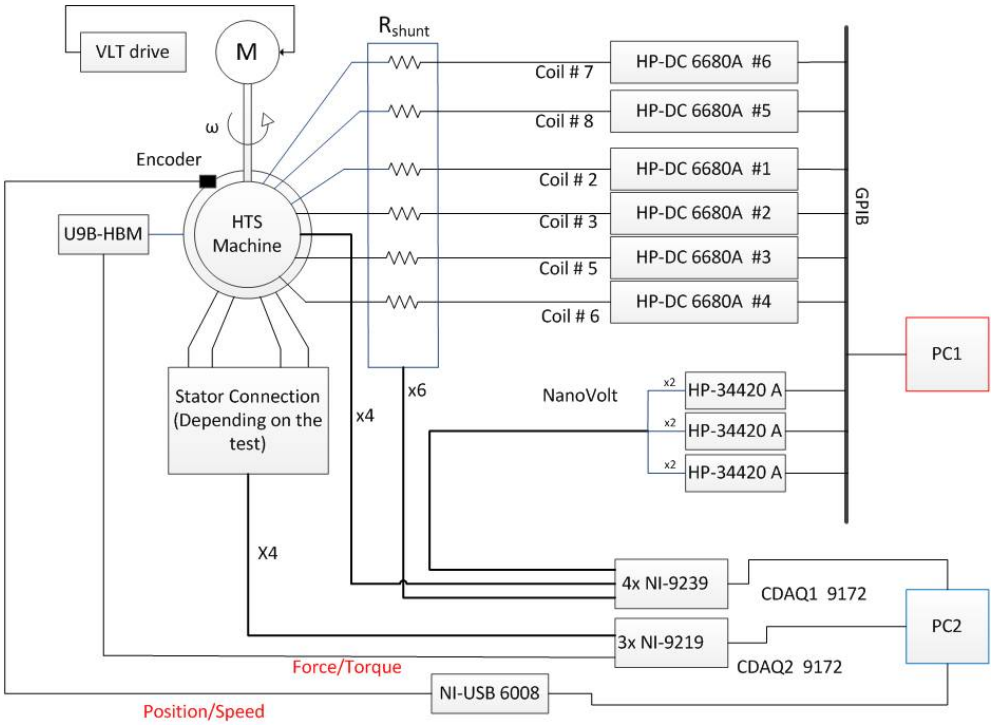

Figure 4.2: Schematic of the Superwind setup auxiliary equipment - The figure illustrates the measurement and control setup used in tests performed on the HTS machine with six dc power supplies. PC1 was used to control the dc power supplies (HP#1 – HP#6) and read the Nanovoltmeters (due to low sampling speed of Nanovoltmeters (one sample/s) the data from the Nanovoltmeters were used only in the case of static experiments). PC2 continuously reads the NI cards with high sampling rate (100 samples/s for NI9219 and $5{\times}10^3$ samples/s – $20{\times}10^3$samples/s for NI9239)

acquisition is illustrated in Fig.4.2. The data acquisitions is performed with 24 bit NI measurement modules NI9239 (135) and NI9219 (136) characterized with simultaneous sampling, high voltage sensitivity and high sampling speeds.

4.2 The armature winding

Design and construction of HTS machine can be very costly due to the number of expensive elements, complex designs and uncertainty related to the low temperature operation and HTS where several iterations in designing phase might be required. Thus, we have decided to keep the focus on the on the HTS specific issues and to try to address challenges such as cryogenics (insulation), HTS coils design and others, so we

could maximize the learning potential relative to the amount of funds invested. Hence, instead of designing and constructing an armature winding corresponding to the design of the HTS field winding (where for example air gap armature winding concept could be used), we have adopted the conventional armature winding from commercially available induction machine. At the later stage, a specific armature winding design could be incorporated in the setup without major complications.

The three phase two pole armature with distributed windings was adopted from a 22 kW, 50 Hz induction machine and custom fitted to a metal cylinder which acts as housing for the armature. Two bearings (137) are placed at the base of the armature bore. The armature winding is designed to rotate in order to avoid challenges of having the rotating parts at cryogenic temperatures. Thus, four slip rings are mounted on the bore making the phase and neutral terminals (for a star connected armature winding) accessible via four brushes. The armature winding is driven with an induction machine drive controlled by a *Danffoss* frequency converter (15 kW (138)) and coupled with a belt transmission. The speed range can be adjusted to any value between 0 – 400 rpm (limit imposed by the choice of bearings and the driving motor).

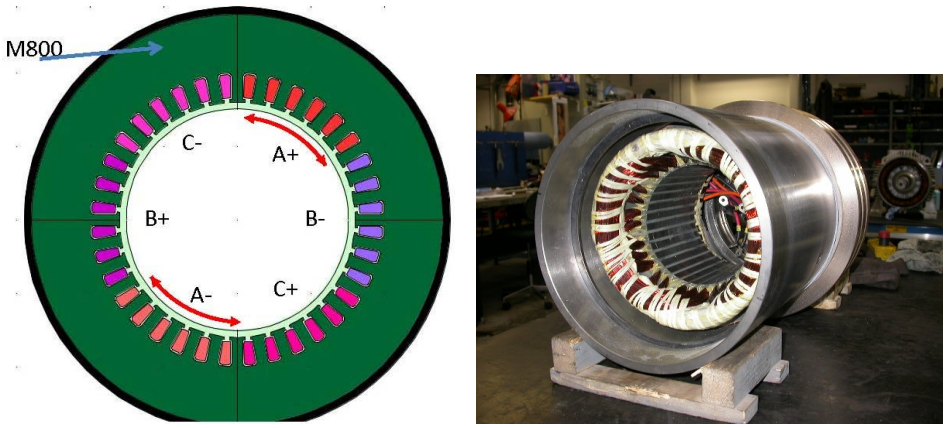

(a) Illustration of the armature winding **(b)** The armature in the metal housing

Figure 4.3: The armature winding. - **(a)** A 2D cross section of the three phase armature winding. The phase belts, occupying six slots per pole, are identified. **(b)** The armature winding during the construction phase. The metal housing, armature winding, 4 slip rings glued to the armature housing, bearing slot and 'O' ring are shown in the photo.

The geometry of the armature steel stack and windings has been inspected and it is illustrated in Fig.4.3a. The steel stack of M800-50A silicon steel (139) has axial

length of 150 mm and rotor diameter of 160 mm. The phase windings are distributed over 36 stator slots in a single layer winding. The nameplate data and parameters of the induction machine from which the armature winding was adopted are presented in Appendix.E while technical drawings are included in Appendix.D.

4.2.1 The number of turns in the phase winding

The number of turns in the slot of the armature winding was not among induction machine documentation and thus it was determined experimentally. The AC power supply has been connected to the phase A and B while a Rogowski current transducer *CWT015* (140) was wrapped around the turns in two slots. The placement of the Rogowski transducer is shown in Fig.4.4. The same arrangement has been repeated but now with Rogowski transducer wrapped around the 8 turns of the phase A current lead.

The phase voltage was varied with an ac power supply, which comprised from a signal generator and an audio amplifier. The recorded values for output voltage for current passing throughout the Rogowski transducer hoop in both cases are presented in the Table.4.1. The number of the turns in the slot is derived as a ratio of the recorded Rogowski transducer output and it can be expressed as

$$Z = 4\frac{V_{turns}}{V_{lead}} \tag{4.1}$$

where the Z, V_{turns} and V_{lead} is the number of turns in one slot of the armature steel, the Rogovski voltage output for the case the transducer is placed around turns in two armature slots and the Rogowski voltage output for the case the transducer is wrapped around 8 turns of the current lead, respectively. The number of turns in one slot converged to 18.

4.2.2 The winding coefficients of the armature winding

It is from interest to investigate the tendency of the armature winding to attenuate harmonics present in the air gap flux. As illustrated in Fig.4.3a, one phase of the armature winding is distributed over 12 slots (making the number of slots per pole and per phase, q, equal to 6) in the winding with 108 turns in total (6×18). The distribution winding coefficient for the armature winding is defined by (141)

No.	V_{turns} [mV] (Wrap around the turns in two armature slots)	V_{lead} [mV] (Wrap around the 8 turns of the current lead)	Z
1	5.44	1.24	17.55
2	10.56	2.4	17.6
3	15.52	3.52	17.63
4	21.0	4.76	17.64
5	26.8	6.04	17.74

Table 4.1: The recorded results from the Rogowski current transducer in the experiment conducted in order to determine the slot number in the armature winding.

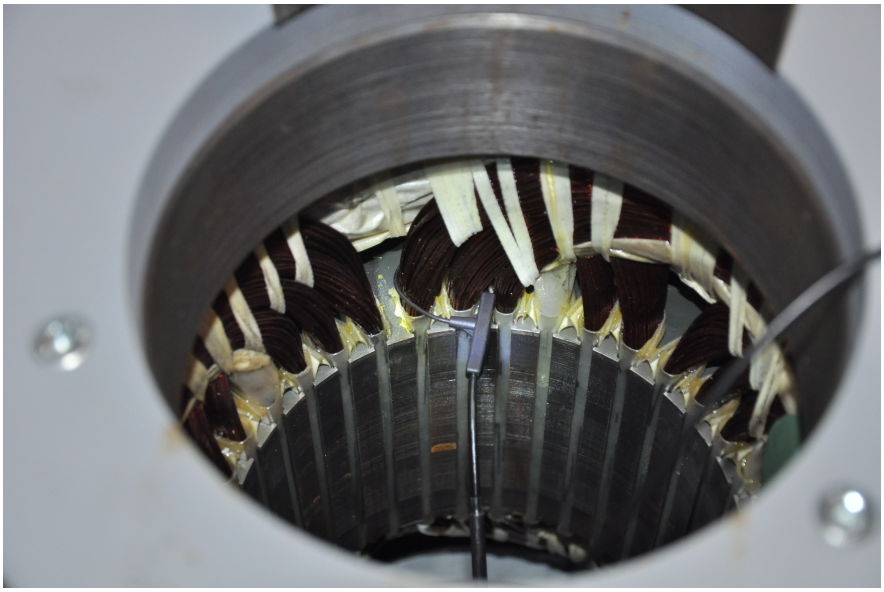

Figure 4.4: Placement of the Rogowski current transducer. - The transducer is wrapped around turns placed in two armature slots.

$$k_{d\nu} = \frac{\left(sin\left(\nu\frac{q\alpha}{2}\right)\right)}{\left(q \cdot sin\left(\nu\frac{\alpha}{2}\right)\right)} \tag{4.2}$$

where the ν is ordinal number of harmonic and α is the angular pitch between two neighboring slots. The pitch winding coefficients for the main and higher harmonics of the armature winding is expressed as

$$k_{p\nu} = sin\left(\nu\frac{\pi}{2}\beta\right) \tag{4.3}$$

where β is the span of the armature sections. The winding coefficients, $k_{w\nu} = k_{d\nu}k_{p\nu}$, for the main and higher harmonics of the armature winding are reported in Table.4.2.

ν	1	3	5	7	9	11	15	17
$k_{w\nu}$	0.9321	0.5079	0.0966	0.0279	0.0	0.0037	0.0056	0.0365

Table 4.2: Armature winding coefficients

4.3 Cryostat

The cooling system and thermal insulation are integral and very important parts of a HTS machine. Several concepts of the cooling system were considered for a cryostat design. The intention of the project was to focus on the electro-magnetic evaluation, analysis and experiments conducted on HTS field winding and HTS machine. Thus, the choice to use the LN_2 temperature range, i.e. from 64 K – 77 K, was made in part to simplify the cooling system requirements but also to challenge the HTS performance. The constructed cryostat is shown in Fig.4.5 in the frame of the HTS machine but without armature cylinder.

4.3.1 The design consideration

The orientation of the cryostat and the three phase winding is vertical (illustrated in Fig.4.1 and Fig.4.5). In addition, a stationary cryostat was chosen in order to simplify mechanical aspects of the design and to allow open bath cooling, ie. LN_2 bath. However, since the difficulty of rotating cooling is expected to be greater than the difficulty of revolving armature, this concept could have merits for wind turbine HTS generator and thus represent valuable experience.

In order to thermally insulate the low temperature chamber from room temperature, the cryostat design needs to inhibit conduction and radiation heat transfer (142, 143). Several materials could be a viable choice for the thermal insulation, like polystyrene foam, powder insulators (107, 144), vacuum, etc. where vacuum has the lowest heat

Figure 4.5: The cryostat. - The cryostat, 1.15m high, is lowered to the armature bore from the top. The bottom torque transfer element and bottom of the cryostat have corresponding pins and slots which are making sure that the cryostat is placed in the axis of rotation.

conduction coefficient (at least one order of magnitude or more depending on the vacuum quality) compared to others.

The radial distance between HTS field winding and an armature winding, i.e. magnetic air gap is an crucial parameter in HTS machine design. The larger the magnetic air gap is, the higher values of MMF are required to produce the same air gap flux density, as seen in Ch.3. Hence, an concept of a machine such as HTS SM with the cold rotor will benefit from the compact thermal insulation placed in the air gap. The vacuum insulation will result in the lowest overall radial thickness of the low temperature insulation enclosure. To investigate the difficulty of vacuum technology and integration into the machine design, we choose to construct the vacuum insulates cryostat.

4.3.2 Choice of material

Low temperature properties (mechanical, thermal, electrical) of materials are often different compared to the room temperature. Thus, the choice of the material for cryostat and outer parts at lower temperature is important.

The composite material and stainless steel were considered as a two candidates from which the cryostat could be built from. The thermal and mechanical properties of composite material are largely dependent on the internal structure of the material, like glass (or carbon) fiber density and orientation. Some of the composite materials and its properties can be found in Table.4.3 (107, 145, 146, 147, 148, 149). The data are presented for stainless steel and fibers individually and for composite with 60% of the fiber content. The G.fib. stands for Glass fiber composite and C.fib. stands for Carbon fiber composites. Next letter identifies orientation of the fibers. B stands for Balanced orientation with fibers placed at 0° and 90° while Q stands for Quasi – isotropic orientation with fibers placed at 0°, 45°, -45° and 90°. The number after, specifies the direction of the specified properties of the composite material. The table indicate that with a carefully engineered composite material, it is possible to achieve very good combination of thermal and mechanical properties (strong material while a good thermal insulator).

However, stainless steel was chosen mainly due to better workability (turning, welding...) and the cost of material, even though the thermal conductivity was higher compared to most of the composite materials shown in the table. This choice has

particular implication for the TTE design where if composite material was used, even better performance could be achieved.

Material	Thermal expansion $[K^{-1}]$	Thermal conductivity [W/m ·K]	Stiffens (E) [Pa]
SS316L	1,30E-05	7.60E+00	2,00E+10
G.fib.-Q 0°	1,17E-05	6,59E-01	2,46E+10
G.fib.-Q 90°	1,17E-05	6,59E-01	2,46E+10
C.fib.-Q 0°	2,82E-06	2,94E+00	5,36E+10
C.fib.-Q 90°	2,82E-06	2,94E+00	5,36E+10
G.fib.-B 0°	1,17E-05	6,59E-01	3,06E+10
G.fib.-B 90°	1,17E-05	6,59E-01	3,06E+10
C.fib.-B 0°	2,82E-06	2,94E+00	7,44E+10
C.fib.-B 90°	2,82E-06	2,94E+00	7,44E+10
AS4 C.fib -0°	-3,60E-07	8,65E+00	2,28E+11
AS4 C.fib -90°	1,80E-05	5,19E+00	1,66E+10
E-Glass fibers	5,40E-06	1,28E+00	7,24E+10
E-Glass fibers	5,40E-06	1,28E+00	7,24E+10
Epoxy	-4,09E-05	1,88E-01	4,28E+09

Table 4.3: Thermal and mechanical properties of composites and steels at 77 K.

4.3.3 Design details

The design constraints for the outer diameter of the cryostat, the integral thickness of the cryostat in the radial direction, the mechanical clearance between the outer wall and the rotating armature, the inner wall, and the HTS winding are all set to be 158 mm, 9 mm, 1 mm and 0.5 mm, respectively. The overall length of the cryostat is 1,15 m, where no strict constraint has been defined for the axial length of the cryostat.

The resulting magnetic air gap between the rotating armature winding and the stationary field winding is 10 mm including all clearances. For comparative reasons, it is noteworthy to state that the induction machine from which the armature winding was adopted had the air gap of 0.9 mm (based on measurement of rotor radius) which is 1.25% of armature bore radius. This HTS machine will have a magnetic air gap of 12.5% of the armature bore radius.

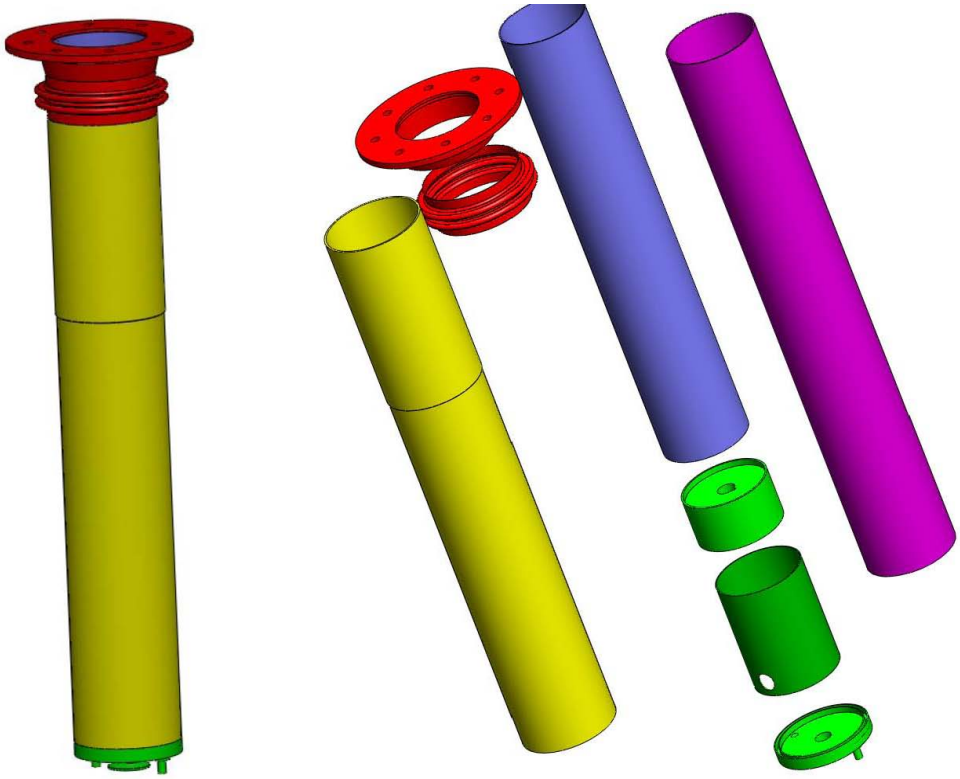

Figure 4.6: The exploded view of the cryostat. - The cryostat is composed from the inner wall (purple) and outer wall cylinder (yellow). The vacuum chamber is in between inner and outer wall. The MLI insulation (magenta) is wound on the inner wall. The torque Transfer Element (green) is located at the bottom of the cryostat. The HTS field winding shaft will lock into the hole on top of the TTE when the HTS field winding is lowered down into LN_2 chamber. The expansion/compression compensator (red) is placed at the warm wall of the cryostat to accommodate thermal expansion/compression of the inner wall of the cryostat due to temperature difference.

4.3.4 Thermal expansion

The thermal contraction of materials have a large implications on the design of a HTS machine. The thermal expansion coefficient for SS is $\sim 0.2\%$. This means that the cold wall of the cryostat will shrink up to 3 mm in the axial direction and 0.3 mm in the radial direction when cooled from 300 K to 77 K.

A corrugated bellow, shown as a part of the cryostat in Fig.4.6 and close up in Fig.4.7 is used to accommodate this difference between the outer and inner walls. Two layers of 0.5 mm SS316L have been shaped as illustrated in Fig.4.7 and welded at the

ends. The maximum compression/elongation for the corrugation element is 12 mm while the axial spring constant is 670 N/mm. The stress caused by the cool down of the inner and outer wall was estimated using FE, where the maximum stress found of 6.7 MPa was deemed to be well within the material limits.

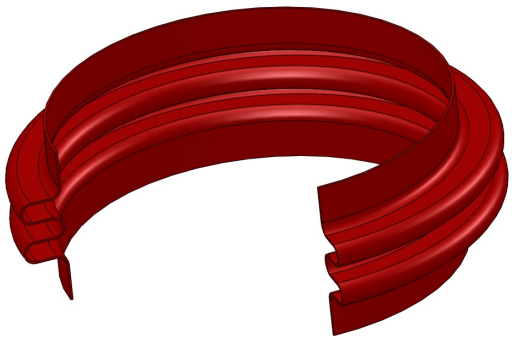

Figure 4.7: The SS corrugation. - The corrugation is placed at the top of the outer wall of the cryostat and it is introduced to compensate the mechanical stress caused by thermal expansion of the material during thermal cycling. A quarter of the corrugation has been cut away to increase visibility.

4.3.5 Torque Transfer Element integrated in the cryostat design

The TTE, fashioned as a SS cylinder with 72 mm for an outer radius and 1.5 mm wall thickness, is illustrated in Fig.4.8. The thermal and mechanical aspects of candidates for a TTE are discussed in more detail in Sec.3.3.2.1.

The following stands as derived in Sec.3.3.2.1: the larger the radius the lower the heat transfer. It was convenient to have a TTE that is naturally continuing onto the inner wall of the cryostat to allow the MLI to be wound without tailoring. This means that the outer radius of the TTE should be the same as the cryostat inner wall, 72 mm (the air gap). With the help of the expression, 3.3, for thickness of the wall of the cylinder derived in the previous chapter, where the value of the 20×10^6 Pa for maximum allowed sheer stress and safety factor n of 3 were used and the design input for the maximum torque set to 250 Nm, the minimal wall thickness for the TTE, $\delta_{wall_{min}}$, is expressed with 4.4. As the thickness of the SS316L cylinder used for the cryostat walls was 1.5mm, the TTE is also made from a cylinder with δ_{wall}= 1.5 mm and $R_{TTE_{out}}$= 72 mm.

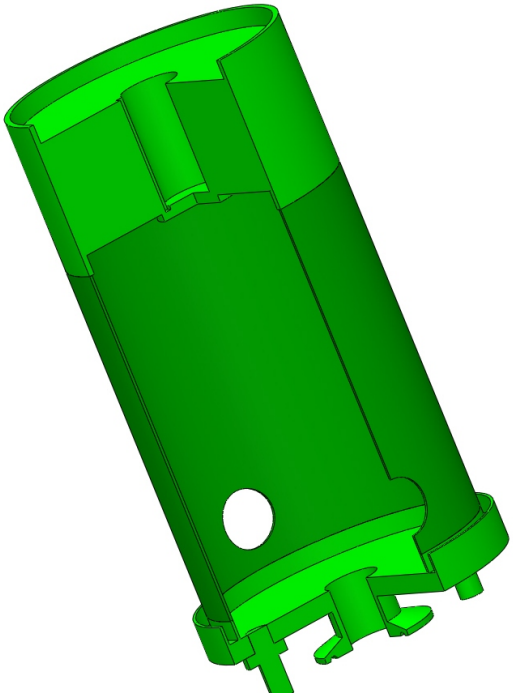

Figure 4.8: The Torque Transfer Element integrated in the cryostat. - The TTE is shown with one quarter cut away to increase visibility. It is welded to the bottom of the LN_2 chamber of the cryostat which accommodates the torque locking shaft socket the HTS field winding is lowered into. The vacuum valve is placed at the bottom of the TTE as an evacuation access point.

Due to orientation, full weight of the cryostat and the field winding will rest on the cryostat walls which will cause some additional stress in the material. The axial load on the TTE comprises the weight of the cryostat, the HTS field winding and LN_2 which in total adds to the 40 kg and the stress caused by the thermal contraction of the inner wall. The total weight would correspond to the stress $\sim 0.5 \cdot 10^6$ Pa for the δ_{wall}= 1.5 mm. This stress is well within the limits of the material (where $\geq 200 \times 10^6$ Pa is usually observed for SS316L stainless steel at 0.2% strain).

$$nT_{max} = \frac{\pi}{2}(R^4_{TTE_{out}} - (R_{TTE_{out}} - \delta_{wall})^4)\frac{\tau_{max}}{R_{TTE_{out}}} \longrightarrow \delta_{wall_{min}} > 1.18mm \qquad (4.4)$$

The corrugation will distribute the weight of the structure mostly on the outer wall. The spring constant of the corrugation is $\sim$ 670 N/mm in the axial direction and the compression of the inner wall of the cryostat is $\sim$3 mm in axial direction which results

in the 2010 N force pulling upwards the inner wall and pushing downwards at the outer wall. The total stress caused by the thermal stress and the weight of the structure in the outer wall of the cryostat is found to be 3.4×10^6 Pa. This discussion proved that the thermal stress and rated electromagnetic torque are not compromising mechanical integrity of the cryostat.

4.3.6 Vacuum

The cryostat vacuum chamber consists of the volume of the space between the inner and outer cryostat walls and the volume inside of the TTE (the chamber inside the TTE is connected to the space between the walls with two holes visible in Fig.4.8). The vacuum chamber was evacuated and the vacuum valve was closed off when the pressure inside of the vacuum chamber was at 10^{-5} mbar (10^{-3} Pa). First pumping took approximately one week and with the cool down, pressure went below 10^{-6} mbar (10^{-3} Pa) due to the cryopumping effect (144, 150, 151).

The out gassing in the vacuum chamber caused by residual impurities on the walls of the cryostat and the MLI insulation was substantial after the first pumping. The pressure increased after the thermal cycle (pumping → cool down → room temperature) to 10^{-2} mbar (10^{-1} Pa).

This issue was planned to be tackled by 'baking' the cryostat were the heaters are introduced around the cryostat and the temperature is raised up to 80°C – 90°C (caution must be exercised with maximum temperature due to MLI limitation) while the vacuum chamber is being evacuated. All humidity and impurities contained in the vacuum chamber would evaporate much faster, leading to higher, longer lasting and faster achievable vacuum. After third pumping the vacuum stayed below 10^{-4} mbar after several thermal cycles and backing was not necessary. However, if the longevity of the vacuum is important, the 'baking' combined with introduction of the 'getter' compounds in to the vacuum chamber of the cryostat is highly recommended (152).

4.3.7 Manufacturing and assembling consideration

Assembling procedure is shown in Fig.4.9. The MLI insulation was wound around the inner wall after the inner wall and TTE were welded to the bottom of the LN_2 chamber. The space in the radial direction of the cryostat is limited due to the magnetic air gap and thus tight tolerances for the concentric accuracy of the walls of the cryostat had

to be set. To achieve high concentric accuracy and roundness over the length of the cryostat was a challenge.

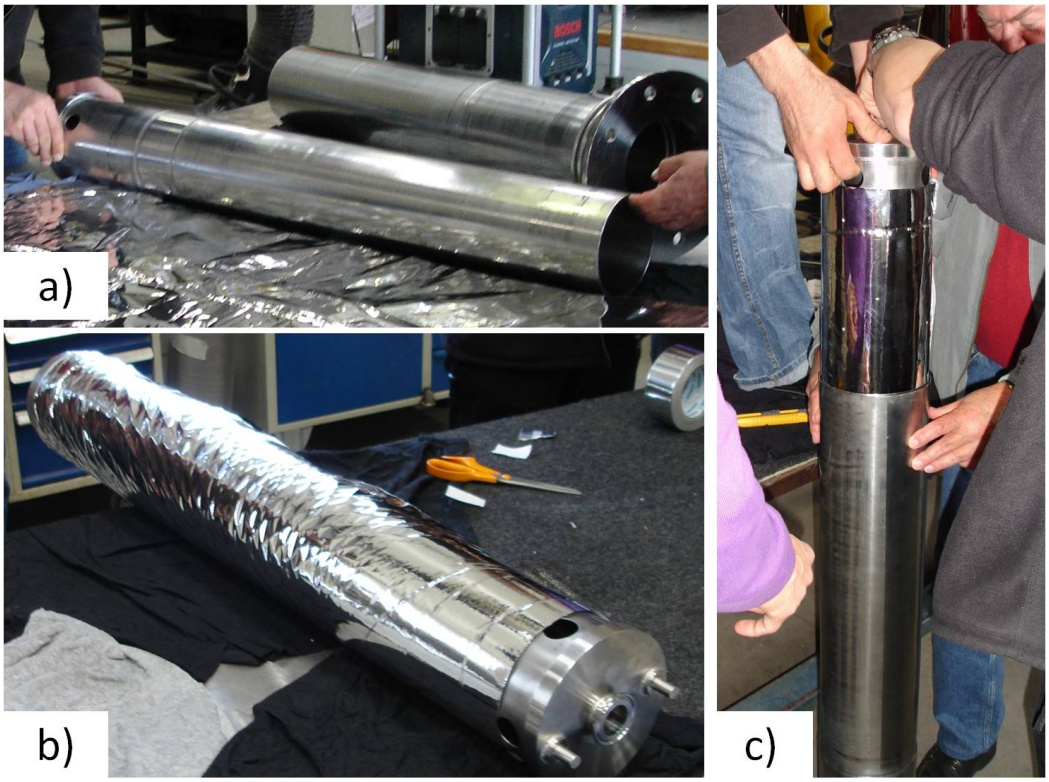

Figure 4.9: The cryostat during assembly phase. - The cryostat was fashioned from two parts, inner and outer wall, welded together at the bottom and the top. (a) The preparation step for applying the MLI insulation on inner wall of the cryostat. Both walls are shown in the photo. (b) The MLI is wound on the inner wall of the cryostat and tied with low emissivity aluminum adhesive tape. (c) Assembling stage for the cryostat. Insertion of the inner wall with MLI insulation into the outer wall of the cryostat.

The sub millimeter tolerances can be achieved by turning the element in a lathe. That usually calls for minimal wall thickness of the cylinder to be $\geq$3 mm, which in this case made turning unfeasible. The highest tolerance achievable with a press rolled sheet of the SS316L stainless steel (SS) to desired radii was found to be 0.5 mm. Thus, two SS316L stainless steel (SS) sheets of 1.5 mm thickness have been pressed rolled and welded into two cylinders with an outer diameter of 158 mm and 143 mm respectively.

The mechanical clearance between the inner and outer wall of the cryostat for both the HTS field winding and the armature winding were set to 1 mm and 0.5 mm, re-

spectively. The radial tolerances were set in such a way that the mechanical clearances defined are the absolute minimum distance allowed between the two parts. This means that the dimension for the outer wall of the cryostat had specified dimensions of 157.5 mm ±0.5 mm to maintain mechanical clearance of at least 1 mm between the armature teeth and the cryostat. As a consequence the vacuum chamber may not be perfectly cylindrical and will not have constant distance between the inner and outer walls (maximum variations of 1 mm).

4.3.8 Heat transfer consideration

To evaluate the integral heat transfered to the LN_2 chamber of the cryostat, it is useful to simplify the geometry of the cryostat. Three sections of the the cryostat were identified and illustrated in Fig.4.10, each of which with different boundary conditions.

The radiation and conduction through residual gas will be dominant in the middle section. The middle section of the inner wall of the cryostat, $750mm$ high, left in Fig.4.10, will be at $77K$ while for the outer wall it can be assumed that it is at room temperature. The top and bottom sections will have temperature gradient from $77K$ to $300K$.

However, to estimate the heat transferred via conduction through the residual gas in the vacuum chamber and radiation, it is better to assume that the inner wall of the cryostat is on $77K$ across the whole length of the cryostat, $1065mm$ (calculated in Fig.4.10). This will cause somewhat higher values for the heat transferred.

4.3.8.1 Conduction heat transfer

The contributions of the heat transfer through the solid for the top and the bottom section of the cryostat and conduction through gas over the middle section of the cryostat will be taken into account in this section.

Conduction in the gas: As the space between the outer and inner wall is much smaller than the length of the cryostat, the problem can be observed as two parallel planes 1065 mm. The walls (planes) are spaced apart 6 mm, but since MLI insulation is wound on the inner wall the space have been reduced to ∼2 mm (details are presented in Appendix.D). The mean free path for air at 77 K and 0.133 Pa ($1.33 \cdot 10^{-3}$ mbar) is ≈9 mm which is a good reference for the minimum value of the pressure that needs to

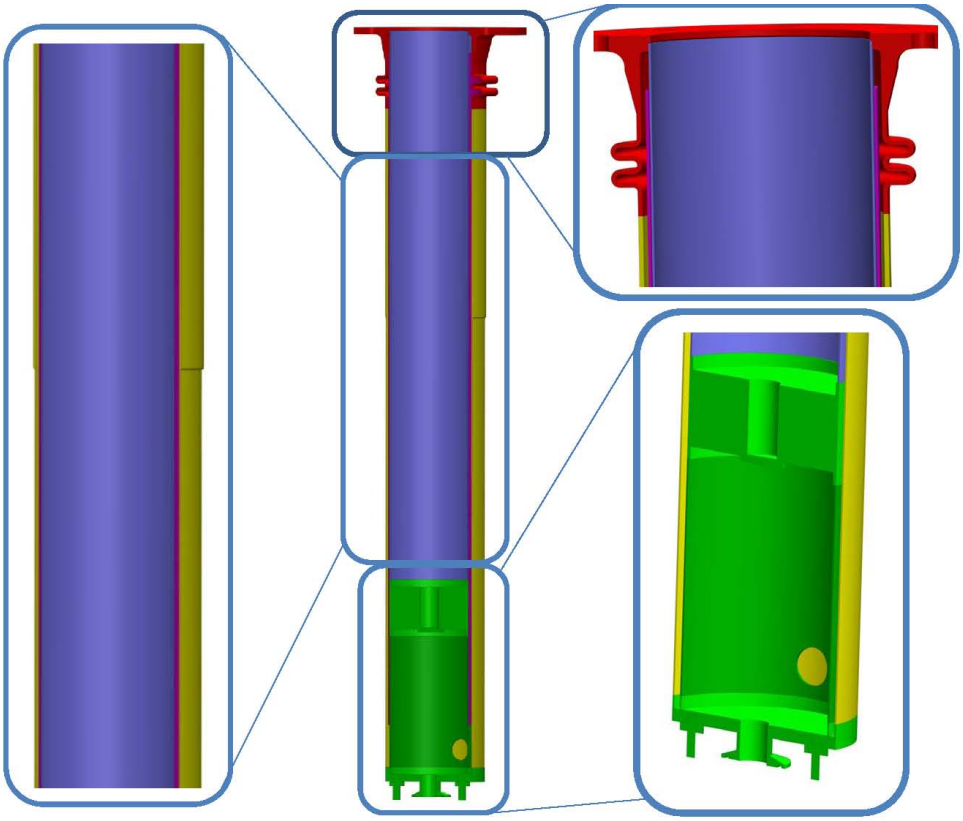

Figure 4.10: Sections of interest for the heat transfer analysis of the cryostat. - The cross section of the 3D CAD model of the cryostat with three sections emphasized. The top of the inner part, not directly exposed to the LN_2, is approximately 120mm. The section exposed to the LN_2, the middle section, is approximately 750mm and bottom section which is actually the TTE is 200 mm long. (The surface between the inner and outer wall of the cryostat including the whole height of the cryostat: $A_{cryo} = 2 \cdot \pi \cdot R \cdot L = 2 \cdot \pi \cdot 0.075[\text{m}] \cdot 1.065[\text{m}] = 0.501 m^2$)

be ensured in the vacuum chamber in order to suppress the heat conduction through gas. The heat transfered per surface area for two parallel plates (107) can be expressed as 4.5

$$\dot{Q}_{gas-conduction} = \hat{\alpha} \frac{(\gamma + 1)}{(\gamma - 1)} \sqrt{\frac{R}{8\pi MT}} P(T_2 - T_1) \tag{4.5}$$

where α is the mean accommodation coefficient of the gas molecules at two planes, γ is the ratio of specific heats at constant pressure and constant volume C_p/C_v, R is universal gas constant, M is the molecular weight of the gas molecules, P is the

gas pressure and T_2 and T_1 the temperatures of the planes with higher and lower temperature, respectively. The above equation can be reduced to

$$\dot{Q}_{gas-conduction} = const \cdot \hat{\alpha} \cdot P \cdot (T_2 - T_1) \tag{4.6}$$

where the *const* will be ≈ 2 and $\hat{\alpha}$ will be ≈ 0.9 for the air at $T = T_1$=77 K. The pressure is in units of Pa, temperature in K and specific heat transfer is in Wm^{-2}. The heat transfered through residual gas is a linear function of the pressure between two planes expressed with

$$\dot{Q}_{gas-conduction}[W/m^2] \approx 402 \cdot P[Pa] \tag{4.7}$$

An estimate of 1.90 W heat transfered via gas conduction was calculated taking the value 10^{-4} mbar (10^{-2}Pa) for the gas pressure and A_{cryo}=0.501m^2 for the active gas heat exchange surface. The pressure of the residual gas in the vacuum chamber is indeed a crucial parameter. The value of 10^{-5} mbar and lower would make this heat transfer negligible. Is is noteworthy to say that maintaining a high vacuum is not trivial and proper measures have to be taken to ensure vacuum quality over a long time (getter compounds, regeneration of vacuum by pumping).

The heat conduction through the solid: The heat transfered through the inner wall from the top and bottom section is determined by the thermal conductivity of the material, $K(T)$, and is given by

$$Q_{conduction} = \frac{A}{L} \int_{T_1}^{T_2} K dT \tag{4.8}$$

where A is the cross section area normal to the heat transfer propagation and L is the distance from the high temperature end (T_2=300 K) to the low temperature end (T_1=77 K). The inner cryostat wall is a cylinder with radius of 72 mm and a wall thickness of 1.5 mm. The cross section area of the wall is $A = \pi(R^2 - (R-\delta)^2)$=671.5 mm^2.

The resulting conduction heat transfer of the cryostat including the cross section area and lengths for bottom and top of the cryostat together with integral thermal conductivity for the temperature range from 300 K to 77 K (64 K) are presented in Table.4.4.

Section	A [m^2]	L [m]	$\int K(T)dT$[W/m] (107)	Q_{cond}[W]
Via Gas @10^{-4}mbar	0.4818	-		1.90 (1.95)
Top	6.7 10-4	0.115	2720 @77K	15.90 (16.60)
TTE	6.7 10-4	0.195	(2850 @64K)	9.35 (9.80)
Shaft	2.8 10-3	0.115		66.90 (70.00)

Table 4.4: Heat transferred by conduction through the residual gas and different sections of the cryostat for 77 K (64 K).

Thus, the estimated heat transfer through the TTE is ∼10 W which is comparable to the design from (105, 118) where TTE was made from composite material (G10) and 60W of heat in total was estimated for 77 K. The table includes the heat transfer estimate for the top shaft. This is included because the cryostat is operated as open LN_2 bath and the HTS field winding had the shaft as a top TTE. This is not optimal and in the future with closing the cryostat, the top TTE will be similar to the existing one at the bottom of the cryostat.

4.3.8.2 Radiation heat transfer

Radiation heat transfer can be a big part of the integral heat transfer in low temperature equipment design. To estimate the heat transfered by radiation, two cylinder walls of the cryostat are assumed to be parallel plates where the heat transfer is given(107) by:

$$Q_{radiation}[W/m^2] = \sigma F_A F_B A_1 (T_1^4 - T_2^4) \tag{4.9}$$

where σ=5.67×10^{-8} $Wm^{-2}K^{-4}$ is the Stefan-Boltzman's constant, A_1 is the surface area of the outer wall, T_1 and T_2 are temperatures of the outer and inner wall, respectively. The emissivity related coefficients for two planes, F_A and F_B are defined as

$$\begin{aligned} F_A &= 1 \\ F_B &= (1/e_1 + 1/e_2 - 1) \end{aligned} \tag{4.10}$$

Values for the emissivity of the stainless steel e is in the range of 0.02-0.1 (107) depending on the surface finish. If the value of 0.03 is taken for both walls, one gets

$$Q_{radiation}[W] = 5.67 \cdot 10^{-8}[\frac{W}{m^2K^4}] \cdot 1 \cdot 0.01526 \cdot (300^4[K] - T_2^4) \tag{4.11}$$

The heat transfered by the radiation for the plates with the total surface of A_{cryo}=0.501 m^2 (along the whole length of the cryostat) and for the 77 K was found to be 3.48 W. This value was over estimated because effective radiation surface was somewhat smaller. Nevertheless, the 3.5 W heat is not small (especially if the cryostat is to operate at lower temperatures, i.e. $\leq$64 K) and thus the MLI was employed to reduce this value. Ten layers of Multi Layer Insulation (MLI) CoolCut 2NW foil (153) was wrapped three times around the outer side of the inner cryostat wall and tied with stainless steel wire and low emissivity aluminum adhesive tape (see Fig.4.9). Each aluminum layer is 12 μm thick and is coated on 0.13 mm polyester substrate (153).

In the ideal case, n layers of MLI should allow only 1/(n+1) part of the radiation (152). For 30 layers of the MLI, which was reported as an optimum number of layers (107), the radiation has been reduced by a factor of 31 resulting in 0.112 W for the total heat transported via radiation. This number would not change much if the cryostat is operated at lower temperatures (double value for 20 K operation).

4.3.9 The evaporation test

The integral heat transfer is the sum of the conduction and radiation heat transfered from 300 K to the low temperature chamber. The dominant influence on the sum is the conduction through the TTE and the top section of the cryostat. The sum of the heat without the shaft contribution is 27.27 W according to the Table.4.4. It is possible to evaluate the heat transfer that the low temperature chamber will experience experimentally by monitoring the evaporation rate of LN_2. The evaporation test was performed, and results are shown in Fig.4.11 for the case where the cryostat is without the HTS field winding.

In this standalone test, the conduction heat through the shaft is not included. The main contributors to the integral heat transfer rate are the TTE, conduction in the residual gas and the radiation. The heat conduction at the top of the cryostat is also not significant here because as the LN_2 evaporates, the cold N_2 gas will per-cool the top section of the inner wall of the cryostat. Two 'boil-off' tests have been performed, one after first pumping and another after several cooling cycles. The heat transfer

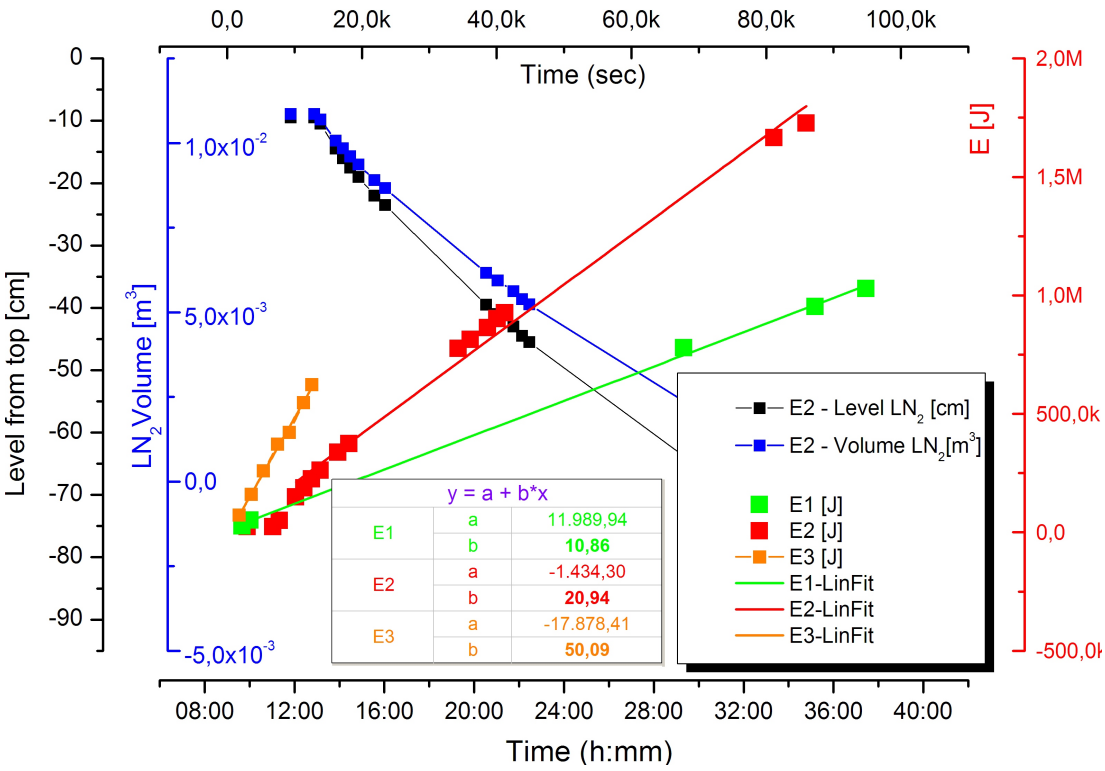

Figure 4.11: The LN_2 'boil-off' data for the cryostat. - The data for evaporated LN_2 are presented for three cases: (a) The cryostat alone after evacuation of the vacuum chamber. (b) The cryostat after few thermal cycles. (c) The cryostat and the HTS field winding including all current leads. The linear fit was performed where the slope represents the average rate of heat transfer in Watts.

rate derived from the first test was in average 10 W where the pressure in the vacuum chamber was below $5{\cdot}10^{-6}$ mbar throughout the whole test. This is in agreement with the results for the conduction and radiation heat transfer, reported in the Table.4.4. In the second test, the vacuum pressure was not measured during the test and the average integral heat transfer rate was determent to be 21 W. The higher heat load is probably due to the higher pressure in the vacuum chamber which was caused by out-gassing. The rate of evaporation was monitored when the HTS field winding was under test too. Here, the added contribution from the shaft and current leads (8 cables in total, each with 10 mm^2 cross section) are of the same order of magnitude as the heat load of the cryostat. The derived integral average heat transfer rate was found to be 50 W. It is important to mention that during the experiments, the level of the LN_2 was

maintained in the range of 10 cm to 30 cm from the top of the cryostat.

4.4 The field winding

The field winding is comprised of a number of HTS coils, maximum 8, supported by the housing for the coils. The field winding steel is optional and can be omitted if the test calls for it. If the cold steel is part of the HTS field winding, the coils are stacked on the steel and the whole structure is supported by the coils housing.

4.4.1 HTS coil

HTS conductors are commercially available in the form of tapes 4 mm – 12 mm wide and 0.1 mm – 0.3 mm thick. Both BSCCO and YBCO are ceramics, brittle by nature. Because of it, 1G and 2G tapes have certain mechanical constraints like minimal bending radius and maximum yield stress. In addition, tapes have also limited twisting ability around the longitudinal axis. As a result only simple, racetrack, coil geometry have been wound with an HTS tape. Constructed coils are listed in Table.4.5 and the illustration of the proposed coil design is shown in Fig.4.12.

All coils have access to the voltage measurement across the whole coil as well as several sections (one or more) in the middle of the winding. All voltage measurement points are accessible on the printed board mounted on the outer frame. Thus, the difference in the performance of the outer and the inner section of the HTS coil can be evaluated, as all turns are not exposed to the same magnetic field and will thus have different critical currents.

4.4.1.1 The HTS coil frame

All coils have the same design. In this way space allocated for the turns in the coil is the same for all coils. Thus, the coil performance can be evaluated. This is very important for an electrical machine design because the critical engineering current density of the coil, $J^e_{c_{coil}}$ is not only a function of the performance of an HTS tape used in the coil but also depends on the insulation material employed, the coil former (structural support) design, cooling requirements of the design (additional channels or conducting cooling bars), etc. So, it is not just an HTS conductor but the HTS coil design and production

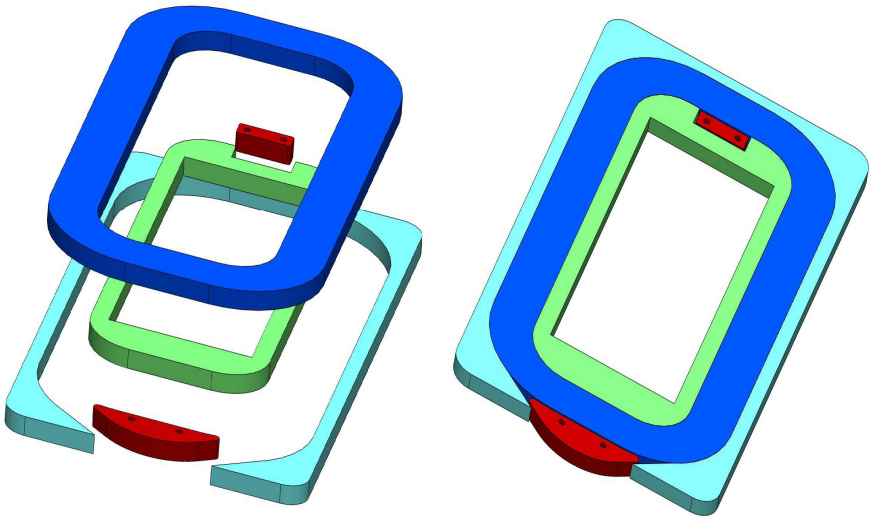

Figure 4.12: The 3D CAD illustration of the Superwind HTS coil design. - The HTS coil is shown in the exploded view at the left, making all parts identifiable. The inner and outer frames, green and light blue, respectively, are made from SS316L. The coil terminals, made from copper are colored red. The ends of the coils are positioned at both the outer and inner frame. The winding process was as follows: The inner frame was mounted on the winding machine. The insulated HTS tape was wound on to the inner frame. All access points for the measurement of the voltage and coils terminals have been soldered at appropriate place during the winding process. The outer frame was added to the wound coil, measurement wires are lead to the circuit board mounted on the outer frame (not shown in the figure) and coil is vacuum impregnated with the epoxy(5).

approach together with the performance of HTS conductor that are being assessed in this way.

The coil *Coil*#4 (not used in experiments) is shown in Fig.4.13. Frame is made form SS316L and both inner and outer frames have a series of holes that are used as a mechanical interface between the coils during the field winding assembling. The design of the coil frame was primarily intended for double pancake coils, where two racetrack coils have been coupled together into one. In that arrangement, the double pancake coil would have both of its accesses to the coil terminals at the outer frame, allowing for a denser packed field winding. However, the coils were operated with individual

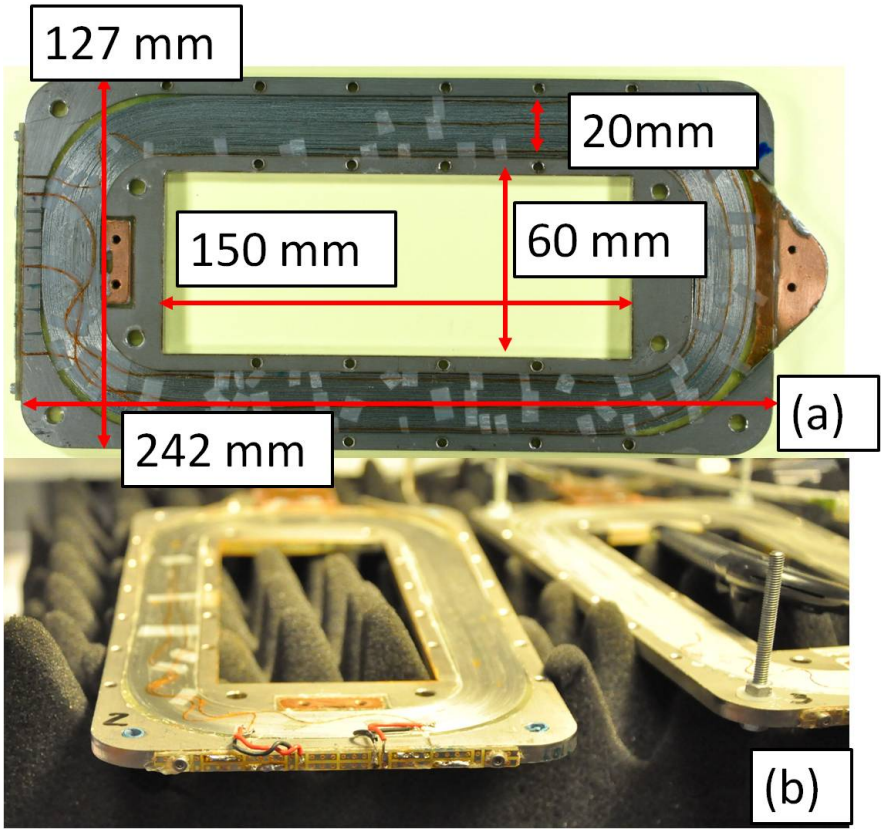

Figure 4.13: The HTS coil - (a) *Coil*#4; (b) *Coil*#2.

supplies and current leads which resulted in a less compact but more flexible setup.

4.4.1.2 Electric insulation for HTS coil

The number of materials that can be used as a electrical insulators at low temperature is limited. Next to having appropriate electrical strength, the insulation material must be able to cope with thermal and also mechanical stresses that the HTS tape will be exposed to during machine operation. The few materials that could be an option include composite (glass fiber tape), Mylar tape, Kapton tape, etc. The insulation level for each coil is determined by transients of the field current and self inductance of the coil. As these are small coils, a voltage insulation level of 100 V would suffice.

As implied in the previous section, electrical insulation has a major implication in the coil performance. The most obvious impact on a coil performance is the critical engineering current density $J^e_{c_{coil}}$ of the coil. If the electrical insulation of the coil needs

to be thick, where the thickness primarily depends from the electrical strength of the material, the $J^e_{c_{coil}}$ of the coil will decrease.

Coil ID	L_{coil} [cm]	No. of Turns	HTS Type	I_c^{sf}, 77 K [A]	Insulation	Voltage access points	Add-In probes
Coil2	2540	48	AMS-1G	120	Glass Fiber	3	Hall sensor
Coil3	2880	51	AMS-1G	120	Glass Fiber	3	Hall sensor
Coil5	2500	46	AMS-1G	120	Glass Fiber	6	Hall sensor, RTD
Coil6	3165	56	AMS348C-2G	120	Glass Fiber	6	Hall sensor
Coil7	7000	125	SP4050-2G	120	Epoxy	3	-
Coil8	7000	125	SP4050-2G	120	Epoxy	3	-

Table 4.5: The HTS coils constructed for the testing. AMS-1G (1) is BSCCO wire from American Superconductor, AMS348C-2G (1) is YBCO coated conductor 348 from American Superconductor and SP4050-2G (2) is YBCO coated conductor from Super Power Inc.

Depending on the type of the HTS tape and insulation employed, the number of turns for different coils can vary. Details about completed HTS coils are presented in Table.4.5.

4.4.2 The HTS field winding

The space allocated for the HTS coils can accommodate a maximum of 8 single HTS coils, each 5 mm thick or 5 double pancake coils (10 single coils) all stacked together. In the HTS field winding, illustrated in Fig.4.14, all coils are placed between 4 aluminum bars which are screwed into the top and bottom flange. The aluminum bars are acting as a housing for the HTS coils with the steel providing all the mechanical support. The position of the coils can be adjusted with spacers placed in between the coils. The coil stack is fixed together with four treads and 8 nuts placed in each corner of the coil. To utilize the versatility of the HTS field winding coils have separate leads, two for each coil.

The current leads are lead to screw terminals where the coils connections can be altered without interfering with the coil arrangement itself. Maximum flexibility is

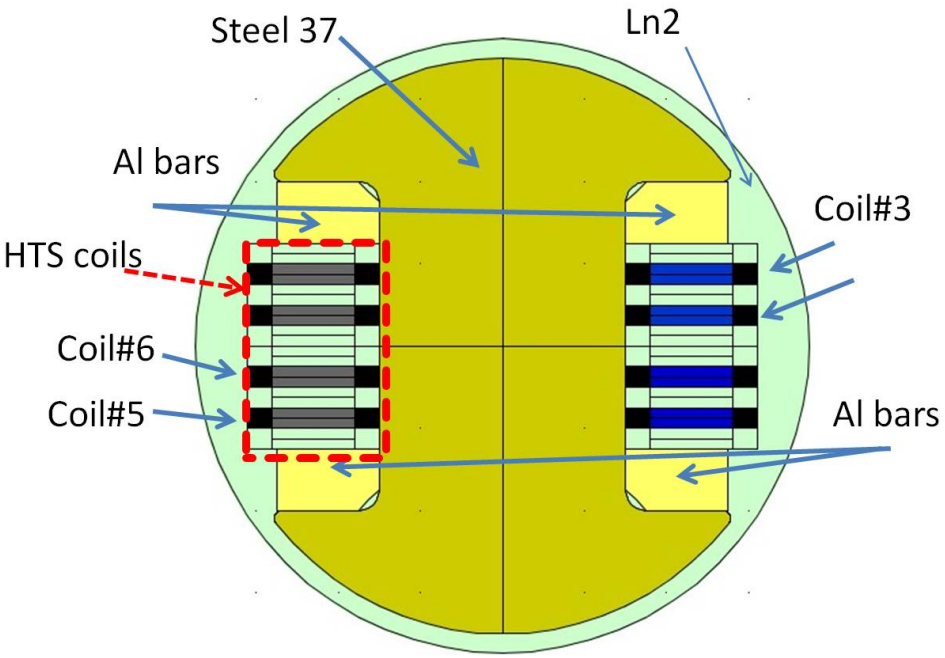

Figure 4.14: HTS field winding - 2D cross section of the HTS field winding with the HTS coils. The arrangement of the coils is the same as in the conducted tests. The space allocated for the HTS coils can accommodate maximum 8 coils (single racetrack coil), each 5 mm thick. The coils are placed between four aluminum bars (yellow) acting as a mechanical support structure. Steel 37, the field winding steel (light green) is fixed by screwing the pole shoe into the steel body and thus exerting the pressure on the aluminum bars.

achieved if each of the current leads are brought outside of the cryostat. Consequently, the increase in the heat input to the LN_2 chamber should be expected as reported in Sec.4.3.8.

4.4.3 Cold steel

The HTS field winding can stand alone (without steel) or the HTS coils could be wrapped around the cold steel. This corresponds to the two types of the HTS machine, so-called air-core machine and the HTS machine more similar to the conventional synchronous machine where the steel is a part of the field winding, as discussed in Ch.3.

The soft carbon steel, named Steel37, has been employed as the field winding steel. The Steel37 was machined from a single piece of steel into three parts, two pole caps and

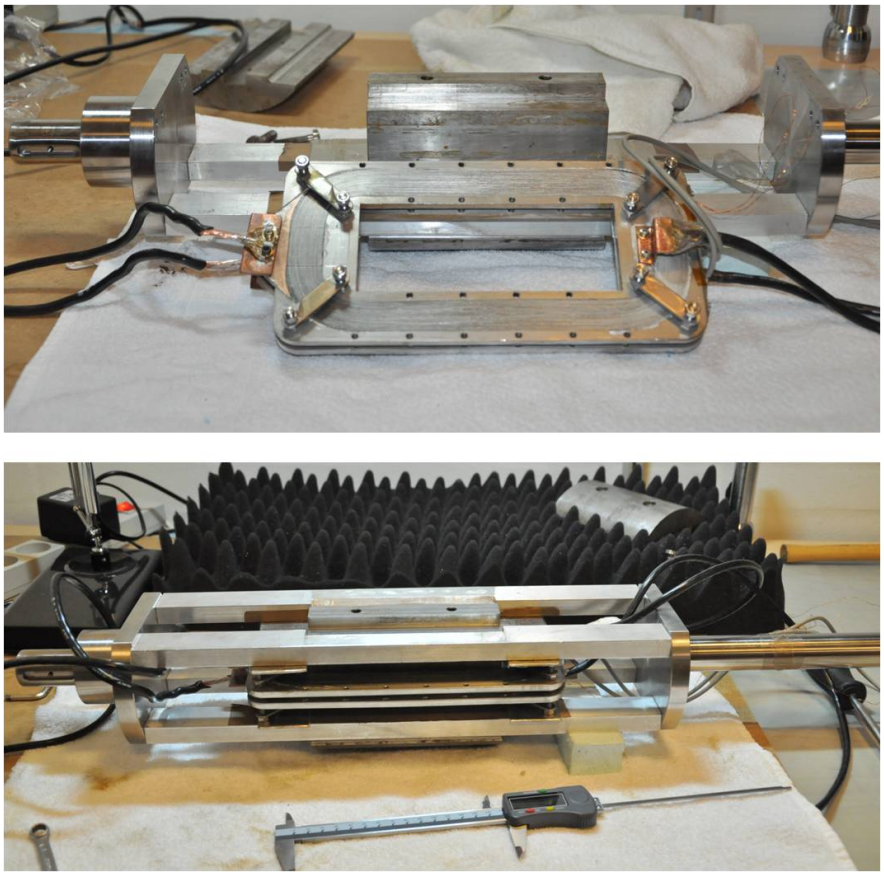

Figure 4.15: HTS field winding - The HTS field winding is shown in assembly phase with two HTS coils mounted on the cold steel.

the middle. The pole caps are screwed into the middle piece (see Fig.4.16). The choice of the steel was made with following consideration. The material should be low cost and the steel should be a monolithic piece and not laminations. In addition, even though in this setup the magnetic air gap is large compared to the conventional machines, the HTS machine flux is in general air dominated (either because of the absence of the steel or because the steel is saturated). Thus, it was of interest to employ the steel with relatively low saturation (see Fig.4.17) in order to examine the implication of the saturation with regard to HTS machine operation (an HTS will experience more leakage flux).

Air gap flux density distribution The pole caps are circular (no pole shaping) with the pole angle τ_{pole}=103.7°. The harmonic content of the air gap distribution can

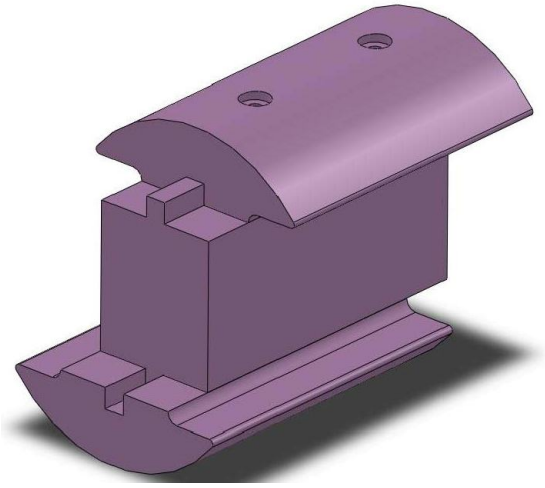

Figure 4.16: The 3D CAD model of the field winding steel - The cold steel where the pole caps are skewed in the middle part.

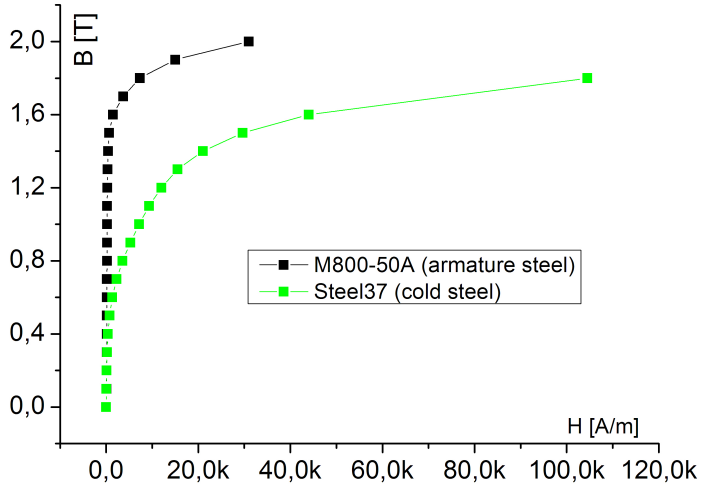

Figure 4.17: The field winding steel - The comparative diagram of permeabilities of armature steel, M800, and the field winding steel, Steel37.

be estimated by assessing the harmonic of the simplified air gap flux density angular distribution. The distribution of the flux density of one pole ($-\pi/2 \leq \theta < \pi/2$) can be represented as a constant value B_m for the angles $-\tau_{pole}/2 \leq \theta \leq \tau_{pole}/2$ and zero for other angels.

$$B_g(\theta) = \begin{matrix} B_m, -\tau_{pole}/2 \leq \theta < \tau_{pole}/2 \\ 0, -\tau_{pole}/2 \geq \theta > \tau_{pole}/2 \end{matrix} \tag{4.12}$$

where the ν is harmonic ordinal. The amplitude of the each harmonic present in the field winding produced air gap flux is express with

$$B_{\nu g} = \frac{2}{\pi} \int_{-\tau_{pole}/2}^{\tau_{pole}/2} B_m cos(\nu\theta) d\theta = \frac{4B_m}{\nu\pi} sin(\frac{\nu\tau_{pole}}{2}) \tag{4.13}$$

A considerable amount of harmonics is expected in the air gap flux density with the 5^{th} leading with 25%. The content of the harmonics is illustrated in Fig.4.18 where harmonic content is derived with approximation presented above (with expression 4.13) is compared to the results derived from FE model.

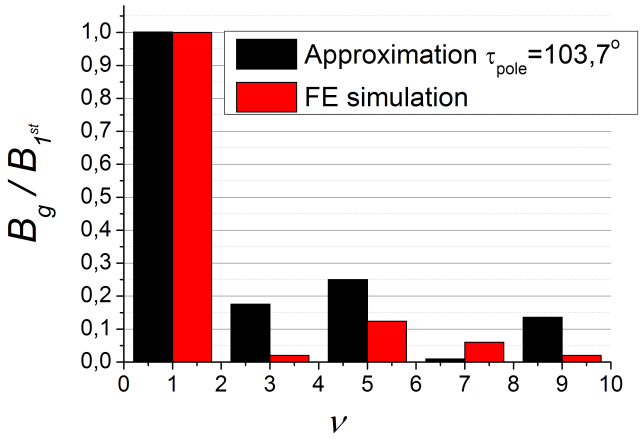

Figure 4.18: The HTS field winding steel harmonic content - The harmonic content for the pole with constant radius of R_{pole}=70 mm and τ_{pole} = 103.7°

In this setup the 5^{th} and the 7^{th} harmonics were deliberately kept in the machine design with intention to allow the analysis of its impact on the HTS coils as they are most common in the conventional machines and are not filtrated in the three phase system (machines or transformers connected into delta). The simplified approach to estimate the harmonic content of the pole cap was verified by means of FE model. A Fourier transform was performed on the air gap flux density derived from FE simulation of one particular case presented in Fig.4.19 where the harmonic content is compared to estimate in Fig.4.18.

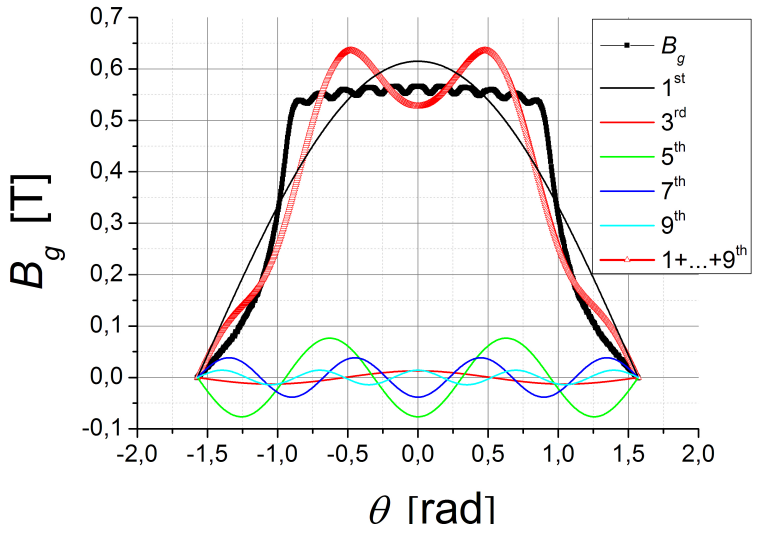

Figure 4.19: Air gap flux density harmonic content - Harmonic content of the air gap flux density derived from the FE model where the field winding had MMF∼12k Ampere-Turns. The figure includes the first five odd harmonics.

Additionally, the harmonic content of the induced voltage could be suppressed in various ways like pole shaping, choice of appropriate armature winding factor all targeting specific harmonic which will be part of future work.

4.4.4 The field winding housing

The HTS field winding is fixed in between 4 aluminum bars which are screwed into the top and bottom shaft. In that way the coils and steel could be mounted independently and a number of field winding arrangements can be investigated (from absence of the field winding steel, experiments with different types of steels used as a cold steel, shapes of pole caps, etc.). Bars are screwed into the top and bottom shaft (see Fig.4.20) with 4 screws per bar. The aluminum bars are acting as a housing for the HTS coils and the steel providing mechanical support. A slot exists in each aluminum bar (see Fig.4.20b) that is adopted to the shape of the cold steel, fixing it to a specific position. The maximum stress of $3.2{\cdot}10^6$ Pa have been found in the coil support structure for the rated electromagnetic torque of 250 Nm, which is well in the material capabilities (where $20{\times}10^6$ Pa is maximum allowed stress for aluminum).

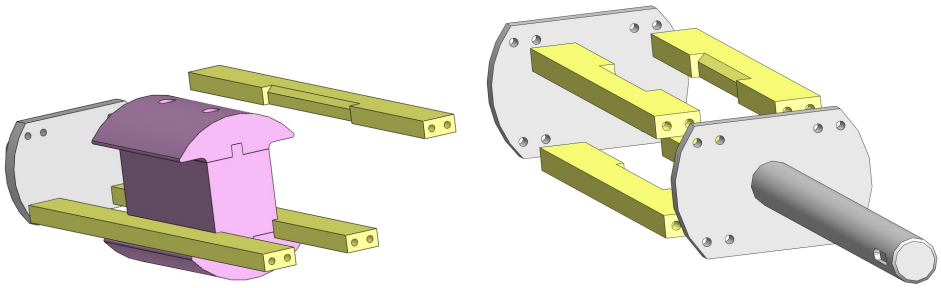

(a) (b)

Figure 4.20: The field winding support -

The HTS housing bars are placed at the far outer radius and not concentric as the shaft would be. The reasoning for this is found in the magnetic design of the HTS field winding. The racetrack coils are planar coils and if the bars are placed at the middle, similar to how the shaft would have to be, no coils could be placed at the middle of the poles where the best performance of the HTS coils would be expected due to the low amount of stray flux. Secondly, if instead the bars were in the middle and the coils were at the outer, the volume allocated for coils would be smaller.

4.5 Torque Measurement

Several brands of torque meters are commercial available (Himmelstein, HBM, Scaime and others). But, with the setup positioned vertically and the absence of the shaft, the commercial torque meters would need to be adopted and their measurement performance could not be guaranteed. Additionally, the cost of the commercial torque meters is substantial.

Instead, the setup is equipped with a custom built torque measurement option, illustrated in the Fig.4.21. Two SS316L plates are placed at the bottom of the cryostat. One plate (bottom plate) is fixed to the frame of the setup (not able to move). The other plate (top plate) has an imprint of the TTE at the bottom of the cryostat, so when lowered down on to that plate, the cryostat and the plate will be locked with respect to the torsion. A spacing between the two planes is maintained with a SS316L ring. The ring fits into concentric slots machined in the top and bottom plates. In this way, the top plate is not able to move in any other direction except to rotate around

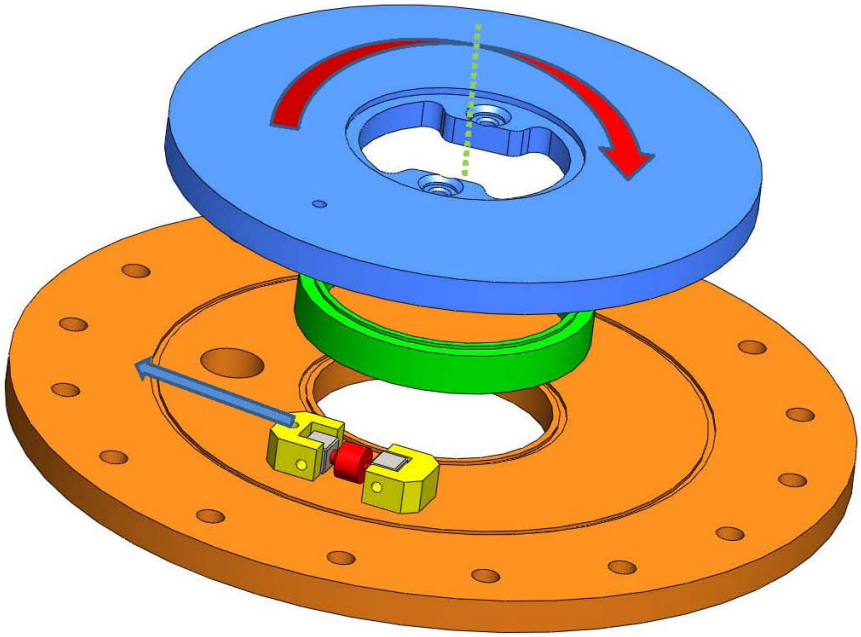

Figure 4.21: Superwind torque measurement assembly - The 3D CAD model of a torque measurement assembly consisting of two plates and a force transducer in between. The bottom plate (orange) is fixed to the frame while the top plate (blue) is fixed to the cryostat's TTE. The ring (green) has the purpose of simple bearing. It allows the rotation around the cryostat's axial axis. The force transducer element (red) is fixed to the bottom plate at one side and to the top plate on the other side (yellow). The torque (red arrow) experienced by the top plate is translated into an elongation force of a force transducer (blue arrow) and finally into a voltage signal from a strain gauge which is proportional to the torque.

its axial axis. The vacuum valve for the vacuum chamber of the cryostat is placed at the bottom of the TTE, hence both plates have openings in the center.

The electromagnetic torque is transferred from the HTS coils and cold steel through the field winding housing and TTE to the top plate of the torque measurement assembly. If the load cell (force transducer) is placed in between the two plates, bottom being fixed to the frame and top to the TTE of the cryostat, the output voltage from the load cell will be proportional to the torque. By adjusting the distance from the axial center of rotation to the load cell, the torque measurement range and sensitivity could be tuned which makes this assembly very flexible.

The HBM-UB9 500 N bidirectional force transducer (154) is used as a load cell.

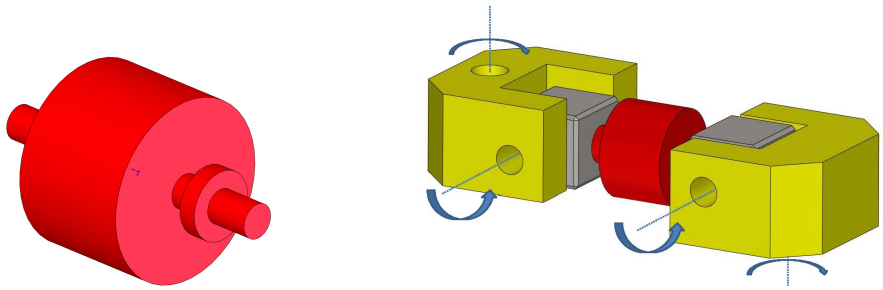

(a) Force transducer HBM-U9B **(b)** Force transducer HBM-U9B

Figure 4.22: Force transducer HBM-U9B - (a) The HBM-U9B 500N force transducer with axial load direction; (b) The force transducer (illustrated red) is screwed into the steel elements (illustrated gray) and fixed with contra screws. The steel elements (gray and yellow) are coupled with the horizontal shafts so that free rotation is allowed, as the blue arrow illustrates. A similar shaft exists for the vertical direction, connecting the plates and joint (yellow)

The UB9 transducer, illustrated in Fig.4.22a, has an integrated full bridge strain gauge with a linear voltage output. The load cells are general very sensitive to the load in the lateral direction (different than the rated direction). To avoid damage of the force cell, there should be no force acting in any other direction than the direction specified as a rated load direction. Thus, the force cell is connected to the plates through custom made joints with two degrees of freedom per joint. As illustrated in Fig.4.22b, the free rotation around the two axes of the joints will make sure that the position of the force transducer will adapt so that the rated load direction is maintained. During the operation the force cell nominal strain is measured in microns which means that the whole torque measurement assembly will be practically stationary. To minimize the friction between top and bottom plate, a 0.5 mm layer of Teflon lubricated with silicon oil was introduced.

The calibration of the torque measurement add-in had to be performed to experimentally determine the output from the load cell and applied torque. In order to carryout the calibration, a Newton meter was connected to a 0.8 m long bar (arm) connected to the top plate of the torque measurement assembly and several values of torque have been applied. The results of the calibration test are presented in the Fig.4.23.

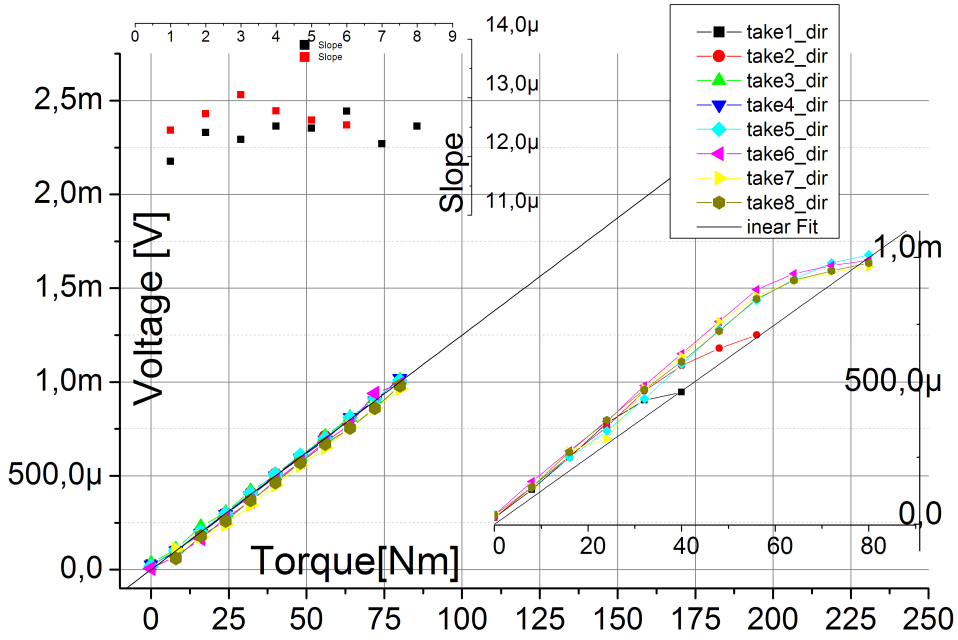

Figure 4.23: Torque measurement assembly calibration. - The relationship between the output voltage of the force cell and the applied torque for eight repeated measurements. The system is experiencing hysteresis, which is reported in the bottom inset, due to the static friction. The linear fit is performed on all 'takes' and the slopes derived are reported in the top inset. The black and red markers are denoting raising path (raising the torque) and returning path (lowering the torque) in the torque cycle.

During the calibration, the difference between strain gauge voltages and applied torques when torque was increased or decreased was observed. Thus, since the voltage value depends on the direction of the change of the applied torque (increasing or decreasing), the measurement assembly performance will have hysteresis nature. The hysteresis present in the voltage - torque relationship is illustrated on the lower inset in the Fig.4.23. This effect is the consequence of the static friction between the top plate and the bottom plate. By averaging the slopes from all experiments, the conversion factor between voltage and torque will be $12.6 \cdot 10^{-6}$ V/Nm.

4.6 Speed and Position Measurement

The speed and position measurement are custom fitted and integrated into the setup. A two channel optical encoder Honeywell HOA0901 – 012 (155) , with optical resolution of 0.45 mm was used. Accordingly, a code–wheel was designed to fit the encoder specification. The code-wheel was drawn in CAD software and printed on the transparent polyester foil (overhead foil) with the standard laser printer and with the standard resolution of 600 dpi. The code-wheel has an optical radius of R_{op}=197.8 mm and $N_{encoder}$=1350 dark–transparent cycles.

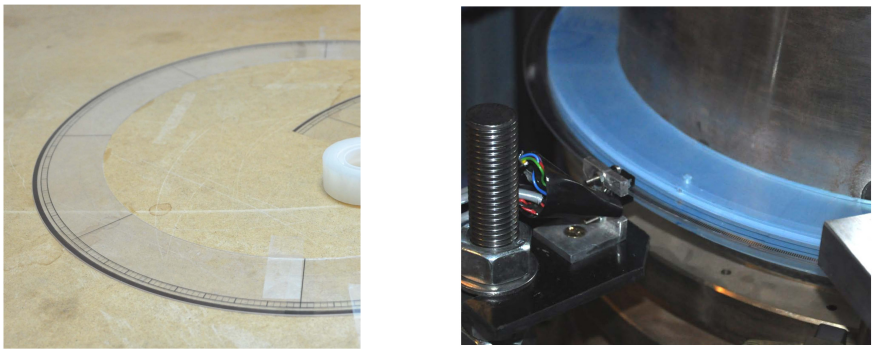

(a) The code-wheel for the encoder under construction

(b) Assembled encoder mounted on armature housing

Figure 4.24: The encoder add-in - (a) The code-wheel drawn with AutoCAD software was printed on a transparent polyester foil (overhead foil) with a standard laser printer in 600 dpi resolution. The code-wheel has an optical radius of R_{op}=197.8 mm and $N_{encoder}$=1350 optical windows. The transparent foil is glued on a 1 mm Plexiglas layer to make the code wheel more rigid. After, the code-wheel was pressed in between two 10 mm Plexiglas rings acting as a encoder housing. (b) The encoder mounted on the armature housing and encoder IC.

The two quadrature counter channels can resolve the direction and the magnitude of the movement with an accuracy of the 0.1 mm which at the R_{op} corresponds to the angle resolution of 0.033°.

4.7 Armature Position Locking

The electromagnetic torque is a function of the magnitudes of the magnetic fields and angle between them, as presented in Ch.3. These parameters, the magnitude of

magnetic field and angular displacement of the armature winding with respect to the HTS field winding and their implication to HTS machine operation are important. At a later time, these parameters can be referred to the performance of the machine under different load conditions. With that purpose, a custom add-in was designed to lock the armature position at arbitrary angle with respect to the field winding (see Fig.4.25). The position of the armature can be monitored with high resolution with the encoder.

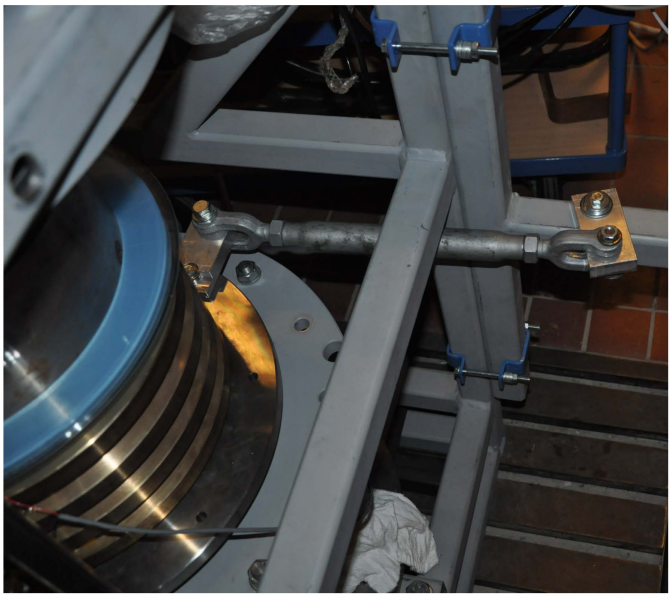

Figure 4.25: Armature winding lock assembly -

The disc attached to the armature housing at the bottom was used as coupling interface between the armature and an adjustable rod. The disk has axial holes along the circumference spaced by 45°. The position of the armature winding is set by adjusting the length of the adjustable rod. The armature position is locked by tightening the two contra nuts on the adjustable rod. The armature is able to rotate up to 60° with full change of the length of the adjustable rod after which the point of coupling on the disk needs to be changed to cover the next 60° (see Fig.4.26).

To investigate the performance of the HTS field winding at different armature fields (armature reaction) and different angles, the static tests were planned where the position of the armature winding with respect to the HTS field winding was controlled with the Armature Position Locking add-in. The test is illustrated in Fig.4.26 where

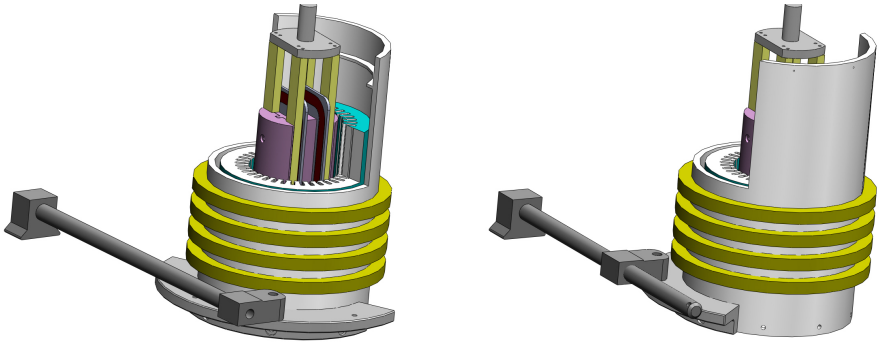

(a) The Armature Position Locking add-in at arbitrary position

(b) Position of the armature winding controlled

Figure 4.26: Procedure for Armature Locking experiment - (a)The Armature Position Locking add-in at arbitrary position. The armature winding is displayed in cut-off mode to correlate its position to the HTS field winding (b) Position of the armature winding controlled with the adjustment of the length of the rod in the Armature Position Locking add-in.

A	B	C	Stator field	A	B	C	Stator field
Two phases				All phases*			
1	-1	0	-30°	1	-0,5	-0,5	0°
1	0	-1	30°	-1	0,5	0,5	180°
0	1	-1	-90°	-0,5	1	-0,5	120°
0	-1	1	90°	0,5	-1	0,5	-60°
-1	1	0	150°	-0,5	-0,5	1	-120°
-1	0	1	-150°	0,5	0,5	-1	60°

Table 4.6: The armature winding field position with respect to the choice of the phases and current direction of each phase.

the armature will rotate 60° for a full change of the length of the adjusting thread. The armature winding, static in space, is powered with a dc current entering one phase and exiting at the other two phases. The direction of the armature flux is thus controlled by the physical position of the armature winding and with the choice of the pairs of phase windings supplied with a current. Table.4.6 contains the angular shift of the armature field direction with respect to the magnetic field axis of phase A for various phase pairs.

As it can be seen from Table.4.6, for an angular span of the armature winding of 60°, every direction of the armature field can be covered by varying phases pairs, as illustrated in Fig.4.27. Using both two and three phases combinations, the number of angles could be doubled (from 6 to 12) but using all three phases calls for two power supplies (or some other way of achieving the half of phase current in other two phases). Due to a limited number of power supplies, just two phases at the time were used in the static experiments.

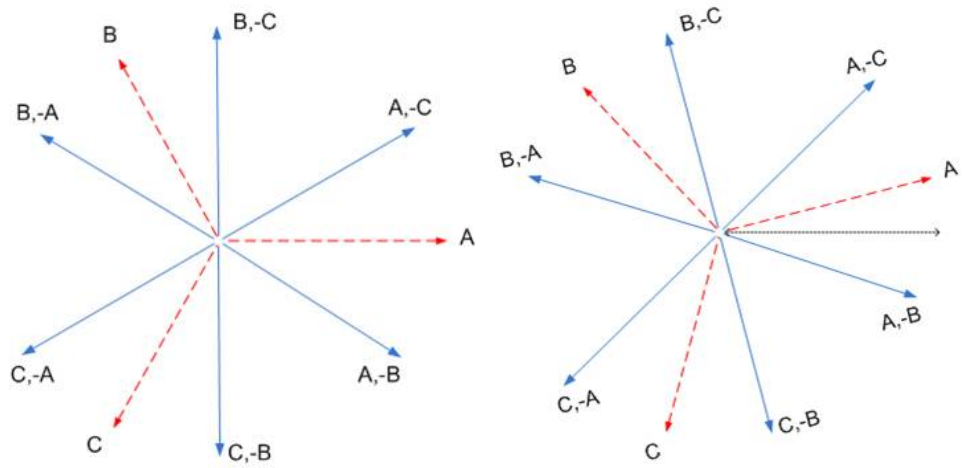

(a) The Armature Position Locking add-in at arbitrary position

(b) Position of the armature winding controlled

Figure 4.27: Armature Locking experiment: angular shift -

The armature reaction with a current I running through two phases is $\sqrt{3}/2$ lower compared to the the armature reaction when supplied with symmetric three phase currents where I is the amplitude of the current waveform. Thus, a correction factor needs to be taken into account when the analysis is carried out.

Chapter 5

Experimental Results and Discussion

"An Experiment, like every other event which takes place, is a natural phenomenon; but in a Scientific Experiment the circumstances are so arranged that the relations between a particular set of phenomena may be studied to the best advantage. " **by James Clerk Maxwell**.

This chapter will describe performed experiments intended to compare the performance of two configurations of the HTS coils in the field winding of the machine. In total, six HTS coils have been employed and all experiments were carried out at 77 K.

First, the HTS coils are characterized individually by determining the critical current and n value. Than the coils were connected into a series connection and performance of both configurations of the field winding were analyzed. Section voltages of the coils were used to confirm critical parameters defined from a coil voltage both for the individual coils and for the field winding. The impact of an armature current on the HTS coils in the field winding was studied in depth where both armature current and an angle between the armature winding and the HTS field winding magnetic axis were varied. The interaction was quantified with the derived relation between the critical current of the field winding and the armature current. Consequently, the operational window of the HTS field winding was defined.

Furthermore, two methods to increase the performance of the HTS field winding are proposed and their implication discussed. Finally the HTS machine parameters are determined and discussed.

5.1 Field winding configurations

Flexibility of the experimental setup was one of the primary milestones of the design as described in the previous chapter. Thus, two different configurations of the field winding were planned to be subjected to experiments in order to investigate conceptual differences between 1G and 2G coils and their position in the field winding.

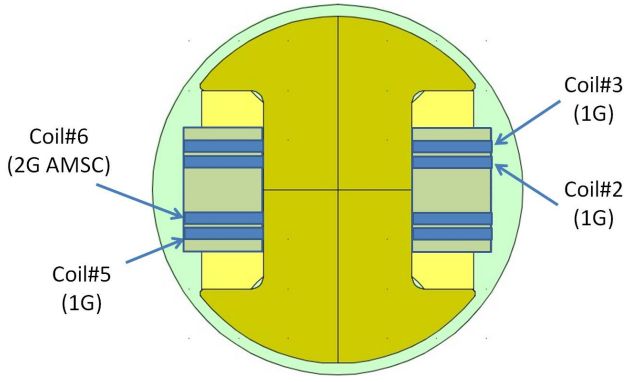

(a) Arr1

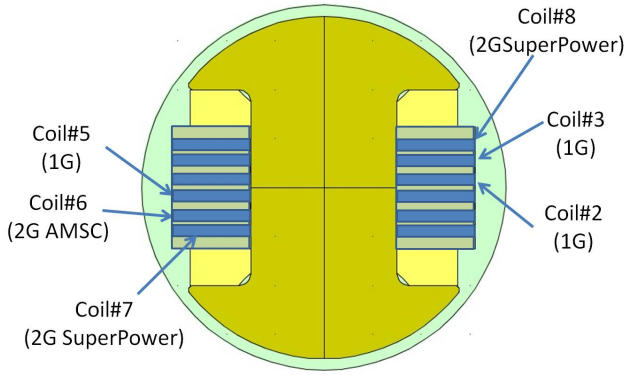

(b) Arr2

Figure 5.1: Field winding configurations - Two arrangements of the field winding.

Two arrangements of the HTS field winding are presented in Fig.5.1. In the first arrangement (Arr1), the HTS field winding comprises 4 coils in total with three 1G

coils ($Coil\#2$, $Coil\#3$ and $Coil\#5$) and one 2G coil ($Coil\#6$). The 1G coils are placed closest to the poles while $Coil\#5$ and $Coil\#6$ are in the middle of the field winding. In the second arrangement, Arr2, the HTS field winding carries 6 coils where additional 2G coils, $Coil\#7$ and $Coil\#8$, have been placed closest to the poles. It can be noticed that the placements of the $Coil\#6$ and $Coil\#5$ were exchanged and $Coil\#5$ is moved to the middle of the field winding. Thus, the performance can be compared to the first arrangement where it is closest to the pole shoe and 1G and 2G technology can be evaluated with respect to the position in the HTS winding.

To make the comparison between Arr1 and Arr2 more transparent, a subset of four coils (from six) in Arr2 have been isolated as a coil set of interest. This includes the same coils as in Arr1 but with alternated positions of $Coil\#5$ and $Coil\#6$ during which $Coil\#7$ and $Coil\#8$ were inactive. This configuration of the field winding will be referred to as Arr2. In addition, the case where all six coils are active ($Coil\#7$ and $Coil\#8$ are active too) will be referred as Arr2-b or Arr2-c, depending on the current of $Coil\#7$ and $Coil\#8$.

Preformed experiments can be divided into two groups, static experiments where the armature winding is stationary and spinning tests where the armature winding is revolving at a given speed. Static experiments are carried out in order to determine and compare performance of the HTS coils in different configurations of the field winding and to define the operational window of the field winding. In addition, these tests will also provide insight in the machine performance as the interaction between the armature and the field winding is analyzed.

The spinning experiments are on the other hand preformed to experimentally determine parameters of the HTS machine such as direct and quadrature inductance, leakage inductance, induced electromotive force and so on.

5.2 HTS coils operation and individual IV curves

The design and performance of the HTS machine is largely governed by the performance of the HTS coils. Thus, the first step is to determine the amount of MMF the HTS coils can generate. As the I_c presents the maximal current the HTS tape can sustain for an indefinite time, it will be used as a parameter defining the boundary of the maximal performance of each HTS coil and ultimately, the field winding. The operational current

in an industrial application should be 40%-90% of I_c (156) in order to ensure safe operation of the winding over its lifetime and minimize the energy loss in the field winding. The choice of operating point and safety margin for an HTS current loading highly depends on the machine design specifications, HTS tape parameters and coil thermal stability (157, 158, 159). Regardless, the critical parameters of an HTS winding must be identified first.

The I_c and n as characterization parameters of superconductors, defined in Ch.2, are derived under assumption that the HTS is in homogeneous conditions with respect to the temperature and magnetic flux (which is the case in the *short sample* experiment (21)). For HTS coils and complex superconducting devices (cables, FCL, machines, magnets, etc.), temperature and flux conditions are not uniform, but the voltage - current relations can be described with a power law dependency. The connection between I_c and n value derived from a *short sample* test and derived from the coil could be made (160) but is not straightforward.

The I_c and n value for the HTS coils are derived from an integral voltage across the entire length of the HTS tape in the coil, U_{coil}, which can be expressed with

$$E_{coil} = \frac{U_{coil}}{L_{coil}} = \frac{E_0}{L_{coil}} \int_0^{L_{coil}} \left(\frac{I}{I_c(\mathbf{B}, T)} \right)^{n(\mathbf{B},T)} dL \rightarrow \frac{U_{coil}}{L_{coil}} = E_0 \left(\frac{I}{I_c} \right)^n \tag{5.1}$$

where L_{coil} is the length of the HTS tape in the coil winding, I is the current of the coil, I_c is the critical current of the HTS coil and n the transition coefficient describing how abrupt the transition between superconducting and resistive state is.

It is important to keep in mind that the I_c determined from the coil voltage could lead to overestimation of the current rating of the HTS coil, especially if the flux distribution across the HTS coil contains large gradients. Therefore, 5.1 should be used with caution when deriving the I_c of the coil where flux gradients are large. Consequently, the analysis of IV curves from different sections of HTS coil coupled with FE simulations can be used as a supplemental analysis in order to verify the critical parameters (I_c and n) derived from the coil voltage (ensuring that all coil segments are operating under similar conditions).

5.2.1 *I-V* of individual HTS coils

Experiments where the current is increased stepwise and the coil voltage is monitored, resulting in characteristic nonlinear current - voltage relation (so called IV curves), were conducted for each coil separately. The current steps were 0.25 A – 5 A depending on desired resolution of the IV curves and the HTS type. The pace of current increase was maintained very slowly, allowing $\sim$ 1 min between each step, so the coil voltage could stabilize.

The IV curves for each coil in the field winding are shown in Fig.5.2 and Fig.5.3 for Arr1 and Arr2, respectively. The I_c of the coil in the self produced leakage flux of the machine is derived from these IV curves and reported in Table.5.1. The values of I_c and n are almost the same for both configurations of the field winding, which is expected.

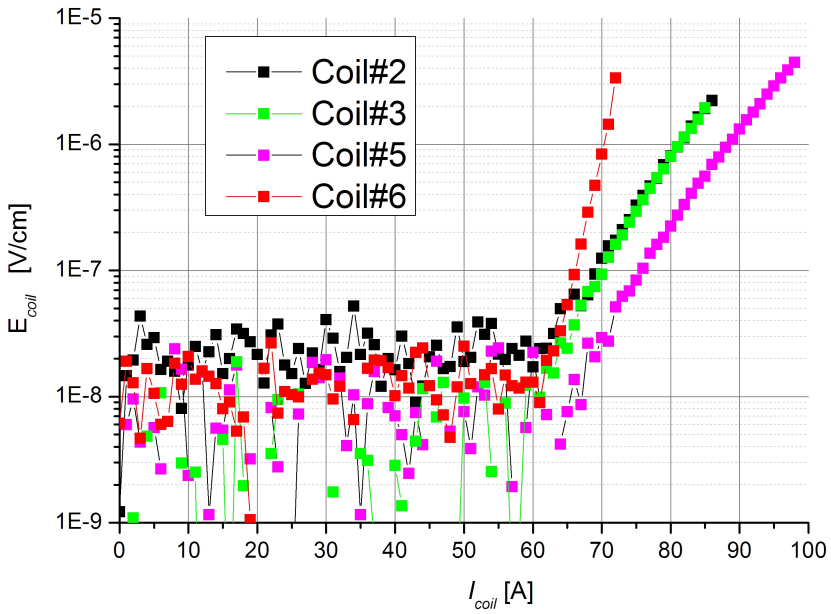

Figure 5.2: The individual IV curves for the four HTS coils in Arr1. - The individual IV curves for *Coil*#2, *Coil*#3, *Coil*#5, *Coil*#6 are presented. Power law fits were preformed and the obtained I_c and n values are listed in Table.5.1 for each of the coils using E_0=1μV/cm (E_0=100μV/m) as a critical voltage criteria.

The coils are mounted on the cold steel in both arrangements and the MMF created by the individual coil ($\sim$ 4000 AmpTurns) is not enough to saturate the cold steel. Most of the flux is contained in the cold steel and the stray flux is mostly parallel to the HTS

tapes. Thus the flux conditions are favorable for the HTS tape performance and are independent from the position of the coils in the field winding.

Derived values for I_c of individual coils are in line with expectations for most of the coils. 1G coils are performing very well in low field conditions with relatively low n value. The 2G coil in Arr1 has significantly higher n value with slightly lower critical current.

The field winding in Arr2 consists of six coils, with $Coil\#7$ and $Coil\#8$ added to the previous set of coils. Unfortunately, the IV curves for the two new 2G coils indicate that the coils were damaged during winding or cool–down. Consequently, defect has reduced their I_c to 12 A and 30 A for $Coil\#7$ and $Coil\#8$ respectively. This is lower than the expected (40 A – 60 A) considering the I_c of the HTS tape in self field. Since the coils are with defect, the IV curves have also a dominant resistive nature seen in the very low n value.

Coil ID	L_{coil} [cm]	No. of Turns	Arr1 $I_c[A]$ - n	Arr1 $J_c^e[A/mm^2]$	Arr2 $I_c[A]$ - n	Arr2 $J_c^e[A/mm^2]$
Coil2	2540	48	81.2 - 15.3	39.0	81.3 - 14.9	38.9
Coil3	2880	51	81.3 - 14.8	41.4	80.8 - 13.9	41.4
Coil5	2500	46	88.5 - 14.5	40.7	88.3 - 14.2	40.7
Coil6	3165	56	70.2 - 52.3	39.3	70.6 - 46.2	39.3
Coil7	7000	125	N/A	N/A	12.4 - 2.8	15.4
Coil8	7000	125	N/A	N/A	31.6 - 3.0	39.5

Table 5.1: Critical parameters derived from IV experiments for six HTS coils. The critical current I_c, n value and engineering current density of a coil, J_c^e, are listed for both configurations of the field winding. The J_c^e was calculated as a ratio of the Amp-Turns the coil has at critical current I_c with the cross section of the coil, A_{coil}=20 mm × 5 mm.

5.2.2 Coil sections

The voltage of the sections for all coils was monitored during IV experiments and was used to verify the value for I_c, derived from the coil voltage. Fig.5.4 displays the IV trace for the inner and outer sections of $Coil\#3$ (details about HTS coils and sensing points are presented in Ch.4 and are included in Appendix.B).

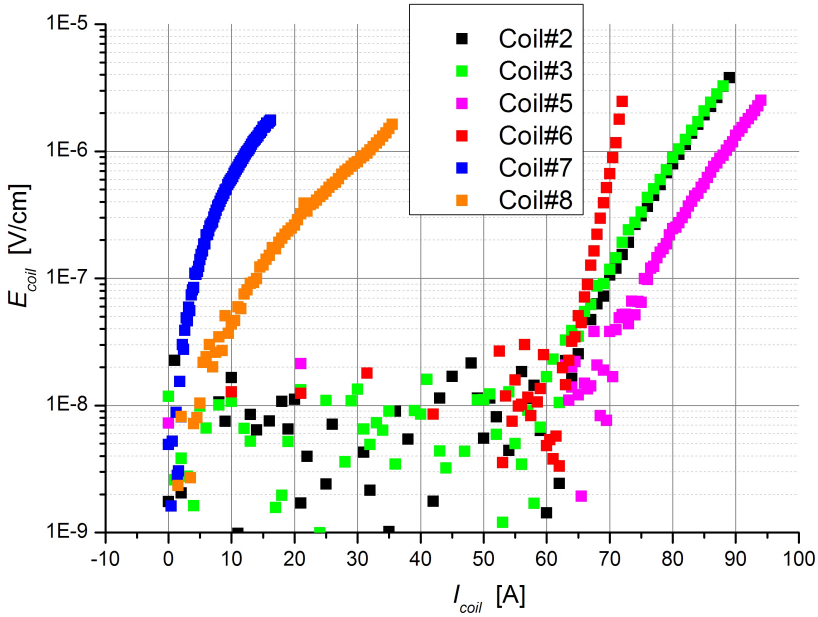

Figure 5.3: The individual IV curves for all six HTS coils in Arr2. - The individual IV curves for $Coil\#2$, $Coil\#3$, $Coil\#5$, $Coil\#6$, $Coil\#7$, $Coil\#8$ are presented. The power law fit was performed and I_c and n values are reported in Table.5.1 for each of the coils using E_0=1μV/cm (E_0=100μV/m) as a critical voltage criteria.

The coil $Coil\#3$ shows a noticeable difference between the performance of the inner and outer sections of the coil for both configurations of the field winding. The difference in the I_c is ∼5 A (the I_c for the inner section is 84 A while the I_c for the outer section is 79 A) for Arr1 and just ∼3 A in the second arrangement of the field winding. According to the IV curves for sections of other coils, the difference between the sections was small and thus it is believed that the I_c derived from the voltage of the coil is sufficiently precise.

Interesting results were obtained when the sections of coils with defects were analyzed. After a closer look into the IV curves of the inner and outer sections of $Coil\#8$, presented in Fig.5.5, it was clear that the inner section of the coil is the one that suffered the damage. Similar performance of sections was observed with $Coil\#7$. Even though this finding has little impact on this particular coil, the information that the inner section of the coil contains defect is very valuable. It indicates that the inner section of the 2G coils based on the SuperPower tape needs to be debugged. At a later stage this information can be used as a useful input for analysis of the winding

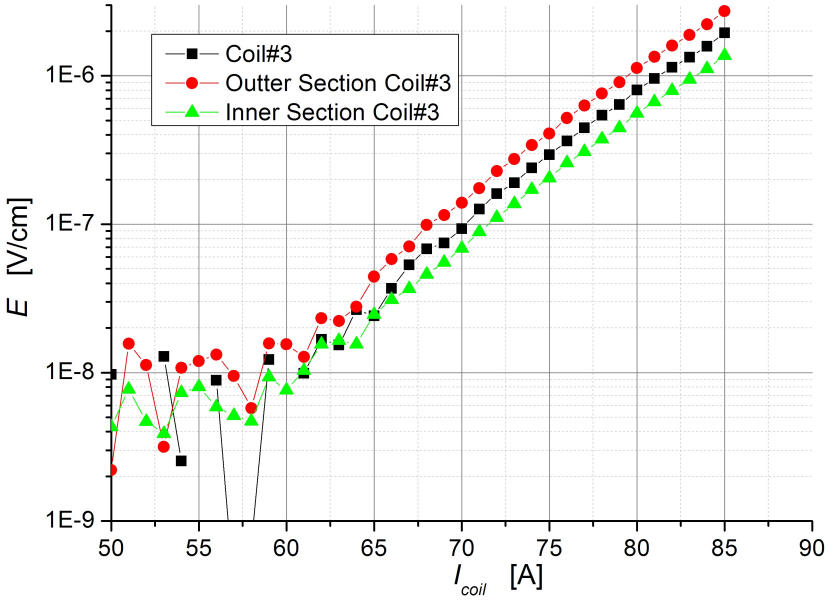

Figure 5.4: The IV curves: Sections of *Coil*#3**.** - The figure shows the IV curve for *Coil*#3 including the coil sections. Only coil *Coil*#3 demonstrates noticeable difference between the performance of the inner and the outer section of the coil. The difference in the I_c is ∼5 A (the I_c for the inner section is 84 A while the I_c for the outer section is 79 A) when the coil is in Arr1.

approach and coil design revision.

Fig.5.5 is showing one more interesting thing. It is noteworthy to mention that during testing, Coil#8 actually quenched at 36 A. A quench is a thermal runaway of the HTS conductor (159) that conducts a current where voltage instantly (vary fast) rises until either HTS tape is destroyed (burnout) or the quench protection system intervenes. The Superwind setup does not have a distinct quench protection system. Instead, the voltage limit of the power supplies used in experiments was kept close to the voltage that the HTS coil would have at critical current (approximately 150%–500% of the critical voltage). In this way, even if a thermal runaway occurs, the voltage and thus the power dissipation of a quenched section will be limited. That is the reason why the voltage of *Coil*#8 stopped at approximately $10E_0$=10 μV/cm. The IV tests were repeated twice after quenching and it was concluded that quenching did not degrade the previously determined value of I_c. The outer section of the coil shows the tendency towards voltage increase at currents above 30 A. This can either be because I_c value of

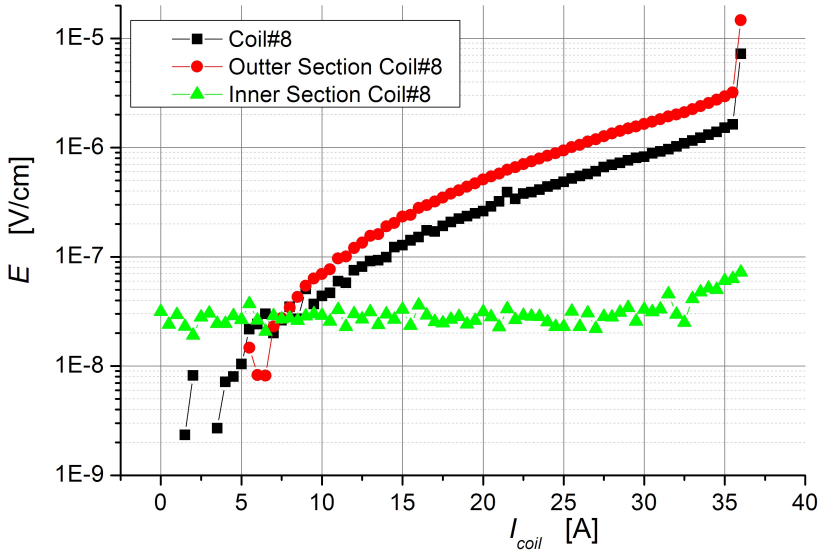

Figure 5.5: The IV curves for outer and inner section of *Coil*#8**.** - The inner section of the coil shows resistive character and indicates that the coil was damaged. The inner section of the coils experienced the quench at 36 A.

the healthy portion of the coil is close (45 A – 55 A) or because the hot spot (quench section) had caused a slight increase in temperature of the whole coil.

It may be an exaggeration because of the defect, but both *Coil*#7 and *Coil*#8 are perfect examples of the value closer investigation of the coil sections have and how largely overestimated the value for I_c based on the coil voltage can be.

5.2.3 Magnetic conditions during IV tests

Before going any further it is important to state that FE simulations used to evaluate the magnetic conditions that the HTS coils were exposed to during the experiments did not include superconducting physics. Thus the current distribution in each of the HTS tapes was simulated as a uniform engineering current density. In reality, the current distribution in the cross-section of the HTS tape will be a function of magnetic field (both vector and history) and the local properties of HTS material (161). Consequently, even though the net current of each turn is the same, each turn of the coils will have a different current distribution where for example edges of the tapes could have J_c and the middle $-J_c/(22)$. Taking this into account and incorporating this effect into FE

simulation is possible (162) and will yield correct magnetic and current distribution in the coil.

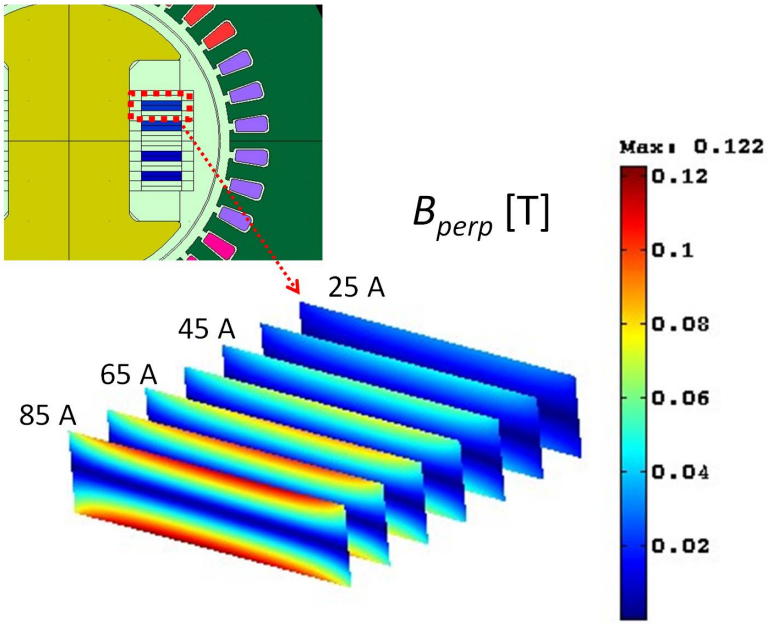

Figure 5.6: The distribution of the flux density perpendicular to the HTS turns in *Coil*#3. - The FE simulation results of the flux density perpendicular to the HTS turns while current of the coil is ramped up from 25 A to 85 A, in steps of 10 A. The FE simulation assumes uniform current distribution in the HTS turns.

However, this chapter will use FE simulations to estimate global magnetic conditions in the field winding and the HTS machine, on which the local current distribution in the turns of the HTS coils has a very limiting effect. To evaluate magnetic conditions during individual IV experiments, FE simulation of the corresponding experiments are analyzed. The coils have during the individual tests generated approximately 70 mT of self field at critical current. The distribution of perpendicular flux to tapes for *Coil*#3 is shown in Fig.5.6.

5.2.4 Summary of IV tests for individual coils

For performed IV tests and critical parameters derived from the measurements, the following stands out:

- The coils *Coil*#2, *Coil*#3, *Coil*#5, *Coil*#6 have performed as expected. The values for the I_c of the coils are in agreement with the values for the I_c of the

HTS tape.

- Both $Coil\#7$ and $Coil\#8$ were found to be defective with significantly lower values of I_c than expected. A portion of the coils have failed to become superconducting and the distinct resistive IV relation was observed.
- During IV experiments, the inner section of $Coil\#8$ survived the quench that happened at 36A.
- Monitoring the voltages of the sections of a coil has proved to be a valuable diagnostic tool for detection of defects, troubleshooting the coil design and coil production process and finally verifying the I_c and n values.
- With exception of $Coil\#3$, the inner and the outer sections of coils have the same tendencies and thus it can be concluded that the I_c derived from the voltage of a coil is sufficiently precise for this particular case. The inner section of $Coil\#3$ exhibits a 5A lower value for I_c.

5.3 The HTS field winding in series

An HTS coil can be seen as a number of short pieces of HTS tape with individual IV curves, where the coil voltage will be a sum of all voltages from short pieces. Ideally, the short section exhibiting the lowest I_c would set the I_c of the coil, but as this information is almost never available, the average I_c is derived using 5.1. A similar approach can be used for a set of HTS coils. If the coils in a field winding are connected into a series connection in such way that individual MMF adds up, all coils will have the same current. The operating point for the HTS field winding connected in to a series will be defined by the coil with the lowest I_c value. In other words, among a number of coils operating with the same current, a coil with voltage equal to the $E_0 L_{coil}$ will be the one with lowest I_c. This is expressed as,

$$MAX\left(\frac{U^i_{coil}}{L^i_{coil}}\right) \leq E_0 \tag{5.2}$$

where the coil index i takes values from the coil ID array for coils present in the field winding. For Arr1 the index i would take values from $[Coil\#3, Coil\#2, Coil\#5, Coil\#6]$.

In the next section results for the Arr1 and Arr2 will be presented and implications of coil placement will be discussed. The IV curves recorded for both configurations of the HTS field winding are presented in the Fig.5.7 and Fig.5.8.

5.3.1 Field winding in Arr1 – series connection

In the first arrangement, the coil limiting the MMF of the HTS field winding is $Coil\#3$ closely followed by $Coil\#5$. As a result, the field winding is able to operate with currents $\leq$52 A. The reduction of I_c of $Coil\#3$ is large (from 81.3 A down to 52.2 A) if I_c of the individual coil and series connected coils are compared. The reduction of the I_c of $Coil\#5$ is even larger (from 88.5 A down to 54.3 A). The I_c reduction is due to the increased magnetic flux density these coils are exposed to.

$Coil\#3$ and $Coil\#5$ are showing larger reductions in the I_c value because their position in the field winding is unfavorable. Due to their proximity to the pole shoes and the tendency of the flux lines to escape cold steel close to pole shoes, these coils will experience significantly higher magnetic flux perpendicular to HTS tape. As the cold steel gradually saturates with increase in the MMF, the leakage flux of the coils will increase, making the reduction of I_c even higher.

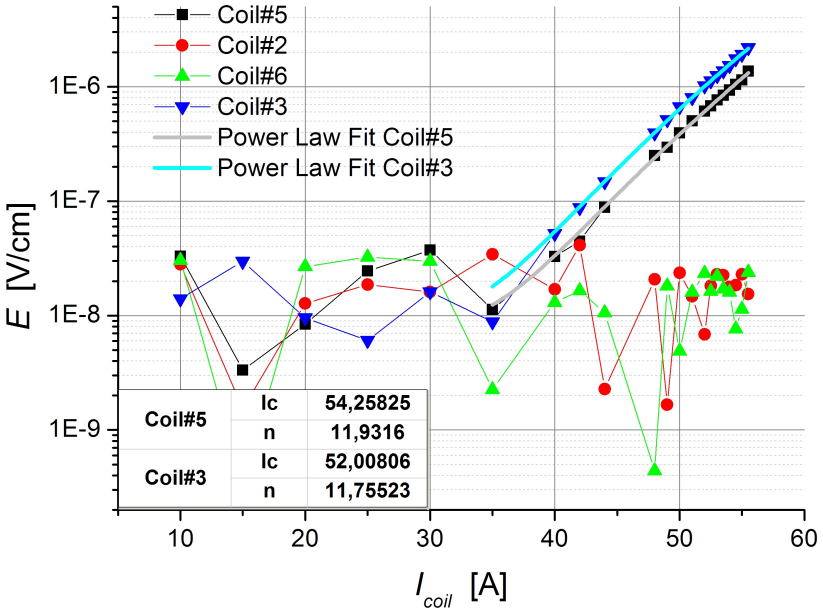

Figure 5.7: The IV curves for HTS field winding in Arr1 - The IV curves recorded for the series connected HTS field winding in the first arrangement.

This is a validation of a well known feature of a 1G HTS conductor, i.e. 1G has high sensitivity to magnetic field (especially to the flux perpendicular to an HTS tape) at high operating temperatures (77 K). The effect of magnetic anisotropy in 1G HTS tape is lower at lower temperatures. The inner coils, *Coil*#2 and *Coil*#6 are according to Fig.5.7, far from critical values. The implication that *Coil*#2 shows no I_c degradation (at least not as same as *Coil*#3) is the indicator that inner coils are exposed to a lower value of magnetic field.

5.3.2 Field winding in Arr2 – series connection

With the field winding in Arr2 and four coils connected in series (excluding the coils *Coil*#7 and *Coil*#8), the IV curves are shown in Fig.5.8. Now the *Coil*#5 is in the middle of the field winding together with *Coil*#2, while *Coil*#3 remained at the same place and *Coil*#6 was placed closer to the pole shoe.

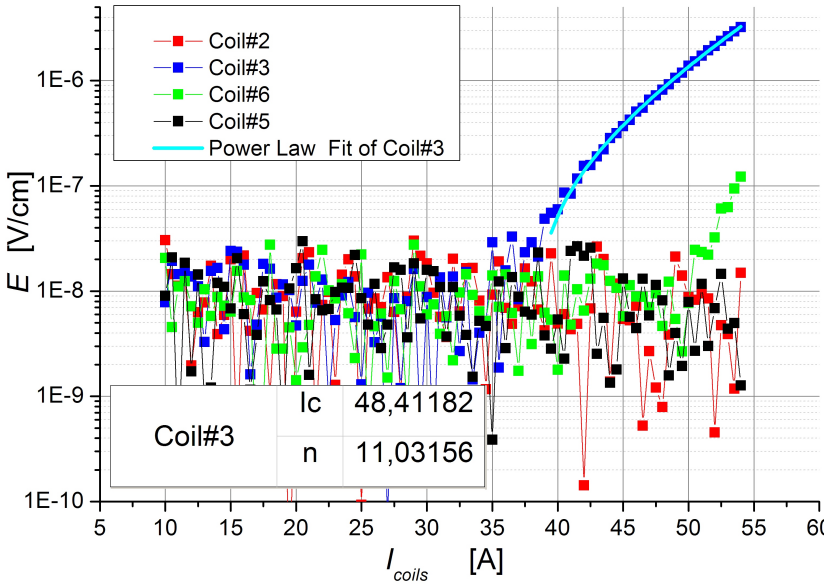

Figure 5.8: The IV curves for HTS field winding in Arr2 - The HTS field winding in Arr2 connected in series.

Here, similar to the Arr1, *Coil*#3 has the lowest I_c, setting at 48.7 A, a slightly lower value then in Arr1. A significant difference in the performance between these two arrangements is seen for *Coil*#5 as expected. Placing *Coil*#5 in the middle of the field winding once again confirms the significance of the magnetic flux density for the coils

wound with 1G tape. As a consequence, $Coil\#5$ in this arrangement indicates that the I_c value is substantially higher than in Arr2. On the other hand, placement of $Coil\#6$ at the outer layer of the field winding did not noticeably degrade its critical current. This will be discussed in more details later on.

5.3.3 $Coil\#3$, a weak link in the field winding

The coil which limits the current of the field winding in both arrangements is $Coil\#3$ and it is of special interest to investigate the nature of the I_c dependence from MMF of the field winding for this coil.

5.3.3.1 Critical current of $Coil\#3$ vs. MMF

To investigate the I_c reduction with respect to the current in the other coils, an experiment was carried out in Arr2, where $Coil\#3$ has slightly lower I_c. The set of IV curves for $Coil\#3$ with the background magnetic field, was recorded. The starting (offset) magnetic field was provided by the other three coils connected in series. Their current was increased stepwise (in steps of 5 A) and kept constant while the IV experiment was performed on $Coil\#3$.

Fig.5.9 presents the results from this experiment. Each contour separating the region in the graph with single color represents specific level of the electric field of $Coil\#3$. The color legend is included in the graph, wherein the number of levels is identified. Instead of fitting a number of IV curves, the I_c tendency can be derived from the electric field level. The contour for electric field equal to E_0 will represent that critical line and it is marked with a wider line (contour) in the graph.

It can be observed that the reduction of I_c is a nonlinear function of background MMF. The reduction can be as high as 50% for Arr2. This is an expected result as the performance of 1G HTS tape at 77 K will strongly depend on magnetic field (both intensity and direction).

5.3.3.2 Magnetic conditions for $Coil\#3$

The magnetic flux density (intensity and distribution) across the field winding for individual coils was reported to be approximately 70 mT for the individual coil IV experiment. Since we saw a high reduction of the I_c when connecting the coils in series,

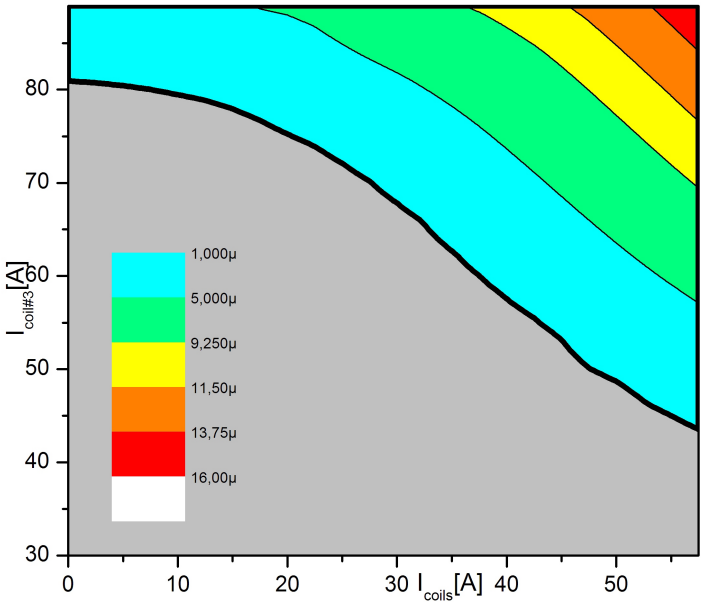

Figure 5.9: Critical current of $Coil\#3$ as a function of background MMF. - The electric field of $Coil\#3$ is presented with different colors. The contour with value equal to E_0 will correspond to the I_c of $Coil\#3$. This contour is emphasized in the graph with increased width of the line. The background magnetic field is generated by current in $Coil\#2$, $Coil\#5$ and $Coil\#6$ connected into series.

it is of interest to see what magnetic conditions are present at the field winding in this case.

An estimate of perpendicular magnetic flux density for $Coil\#3$ in both arrangements are presented in Fig.5.10 and Fig.5.11. The results are showing that the HTS tapes of $Coil\#3$ are exposed to the maximal magnetic flux density of $\leq$200 mT at I_c which is three times higher than in the individual IV test. The simulation shows slightly lower value of 183 mT for $Coil\#3$ in Arr1 compared to 195 mT observed for Arr2. Even though these simulations do not represent precise flux distribution in the HTS coil, the results from FE and experiments are in agreement (Since $Coil\#3$ has I_c=52 A for Arr1 and I_c=49 A for Arr2). This confirms that uniform current density of the HTS coil used in the FE model is sufficient to predict the magnetic conditions of an HTS coil.

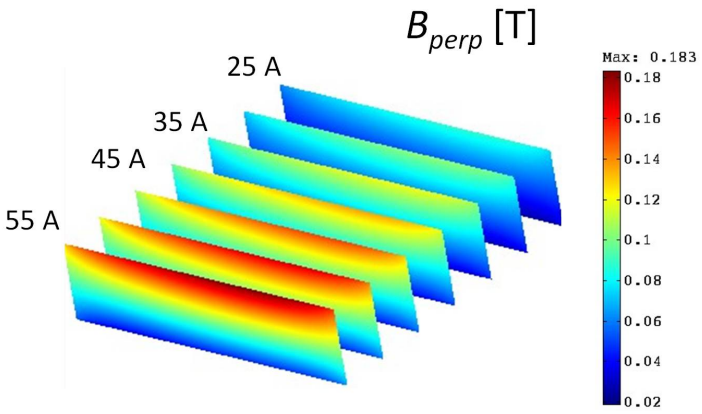

Figure 5.10: Arr1 - The distribution of the perpendicular flux density for *Coil*#3 while field winding in Arr1 is connected in series. Each color-plot slice represents the perpendicular flux distribution turns of the coil *Coil*#3 are exposed to. Current of the winding was increased from 25A–55A in steps of 5A.

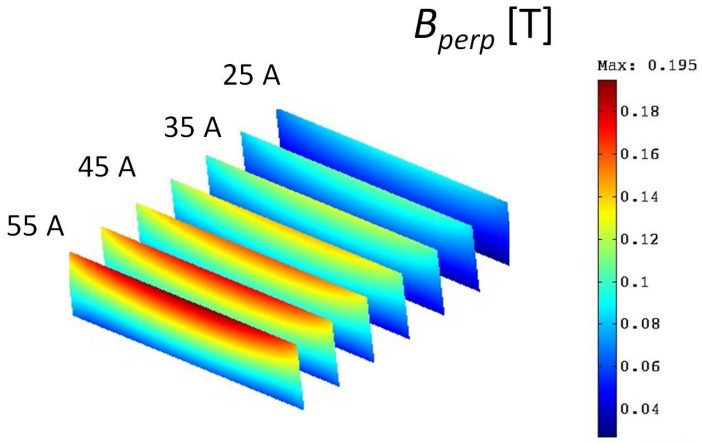

Figure 5.11: Arr2 - The distribution of the perpendicular flux density for *Coil*#3 while field winding in Arr2 is connected in series. Each color-plot slice represents the perpendicular flux distribution turns of the coil *Coil*#3 are exposed to. Current of the winding was increased from 25A–55A in steps of 5A.

5.3.4 Comparing 1G and 2G coils

The premise of the Superwind setup in part was to investigate both 1G and 2G HTS technology. One way to compare the performance of these could be by comparing the performance of 1G and 2G coils in different configurations of the field winding. With that reason, field winding was assembled and tested in two arrangements, and the coils

in the focus of the discussion are *Coil*#5 and *Coil*#6.

Comparing Arr1 and Arr2, the tendencies of *Coil*#5 to have larger reduction of I_c if placed closer to the pole shoe (Arr1) than if placed in the middle of the coil stack (Arr2) implies that the performance of 1G coils could be improved substantially if they are strategically placed in the field winding. To investigate the degree of the improvement the change of position can cause, we will analyze *Coil*#5 in Arr2 and compare it to Arr1. Even though, *Coil*#6 was far from its I_c in both arrangements, according to Fig.5.7 and Fig.5.8, in order to compare 2G coil performance to 1G coils, we need to investigate how the performance of *Coil*#6 changed between arrangements. This will be presented in next section.

5.3.4.1 Performance of *Coil*#6 (based on AMS348 2G HTS tape)

The reduction of the I_c value for *Coil*#6 can be observed in Fig.5.12, where the family of the IV curves was recorded in the background field (generated by the other three coils). The current in the three coils was increased in steps of 10 A from 0 A to 60 A and kept constant during the IV experiment. The results in Fig.5.12 are for Arr1.

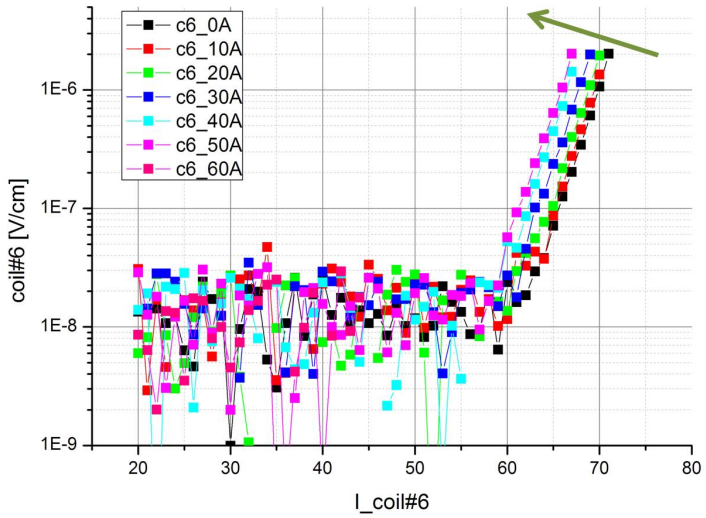

Figure 5.12: The IV curves of *Coil*#6 in the field winding - The IV curves have indicated a change in I_c due to background flux of *Coil*#6.

The increase in the magnetic field of the field winding will cause the IV curve of the coil to gradually move to the left as indicated in the Fig.5.12 with the green arrow.

This can be quantified with a reduction in I_c value of the coil. The critical current of $Coil\#6$ as a function of the current in the other three coils is presented in the Fig.5.13 for both arrangements. For the Arr1, the plot is constructed from a number of power law fits performed for the IV curves presented in the Fig.5.12 where the power law fit was performed in order to investigate the change in I_c of the coils but also of the n value as a function of the current in other three coils. We can see that the reduction in critical current of this coil is approximately 6% (from 70 A down to 65.8 A) while the n value stayed more or less the same. For the field winding in the second arrangement no power law fits have been performed, but instead the average electrical field defined by 5.1 equal to 1μV/cm (100μV/m) was identified as a function of $I_{Coil\#6}$ and the current in other three coils connected in series, I_{coils}. The decrease of I_c of $Coil\#6$ in Arr2 is $\sim$15% (from 71A down to 61A) which is larger than in Arr1.

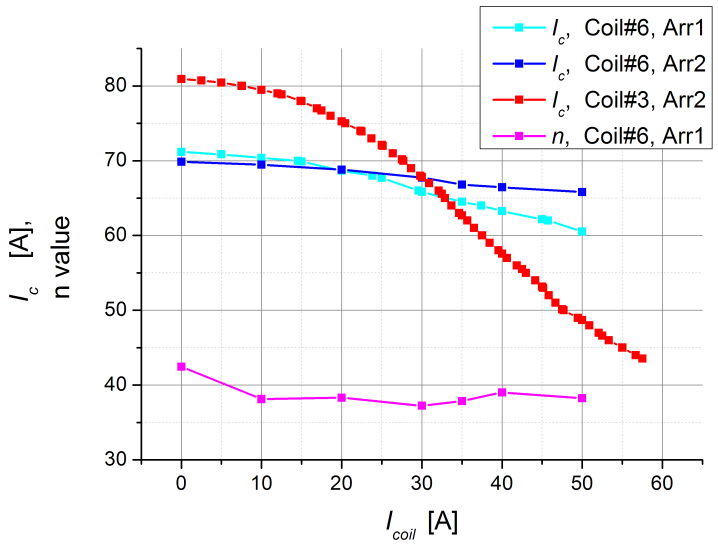

Figure 5.13: The I_c and n of $Coil\#6$ versus current in the other three coils for Arr1 and Arr2. - The influence of background field from other coils in the HTS field in the Arr1 and Arr2 on the I_c and n value of $Coil\#6$. The I_c of $Coil\#3$ is included to illustrate the degree of difference between two types of HTS. The 1G HTS has substantially higher I_c in the low field where the 2G HTS is less susceptible to the magnetic field.

5.3.4.2 Performance of *Coil*#5

Coil#5 is the representative of the 1G coils which had both outer and inner positions in the field winding in Arr2 and Arr1, respectively. For Arr1, the I_c of the field winding presented in Fig.5.7 reveals that *Coil*#5 has a critical current of 54.2 A. Thus, from the individual coil IV experiment to the series connected field winding, the I_c of the coil has reduced from 88.5 A (see the Table.5.1) to 54.2A which adds to the 39% reduction due to the increase in magnetic flux.

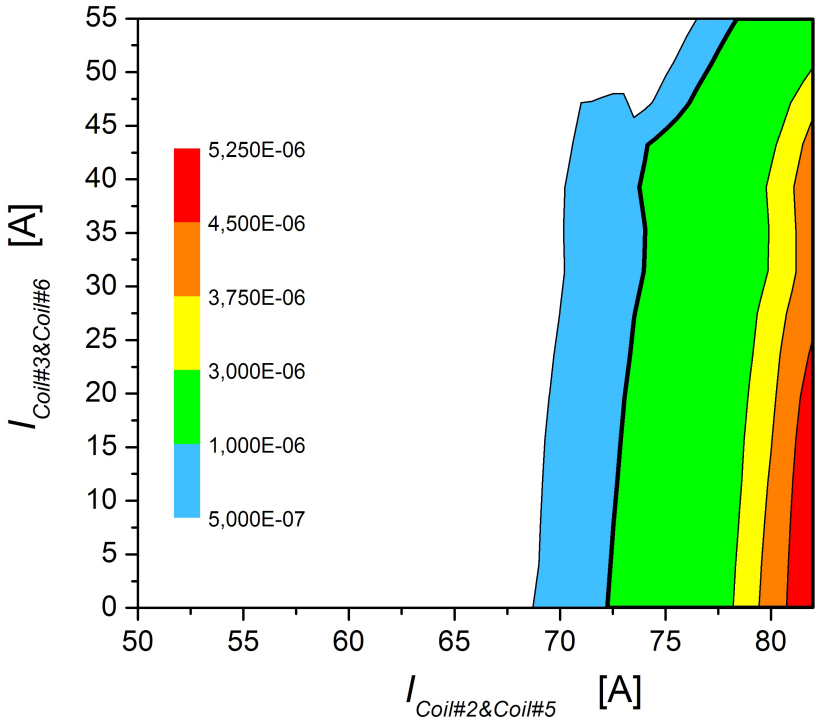

Figure 5.14: Electric field of *Coil*#5 in Arr2 - The electric field of *Coil*#5 in Arr2 is shown as a function of the current in *Coil*#5 and *Coil*#2 at X axis and the current in *Coil*#6 and *Coil*#3 at Y axis. Color legend of the electric field level is included where the E_0 level is between blue and green surface.

A slightly different experiment was carried out in the case of the field winding in Arr2. The inner and outer coils were paired up, making *Coil*#2 and *Coil*#5 the first and *Coil*#3 and *Coil*#6 the second coil pair. Each pair had one current supply. This was done in order to maintain the symmetry of the magnetic flux in the field winding and still show improved performance of *Coil*#5. Thus, here the background field is

created by the second pair of coils and the IV experiment included both coils in the first pair. The voltage of $Coil\#5$ is presented in Fig.5.14 as a function of these two currents.

This experiment cannot be directly compared to the $I_c(I_{Coils})$ derived for other coils ($Coil\#3$ and $Coil\#6$) since $Coil\#2$ and $Coil\#5$ are paired together. Still, if we know that the I_c of $Coil\#5$ in Arr1 is ∼55 A and compare this to the I_c of $Coil\#5$ in Arr2 of ∼75 A for the described experiment, it is clear that 1G coils perform much better if placed in the middle of the coil stack. The E_0 electric field level is at the range of ∼70 A at far the right of the plot and with increasing $I_{Coil\#3Coil\#5}$, this line migrates further right. This effect will be discussed in more depth further on in the Sec.5.6.2.

5.3.5 Summary for the HTS field winding connected into a series

- Field winding connected in series in Arr1 has I_c=52.0 A which is limited by $Coil\#3$.
- Field winding connected in series in Arr2 has I_c=48.7 A which is also limited by $Coil\#3$.
- The $I_c(I_{Coils})$ for $Coil\#3$ have showed a nonlinear reduction of I_c with reduction equally great in both arrangements of field winding (40% for Arr2).
- Analysis of sections of $Coil\#3$ have confirmed that the outer section of the coil has ∼3 A lower value of I_c than the inner section.
- The $I_c(I_{Coils})$ for $Coil\#6$ have showed mild nonlinear reduction tendency of I_c with reduction of 6% for Arr1 and 15% for Arr2 at corresponding critical currents.
- The performance of $Coil\#5$ was found to be better for Arr2. The coil was capable of carrying ≤75 A for much higher values of MMF of the field winding than the MMF of the field winding at 48.7 A which is the critical current for Arr2.
- Comparison of 1G and 2G coils in both arrangements have clearly identified 2G coils as less sensitive to the placement variations in the coils stack.
- Comparison of 1G and 2G coils in both arrangements have also clearly identified 1G coils as extremely sensitive to the placement variations in the coils stack.

5.4 Interaction of Armature and HTS field winding

The analysis of the operation and performance of the HTS field winding described so far did not include an interaction of the field winding with the armature winding. Since both arrangements of the HTS field winding have shown sensitivity to magnetic field (self generated), the effects of the armature reaction as a source of external field should not be neglected.

Two parameters have been used to describe this interaction: the armature reaction or I_a in Amps and the angle between the armature winding and the field winding magnetic axis or γ in degrees. An additional parameter was used during the experiments, ϕ, which afterwards was used to derive γ. In the Locked Armature experiment, it was not possible to precisely align the magnetic axis of the phase A and the field winding. Instead, arbitrarily position of the armature was chosen for which ϕ=0°. The correlation between γ and the ϕ will be derived later on when the measured torque as a function of ϕ is examined.

To get a proper scaling between the amplitude of the three phase armature reaction, I_{a3ph} and the armature reaction generated with two phases running with I_a and -I_a, the correction coefficient of $\sqrt{3}/2$ should be applied. The rated amplitude of the phase armature current is $I_{a3ph} = \sqrt{2}\cdot 23.5$ A= 33.2 A, which means that the value of I_a corresponding to the rated armature reaction (maximal value) is 28.8 A. During the Locked Armature experiments, the armature reaction had to be restricted to $I_a \leq 20$ A in order to limit the temperature rise of the winding and also due to the voltage limit of the DC power supply which was used.

During the experiments with locked armature winding, described in the Sec.4.7, the voltages of the HTS field winding have been monitored as a function of I_a and ϕ. As $Coil\#3$ is the 'bottleneck' of the field winding with lowest I_c in both arrangements, the results shown will mainly focus on $Coil\#3$.

5.4.1 $E_{Coil\#3}$ for Arr2 Locked Armature experiment

The electrical field of $Coil\#3$ in Arr2 shown in Fig.5.15, Fig.5.16 and Fig.5.17 are presented as a function of the armature reaction at X axis and the ϕ at the Y axis.

For the field winding in Arr2 with current of 40 A, the electric field is presented as a 3D surface in Fig.5.15. The voltage is well below E_0 for all angles and all armature

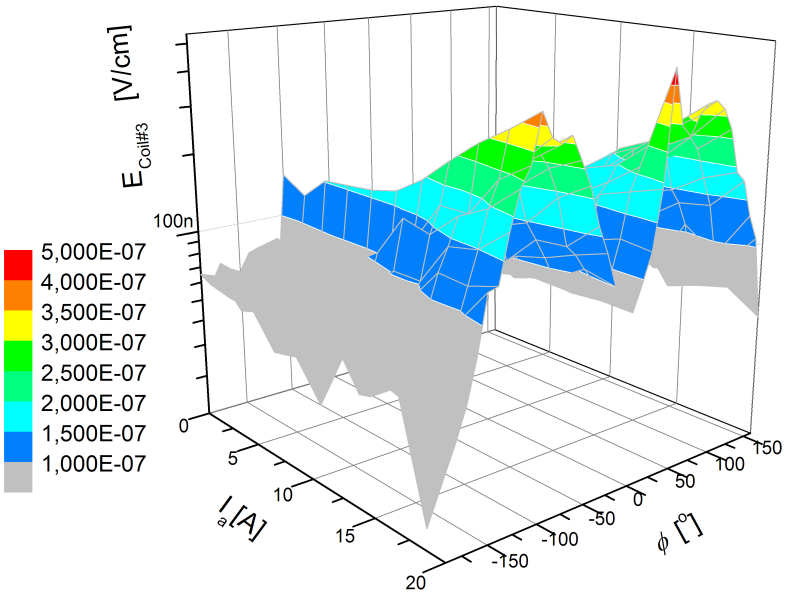

Figure 5.15: *Coil*#3 **in Arr2 with** I_{coil}**=40 A** - The HTS field winding in Arr2 is connected in series and is supplied with I_{coil}=40 A. The average electric field of the coil is at the Z axis with color legend corresponding to electric field levels. The armature reaction, I_a, with values from 0 A – 20 A is at the X axis and the span of 360° of the ϕ at Y axis.

reactions and because the measured voltage was very small, a certain level of noise is present in the graph. We can see from Fig.5.16, where the field current is 45 A, that the electric field of *Coil*#3 reaches $E_0 = 100\mu$V/m for I_a =20 A for angles ϕ ∼85° and ϕ ∼-95° while for all other angles is well below E_0. This clearly indicates that the performance of the HTS field winding will be a function of the armature reaction.

The case where the HTS field winding operates with 50 A in Arr2 is presented in Fig.5.17. The electric field of the coil has the same tendency of having the maximal value at the ϕ ∼85° and ϕ ∼-95°. The level of electric field indicates that with 50 A, the HTS field winding almost always operates with current above I_c, except for the ϕ ∼-185°. For this value, we can observe that the electric field that was initially above E_0 for I_a=0 A, but is below E_0 with increasing armature reaction. These results could be used to define the critical current of the HTS field winding, defined as the field winding current for which the nominal armature reaction at any angular displacement would not cause the coil voltage to become higher than $E_0 L_{coil}$,which would present

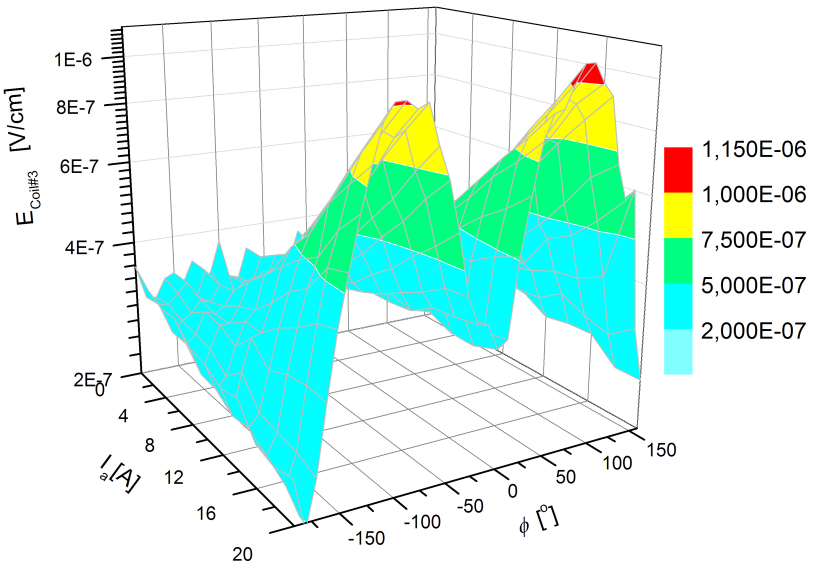

Figure 5.16: *Coil#3* **in Arr2 with** I_{coil}**=45 A** - The HTS field winding in Arr2 is connected in series and is supplied with I_{coil}=45 A. The average electric field of the coil is at the Z axis with color legend corresponding to electric field levels. The armature reaction, I_a, with values from 0 A – 20 A is at the X axis and the span of 360° of the ϕ at Y axis.

the maximal operating current of the field winding. In order to define this current, the presented result will need to be extrapolated to I_a=28.8 A. None of the operation safety margin is considered here since we are interested in critical parameters. However since the armature current of an electric machine during its lifetime will have excursions to the higher values than nominal (short time overload and fault conditions), the process of defining the maximal HTS current loading will need to take that into account too.

The same experiment was performed for the field winding connected in Arr1 where *Coil#3* showed similar tendencies. The results are included in the Appendix.F.1

5.4.2 Torque-angle correlation

As the basis of electric machine operation is an interaction between two magnetic fields, consequently an electromagnetic torque developed by this interaction is an important parameter for the machine analysis. Electromagnetic torque acting on the field winding

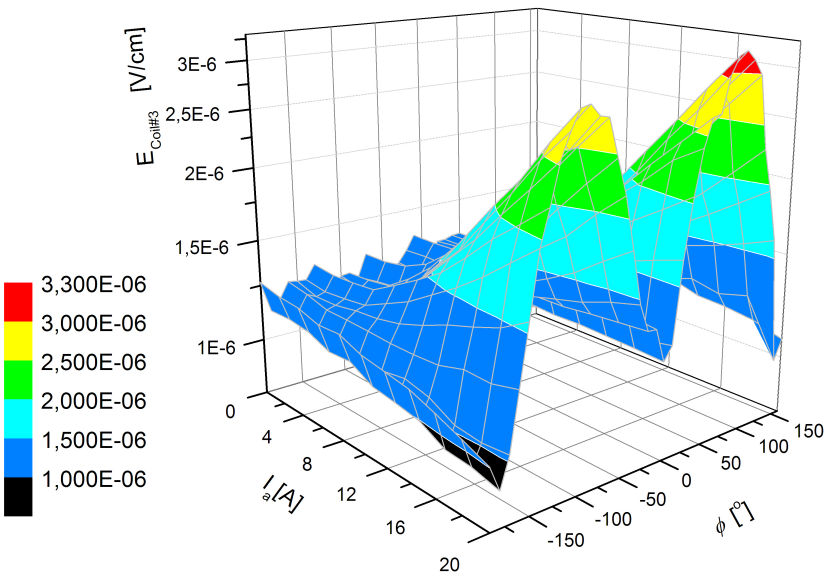

Figure 5.17: *Coil*#3 **in Arr2 with** I_{coil}**=50A** - The HTS field winding in Arr2 is connected in series and is supplied with I_{coil}=50A.

was measured during experiments with the Locked Armature. The results for the case when the field winding is in Arr2-c where four coils (*Coil*#3, *Coil*#2, *Coil*#5, *Coil*#6) are supplied with 50A and two damaged coils (*Coil*#7, *Coil*#8) supplied with 10A, is presented in Fig.5.18. More about this operating mode will be discussed in the following section Sec.5.6.2. The torque as a function of the armature reaction and the current of the field winding corresponds closely to the magnetic permeability of the cold steel where the effects of saturation are becoming visible at higher currents. It is also noticeable that the 2^{nd} torque harmonic, ie. reluctance torque, is very weak.

The torque versus angle 2D plot for I_a=20 A is compared to the torque-angle derived with FE simulation corresponding to the same conditions and is shown in Fig.5.19.

The measured results are in good agreement with the FE simulation. For the presented case, the torque was fitted with the sum of harmonic functions, presented in 5.3, where the main harmonic $T_{1^{st}}$=49.54 Nm and the reluctance torque $T_{2^{nd}}$=0.16 Nm for the presented case. The reluctance torque has been estimated by FE model and the value of $T_{2^{nd}}$ = 4.5 Nm was observed for no field current (when Steel37 is not saturated) and with I_a = 20 A. Its value decreased rapidly with the increase of the

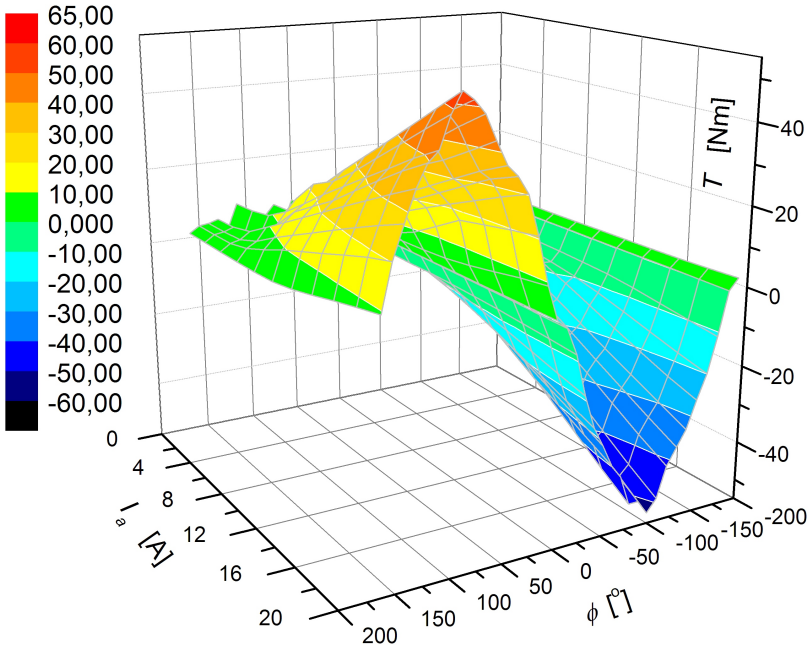

Figure 5.18: The torque $T(\phi, I_a)$ for Arr2-c with $I_{Coil} = 50A$ - The HTS field winding in Arr2-c was supplied with $50A$

MMF of the field winding since the cold steel started to saturate, resulting in 0.16 Nm for the above presented case.

$$T(\gamma) = T_{1^{st}} sin(\gamma) + T_{2^{nd}} sin(2\gamma) \tag{5.3}$$

From Fig.5.19 the correlation can be found between the mechanical angle, ϕ and the angle between magnetic axis of the armature winding and the field winding, γ. We will adopt the convention that γ is zero when the armature magnetic axis is collinear to the magnetic axis of the field winding (d-axis), as illustrated in the Fig.5.21. Consequently, at γ=0° the torque will be zero as well. After including $\gamma = \phi + 5°$, the measured and simulated results will become angularly synchronized as presented in Fig.5.19.

The linear approximation was made to derive the relation between the torque, MMF of the field winding and the armature reaction at the ϕ=90°. The equation used for the fit is defined with 5.4 and the performed fit resulted (for the data presented in the 5.20) with the K_T=2.64×10^{-4} NmA^{-2}.

$$T_{1^{st}} = K_T \cdot MMF \cdot I_a \tag{5.4}$$

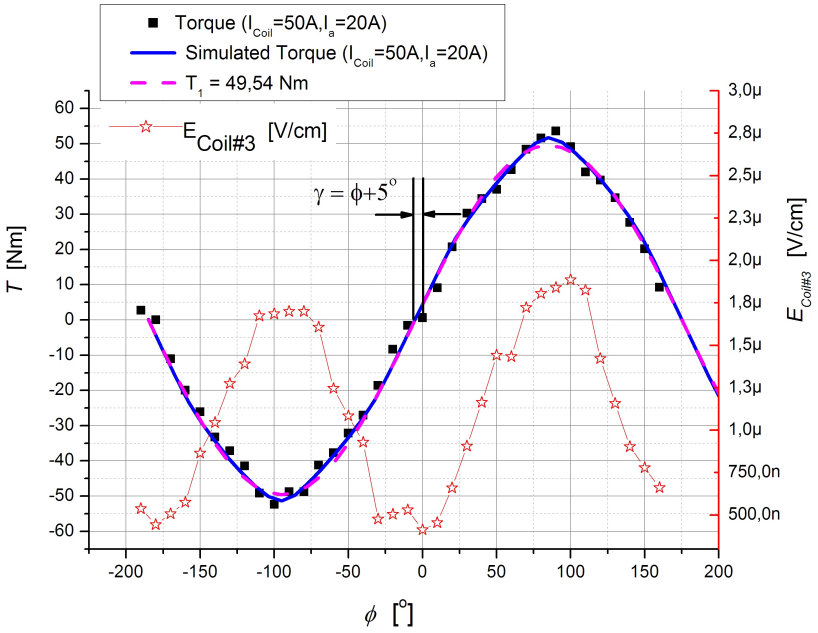

Figure 5.19: Comparison between measured torque and FE simulation. - Comparison between measured torque for the current of 50 A of the HTS field winding in Arr2-c and the corresponding FE simulation of Locked Armature experiment. The figure includes derived first harmonic of the torque for angular shift of $\gamma = \phi + 5°$. The figure also includes the electric field of the $Coil\#3$ during the experiments which allows conclusions on the correlation between the HTS field winding performance and the relative position (instead of absolute expressed with ϕ) of the armature reaction with respect to the HTS field winding.

where MMF the magneto motive force of the field winding and I_a is the value of dc current flowing in two phases.

5.4.3 Locked Armature Experiment - Extrapolation of the results

In order to estimate what would be the maximal operating current of the HTS field winding with the rated armature current, we need to extrapolate recorded results (to the rated or higher values or armature reaction). Considering that (in theory) an armature reaction could be at any angle with respect to the field winding, it would be useful to spend a few words to identify the characteristic operating positions and their implication. Four characteristic cases are illustrated in Fig.5.21.

From the previous section we derived the $\gamma(\phi) = \phi + 5^o$ relation for both arrange-

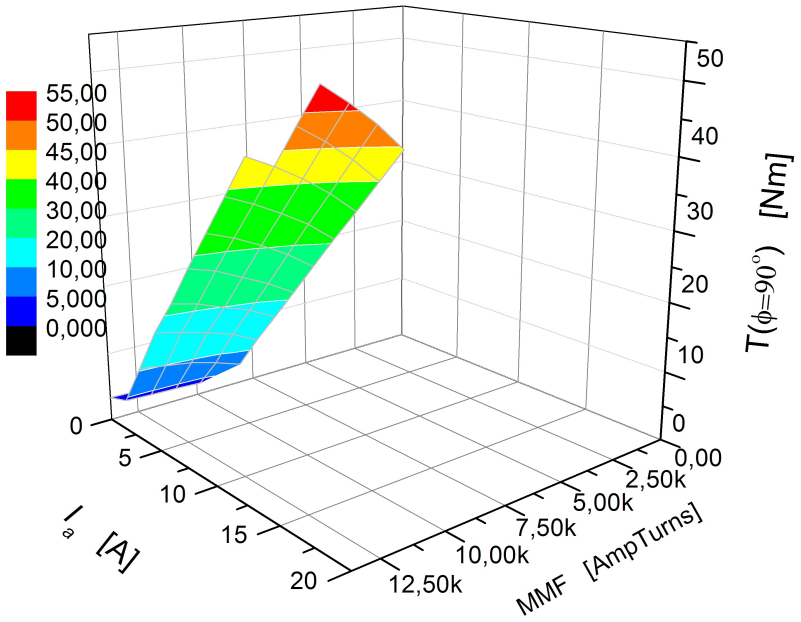

Figure 5.20: The torque $T(MMF, I_a)$ for Arr2-c at ϕ=90° - The $T(I_a, I_{Coil})$ for $35A \leq I_{Coil} \leq 50A$ and $0A \leq I_a \leq 20A$.

ments and thus the electric field graphs presented so far can be related to γ and to the characteristic positions presented in Fig.5.21. Consequently, the angles where armature reaction has the largest impact on the coils are corresponding to the angles where the electromagnetic torque has its extremes, ie. γ=±90° (Fig.5.21b and Fig.5.21c). The slight difference between these two was observed in the electric field of the analyzed coils presented in Fig.5.19 but this was deemed insignificant to account for any of the physical aspects which are in the focus.

The other two characteristic positions presented in Fig.5.21 where the MMF of the armature and the field winding are collinear, ie. for γ=±180°, would correspond to the sections with lowest impact of armature reaction on the electric field of analyzed coils. Between these two positions considerable difference in measured electric field can be observed. The case where the electric field of the coils is slightly increasing with an increase in armature reaction would correspond to Fig.5.21a, while if the position of the MMF are as in Fig.5.21d, the electric field of the coils will experience slight decline with an increase in armature reaction. As these characteristic positions are corresponding to specific load regimes in the machine (as boundary cases defined in Fig.5.21), it is

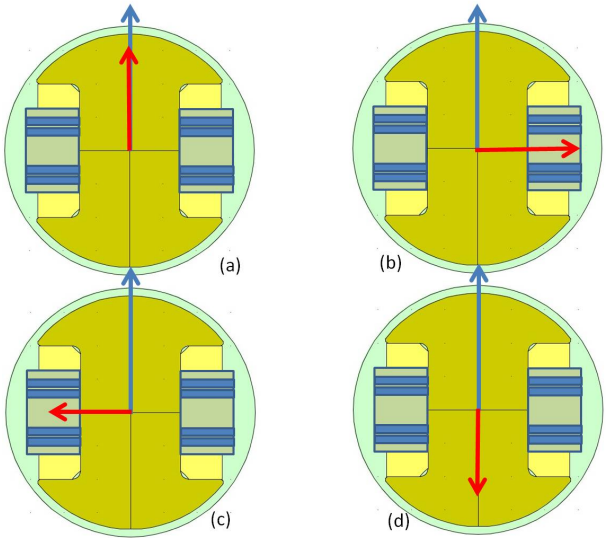

Figure 5.21: Four (boundary) cases of armature and field winding interaction. - This figure presents four characteristic operating regimes for an electric machine. These are identified as positions of interest for the analysis of field winding (the blue arrow) and armature (the red arrow)interaction with respect to the HTS field winding performance. (a) The γ=0°, which corresponds to the reactive (capacitive for generators or inductive for motors) load; (b) γ=90°, which corresponds to the maximal active load; (c) γ=180°, which corresponds to the maximal active (breaking) load; (c) γ=-90°, which corresponds to the reactive (capacitive for motors or inductive for generators) load.

important to understand the implications that each load would have on the HTS field winding as we proceed to extrapolate and define the operating window of the same field winding.

From Sec.5.4.1, we can identify ϕ=85° as the one where the coil ($Coil\#3$) exhibits highest voltages. Thus, recorded data for voltage of $Coil\#3$ at ϕ=85° (corresponding to γ=90°) is presented as a 3D graph where the coil voltage is presented as a function of the current in the field winding and the armature reaction, shown in Fig.5.22. By identifying electric field level equal to E_0, the critical current of the coil (and thus field winding too) can be expressed as function of armature reaction. Hence, in order to derive this function, first a surface fit needs to be performed for the surface presented in Fig.5.22. Since the electric field of the coil follows the power law regardless is it the armature current or coil current that is increasing, this dependence would be a linear function of both I_a and I_{coil} if it is presented as a *log* plot. This is a convenient way

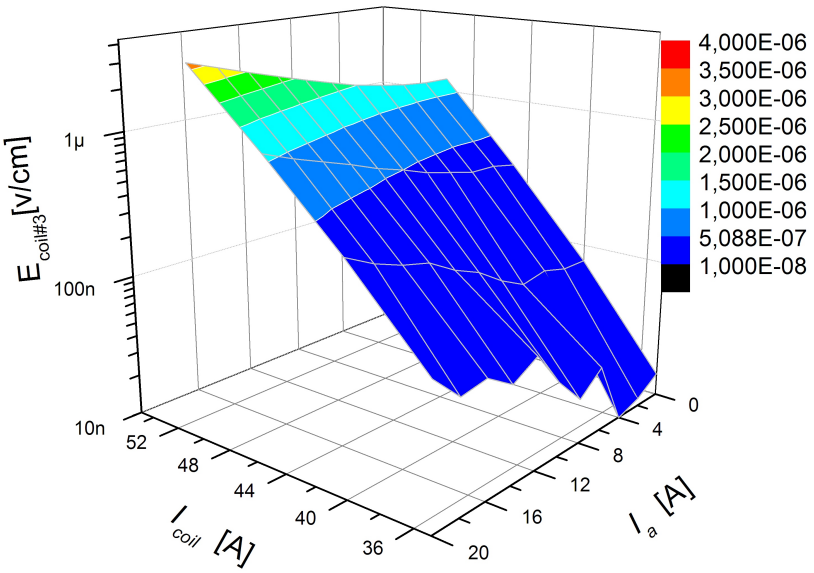

Figure 5.22: Electric field of $Coil\#3$ **for** ϕ**=85°** - The figure is presenting the HTS field winding in Arr2 where the level of the electric field can be identified with the color legend. The particular cases have been presented: where the armature reaction has significant impact on the I_c of the coils, i.e. ϕ=85°.

to express the tendency of the electric field of the coil and hence it was adopted here. The equation for the plane which the data were fitted to had the form presented in 5.5.

$$Log(E_{Coil\#3}) = Log(E_{offset}) + a \cdot I_{coil} + b \cdot I_a \tag{5.5}$$

The coefficients for the fitted plane are as follows $Log(E_{offset})$=-11.92, a=0.1176, b=0.0327. Next, by finding the cross between planes defined with 5.5 and $E_{Coil\#3} = E_0$ will finally result in $I_c(I_a, \gamma = 90°)$ of the HTS field winding. The derived critical current of the field winding is shown in Fig.5.24 together with recorded data (used for extrapolation). For the rated armature current, I_a=28.8 A, the estimate of the critical current of the field winding would be $I_c(I_a = 28.8A, \gamma = 90°)$= 42.3 A, as illustrated with 5.6. This represents approximately 15% reduction of the field winding MMF current capacity compared with no load (I_a=0 A).

$$I_c(I_a, \gamma = 90°) = \frac{1}{a}(Log(E_{offset}) - Log(E_0)) - \frac{b}{a} \cdot I_a = 50.34 - 0.28 \cdot I_a \tag{5.6}$$

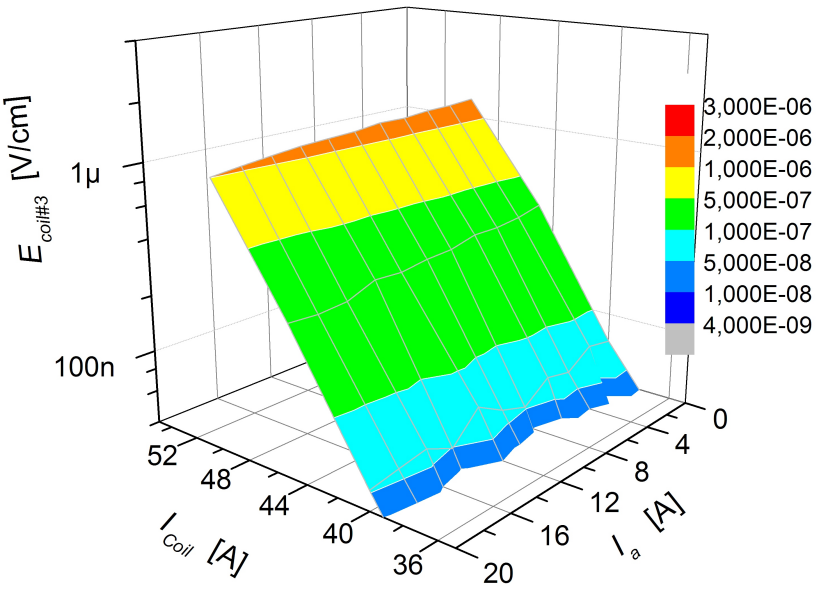

Figure 5.23: Electric field of $Coil\#3$ **for** ϕ**=-185°** - The figure is presenting the HTS field winding in Arr2 where the level of the electric field can be identified with the color legend. The particular cases have been presented: where the armature reaction has small impact on the I_c of the coils, i.e. ϕ=-185° (γ=90°).

At the other hand, electric field of the coil for ϕ=-185° (or γ=-180° which is illustrated by Fig.5.21d) as a function of both the field winding current and the armature reaction is presented in Fig.5.23. The same procedure was carried out for this case (surface fit and the cross between the fit and E_0) and the resulting extrapolation of the critical current, $I_c(I_a, \phi = -185°)$, is also presented in Fig.5.24. Thus, the HTS field winding current $I_c(I_a = 28.8A, \gamma = -180°)$=50 A at ϕ=-185° would correspond to the critical current at rated armature reaction, as expressed with

$$I_c(I_a, \gamma = -180°) = \frac{1}{a}(Log(E_{offset}) - Log(E_0)) - \frac{b}{a} \cdot I_a = 49.15 + 0.0197 \cdot I_a \quad (5.7)$$

The fits and recorded data presented in Fig.5.24 are not perfectly aligned. Performed fits were made to be a conservative prediction of I_c for the HTS field winding. Furthermore, this extrapolation did not include effects of additional saturation of magnetic teeth and pole shoes due to the higher armature current. However, results from FE simulations have confirmed that the flux of $Coil\#3$ (parallel and perpendicular), was in fact a linear function of armature current including rated armature reaction.

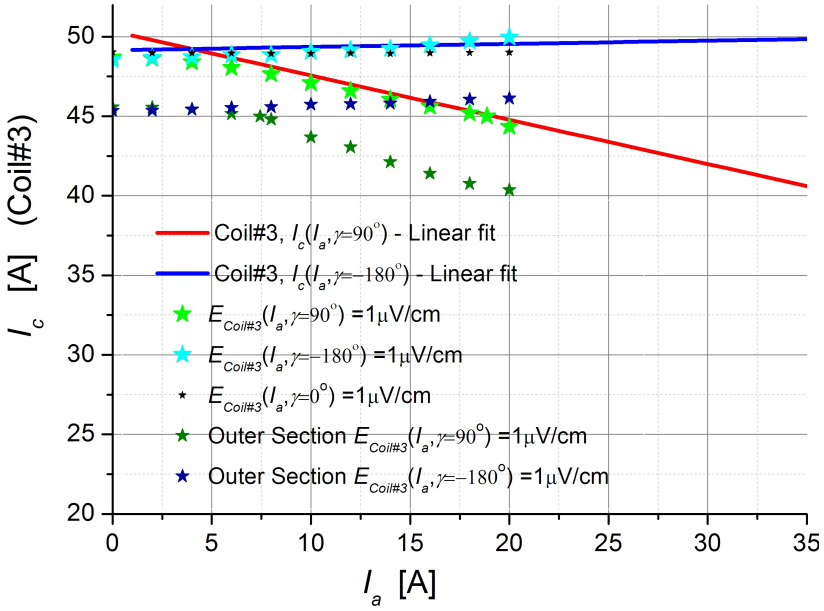

Figure 5.24: The I_c of $Coil\#3$ as a function of the armature reaction for Arr2. - The plot contains data from experiments, shown by a data markers, and extrapolation lines. The extrapolation was performed for ϕ=85° (γ=90°) and ϕ=-185° (γ=-180°). The experimental data include also ϕ=-5° (γ=0°).

$$I_c(I_a,\gamma) = \frac{I_c^q(I_q) + I_c^d(I_d)}{2} + \frac{I_c^d(I_d) - I_c^q(I_q)}{2} cos(2\gamma) \tag{5.8}$$

The $I_{coil} = I_c(I_a, \gamma = 90)$ represents the maximal value of the field current when the armature reaction is in the q axis while $I_{coil} = I_c(I_a, \gamma = 180)$ represents the maximal value of the field current when the armature reaction is in the d axis. It is also true that $I_c(I_a, \gamma = 180°) \geq I_c(I_a, \gamma = 90°)$. Hence, a second harmonic function expressed in 5.8 can be used as a first approximation for $I_c(I_a, \gamma)$ instead of deriving full angular dependence.

If $I_c(I_a, \gamma = 90°)$ is named I_c^q and $I_c(I_a, \gamma = 180°)$ is named I_c^d, since each are caused by the armature current in the corresponding axis, the expression 5.8 can be used to define the critical current as a function of the armature reaction and the load angle. To verify this approximation for all angles, the expression 5.8 was compared to the experimental data for I_a=16 A. Both are presented in Fig.5.25, where it can be seen that approximation and experimental data are in good agreement.

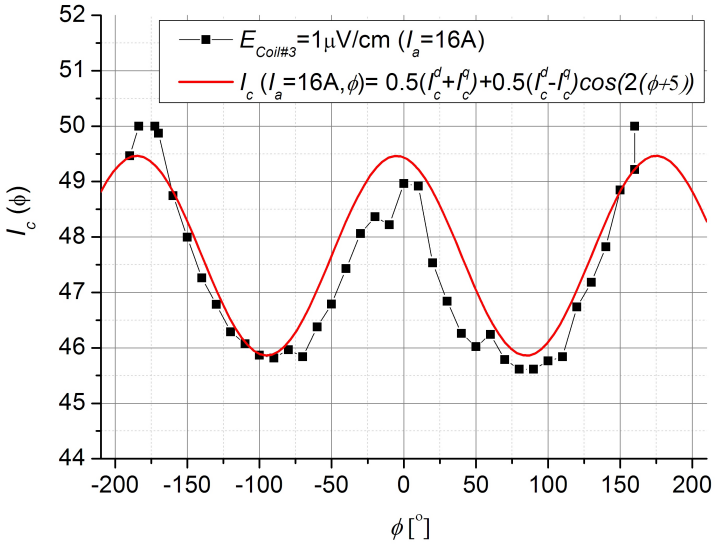

Figure 5.25: Comparison of $I_c(I_a, \phi)$ from experiments and second harmonic approximation for I_a=16 A - Experimental critical current for Ia=16 A was derived from the condition $E_{Coil\#3}$=1 μV/cm while second harmonic approximation is plotted with the help of 5.6, 5.7 and 5.8 and for I_a=16 A

5.4.4 Performance verification - *Coil*#3 sections

So far, a low level of discrepancy, if any, has been observed between inner and outer sections of the turns in individual IV curves of the coils. Yet, the armature reaction can have a prevailing influence on the HTS coil performance, as seen in previous sections. Consequentially, sections of the critical coils should be investigated for Locked Armature experiments as well in order to confirm the derived critical parameters of the HTS field winding. The illustration in Fig.5.26 shows the nature of the change in more detail.

The tendency of the electric field of sections of *Coil*#3 have been presented as a ratio of the electric field for the outer and for the inner section and are presented for the case when the field winding was supplied with 45A in Arr2. The ratio, presented in Fig.5.27, which for this case have values between 1.7 and 2.1, is a function of ϕ too. For the outer section of the coil *Coil*#3, the electric field profile is presented in Fig.5.28. Comparing this profile to Fig.5.16, it is obvious that the outer section has a much larger portion of the electric field above E_0. Consequently, in order to take into account reduced capacity of the outer section of the coil, the adjustment of the extrapolation procedure from Sec.5.4.3 is in order. After analysis of the data from the

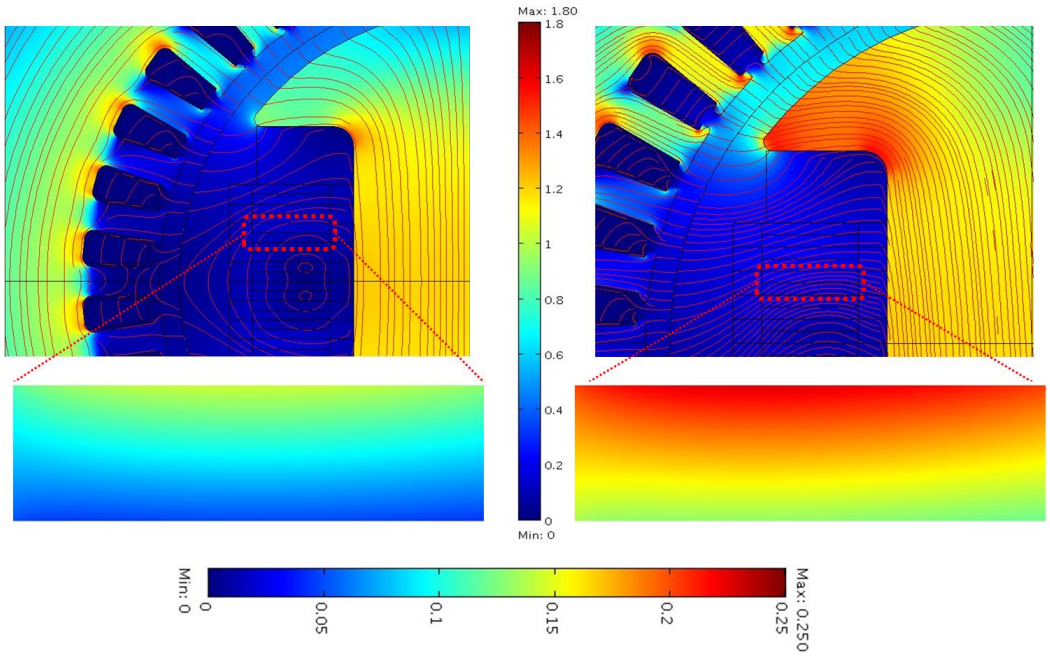

Figure 5.26: The FE simulation of Locked Armature Experiment for γ=90°, $I_{Coil\#3}$= I_{Coil}= 40 A, and I_a=0.0 A and I_a=30 A - This figure represents the FE simulations corresponding to the Locked Armature Experiment condition. The plot of magnetic flux density for I_a=0 A is presented on the left side of the figure while for I_a=30 A is at the right side. The vertical color legend with maximum of 1.80 T at dark red and 0.0 T at dark blue end is common for both flux plots. Additional graphs of the perpendicular magnetic flux density at $Coil\#3$ have been enlarged and placed below corresponding plots as the dashed red lines suggests. These plots share a common horizontal color legend with 0.25 T as a maximum at the dark red and 0.0 T as a minimum at the dark blue end. Perpendicular flux will increase linearly with the increase if armature reaction at γ=90°. The flux lines have been included as well.

outer section with respect to the extrapolation prediction, the reduction of ∼4 A was observed in I_c, which means that revised extrapolation lines would be paralleled to the previously derived extrapolation lines (vertically migrated down). Only experimental data (not corrected prediction linear fits for the outer section of $Coil\#3$) are presented in Fig.5.24 in order to illustrate the effect of sections current rating.

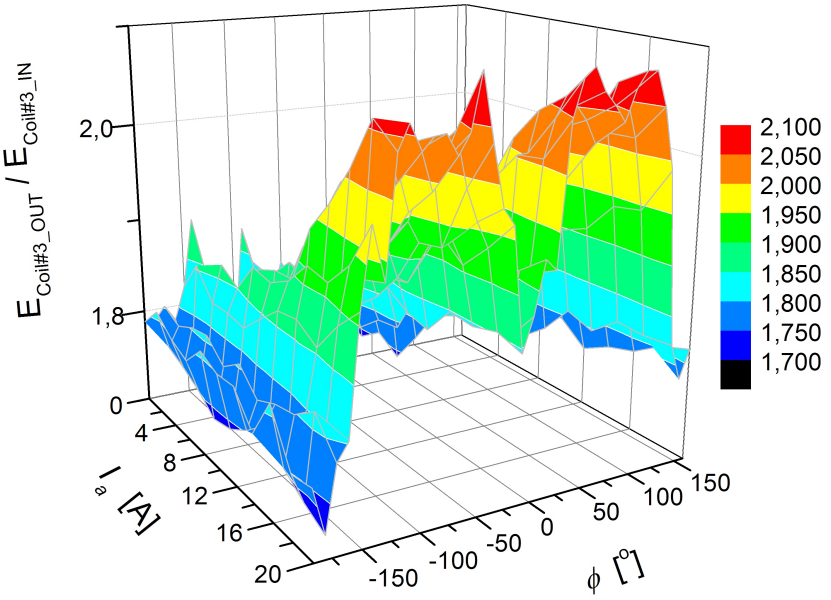

Figure 5.27: $E_{Coil\#3-OUT}/E_{Coil\#3-IN}$ - The figure illustrates the tendency of the ratio of electric fields of the outer and the inner section of Coil#3 for the field winding in Arr2. The ratio indicates that the outer section of the coil has higher voltage drop and is exposed to a higher value of the perpendicular magnetic flux than the inner section. This is in line with the simulation results in Fig.5.26.

5.4.5 Summary for HTS field winding - armature interaction

- The armature reaction does have significant influence on the HTS performance.
- The influence of the armature reaction on HTS field winding depend on the angle between a magnetic axis of the armature winding and the HTS winding.
- In both arrangements $Coil\#3$ was the coil with lowest I_c, which implies that conclusions derived regarding coil placement recommendations will not be affected by the armature current.
- Extrapolation of recorded results was performed for the HTS field winding in Arr2 and values of I_c^d=49.95 A and I_c^q=42.3 A were found for rated armature reaction.
- A second harmonic approximation of maximal field current as a function of γ (or ϕ) was proposed: $I_c(I_a, \gamma) = 0.5(I_c^d + I_c^q) + 0.5(I_c^d - I_c^q)cos(2\gamma)$ and compared

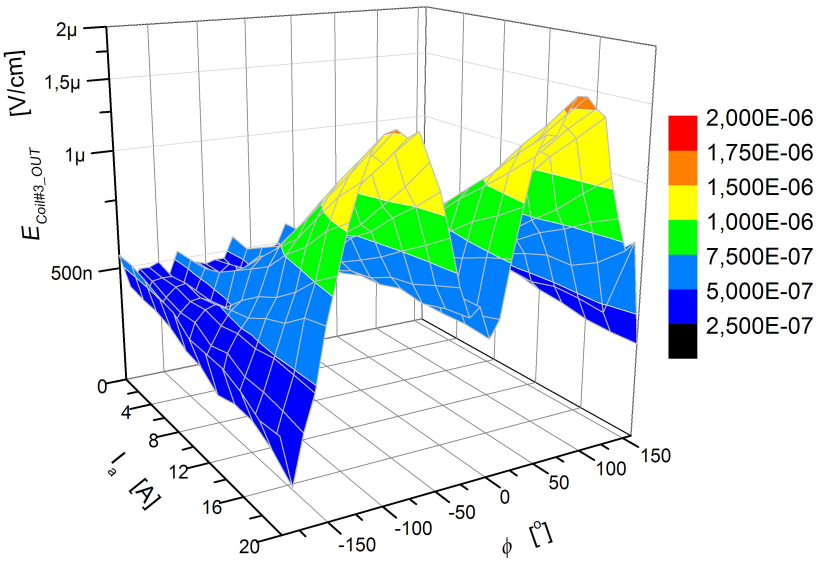

Figure 5.28: $E_{Coil\#3-OUT}$ - The figure indicates the impact of the armature reaction, both intensity and angular displacement, on the discrepancy in the performance of the coil turns. The I_a=30A which is slightly higher than the rated armature reaction.

to the experimental data. The approximation is in the good agreement with experimental data.

- Electromagnetic torque was analyzed for one configuration of the field winding. A small value of the reluctant torque was observed in recorded results (which is due to saturation of the cold steel). A surface fit of the electromagnetic torque resulted with $T_{1^{st}}$[Nm]=2.64 $\times 10^{-4}$ [NmA^{-}2] $\times$ MMF [AmpTurns] $\times$ I_a [A], where MMF is magneto motive force of HTS field winding and I_a is armature current (two phase, dc as in the experiments) in q axis.

- The discrepancy in performance of the turns in $Coil\#3$ is a function of the armature reaction. Approximately 4 A higher I_c was observed for the inner section of $Coil\#3$.

5.5 Armature driven HTS supply - General recommendation

As seen so far, magnetic anisotropy of the HTS field winding has caused different responses of the HTS field winding to the armature reaction at different angles. Thus, the operation conditions could be formulated for both an armature winding and a field winding of an HTS machine, such that the maximized power output is maintained (assuming these are in controllable configuration). The boundary conditions for the maximal operating current of the HTS field winding have been defined as functions of an armature reaction, ie. $I_c(I_d, I_q)$.

The conventional design of the HTS machine would specify the maximal value of MMF of the field winding which corresponds to the rated (or maximal taking into account safety margin) armature reaction and its impact on the I_c of the field winding. From Sec.5.4.3, this would correspond to the $I_{Coil} \leq I_c^q$= 42.3 A for any armature current (less or equal to rated value). If instead, the field current is adjusted to follow the $I_c(I_d, I_q)$[1], higher MMF would become available for lower values of armature current. This in turns means that same power output (torque) can be achieved with a lower value of armature current which in turns will result in lower loss in the armature winding and better partial load efficiency of the machine.

For Sperwind machine, the difference between maximal current of the field winding with rated armature current in q axis and with no armature current in q axis is 50 A/42 A$\sim$1.19. If the machine was designed in a conventional way, the maximal field current corresponding to the rated torque would be I_{Coil} $\leq$42 A or 40%–80% of this value if the safety margin is included. For a 50% loaded machine (half of the rated torque at rated speed, ie.τ=0.5 p.u.), the armature current in q axis would need to be half of the rated value, ie. τ= MMF $\times$ I_q = 1 p.u.$\times$ 0.5 p.u. = 0.5 p.u. Now, with the proposed method, since the armature current is lower than the nominal value, in the case of Superwind machine, a 10% higher field current can be allowed.This will in turn reduces I_q from 0.5 p.u. to 0.45 p.u. which would decrease armature loss by $\sim$18% compared to the previous example. Thus, if an HTS machine is to operate substantial time in partial load (with is the case for wind turbine generators), a significant savings

[1]Note: Described control concept for a field winding of an HTS machine is pending for a patent application with Dr.Bogi B. Jensen and Nenad Mijatovic listed as inventors.

in the both energy and cost can be achieved through proposed control strategy. On the other hand, the dynamic changes in the field current of the HTS field winding will generate ac loss in the winding. This loss and the time constant of the field winding (inductance and voltage insulation) will be limiting factors for the dynamics (how fast the tracking of I_q can be) of the proposed control of the field winding current. Hence, a balance between these will need to be obtained.

5.6 Boosting an HTS field winding's performance

In this section two methods for increase of maximal operating MMF of the HTS field winding are proposed. The first method is based on the difference between the HTS coils and their current capacity. This method suggests multiple power supplies as a way of achieving higher values of MMF from an HTS winding. The second method proposes the placement strategy for 2G coils and it presents the analyses of its impact on the neighboring coils.

5.6.1 Multiple current supplies

It is clear from the figures Fig.5.7 and Fig.5.8 that the inner coils, namely $Coil\#2$ and $Coil\#6$ in Arr1 and $Coil\#2$ and $Coil\#5$ in Arr2 are substantially far from critical currents in the series connected field winding. If each coil is supplied from an independent power supply, the current in the coil could be set to a value that is optimal with respect to a number of objectives, where maximizing the MMF of the HTS field winding would be an obvious one.

If the HTS coils in the HTS winding are allowed to carry different currents, the same MMF can be achieved with a substantially lower amount of HTS tape (133) where a 50% reduction was reported as a theoretical maximum that could be achieved for 2G coils at 20 K. Several examples of the multiple power supplies have been experimentally tested in order to examine the potential of this method. As far as to the author's knowledge, this approach is novel to an HTS machine design and it was not suggest in any of the published HTS machine designs. With four Hewlett Packard DC power supplies in Arr1 or six in Arr2, the setup allowed each coil to have an independent current supply. Thus, 5.2 will become 5.9

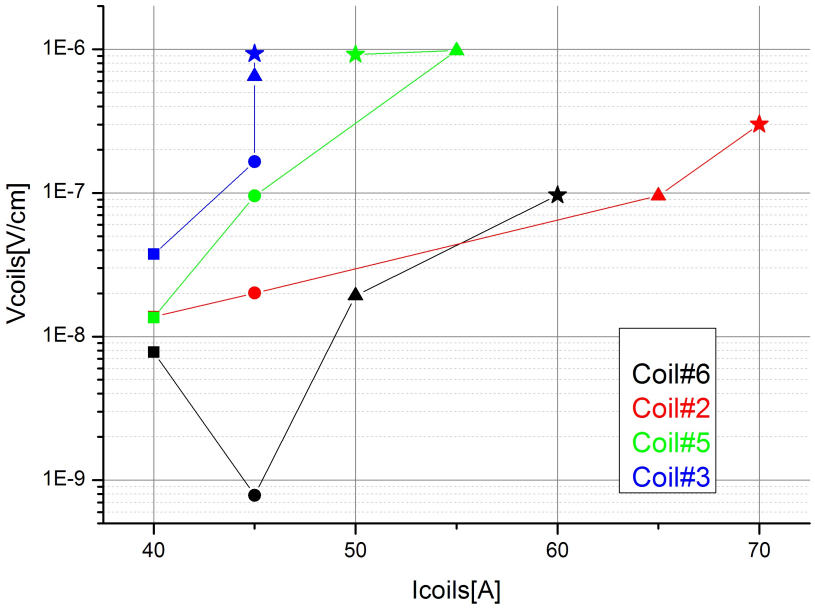

Figure 5.29: The trace of voltages of the coils with four power supplies while the HTS field winding is in Arr1. - Coil currents in the plot are: square - $[Coil\#2{-}40A; Coil\#3{-}40A; Coil\#5{-}40A; Coil\#6{-}40A]$, circle - $[Coil\#2{-}45A; Coil\#3{-}45A; Coil\#5-45A; Coil\#6-45A]$, triangle - $[Coil\#2-65A; Coil\#3-45A; Coil\#5-55A; Coil\#6-50A]$ star - $[Coil\#2-70A; Coil\#3-45A; Coil\#5-50A; Coil\#6-60A]$

$$\forall \left(\frac{U^i_{coil}}{L^i_{coil}} \right) \leq E_0 \tag{5.9}$$

where the coil index i takes values from the coil ID array for coils present in the field winding. For Arr1 the index i would take values from the array of the coils ID present in the winding, i.e $[Coil\#3, Coil\#2, Coil\#5, Coil\#6]$. The current limit for HTS winding in the Arr1 connected in series is I_c= 52 A (set by $Coil\#3$). Any additional increase in the current of any other coil would cause exponential voltage increase of $Coil\#3$ due to increase in the perpendicular flux. Setting the current of $Coil\#3$ to some lower value, for example 45 A, allows higher flux density $Coil\#3$ is exposed to and thus an increases in the total MMF. To demonstrate the potential of the multiple power supplies, two sets of coil currents have been found to satisfy the condition expressed with 5.9 and are illustrated in Fig.5.29, where electric field of each coil is presented for the corresponding current. The points with same data markers are identifying one combination of composition of coils currents. Because the number of sources is not

small (four), and due to the time constraints only several operating points with higher MMF have been identified, hence the degree of the improvement may be even higher than presented here but that would call for extensive experiments and purpose built search algorithm in Lab View. Nevertheless, even for presented cases, having the coils carrying currents close to their individual I_c, the total MMF of the HTS field winding in Arr1 was increased by 12% compared to the series connected HTS coils with current of 50 A. The coil exhibiting the highest increase in operating current is $Coil\#2$ with 40% higher current compared to the series connected HTS coils.

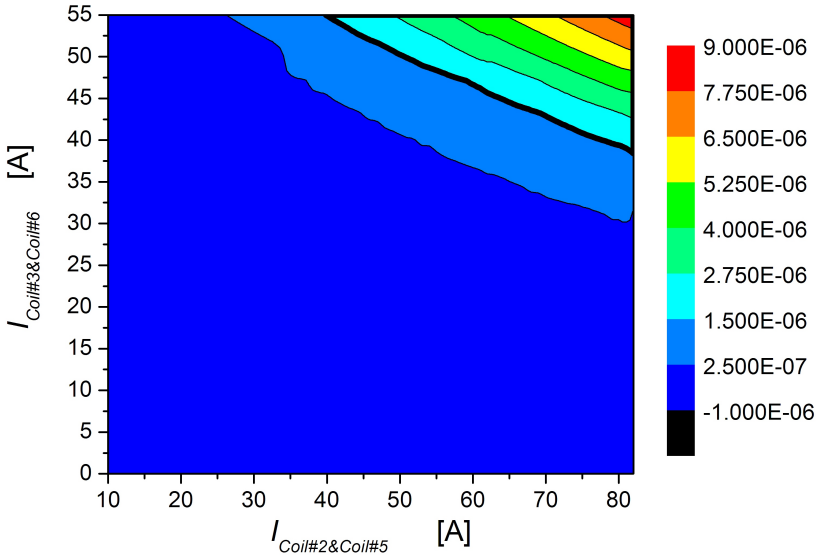

Figure 5.30: $Coil\#3$ - This figure presents the I_c contours for $Coil\#3$ and $Coil\#5$. Two power supplies have been used, one for each pair, and I_c contours are presented as function of these currents. It can be observed that the inner pair of coils, $Coil\#5$ and $Coil\#2$, has much higher I_c compared to $Coil\#3$ and $Coil\#6$.

The question of the system complexity should be raised, since the higher number of current leads or complex low temperature power electronics elements and multi terminal brushless exciters would increase the system complexity. Thus, in the spirit of minimizing the complexity of the proposed system, it is also of interest to investigate how much increase in MMF can be expected from each additional power supply.

In Arr2, two pairs of coils have been connected in series. Two power supplies are used where the first one is connected to the coil pair comprised of $Coil\#3$ and $Coil\#6$ and the second power supply to the coil pair comprised of $Coil\#2$ and $Coil\#5$. The

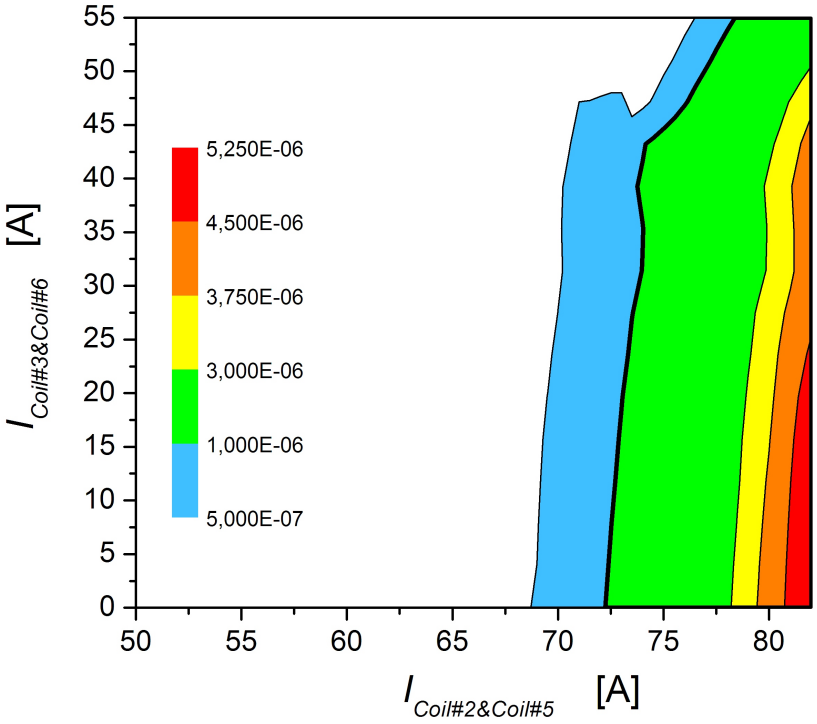

Figure 5.31: *Coil*#5 - This figure presents the I_c contours for *Coil*#3 and *Coil*#5. Two power supplies have been used, one for each pair, and I_c contours are presented as a function of these currents. It can be observed that the inner pair of coils, *Coil*#5 and *Coil*#2, has much higher I_c compared to *Coil*#3 and *Coil*#6.

I_c lines for *Coil*#3 and *Coil*#5 are illustrated in Fig.5.30 and Fig.5.31. For a winding connected into a series, with I_c ∼50 A, the MMF of the field winding would be 50 A (48+51+46+56)= 10050 AmpTurns. From Fig.5.30 and Fig.5.31, we can see that if the current of *Coil*#3 is set to be 42 A, *Coil*#5 will be able to carry 72 A. The MMF of the field winding in this case would be 42 A (51+56) +72 A (48+46) =11262 AmpTurns which represents an increase of 12%. The same level of increase was achieved with only two power supplies instead of four as in the previously presented example. This implies that the substantial increase in MMF of the field winding is possible with only one additional power supply.

The cost of the HTS tape is the prevailing cost of the HTS machine and the multiple current supplies approach can be an effective method to reduce the amount of HTS required for a given MMF. However, the implications a multi power supply method would have on the cost of the whole system needs to be evaluated before this method

can claim any advantage.

5.6.2 Effective Flux Shielding by HTS coils

From the previous section we have seen that with the introduction of additional power supplies, the performance of the individual HTS coils can be substantially increased which will ultimately result in better utilization of HTS material and could reduce cost for HTS machine. Also, the importance of HTS coils placement was shown in Sec.5.3.4 with the example of $Coil\#6$ and $Coil\#5$ as representatives of 2G and 1G technology in both the field winding configurations.

Coils with defects, $Coil\#7$ and $Coil\#8$, were not in any of the discussions so far, since they would limit the performance of the field winding. Yet, they are capable of carrying low currents and provide some MMF. In Arr2, $Coil\#7$ and $Coil\#8$ have been placed strategically at the outer position in the HTS field winding (close to the pole shoes) as representatives of 2G coils due to its lower magnetic sensitivity, compared to 1G coils. This section explores the additional value of having $Coil\#7$ and $Coil\#8$ active in the field winding, not in the terms of MMF of these coils but their effects on the performance of the HTS field winding in Arr2. Thus, Arr2 with $Coil\#7$ and $Coil\#8$ active will be referred to as Arr2-b and Arr2-c for the case when these coils are fed with 5 A and 10 A respectively.

The electric fields of $Coil\#3$ for I_{Coil}=50A running in Arr2-b and Arr2-c are shown in Fig.5.32a and Fig.5.32b. Comparing these with the case when only four coils are active, presented in Fig.5.17, it is obvious that the percentage of the electric field of $Coil\#3$ that is below E_0 is increased with the increase of the current of $Coil\#7$ and $Coil\#8$. The increase in the critical current of $Coil\#3$ including the influence of armature reaction can be derived following the same procedure presented in Sec.5.4.3. The experimental results for γ=90° are shown in Fig.5.33 where it can be observed that with the increase in current of $Coil\#7$ and $Coil\#8$, the critical current of $Coil\#3$ will increase as well. The maximal increase of 3 A can be observed.

As this increase is mainly due to corrective action of the MMF of $Coil\#7$ and $Coil\#8$ on the stray flux lines seen by $Coil\#3$, this increase is highest for low values of I_a. This is validated with FE simulations as illustrated in Fig.5.34, where the effects of the flux shielding were extrapolated for the case if the defected coils were operational and are able to operate with $\geq$25 A. The FE simulations have confirmed that the

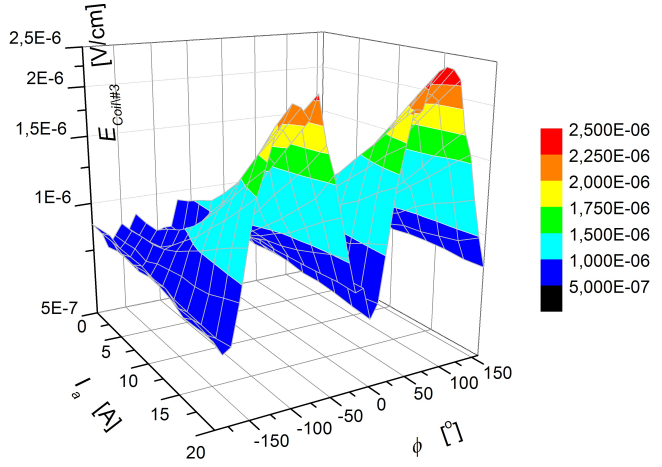

(a) Arr2-b

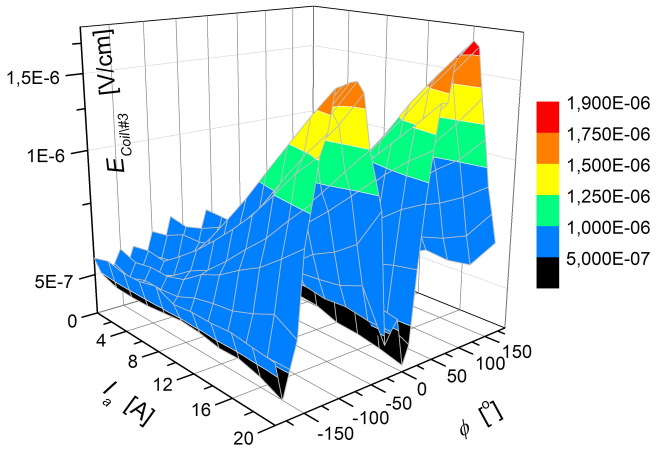

(b) Arr2-c

Figure 5.32: The electric field for $Coil\#3$ - (a)The electric field of $Coil\#3$ for I_{Coil}=50 A for the field winding in Arr2-b. The current of $Coil\#7$ and $Coil\#8$ is 5 A; (b)The electric field of $Coil$ for I_{Coil}=50 A for the field winding in Arr2-c.The current of $Coil\#7$ and $Coil\#8$ is 10 A.

effects of flux shielding are function of the currents of $Coil\#7$ and $Coil\#8$ and that for higher currents, more flux shielding is provided. For the current of 50 A, the magnetic conditions $Coil\#3$ is experiencing are similar to the individual IV experiments which implies that the I_c of $Coil\#3$ could be boosted up to 70 A – 80 A.

Thus, as the portion of total MMF generated by $Coil\#7$ and $Coil\#8$ of the field winding is increasing, so will the perpendicular flux these coils are exposed to. However,

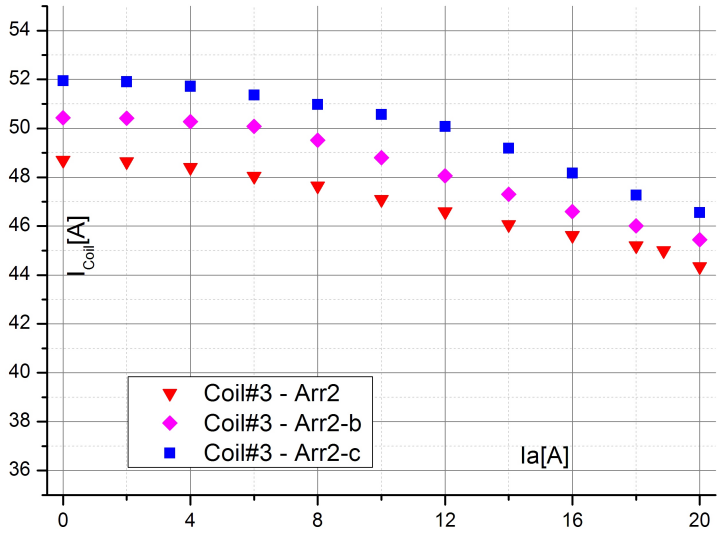

Figure 5.33: The critical current of $Coil\#3$ based on the E_0=1μV/cm criteria, as a function of I_{Coil} and I_a for the field winding in Arr, Arr-b and Arr-c. - This plot illustrates an increase in the critical current of $Coil\#3$ (while part of the series connected field winding) with increase of the current in coils $Coil\#7$ as $Coil\#8$ from 0A to 10A. The discussion was made for γ=90° where the armature reaction impact is the highest.

in two pole machine, if these coils are placed as $Coil\#7$ and $Coil\#8$ are, the perpendicular flux inner coils are exposed to is decreasing correspondingly, ie. flux shielding. The strategic placement of the HTS coils (both 1G and 2G) is of the essence. It is not only that the 2G coils are more suitable to be placed in the field winding where the flux is mostly perpendicular to the turns, but having compact high MMF coils (high engineering current density) placed at outer position will also substantially improve the conditions for the neighboring coils further in the coil stack.

5.6.3 Summary for improving the HTS field winding performance

- By incorporating the multiple current supplies in the design approach of an HTS machine, substantial savings could be achieved where 12% increase in total MMF was observed in the Superwind machine while in the same time the increase in performance of $Coil\#2$ was ~40%.

- A 12% increase in performance of the HTS field winding was observed too for the case of two power supplies in total. Hence, number of additional power supplies

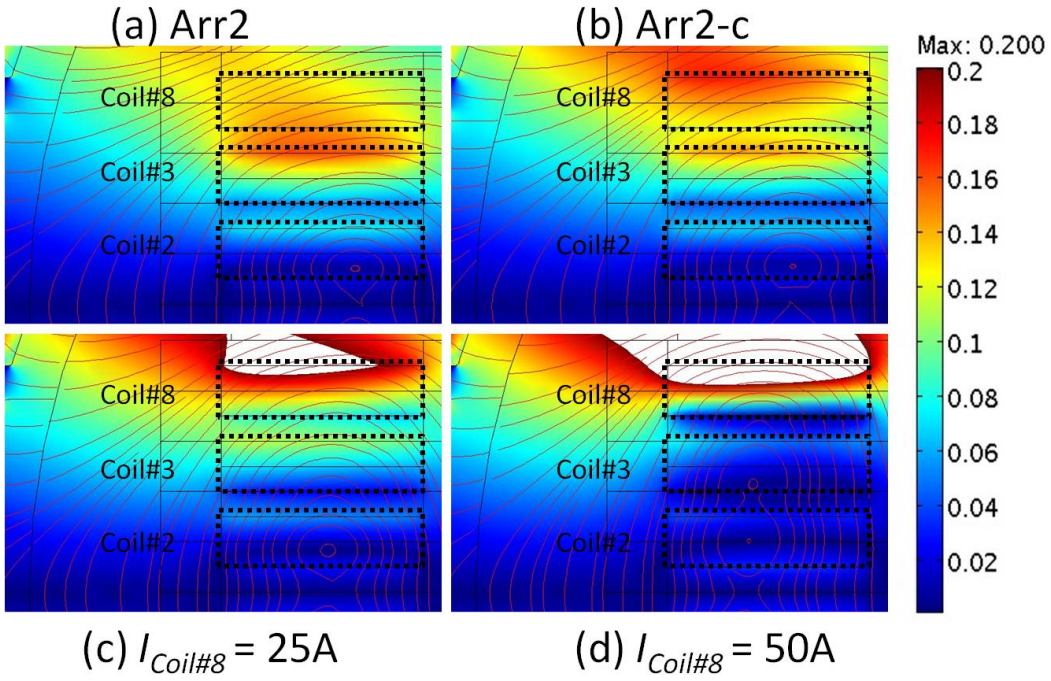

Figure 5.34: The perpendicular flux density plots for various currents of $Coil\#7$ **and** $Coil\#8$ **and for** I_a**=0A and** I_{Coil}**=45A.** - The color legend is common for all flux plots. Areas with no color (in (c) and (d)) are where the perpendicular flux density is higher than 200 mT. **(a)** Flux plot of the HTS field winding in Arr2, with indicated flux lines. **(b)** Flux plot of the HTS field winding in Arr2-c. With 10A running in $Coil\#7$ and $Coil\#8$, the slight change in the perpendicular flux of the $Coil\#3$ is observed. **(c)** With $25A$ running in $Coil\#7$ and $Coil\#8$, the substantial change in the perpendicular flux of the $Coil\#3$ is observed (50% reduction from Arr2) . **(d)** With $50A$ running in $Coil\#7$ and $Coil\#8$, the perpendicular flux of the $Coil\#3$ is ∼50 mT, similar to the magnetic condition for the IV curve of $Coil\#3$.

can be optimized in order to reduce the cost and complexity of proposed approach.

- The placement of 1G and 2G coil proved to be crucial where recommendation to place 2G coils in regions with high perpendicular flux density would result in the HTS field winding with better higher MMF. If instead of $Coil\#3$ in Arr2, the clone of $Coil\#6$ was used, the critical current of the HTS field winding connected into a serous would be ge65A which is ∼ 30% higher than observed in experiments where $Coil\#3$ is the bottleneck.

- An additional benefit of compact MMF (high J_e) of 2G coils is seen in improved

magnetic conditions for inner coils.

5.7 The HTS machine parameters and performance

The parameters of the HTS machine will be determined on the basis of experimental data and FE simulation. No load and short circuit experiments were performed for several speeds and operating MMF of the field winding. As the Superwind HTS machine utilizes an armature winding designed for a high speed machine and since the speed of the setup is limited to 400 rpm, the output frequency and induced voltage are expected to be low. Consequently, only loads with low impedance could be used.

5.7.1 Armature No load test

The No-Load voltage was measured in a No-Load test conducted at several speeds (with maximum speed of 312 rpm) and validated via 2D FE simulation. Both measured and simulated results are presented in the Fig.5.35 for the speed of 115 rpm, where as it can be observed, the simulated results for the induced voltage are in good agreement with measurements.

As the magnitude of the induced voltage is a direct indicator of the flux linkage in the machine, the induced voltage in the machine can be correlated to the air gap magnetic flux density. The armature design value for an air gap magnetic flux density could be used as a good reference point for comparing achieved values of the air gap flux density. This is derived as rated armature phase voltage, 400 V, multiplied with the relative speed of the machine in the experiment where the base speed would be the rated synchronous speed of the armature winding, 3000 rpm. The lower value of induced voltage in the phase winding is a consequence of the poor magnetic permeability of the cold steel, Steel37 (for B-H curve see Sec.4.4.3) and large magnetic air gap (10 mm). If instead the high permeability steel is used (for example, M800), both the flux linkage and the HTS current capacity could be boosted on the account of the decrease of the leakage flux of the HTS field winding.

With four HTS coils operated at 77 K for the HTS field winding in Arr1 connected into a series, the highest induced phase voltage was 11.1 V for the speed of 115 rpm. The field current in this case was 50 A. This corresponds to the peak flux density of 0.58 T in the 10 mm air gap. When multiple supplies were used, the maximal value of the

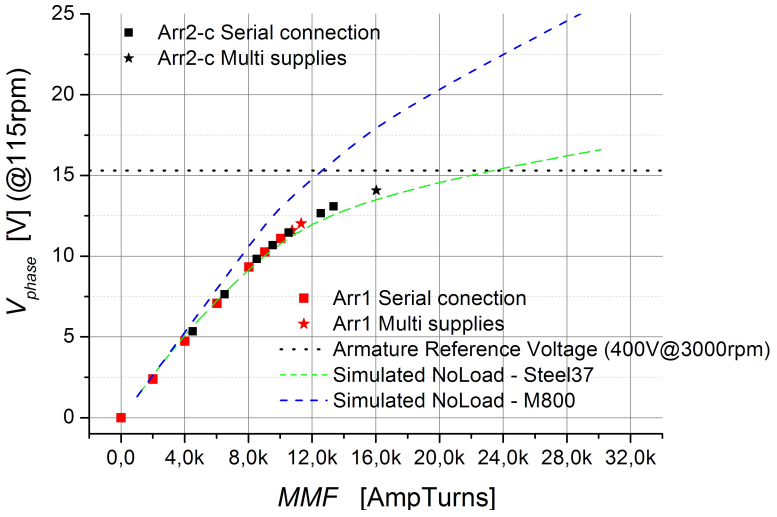

Figure 5.35: The trace of the No-Load voltage for the HTS field winding Arr1 and Arr2. - No Load phase voltage for the HTS field winding Arr1 and Arr2 at 115rpm. Star markers are used in the case when multi power supplies were used. A constant voltage dotted line is illustrating the 115×rpm 400 V / 3000 rpm voltage level. Dashed blue and green lines are representing simulation estimates for No-Load voltage induced if M800 and Steel37 steel are used as a cold steel, respectively.

phase voltage recorded was 12 V with the set of currents for $Coil\#2$ with 70 A, $Coil\#3$ with 45 A, $Coil\#5$ with 50 A and $Coil\#6$ with 60 A. This constitutes approximately 78% of the reference voltage (400 V @3000 rpm). In the Arr2-c with multiple power supplies, with the help of MMF from the 2G coils with a defect, the maximal induced No Load voltage was 14 V which constitutes 91% of the reference voltage. Thus, it can be concluded that if $Coil\#7$ and $Coil\#8$ were operational, the field winding in Arr2 would be able to create the air gap flux density higher than 0.75 T which would induce voltage higher than the rated voltage (15.33 V).

5.7.2 Armature short circuit

The short circuit experiment was performed for several speeds and several values of MMF. Results from the experiments are presented in Fig.5.37. The short circuit characteristics, as expected, are linearly scaled with I_{coil}. FE simulation was carried out for a few selected cases corresponding to the experiments which were compared with experimental data. The measured and the simulated short circuit current waveforms for one of these cases, presented in Fig.5.38, are found to be in good agreement.

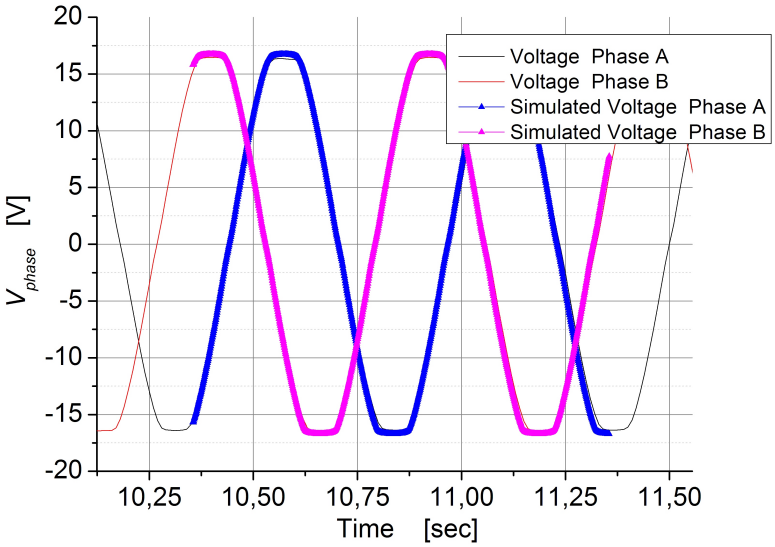

Figure 5.36: The voltage waveform trace for the No Load experiment at 115rpm - The figure illustrates measured phase voltage and the result from a FE simulation corresponding to the No load experiment. The measured (triangles) and simulated (lines) results are in very good agreement.

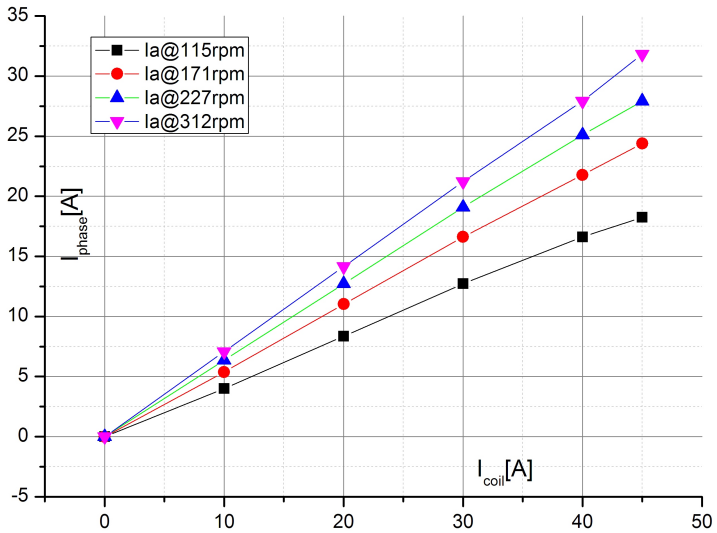

Figure 5.37: Short Circuit Test - The armature winding during the three phase short circuit at several speeds and MMF values. As expected, the short circuit characteristics are linear functions of excitation current.

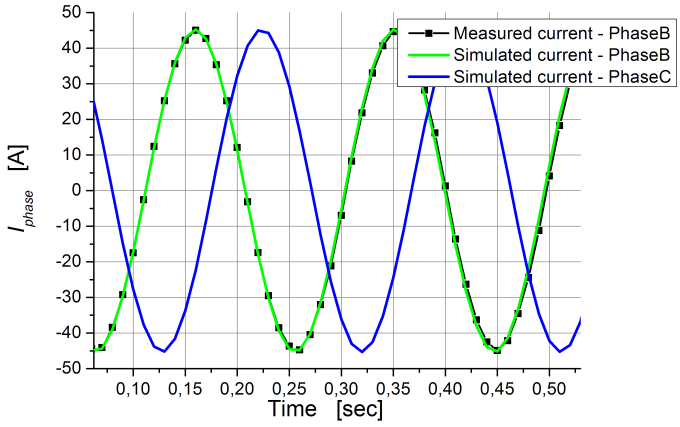

Figure 5.38: The FE simulation of the short circuit experiment. - The figure presents the recorded results and the results from simulation for the short circuit at 312 rpm and for the field current 45 A in Arr2

5.7.3 Estimation of machine parameters

The machine parameters were estimated from a 2D FE model where the self inductance of the phase winding A was found to be

$$L_{aa} = L_{aa0} + L_{aa2} * cos(2\theta) \tag{5.10}$$

$$L_{ab} = -L_{ab0} + L_{ab2} * cos(2\theta - \frac{2\pi}{3}) \tag{5.11}$$

where L_{aa0}= 8×10^{-3}H and L_{aa2} = 3×10^{-3}H. The L_{ab0} was found to be 4×10^{-3}H and $L_{ab0} = L_{ab2}$ which leads to the values of L_d = 16.5×10^{-3}H and L_q= 7.5×10^{-3}H (124) defined by 5.12 and 5.13.

$$L_d = L_{aa0} + L_{ab0} + 3L_{aa2}/2 \tag{5.12}$$

$$L_q = L_{aa0} + L_{ab0} - 3L_{aa2}/2 \tag{5.13}$$

The self and mutual inductances of the phase winding were estimated for a saturated magnetic circuit. Now, we can compare these values with experimental results from no load and short circuit experiments. It is possible to derive the values of L_d and L_q from

performed short circuit and no load experiments where the voltage balance equations for d and q axis, written for short circuit (V_d=0V and V_q=0V) are expressed in 5.14 and 5.15

$$R_a I_d = \omega L_q I_q \tag{5.14}$$

$$E_{noload} = R_a I_q + \omega L_d I_d \tag{5.15}$$

where E_{noload} is the no load voltage for given speed and MMF while ω is the angular frequency at given speed. The impedance defined as no-load voltage divided with short circuit current for a salient pole machine can be expressed as 5.16

$$Z = \frac{E_{noload}}{I_{short}} = \frac{R_a^2 + \omega^2 L_d L_q}{\sqrt{R_a^2 + \omega^2 L_q^2}} \tag{5.16}$$

where R_a=0.48Ω is the resistance of the phase winding (@90°C). The values of impedance, Z, derived from the experiments by simple devision of no load voltage and corresponding armature current from short circuit experiment are presented in Fig.5.39 for five values of I_{Coil} and four different speeds. Due to saturation of cold steel, the values for Z are slightly lower for higher field currents. The curve presented in the figure with the red line is the fit performed for Z($I_{Coil=45A}$) from where the values L_d=23.5×10^{-3}H and L_q =15×10^{-3}H were found. Compared to the FE estimate, the experimentally determined values are higher by ∼7.5×10^{-3}H which is most likely due to the leakage inductance of the end connections of the phase windings (not present in the 2D FE model cannot be used).

If these values for inductances are extrapolated to the rated values for armature winding, (400V, 23.5A, 3000rpm), the inductances expressed in per unit (p.u.) would be: L_d=0.43 p.u. and L_q=0.27 p.u.

5.7.4 Summary for the HTS machine parameters

- The no load voltage test confirmed that with 4 coils in Arr1 and 50 A, the induce voltage was 11,1V which constitutes 72% of reference armature voltage. The air gap flux density across 10 mm magnetic air gap was found to be 0.58 T

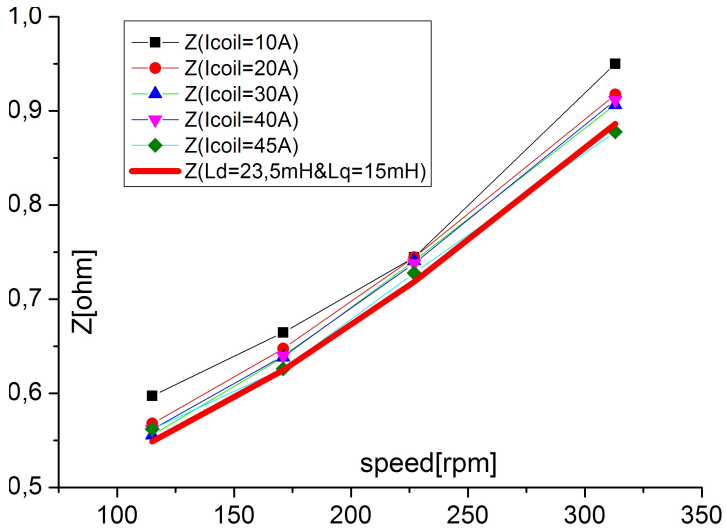

Figure 5.39: Impedance Z calculated for No Load and Short Circuit experiments - The impedance as defined in expression 5.16 for several speeds and values of the field current.

- By operating with multiple current supplies in Arr2-c, the induced voltage was increased up to 91%.
- Parameter analysis of the HTS machine have confirmed the air dominated design due to large magnetic air gap and low permeability of cold steel with low values of L_d and L_q.

Chapter 6

Conclusion and Future Work

6.1 Conclusion

In the design process of the machine setup, a number of challenges were addressed among which two stands out: the cryostat design and Torque Transfer Element (TTE). The cryostat design showed that with a rather simple design and low cost technology and material (such as stainless steel), remarkable thermal and mechanical performances can be achieved. The compact design of the vacuum insulated cryostat with 10 mm net thickness resulted in ∼10 W of heat transfer at 77 K (for properly evacuated vacuum chamber). Even though, the 10 mm thick thermal insulation presents 12.5% of the air gap radius in this particular design, the implication of this achievement is encouraging for larger machines, particularly for the machines with a high pole number where the pole surface relative to the magnetic air gap is not large.

The heat transfer of only 10 W at 77 K is achieved due to an optimized design of the Torque Transfer Element which is integrated into the cryostat and is identified as an element with the largest contribution to the net heat load. Realizing the significance of the optimization of the thermal and mechanical properties, general recommendation towards a TTE geometry are presented and their validity verified in the design (the TTE with 10 W compared to the alternative - a shaft with an estimate of ∼60 W).

The HTS coil design confirmed the robustness of the both the 1G and 2G HTS tape from AMSC (1) while problems with the 2G Superpower HTS tape was observed in both constructed coils, indicating the sensitivity of the HTS tape and the importance of the coil design. The difference between these, beside the fabrication method, was in the

electric insulation used. The solution where an epoxy coating is applied to the HTS tape as an insulating layer consequently should increase the engineering current density of the coil ($Coil\#7$ and $Coil\#8$ have 2.5 times more turns compared to the others coils). However, both $Coil\#7$ and $Coil\#8$ were damaged most likely due to the thermal stress/strain which delaminated the HTS and thus degraded the I_c. Interestingly, the I_c value of the coils did not degrade with repeating cool-down which would be expected. Therefore, further investigations are required to understand and ensure that the coil design can mitigate a damaging mechanical stresses.

To the author knowledge, the Superwind HTS machine, next to being the first HTS SM developed in Denmark, is the first HTS SM to operate with the combination of HTS conductors, both 1G and 2G type. This design approach, employing several types of the HTS conductors, was proposed as a method to increase the performance of the HTS field winding, but also to achieve a better value of the investment in HTS (since the 2G is twice the cost of 1G at the moment). Thus, the two arrangements of the HTS field winding with different placement of the 1G and 2G coils were tested. The 2G coil, $Coil\#6$, with $\sim$15% of I_c reduction has a lower degree of sensitivity to the magnetic field and thereby to the placement in the HTS field winding, compared to the 1G coils (see Fig.5.13). In both arrangements, $Coil\#3$ (the 1G coil) placed closest to the pole shoe was the coil with the lowest I_c, which limited the current of the field winding to $\sim$50 A. However, the significant improvement in the current capacity was observed in the case of $Coil\#5$ (1G coil),when placed in Arr1 (close to the pole shoe), where the coil had $I_c \sim 50$ A but when placed in Arr2 (the middle of the coil stack) an $I_c \geq$80A (see Fig.5.14). Thus, almost 40% (50/80) of the turns of the coil could be omitted if the coil is strategically placed which presents substantial amount of HTS savings. As a general recommendation for combining 1G and 2G tapes in a machine, BSCCO coils should comprise only the inner coils in the field winding stack, whereas YBCO should be used as outer coils.

The second approach towards higher MMF of the HTS field winding, not used in machine design so far, is a multi power supply approach, where the number of current sources is increased so that a coil with large difference between operating and critical current could be utilized better. In the experimental setup each coil had its own power supply which made this configuration highly flexible. Several combinations of currents were supplied to the field winding (each coil separately) and a $\sim$12% increase

in the MMF of the field winding was achieved. The same increase in the MMF was observed using only two power supplies implying that expected increase in the MMF will not scale linearly with the number of power supplies. Due to the fact that both the 1G and 2G HTS have significant sensitivity to magnetic field (including magnetic anisotropy), a HTS coil segments in different field orientation would have different current capabilities. Thus, it is expected that by employing multiple supplies even larger saving would be possible in a large machine. The HTS is (and will for a long time be) the largest contributor to the cost of a HTS machine whereby the reduction of the required amount would easily justify an additional power supply.

Finally, the HTS field winding showed substantial difference between d and q orientations of the armature reaction. While in the d axis, the armature had actually beneficial effect by slightly enhancing the current capacity of the field winding. At the contrast, for the armature reaction in the q axis the reduction of the critical current was the greatest. The difference between I_c of the field winding for no load and rated armature reaction in the q axis was found to be $\sim$20%. From the observed tendency of I_s, the control strategy of the excitation current was proposed with the aim to increase the performance of a HTS machine.

Depending on the degree of difference between the I_c at no load and at full load, substantial reduction of the armature loss can be achieved if the current of the field winding would adjust to the armature reaction in q axis. For 50% of partial load, a $\sim$20% lower loss could be achieved by introducing this control approach assuming the I_c will have the same reduction (20%) as in the case of the Superwind machine. A balance between the ac loss of the HTS generated by the variations of the field current and the armature losses saved by the proposed control will be a limiting factor to how fast load changes which could be followed.

6.2 Afterlife of the Superwind test machine

The work presented in this thesis is the initial step in a larger research effort targeted to develop HTS machines. The learning potential of the constructed experimental setup is very high. Hence, I would like to indentify few of the research directions and opportunities the setup can be used for.

6.2.1 Lowering the operating temperature

The operating temperature of a HTS device has a prevailing impact on its performance. We have so far only conducted experiments at 77 K. However it would be fairly easy, with modest additional funds, to incorporate a closed system conduction cooling where the cooling would be performed by a commercial cryocooler. This could be done by construction of an appropriate lid for the cryostat top. The expected net heat load of the machine (based on the thermal calculation performed in Ch.4) would not exceed 50 W even at 20 K, hence one cryocooler would suffice.

The motivation for lowering the temperature stems from the fact that the HTS tapes have an order of magnitude higher I_c at 20 K than at 77 K. Hence, with just four coils (from Arr1) cooled down at 20 K, the MMF coils would be able to generate would correspond to the $\geq$ 80k Amp –turns. Consecutively, resulting air gap flux would exceed $\sim$1.5 T in the machine has cold steel or would be $\sim$0.5 T in the case of air core machine. Other characteristics of the HTS are changing with temperature as well such as the degree of magnetic anisotropy (1G tape), thermal conductivity of materials impacting the thermal equilibrium of conductors when quench occurs, etc. Therefore, it is important to investigate these as well at the lower temperature.

6.2.2 HTS ac loss investigation

All experiments with revolving armature will generate an ac component of the flux in the machine, hence it is possible to measure and study ac losses in the machine. The HTS field winding had a number of hall probes integrated into the coils, which allow for flux perturbations to be correlated to the voltage and current of the coil.

Additionally, this study may identify the nature of the ac losses in the machine since this loss is not of the same nature as the one found in an ac application of HTS. In the general case, a dc current with a smaller ac component is flowing through the HTS, whereas the HTS tapes in the machine will be exposed to a dc flux on top of which an ac fluctuation is superposed. None of the analytical studies addressing the HTS ac losses have covered this particular case. Thereby, the only way to assess these would be measurements experiments or FE methods (which must be verified by the measurement). It is noteworthy to mention that an extensive work has been done by a

colleague of mine, Victor M. Rodriguez Zermeno, on FE modeling based on the HTS physics (2G) that could be used to derive the ac losses of the HTS coils and machines.

6.2.3 HST tape types and different coil designs

We have tested three types of HTS tape. Two produced by AMSC performed as expected during the coil manufacturing and testing, whereas 2G tape produced by SuperPower, even though promising a doubling of the engineering current, proved to be challenging in practice (damaged by a thermal stress). Therefore, the importance of both coil design (insulation, winding procedure, condition monitoring, cooling, etc.) and HTS choice is emphasized throughout this thesis.

A number of HTS conductors are expected to become available in the future. The tapes from different manufacturers, employing different production techniques, may have different characteristics (mechanical, thermal, electrical, etc.). As the implications of these could challenge the coil fabrication, as we found to be the case with SuperPower 2G tape, it is crucial to examine and test various concepts and types of HTS tapes.

References

[1] American Superconductor Inc. Technical report, http://www.amsc.com/. xix, 10, 13, 14, 15, 34, 73, 137

[2] SuperPower Inc. Technical report, http://www.superpower-inc.com/. xix, 13, 15, 34, 73

[3] G. Klaus, M. Wilke, J. Frauenhofer, W. Nick, and H.-W. Neumuller. **Design Challenges and Benefits of HTS Synchronous Machines**. In *Proc. IEEE Power Engineering Society General Meeting*, pages 1–8, 2007. 1, 170

[4] N. Mijatovic, A.B. Abrahamsen, C. Træholt, E. Seiler, M. Henriksen, V.M. Rodriguez-Zermeno, and N.F. Pedersen. **Superconducting generators for wind turbines: Design considerations**. In *Journal of Physics: Conference Series*, **234**, page 032038. IOP Publishing, 2010. 1, 36, 170

[5] A.B. Abrahamsen, B.B. Jensen, E. Seiler, N. Mijatovic, V.M. Rodriguez-Zermeno, N.H. Andersen, and J. Østergård. **Feasibility study of 5 MW superconducting wind turbine generator**. *Physica C: Superconductivity*, 2011. 1, 71, 170

[6] H.K. Onnes. **Investigations into the properties of substances at low temperatures, which have led, amongst other things, to the preparation of liquid helium**. *Nobel Lecture*, pages 333–335, 1913. 6, 7

[7] Department of Energy Basic Energy Sciences. http://science.energy.gov/. 6

[8] J.G. Bednorz and K.A. Müller. **Possible highT c superconductivity in the Ba- La- Cu- O system**. *Zeitschrift für Physik B Condensed Matter*, **64**(2):189–193, 1986. 6

[9] A. Khurana. **Bednorz and Müller Win Nobel Prize for New Superconducting Materials**. *Physics Today*, **40**:17, 1987. 6

[10] T.P. Sheahen. *Introduction to high-temperature superconductivity*. Plenum, New York, NY (United States), 1994. 6, 7, 8

[11] MK Wu, JR Ashburn, CJ Torng, P.H. Hor, RL Meng, L. Gao, Z.J. Huang, YQ Wang, and CW Chu. **Superconductivity at 93 K in a new mixed-phase Y-Ba-Cu-O compound system at ambient pressure**. *Physical Review Letters*, **58**(9):908–910, 1987. 6

REFERENCES

[12] A. Mourachkine. *Room-temperature superconductivity*. Cambridge International Science Publishi, 2004. 6

[13] DG Hinks, H. Claus, and JD Jorgensen. **The complex nature of superconductivity in MgB2 as revealed by the reduced total isotope effect**. *Nature*, **411**(6836):457–460, 2001. 6

[14] GF Chen, Z. Li, D. Wu, G. Li, WZ Hu, J. Dong, P. Zheng, JL Luo, and NL Wang. **Superconductivity at 41 K and Its Competition with Spin-Density-Wave Instability in Layered CeO_ {1-x} F_ {x} FeAs**. *Physical review letters*, **100**(24):247002, 2008. 6

[15] D.G. Fink, H.W. Beaty, and H.W. Beaty. *Standard handbook for electrical engineers*. McGraw-Hill, 1993. 7

[16] D. Fishlock. *GUIDE TO SUPERCONDUCTIVITY*. 1970, 1969. 7

[17] RD Parks and M. Tinkham. *Superconductivity Vols. 1, 2*, **23**. 1970. 7

[18] H. Suhl, BT Matthias, and LR Walker. **Bardeen-Cooper-Schrieffer theory of superconductivity in the case of overlapping bands**. *Physical Review Letters*, **3**(12):552–554, 1959. 7

[19] J. Bardeen, L.N. Cooper, and J.R. Schrieffer. **Theory of superconductivity**. *Physical Review*, **108**(5):1175, 1957. 7

[20] J.R. Schrieffer and J.S. Brooks. *Handbook of high-temperature superconductivity: theory and experiment*. Springer Verlag, 2007. 8, 10

[21] MD Sumption, M. Bhatia, M. Rindfleisch, M. Tomsic, and EW Collings. **Transport properties of multifilamentary, in situ route, Cu-stabilized MgB2 strands: one metre segments and the Jc (B, T) dependence of short samples**. *Superconductor Science and Technology*, **19**:155, 2006. 9, 90

[22] B. Seeber. *Handbook of Applied Superconductivity: Applications*, **2**. Taylor & Francis, 1998. 10, 95

[23] A.V. Narlikar. *Frontiers in superconducting materials*. Springer Verlag, 2005. 10

[24] M. Kikuchi, T. Kato, K. Ohkura, N. Ayai, J. Fujikami, K. Fujino, S. Kobayashi, E. Ueno, K. Yamazaki, S. Yamade, et al. **Recent development of drastically innovative BSCCO wire** $(DI - BISCCO)$. *Physica C: Superconductivity*, **445**:717–721, 2006. 10

[25] Sumitomo Electric Industries. Technical report, http://global-sei.com. 10, 11

[26] Bruker Energy & Supercon Technologies. Technical report, http://www.bruker-est.com/. 10

[27] Zenergy Power. Technical report, http://www.zenergypower.com/. 10

[28] Asger Bech Abrahamsen. **Superconductor based energy production**. In *Materialer og energi*, pages 131–150, Lyngby, 2008. DMS. 12, 13, 14

[29] P. Paturi, T. Kulmala, J. Raittila, J.C. Grivel, R. Laiho, and NH Andersen. **Texture of YBCO/Ag PIT-tapes**. *Physica C: Superconductivity*, **408**:935–936, 2004. 12

[30] DA Korzekwa, JF Bingert, EJ Podtburg, and P. Miles. **Deformation processing of wires and tapes using the oxide powder in tube method**. *Applied superconductivity*, **2**(3-4):261–270, 1994. 12

[31] DK Finnemore, KE Gray, MP Maley, DO Welch, DK Christen, and DM Kroeger. **Coated conductor development: an assessment**. *Physica C: Superconductivity*, **320**(1-2):1–8, 1999. 12

[32] A. GOYAL, M. Parans Paranthaman, and U. Schoop. **The RABiTS approach: Using rolling-assisted biaxially textured substrates for high-performance YBCO superconductors**. *MRS bulletin*, **29**(8):552–561, 2004. 12

[33] MW Rupich, U. Schoop, DT Verebelyi, C. Thieme, W. Zhang, X. Li, T. Kodenkandath, N. Nguyen, E. Siegal, D. Buczek, et al. **YBCO coated conductors by an MOD / RABiTS process**. *Applied Superconductivity, IEEE Transactions on*, **13**(2):2458–2461, 2003. 12, 13

[34] P.J. Martin, H.A. MacLeod, R.P. Netterfield, CG Pacey, and W.G. Sainty. **Ion beam assisted deposition of thin films**. *Applied Optics*, **22**(1):178–184, 1983. 13

[35] Y. Jung, C.J. Sheehan, J.Y. Coulter, V. Matias, and D. Youm. **Pushing Coated Conductor Critical Currents Beyond 1 kA per cm Width: Stacks of YBCO Layers**. *Applied Superconductivity, IEEE Transactions on*, (99):1–1. 13

[36] SR Foltyn, QX Jia, PN Arendt, L. Kinder, Y. Fan, and JF Smith. **Relationship between film thickness and the critical current of YBaCuO-coated conductors**. *Applied Physics Letters*, **75**:3692, 1999. 13

[37] MP Siegal, PG Clem, JT Dawley, RJ Ong, MA Rodriguez, and DL Overmyer. **All solution chemistry approach for YBaCuO coated conductors**. *Applied physics letters*, **80**:2710, 2002. 13

[38] V. Boffa, G. Celentano, L. Ciontea, F. Fabbri, V. Galluzzi, U. Gambardella, G. Grimaldi, A. Mancini, and T. Petrisor. **Influence of film thickness on the critical current of $YBa2Cu3O7 - x$ thick films on Ni-V biaxially textured substrates**. *Applied Superconductivity, IEEE Transactions on*, **11**(1):3158–3161, 2001. 13

[39] THEVA. http://www.theva.com/infobase/publikationen. 14

[40] MW Rupich, U. Schoop, DT Verebelyi, CLH Thieme, D. Buczek, X. Li, W. Zhang, T. Kodenkandath, Y. Huang, E. Siegal, et al. **The development of second generation HTS wire at American Superconductor**. *Applied Superconductivity, IEEE Transactions on*, **17**(2):3379–3382, 2007. 14

REFERENCES

[41] A.B. Abrahamsen, N. Mijatovic, E. Seiler, T. Zirngibl, C. Træholt, P.B. Nørgård, N.F. Pedersen, N.H. Andersen, and J. Østergaard. **Superconducting wind turbine generators**. *Superconductor Science and Technology*, **23**:034019, 2010. 14, 162, 163, 167, 168, 170

[42] T. Kagiyama, K. Yamazaki, M. Kikuchi, S. Yamade, T. Nakashima, S. Kobayashi, K. Hayashi, K. Sato, J. Shimoyama, M. Inoue, et al. **Recent Progress in High Performance Ag-Sheathed Bi2223 Wire (DI-BSCCO)**. In *IOP Conference Series: Materials Science and Engineering*, **18**, page 152001. IOP Publishing, 2011. 14

[43] C. Lewis and J. Muller. **A direct drive wind turbine HTS generator**. In *Power Engineering Society General Meeting, 2007. IEEE*, pages 1–8. IEEE, 2007. 14, 166

[44] V. Selvamanickam, Y. Chen, X. Xiong, Y.Y. Xie, M. Martchevski, A. Rar, Y. Qiao, R.M. Schmidt, A. Knoll, K.P. Lenseth, et al. **High performance 2G wires: From R&D to pilot-scale manufacturing**. *Applied Superconductivity, IEEE Transactions on*, **19**(3):3225–3230, 2009. 14, 15

[45] M.W. Rupich, X. Li, C. Thieme, S. Sathyamurthy, S. Fleshler, D. Tucker, E. Thompson, J. Schreiber, J. Lynch, D. Buczek, et al. **Advances in second generation high temperature superconducting wire manufacturing and R&D at American Superconductor Corporation**. *Superconductor Science and Technology*, **23**:014015, 2010. 14

[46] A. B. Abrahamsen, N. Mijatovic, E. Seiler, M. P. Sorensen, M. Koch, P. B. Norgard, N. F. Pedersen, C. Traeholt, N. H. Andersen, and J. Ostergard. **Design Study of 10 kW Superconducting Generator for Wind Turbine Applications**. *IEEE-J-ASC*, **19**(3):1678–1682, 2009. 15

[47] The Silver Institute. http://www.silverinstitute.org/2000pres.php. 15

[48] M. Humphries. *Rare Earth Elements: The Global Supply Chain*. DIANE Publishing, 2010. 15, 170, 171

[49] SR Foltyn, L. Civale, JL MacManus-Driscoll, QX Jia, B. Maiorov, H. Wang, and M. Maley. **Materials science challenges for high temperature superconducting wire**. *Nature materials*, **6**(9):631–642, 2007. 16

[50] P.N. Barnes, M.D. Sumption, and G.L. Rhoads. **Review of high power density superconducting generators: Present state and prospects for incorporating YBCO windings**. *Cryogenics*, **45**(10-11):670–686, 2005. 17, 28

[51] CJ Oberhauser and HR Kinner. **SOME CONSIDERATIONS IN THE DESIGN OF A SUPERCONDUCTING ALTERNATOR.** Technical report, Dynatech Corp., Cambridge, Mass., 1967. 17

[52] A. Hughes and TJE Miller. **Analysis of fields and inductances in air-cored and iron-cored synchronous machines**. *Proc. IEE*, **124**(2):121–126, 1977. 19, 36, 37, 39, 41

[53] TJE Miller and A. Hughes. **Comparative design and performance analysis of air-cored and iron-cored synchronous machines**. *Proc. IEE*, **124**(2):127–132, 1977. 19, 36, 39

[54] S.S. Kalsi. *Applications of High Temperature Superconductors to Electric Power Equipment*. Wiley-IEEE Press, 2011. 19, 23, 24, 25, 27

[55] J.M. Fogarty. **Development of a 100 MVA high temperature superconducting generator**. In *Power Engineering Society General Meeting, 2004. IEEE*, pages 2065–2067. IEEE, 2004. 20, 21

[56] L. Li, T. Zhang, W. Wang, J. Alexander, X. Huang, K. Sivasubramaniam, ET Laskaris, JW Bray, and JM Fogarty. **Quench test of HTS coils for generator application at GE**. *Applied Superconductivity, IEEE Transactions on*, **17**(2):1575–1578, 2007. 21, 42

[57] JA Urbahn, RA Ackermann, X. Huang, ET Laskaris, K. Sivasubramaniam, and A. Steinbach. **The thermal performance of a 1.5 MVA HTS generator**. In *AIP Conference Proceedings*, **710**, page 849, 2004. 21

[58] S.S. Kalsi, K. Weeber, H. Takesue, C. Lewis, H.W. Neumueller, and R.D. Blaugher. **Development status of rotating machines employing superconducting field windings**. *Proceedings of the IEEE*, **92**(10):1688–704, 2004. 21, 23, 28

[59] P. Tixador. **Development of superconducting power devices in Europe**. *Physica C: Superconductivity*, **470**(20):971–979, 2010. 21

[60] L. SANFORD. **German hydro plant is the first to install an HTS generator**. *Modern power systems*, (GERMANY):22–23, 2007. 21

[61] R. Fair, C. Lewis, J. Eugene, and M. Ingles. **Development of an HTS hydroelectric power generator for the hirschaid power station**. In *Journal of Physics: Conference Series*, **234**, page 032008. IOP Publishing, 2010. 21

[62] B. Grzesik, M. Stepien, K. Bodzek, R. Fair, and M. Ingles. **Tests of a vacuum gauge for an HTS hydrogenerator**. In *Power Electronics and Motion Control Conference (EPE/PEMC), 2010 14th International*, pages T15–13. IEEE. 21

[63] B.B. Gamble, S. Kalsi, G. Snitchler, D. Madura, and R. Howard. **The status of HTS motors**. In *Power Engineering Society Summer Meeting, 2002 IEEE*, **1**, pages 270–274. IEEE. 22, 24, 28, 182

[64] M. Frank, J. Frauenhofer, P. Van Hasselt, W. Nick, H.W. Neumueller, and G. Nerowski. **Long-term operational experience with first siemens 400 kW HTS machine in diverse configurations**. *Applied Superconductivity, IEEE Transactions on*, **13**(2):2120–2123, 2003. 22, 23, 42

[65] J. Frauenhofer, J. Grundmann, G. Klaus, and W. Nick. **Basic concepts, status, opportunities, and challenges of electrical machines utilizing high-temperature superconducting (HTS) windings**. In *Journal of Physics: Conference Series*, **97**, page 012189. IOP Publishing, 2008. 22, 23, 28, 29, 181, 182

[66] JP Voccio, BB Gamble, CB Prum, and HJ Picard. **125 HP HTS motor field winding development**. *Applied Superconductivity, IEEE Transactions on*, **7**(2):519–522, 1997. 23

[67] D. Aized, BB Gamble, A. Sidi-Yekhlef, JP Voccio, DI Driscoll, BA Shoykhet, and BX Zhang. **Status of the 1000 HP HTS motor development**. *Applied Superconductivity, IEEE Transactions on*, **9**(2):1197–1200, 1999. 23

[68] G. Papst, BB Gamble, AJ Rodenbush, and R. Schöttler. **Development of synchronous motors and generators with HTS field windings**. *Superconductor Science and Technology*, **10**:924, 1997. 23

[69] HW Neumüller, W. Nick, B. Wacker, M. Frank, G. Nerowski, J. Frauenhofer, W. Rzadki, and R. Hartig. **Advances in and prospects for development of high-temperature superconductor rotating machines at Siemens**. *Superconductor Science and Technology*, **19**:S114, 2006. 23

[70] W. Nick, M. Frank, G. Klaus, J. Frauenhofer, and H.W. Neumuller. **Operational Experience With the World's First 3600 rpm 4 MVA Generator at Siemens**. *Applied Superconductivity, IEEE Transactions on*, **17**(2):2030–2033, 2007. 23, 24, 40, 42

[71] M. Wilke, K. Schleicher, G. Klaus, W. Nick, H.W. Neumuller, J. Frauenhofer, K. Kahlen, and R. Hartig. **Numerical calculations for high-temperature superconducting electrical machines**. In *Electrical Machines, 2008. ICEM 2008. 18th International Conference on*, pages 1–6. IEEE. 23

[72] A.P. Malozemoff. **The new generation of superconductor equipment for the electric power grid**. *Applied Superconductivity, IEEE Transactions on*, **16**(1):54–58, 2006. 24

[73] S.S. Kalsi, D. Madura, and M. Ingram. **Superconductor synchronous condenser for reactive power support in an electric grid**. *Applied Superconductivity, IEEE Transactions on*, **15**(2):2146–2149, 2005. 24

[74] SS Kalsi, BB Gamble, G. Snitchler, and SO Ige. **The status of HTS ship propulsion motor developments**. In *Power Engineering Society General Meeting, 2006. IEEE*, pages 5–pp. IEEE, 2006. 24, 40

[75] J. Buck, B. Hartman, R. Ricket, B. Gamble, T. MacDonald, and G. Snitchler. **Factory testing of a 36.5 MW high temperature superconducting propulsion motor**. *Fuel Tank to Target: Building the Electric Fighting Ship at American Society of Naval Engineers Day 2007*. 24, 40

[76] H. Wen, W. Bailey, M.K. Al-Mosawi, K. Goddard, C. Beduz, and Y. Yang. **Further Testing of an Iron-Cored HTS Synchronous Generator Cooled by Liquid Air**. *Applied Superconductivity, IEEE Transactions on*, (99):1–1. 24

[77] H. Wen, W. Bailey, K. Goddard, M. Al-Mosawi, C. Beduz, and Y. Yang. **Performance test of a 100 kW HTS generator operating at 67 K–77 K**. *Applied Superconductivity, IEEE Transactions on*, **19**(3):1652–1655, 2009. 24, 40, 41

[78] K.F. Goddard, B. Lukasik, and J.K. Sykulski. **Alternative designs of a superconducting synchronous generator: the Southampton approach**. In *Electrical Machines, 2008. ICEM 2008. 18th International Conference on*, pages 1–6. IEEE. 24

[79] MK Al-Mosawi, W. Bailey, C. Beduz, K. Goddard, and Y. Yang. **Development of a coreless HTS synchronous generator operating at sub-cooled liquid nitrogen temperatures**. In *Journal of Physics: Conference Series*, **97**, page 012205. IOP Publishing, 2008. 24

[80] MK Al-Mosawi, K. Goddard, C. Beduz, and Y. Yang. **Coreless HTS synchronous generator operating at liquid nitrogen temperatures**. *Applied Superconductivity, IEEE Transactions on*, **17**(2):1599–1602, 2007. 24

[81] YK Kwon, SK Baik, EY Lee, JD Lee, YC Kim, TS Moon, HJ Park, WS Kwon, SH Lee, JP Hong, et al. **Status of HTS Motor Development in Korea**. In *Power Engineering Society General Meeting, 2007. IEEE*, pages 1–5. IEEE. 24

[82] YK Kwon, HM Kim, SK Baik, EY Lee, JD Lee, YC Kim, SH Lee, JP Hong, YS Jo, and KS Ryu. **Performance test of a 1 MW class HTS synchronous motor for industrial application**. *Physica C: Superconductivity*, **468**(15-20):2081–2086, 2008. 24, 28

[83] YK Kwon, SK Baik, EY Lee, JD Lee, JM Kim, YC Kim, TS Moon, HJ Park, WS Kwon, JP Hong, et al. **Status of HTS motor development for industrial applications at KERI & DOOSAN**. *Applied Superconductivity, IEEE Transactions on*, **17**(2):1587–1590, 2007. 24, 25

[84] C. Lewis. **Direct drive superconducting wind generators**. *Wind Power Generation and Wind Turbine Design*, page 303, 2010. 25

[85] AMSC. http://www.amsc.com/documents/displaypdf.php?id=7516. 25

[86] P. Tixador, Y. Brunet, P. Vedrine, Y. Laumond, and JL Sabrie. **Electrical tests on a fully superconducting synchronous machine**. *Magnetics, IEEE Transactions on*, **27**(2):2256–2259, 1991. 25

[87] I. Muta, H. Tsukiji, T. Hoshino, and E. Mukai. **Electrical characteristics of fully superconducting synchronous generator in persistent excitation mode**. *Magnetics, IEEE Transactions on*, **28**(1):434–437, 1992. 25

[88] Y. Jiang, R. Pei, Q. Jiang, Z. Hong, and TA Coombs. **Control of a superconducting synchronous motor**. *Superconductor Science and Technology*, **20**:392, 2007. 25

[89] P. Tixador and H. Daffix. **Conceptual design of an electrical machine with both low and high T c superconductors**. *Applied Superconductivity, IEEE Transactions on*, **7**(4):3858–3865, 1997. 25

[90] MP Oomen, R. Nanke, and M. Leghissa. **Modelling and measurement of ac loss in BSCCO/Ag-tape windings**. *Superconductor Science and Technology*, **16**:339, 2003. 25

[91] S. Fukui, T. Noguchi, J. Ogawa, M. Yamaguchi, T. Sato, O. Tsukamoto, and T. Takao. **Numerical study on AC loss minimization of multi-layer tri-axial HTS cable for 3-phase AC power transmission**. *Applied Superconductivity, IEEE Transactions on*, **17**(2):1700–1703, 2007. 25

[92] Advance Magnetic Lab. http://www.magnetlab.com/energy/electrical-machinery/. 25

[93] J. Sim, K. Lee, G. Cha, and J.K. Lee. **Development of a HTS squirrel cage induction motor with HTS rotor bars**. *Applied Superconductivity, IEEE Transactions on*, **14**(2):916–919, 2004. 26

[94] CL Goodzeit, RB Meinke, and MJ Ball. **A superconducting induction motor using double-helix dipole coils**. *Applied Superconductivity, IEEE Transactions on*, **13**(2):2235–2238, 2003. 26

[95] G. Morita, T. Nakamura, and I. Muta. **Theoretical analysis of a YBCO squirrel-cage type induction motor based on an equivalent circuit**. *Superconductor Science and Technology*, **19**:473, 2006. 26

[96] T. Konishi, T. Nakamura, T. Nishimura, and N. Amemiya. **Analytic Evaluation of HTS Induction Motor for Electric Rolling Stock**. *Applied Superconductivity, IEEE Transactions on*, (99):1–1. 26

[97] J. Sim, M. Park, H. Lim, G. Cha, J. Ji, and J. Lee. **Test of an induction motor with HTS wire at end ring and bars**. *Applied Superconductivity, IEEE Transactions on*, **13**(2):2231–2234, 2003. 26

[98] B. Oswald, KJ Best, M. Setzer, M. Söll, W. Gawalek, A. Gutt, L. Kovalev, G. Krabbes, L. Fisher, and HC Freyhardt. **Reluctance motors with bulk HTS material**. *Superconductor Science and Technology*, **18**:S24, 2005. 26

[99] B. Oswald, K.J. Best, M. Setzer, M. Söll, W. Gawalek, A. Gutt, L. Kovalev, L. Fisher, G. Krabbes, and HC Freyhardt. **Optimization of Our SC HTS Reluctance Motor**. In *AIP Conference Proceedings*, **711**, page 879, 2004. 26

[100] P. Campbell. **Principles of a permanent-magnet axial-field DC machine**. *Proc. IEE*, **121**(12):1489–1494, 1974. 26

[101] B.W. Strohm. **Voltage homopolar machine**, September 19 1995. US Patent 5,451,825. 26

[102] AD Appleton. **Superconducting dc machines**. *Superconducting Machines and Devices: Large Systems Applications*, **1**:219–277, 1974. 27

[103] T. Curcic and S.A. Wolf. **Superconducting hybrid power electronics for military systems**. *Applied Superconductivity, IEEE Transactions on*, **15**(2):2364–2369, 2005. 27

[104] J.G. Weisend et al. *Handbook of cryogenic engineering*. Taylor & Francis Philadelphia, PA, 1998. 27

[105] M.K. Al-Mosawi, C. Beduz, and Y. Yang. **Construction of a 100 kVA high temperature superconducting synchronous generator**. *Applied Superconductivity, IEEE Transactions on*, **15**(2):2182–2185, 2005. 28, 30, 67

[106] S.W. Van Sciver. **Cryogenic systems for superconducting devices**. *Physica C: Superconductivity*, **354**(1-4):129–135, 2001. 28

[107] T.M. Flynn and Inc NetLibrary. *Cryogenic engineering*. Marcel Dekker New York, 1997. 28, 55, 57, 65, 67, 68

[108] R.A. Ackermann, K.G. Herd, and W.E. Chen. **Advanced Cryocooler Cooling for MRI Systems**. *Cryocoolers 10*, pages 857–867, 2002. 28

[109] CryoMech. http://www.cryomech.com/AL325.php. 28

[110] CryoMech. http://www.cryomech.com/PT63.php. 29

[111] R. Radebaugh. **Development of the pulse tube refrigerator as an efficient and reliable cryocooler**. *Proc. Institute of Refrigeration (London)*, **2000**, 1999. 29

[112] J. Ko, S. Jeong, H. Kim, J. Jung, J. Choi, S. In, M. Sohn, and Y.K. Kwon. **Rotating Cryocooler for Superconducting Motor**. In *AIP Conference Proceedings*, **823**, page 653, 2006. 29

[113] JM Poncet, A. Ravex, and I. Charles. **Developments on single and double stage GM type pulse tube cryorefrigerators**. *Cryocoolers 11*, pages 229–233, 2002. 29

[114] J.L. Kirtley Jr, J.L. Smith Jr, and S.D. Umans. **Cryogenic isolating torque tubes for a superconducting generator-detailed model and performance analysis**. *Energy Conversion, IEEE Transactions on*, **6**(2):267–273, 1991. 30

[115] TE Laskaris and KF Schoch. **Superconducting rotor development for a 20 MVA generator**. *Power Apparatus and Systems, IEEE Transactions on*, (6):2031–2039, 1980. 30

[116] A. Ueda. **Rotor for a superconducting rotating electric machine**, April 14 1987. US Patent 4,658,170. 30

[117] K.J. Baumann. **Flexible coupling for rotor elements of a superconducting generator**, September 26 1978. US Patent 4,117,357. 30

[118] W.O.S. Bailey, M. Al-Mosawi, Y. Yang, K. Goddard, and C. Beduz. **The design of a lightweight HTS synchronous generator cooled by subcooled liquid nitrogen**. *Applied Superconductivity, IEEE Transactions on*, **19**(3):1674–1677, 2009. 30, 67

[119] P. Kummeth, M. Frank, W. Nick, G. Nerowski, and H.W. Neumueller. **Development of synchronous machines with HTS rotor**. *Physica C: Superconductivity*, **426**:1358–1364, 2005. 30, 40

[120] B.B. Gamble and G.L. Snitchler. **Superconducting synchronous motor construction**, July 7 1998. US Patent 5,777,420. 31

[121] B.A. Shoykhet. **Composite torque tube for superconducting motor**, October 10 2000. US Patent 6,129,477. 31

[122] J. Dewolf. *Mechanics Of Materials (In Si Units)*. McGraw-Hill Education (India) Pvt Ltd, 2004. 32

[123] M.Yazdanian, P.Erhaminia, M.RZolghadri, and M.Fardmanesh. **Investigation of iron-cored Structure in HTS Synchronous Machine for Industrial Application**, 2011. Presented at conference. 38

[124] P. Kundur, N.J. Balu, and M.G. Lauby. *Power system stability and control*, **141**. McGraw-Hill New York, 1994. 39, 134

[125] M. Beckenbach, F. Hornung, M. Klaser, P. Leys, B. Lott, and T. Schneider. **Manufacture and test of a 5 T Bi-2223 insert coil**. *Applied Superconductivity, IEEE Transactions on*, **15**(2):1484–1487, 2005. 42

[126] J.R. Miller. **The NHMFL 45-T hybrid magnet system: Past, present, and future**. *Applied Superconductivity, IEEE Transactions on*, **13**(2):1385–1390, 2003. 42, 44

[127] D.W. Hazelton, V. Selvamanickam, J.M. Duval, D.C. Larbalestier, W.D. Markiewicz, H.W. Weijers, and R.L. Holtz. **Recent developments in 2G HTS coil technology**. *Applied Superconductivity, IEEE Transactions on*, **19**(3):2218–2222, 2009. 43

[128] A. Ghattas, M. Annabi, M. Zouaoui, F.B. Azzouz, and M.B. Salem. **Flux pinning by Al-based nano particles embedded in polycrystalline (Bi, Pb)-2223 superconductors**. *Physica C: Superconductivity*, **468**(1):31–38, 2008. 43

[129] A. Korpela, J. Lehtonen, R. Mikkonen, and R. Perälä. **Temperature dependent current-voltage characteristics of an HTS coil having a poor resistive joint**. *Physica C: Superconductivity*, **386**:457–461, 2003. 44

[130] M. Kang, K. Lee, G. Cha, and H. Lee. **Design Method of a High Field HTS Magnet Consisting of Pancake Windings Having Different Current in Each Pancake Winding**. *Applied Superconductivity, IEEE Transactions on*, **18**(2):1537–1540, 2008. 44

[131] K. Lee, M. Kang, G. Cha, H. Lim, and T. Ahn. **Properties of an HTS magnet with pancake windings excited by multiple power sources**. *Applied Superconductivity, IEEE Transactions on*, **18**(2):1533–1536, 2008. 44

[132] V. Cavaliere, M. Cioffi, A. Formisanao, and R. Martone. **Shape optimization of high Tc superconducting magnets**. *Magnetics, IEEE Transactions on*, **38**(2):1129–1132, 2002. 45

[133] N. Mijatovic, B. B. Jensen, A. B. Abrahamsen, V. M. R. Zermeno, C. Traeholt, and N. F. Pedersen. **Coil Optimization for High Temperature Superconductor Machines**. *IEEE-J-ASC*, **21**(3):1136–1140, 2011. 46, 123

[134] Comsol. **http://www.comsol.com/products/multiphysics/**, 2011. 46

[135] 24-Bit Universal AI NI 9239. http://sine.ni.com/nips/cds/view/p/lang/en/nid/208797. 51

[136] 24-Bit Universal AI NI 9219. http://sine.ni.com/nips/cds/view/p/lang/en/nid/208789. 51

[137] Koyo Bearing. http://www.danskkuglelejecenter.dk/koyolejer3.html. 52

[138] Danffoss Serial No.131b1673. http://www.danfoss.com/Denmark. 52

[139] P. Beckley. *Electrical steels for rotating machines*. Number 37. Inst of Engineering & Technology, 2002. 52

[140] Rogowski current transducer CWT015. http://www.powertekuk.com/cwtmini.htm. 53

[141] Juha Pyrhnen, Tapani Jokinen, and Valria Hrabovcov. *Design of rotating electrical machines*, pages i–xxv. John Wiley & Sons, Ltd, 2008. 53

[142] F.P. Incropera and D.P. De Witt. *Fundamentals of heat and mass transfer*. John Wiley and Sons Inc., New York, NY, 1985. 55

[143] F. Incropera and D. DeWitt. *Introduction to heat transfer*. John Wiley and Sons Inc., New York, NY, 1985. 55

[144] JE Fesmire. **Aerogel insulation systems for space launch applications**. *Cryogenics*, **46**(2-3):111–117, 2006. 55, 62

[145] D. Hull and TW Clyne. *An introduction to composite materials*. Cambridge Univ Pr, 1996. 57

[146] Aage Lystrup. **Typical properties of fibre composites:For preliminary design of fibre composite components for super conductor wind turbine generator**. Technical report, Ris National Laboratory for Sustainable Energy, Technical University of Denmark, Roskilde, Denmark,December 2008, Ris-I-2789(EN), 2008. 57

[147] DK Hale. **The physical properties of composite materials**. *Journal of Materials Science*, **11**(11):2105–2141, 1976. 57

[148] R.L. Tobler and D.T. Read. **Fatigue resistance of a uniaxial S-glass/epoxy composite at room and liquid helium temperatures**. *Journal of Composite Materials*, **10**(1):32, 1976. 57

[149] M. Surendra Kumar, N. Chawla, A. Priyadarsini, I. Mishra, and BC Ray. **Assessment of microstructural integrity of glass/epoxy composites at liquid nitrogen temperature**. *Journal of reinforced plastics and composites*, **26**(11):1083, 2007. 57

[150] W. Meeks and Y. Zlobinsky. **Vacuum drying system with cryopumping of solvent recovery feature**, November 23 1993. US Patent 5,263,268. 62

[151] HK Yeom, YJ Hong, SJ Park, TB Seo, KC Seong, and HJ Kim. **Study of cryogenic conduction cooling systems for an HTS SMES**. *Applied Superconductivity, IEEE Transactions on*, **17**(2):1955–1958, 2007. 62

[152] K.D. Timmerhaus. *Advances in cryogenic engineering*, **39**. Plenum Publishing Corporation, 1994. 62, 68

[153] **http://www.ruag.com/en/Space/Products/**. 68

[154] HBM UB9 500N. http://www.hbm.com/en/geoipcn=2. 80

[155] HOA 0901 012. http://sensing.honeywell.com/index.cfm/ciid/154366/laid/1.htm. 83

[156] C.P. Poole. *Handbook of superconductivity*. Academic Press, 2000. 90

[157] Y. Iwasa. *Case studies in superconducting magnets: design and operational issues*. Springer Verlag, 2009. 90

[158] L. Dresner. **Quench energies of potted magnets**. *Magnetics, IEEE Transactions on*, **21**(2):392–395, 1985. 90

[159] F. Trillaud, M.C. Ahn, J. Bascunan, W.S. Kim, J.P. Voccio, and Y. Iwasa. **Quench behavior, quench protection of a YBCO test coil assembly**. *Applied Superconductivity, IEEE Transactions on*, **18**(2):1329–1332, 2008. 90, 94

[160] SX Dou, HK Liu, MH Apperley, KH Song, and CC Sorrell. **Critical current density in superconducting Bi-Pb-Sr-Ca-Cu-O wires and coils**. *Superconductor Science and Technology*, **3**:138, 1990. 90

[161] T.P. Sheahen. **Introduction to high-temperature superconductivity**. *????????*, 1994. 95

[162] V. M. Rodriguez-Zermeno, N. Mijatovic, C. Traeholt, T. Zirngibl, E. Seiler, A. B. Abrahamsen, N. F. Pedersen, and M. P. Sorensen. **Towards Faster FEM Simulation of Thin Film Superconductors: A Multiscale Approach**. *IEEE-J-ASC*, **21**(3):3273–3276, 2011. 96

[163] European Commission Energy. **Energy infrastructure priorities for 2020 and beyond - A Blueprint for an integrated European energy network**. Technical report, http://ec.europa.eu/energy/observatory. 160, 161, 167

[164] C. Breidenich, D. Magraw, A. Rowley, and J.W. Rubin. **The Kyoto Protocol to the United Nations Framework Convention on Climate Change**. *The American Journal of International Law*, **92**(2):315–331, 1998. 160

[165] J.P. Weyant and J. Hill. **The costs of the kyoto protocol**. *The Energy Journal (Special Issue)*, 1999. 160

[166] D. Bodansky. **The Copenhagen Climate Change Conference**. *American Journal of International Law*, **104**(2):230–240, 2010. 160

[167] AR IPCC. **Intergovernmental Panel on Climate Change**. 2007. 161

[168] European Environmental Agency Technical report. **Europe's onshore and offshore wind energy potential - An assessment of environmental and economic constraints**. Technical report, http://ec.europa.eu/energy/observatory. 161, 162

[169] T. Burton. *Wind energy: handbook*. Wiley, 2001. 162, 164

[170] T. Ackermann and J. Wiley. *Wind power in power systems*, **140**. Wiley Online Library, 2005. 163, 164, 165

[171] Vladislav Akhmatov. *Induction Generators for Wind Power*. Multi Science Publishing Co Ltd, 2009. 163, 164, 165

[172] E. Muljadi and CP Butterfield. **Pitch-controlled variable-speed wind turbine generation**. *Industry Applications, IEEE Transactions on*, **37**(1):240–246, 2001. 163, 164

[173] Q. Wang and L. Chang. **An intelligent maximum power extraction algorithm for inverter-based variable speed wind turbine systems**. *Power Electronics, IEEE Transactions on*, **19**(5):1242–1249, 2004. 163

[174] KH Bergey. **The Lanchester-Betz limit**. *Journal of Energy*, **3**:382–384, 1979. 164

[175] H. Li and Z. Chen. **Overview of different wind generator systems and their comparisons**. *Renewable Power Generation, IET*, **2**(2):123–138, 2008. 166, 170

[176] H. Li, Z. Chen, and H. Polinder. **Optimization of multibrid permanent-magnet wind generator systems**. *Energy Conversion, IEEE Transactions on*, **24**(1):82–92, 2009. 166, 169

[177] Henrik Bindner Lars Sondergaard. **Undersogelse af generatorkoncepter til vindmoller - Direkte drevet generator til gearlos vindmolle**. Technical report, Forskningscenter Riso, Roskilde, http://ec.europa.eu/energy/observatory, 1995. 166

[178] S. Eriksson, H. Bernhoff, and M. Leijon. **Evaluation of different turbine concepts for wind power**. *Renewable and Sustainable Energy Reviews*, **12**(5):1419–1434, 2008. 166

[179] H. Polinder, F.F.A. Van der Pijl, G.J. De Vilder, and P.J. Tavner. **Comparison of direct-drive and geared generator concepts for wind turbines**. *Energy conversion, IEEE transactions on*, **21**(3):725–733, 2006. 166, 169

[180] R. Harrison, E. Hau, and H. Snel. *Large wind turbines: design and economics*. Wiley, 2000. 166, 168

[181] European Wind Energy Association. **Offshore statistics 2007 and 2008 European Wind Energy**. Technical report, http://www.ewea.org. 167, 168, 169

[182] European Wind Energy Association. **Pure Power Wind energy targets for 2020 and 2030**. Technical report, http://www.ewea.org/fileadmin/ewea-documents/documents/publications/reports/Pure-Power-Full-Report.pdf. 167

[183] J. Munksgaard and P.E. Morthorst. **Wind power in the Danish liberalised power market–Policy measures, price impact and investor incentives**. *Energy Policy*, **36**(10):3940–3947, 2008. 168

[184] RisøNational Laboratory DTU. **Design limits and solutions for very large wind turbines A 20 MW turbine is feasible**. Technical report, EWEA UP-Wind, http://www.ewec2011.info/fileadmin/ewec2011-files/documents/New-research-shows-20-MW-wind-turbines-are-feasible, 2011. 168

[185] M. Junginger, A. Faaij, and W.C. Turkenburg. **Cost reduction prospects for offshore wind farms**. *Wind Engineering*, **28**(1):97–118, 2004. 168

[186] M. Junginger, A. Faaij, and WC Turkenburg. **Global experience curves for wind farms**. *Energy policy*, **33**(2):133–150, 2005. 168

[187] H. Li and Z. Chen. **Design optimization and site matching of direct-drive permanent magnet wind power generator systems**. *Renewable Energy*, **34**(4):1175–1184, 2009. 169

[188] MA Khan and P. Pillay. **Design of a PM wind generator, optimised for energy capture over a wide operating range**. In *Electric Machines and Drives, 2005 IEEE International Conference on*, pages 1501–1506. IEEE, 2005. 169

[189] Areva. **M5000 Offshore Windpower**. Technical report, Areva, http://www.areva-wind.com/1/M5000/konzept/. 170

[190] Enercon. **E127 7.5MW wind turbine**. Technical report, Enercon, http://www.enercon.de/en-en/66.htm. 170

[191] Y. Chen, P. Pillay, and A. Khan. **PM wind generator topologies**. *Industry Applications, IEEE Transactions on*, **41**(6):1619–1626, 2005. 170

[192] G. Snitchler, B. Gamble, C. King, and P. Winn. **10 MW Class Superconductor Wind Turbine Generators**. *Applied Superconductivity, IEEE Transactions on*, **21**(3):1089 –1092, june 2011. 170

[193] E. Spooner. **Fully slotless turbogenerators**. *Proc. IEE*, **120**(12):1507–1518, 1973. 181, 182

[194] AF Anderson. **Discussion on fully slotless turbo-generators**. *Proc. IEE*, **122**(1):75–79, 1975. 181, 182

[195] R. Hawley. **Future trends in electricity generation**. *Electronics and Power*, **20**(4):134–139, 1974. 181

[196] M. Watanabe, M. Takahashi, N. Takahashi, and T. Tsukui. **Experimental study of a practical airgap winding stator arrangement for large turbine generators**. *IEEE TRANS. POWER APPAR. AND SYS.*, **100**(4):1901–1910, 1981. 181

[197] M. Takahashi, M. Watanabe, N. Takahashi, M. Kitamura, N. Maki, and M. Ooi. **Performance evaluations of 50 MVA airgap winding stator for superconducting generator**. *Energy Conversion, IEEE Transactions on*, **4**(2):264–271, 1989. 181

[198] E Davies. **Airgap windings for large turbogenerators**. *IEE Proceedings*, **118**(3/4):529–535, March/April 1971. 181

[199] G. Klaus, M. Wilke, J. Frauenhofer, W. Nick, and H.W. Neumuller. **Design challenges and benefits of HTS synchronous machines**. In *Power Engineering Society General Meeting, 2007. IEEE*, pages 1–8. IEEE, 2007. 182

[200] A. Krawczyk and S. Wiak. **THE CALCULATION OF RADIAL FORCES EXERTED ON THE STATOR SLOT CONDUCTORS OF SYNCHRONOUS GENERATORS IN STEADY AND TRANSIENT OPERATING STATES**. *Electromagnetic Fields in Electrical Engineering*, page 213, 2002. 182

[201] M. K. Al-Mosawi, K. Goddard, C. Beduz, and Y. Yang. **Coreless HTS Synchronous Generator Operating at Liquid Nitrogen Temperatures**. *Applied Superconductivity, IEEE Transactions on*, **17**(2):1599–1602, 2007. 201

[202] W. Bailey, H. Wen, M. Al-Mosawi, K. Goddard, and Y. Yang. **Testing of a Lightweight Coreless HTS Synchronous Generator Cooled by Subcooled Liquid Nitrogen**. *Applied Superconductivity, IEEE Transactions on*, (99):1–1. 201

Appendix A

Wind energy

They did not know it was impossible, so they did it. **by Mark Twain**

The population of the world has surpassed 7 billion in numbers and it is projected to double in coming decades. Energy demand, availability, and cost will become limiting factors with regard to what extend the global society is able to tackle issues such as poverty, hunger, unrest among nations and social justice on global level.

Wind as an energy resource is an important part of the strategy for a renewable future. In this chapter, breakdown by the primary fuels of the World and European energy requirements are presented. The plan to increase the share of renewable energy in the energy market of Europe put forward by the European Commission (EC) is discussed, where a large part of the increase is based on the wind energy.

The current state, trends, growth goals and challenges of offshore wind power, a branch of the wind industry projected to experience rapid growth, are explained and potential benefits of HTS wind turbine generator are identified.

A.1 Wind as an energy resource

In order to understand the importance and nature of the wind as an energy resource, it is important to understand what is the energy demand of the European Union (EU) and the world. A breakdown by primary source will give an overview of the share

renewable energy has at the moment. Several scenarios predicting the growth of the renewables in Europe are based on projected needs and carbon limits put forward by the European Commission. Thus, wind energy, particularly offshore wind, is predicted to become an important milestone for the renewable future of Europe.

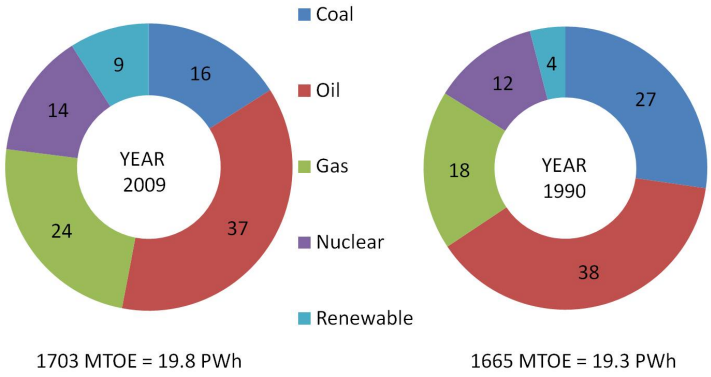

Figure A.1: Energy demand of EU-27 in last 20 years. - The figure compares EU-27 energy consumption in 1990 and 2009. Share in percentage of primary sources of energy is specified (163).

A.1.1 Energy profile of EU

The total energy consumption of 27 European member states (EU-27) in 2009 was 1703 Million Tons of Oil Equivalent (MTOE), as illustrated in the Fig.A.1, where roughly half was produced in Europe and the rest was import(163).

Fossil fuels (oil, gas and coal) are accounting for more than 80% of the energy demand which is slightly higher than 1200 MTOE. In EU-27, import of oil accounted for 80% of the total oil used while gas reached 65% in 2008 (163). The renewable energy in 2009 had 9% of the European energy share which compared to 4% in 1990 is a substantial increase. There are many indicators that the world dependency on fossil fuels must be addressed in the next decades in order to formulate solutions to problems such as fuel import dependence, lack of resources and global climate change. International agreements like the Kyoto protocol in the 90's (164, 165) and similar ones in recent years (166) have tried to restrict the amounts of CO_2 emitted by rapid expansion of fossil fuel driven energy production. The $50\% - 80\%$ reduction of CO_2

emission by the year 2050 (167) is proposed by the Intergovernmental Panel on Climate Change (ICPP).

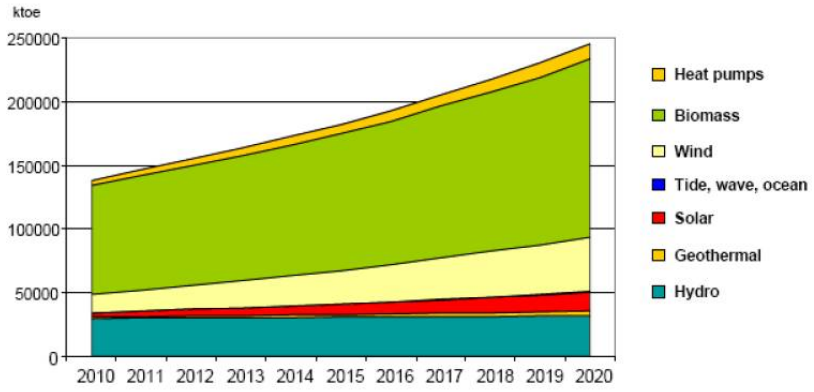

Figure A.2: The renewable energy development scenario. - The figure presents renewable energy growth prediction as a share of the branches of renewable sources up to 2020. The scenario proposed by EU commission includes doubling of share of wind and solar energy by the end of the decade. Reproduced from:(163).

In EU-27, targets of 20% greenhouse gas reduction by 2020 compared to the 1990 level, 20% of energy demand supplied by renewable sources and a 20% reduction of the energy consumption (seen throughout an increase in energy efficiency) have been proposed by the European Commission and agreed among the member states as an initial step towards addressing the climate challenge(163).

Among renewable energy sources, most developed are biomass, wind and solar. The proposal of the EU commission on how the growth of the renewable energy could unfold is presented in the Fig.A.2. Biomass is targeted to replace the fossil fuels in the transportation sector, which constitute 33% of the total carbon emissions(163). Wind and solar energy are adding to the electricity generation.

A.1.2 Wind resource

The northern part of Europe has the fastest average wind speeds as illustrated in the Fig.A.3a (168). Denmark, United Kingdom, France, Netherlands and Germany have average wind speeds of 4 m/s – 6 m/s onshore and above 9 m/s offshore measured at 80 m and 120 m hub elevation for on and off shore, respectively. Consequently, the highest

wind energy densities are found offshore in the North Sea and along the coastline of northern Europe as illustrated in Fig.A.3b.

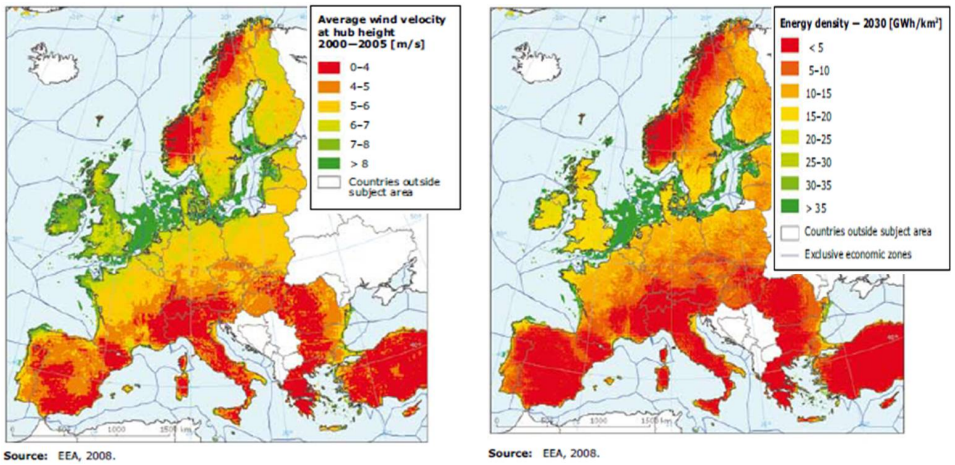

(a) Map of average wind speeds. **(b)** Map of wind energy density.

Figure A.3: Regional wind resources in EU - (a) Wind speed measured at 80 m for onshore and 120 m for offshore hub elevation (b) Average wind energy density derived from average wind speed. Reproduced from:(168)

The European Wind Energy Association (EWEA) has formulated scenarios that predict a need for 300 GW of installed wind power by 2030. A share of 120 GW is expected to be installed offshore (41).

A.2 Wind turbine operation and scaling

A review of the basics of operation for conventional horizontal wind turbine is presented here. It is necessary to understand and identify important aspect of wind turbines scaling and operation in order to perform proper analysis of the different concepts of wind turbines and come to the optimal solution.

The layout of a horizontal three bladed wind turbine (offshore) is illustrated in Fig.A.4. The rotor radius R is given by the blade length, a nacelle size by the lengths a, b and c and a tower height by h. The average velocity of the incoming wind passing the rotor plane is v_0. The velocity of the tip of the blade is v_{TIP}. The kinetic energy of wind can be expresses as (169)

$$P_w = \frac{1}{2}\rho R^2 \pi v_0^3 \tag{A.1}$$

where $\rho = 1.225kg/m^3$ is air density (at T= 15°C). The aerodynamic efficiency of a wind turbine is defined by the power coefficient $C_p(\lambda, \beta)$. Due to the aerodynamic efficiency only a fraction of energy contained in the wind, P_w, is converted into mechanical power.

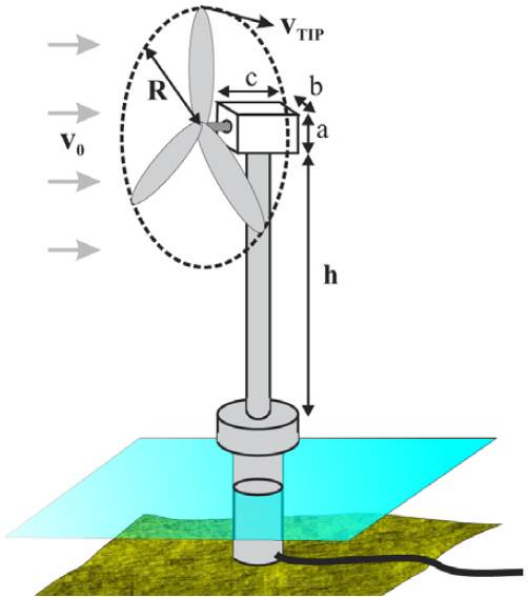

Figure A.4: Wind turbine dimensions. - Illustration of turbine with a rotor blade radius of R, a nacelle size given by a, b and c, and tower height h. The turbine is shown in an offshore installation placed on a static foundation. Reproduced from:(41)

Aerodynamics of the rotor (and efficiency of energy conversion) can be described by the tip speed ratio λ and by the pitch angle β (170). The tip speed ratio presents a ratio between the incoming wind velocity v_0 and the tip speed of the wind turbine blade $R \cdot \omega$ (171). The pitch is the angle of the blade with respect to the rotor plane and it is used to control the level of energy conversion. The pitching is generally used for wind speed higher than nominal where kinetic power contained in wind becomes too high (171).

The power coefficient C_p has a maximum with respect to λ since the extraction of the kinetic energy depends on the change of the wind velocity before and after the rotor plane(172, 173). As a two case studies we can look at the rotor at stand still and at very fast revolution. If the blades are at stand still, all the wind is passing the rotor plane without interaction. At the other hand, if the blades are rotating very fast, the

rotor plane will appear as a solid disk deflecting all the wind around the rotor plane. The theoretical maximum for power coefficient is defined by Betz limit (C_{pMAX}= 0.593 (174)) when the wind speed passing the rotor plane is 1/3 of the speed of incoming wind (169). For large turbines today this values are in range of 0.42-0.5(170, 171). Taking aerodynamic efficiency into account, the mechanical power at the shaft of the turbine becomes

$$P_T = P_w C_p(\lambda, \beta) = \frac{1}{2}\rho R^2 \pi v_0^3 C_p(\lambda, \beta) = \frac{1}{2}\rho R^2 \pi v_0^3 C_{pMAX} \tag{A.2}$$

where $\lambda = V_{TIP}/v_0 = \omega R/v_0$ is the tip speed ratio and ω is the rotation speed of the turbine blades. The maximum power coefficient of a wind turbine is a constant value given by the tip speed ratio called the optimum tip speed, i.e $\lambda_{OPT} = R\omega/v_0$. Thus, if the rotor speed of a variable speed wind turbine is controlled in such a way to follow the wind speed as expressed

$$\omega = v_0 \lambda_{OPT}/R \tag{A.3}$$

where the optimal tip speed is defined as

$$\lambda_{OPT} = R\frac{\omega_{nom}}{v_{0nom}} \tag{A.4}$$

and where ω_{nom} and v_{0nom} are nominal revolution speed and wind speed for a given turbine, the power coefficient can be assumed to be constant over a full range of wind speeds, ie. $C_p(\lambda_{OPT}) = C_{pMAX}$. The values of 0.48 for C_{pMAX} and 7.5 for optimal tip speed ratio can be realistically adopted for MW class turbines (172). Consequently, the following conclusions in relation to scaling of wind turbines do stand out:

- The power rating of a wind turbine scales with swept area of turbine rotor, i.e. square of length of blades (derived from A.1).
- The nominal rotation speed of a turbine rotor scales as 1/R (derived from A.3), since the optimal tip speed ratio is a constant value for all turbines of the same type (169).

As a consequence of the derived scaling rules, the rated torque of a wind turbine will scale as the cube of the rotor radius, as expressed with A.5.

$$T_t = \frac{P_T}{\omega} \sim R^3 \tag{A.5}$$

The implication of A.5, although the analysis above was simplified, is that the torque rating (mechanical) of a turbine will scale faster than the power rating.

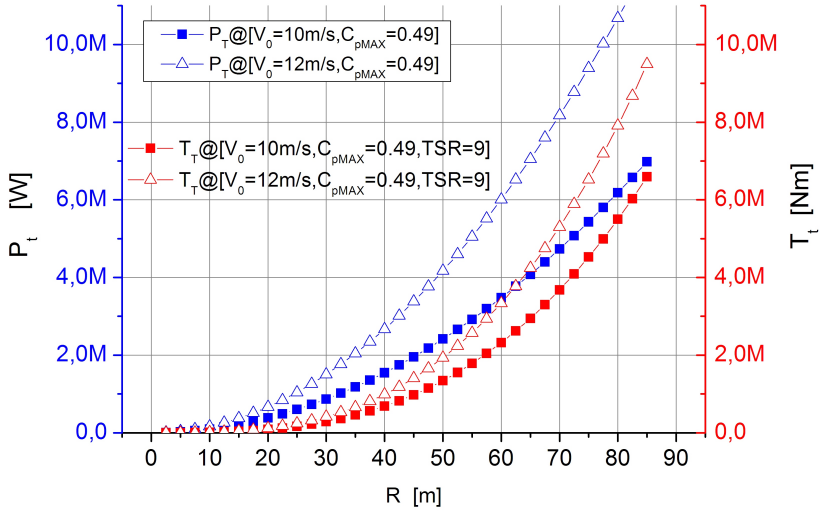

Figure A.5: Scaling of wind turbine power and torque with radius of rotor. - An example for scaling of rated power and torque of a three bladed wind turbine with length of blades for two wind speeds, 10m/s and 12 m/s. The tip speed ration (TSR) is set to be 9 (higher value is characteristic for a offshore turbine since) and C_{pMAX}= 0.49

The figure confirms the derived tendency of rated torque. It will increase faster than the power output of a turbine with increase of rotor diameter. The large impact the rated wind speed has on the torque and power characteristic of a turbine should be also noticed, which works in favor of offshore wind where wind speeds are higher.

A.2.1 Wind turbine drive train concepts

So far, only scaling of turbines was considered. Yet a choice of drive train does have a significant implication to the overall design and operation of wind turbines. With the development of the wind industry, a number of drive train concepts have evolved and changed over time. An illustration of the two most common drive trains is presented in the Fig.A.6 (171). Today's MW turbines are almost exclusively variable speed turbines due to energy capture and power system integration benefits (170, 171). Classification

of turbines may be carried out on basis of control strategies, and the types of electric generators employed in drive train, etc. Most often the classification is made on the basis of a gearbox in the drive train. Thus, two classes are geared and gearless drive trains.

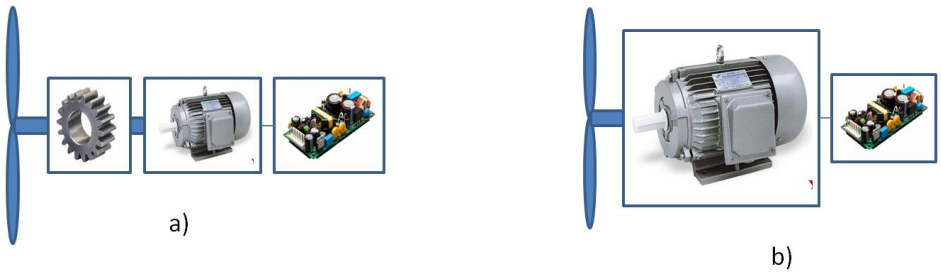

Figure A.6: Illustration of wind turbine drive trains - (a) A geared drive train comprising a multistage gearbox, high speed generator and power electronic control unit (b) a gear less drive train comprising large low speed generator and power electronic control unit.

A geared drive train has a gearbox (with gear ratio of $\sim$ 100) placed between a high speed electric generator and the wind turbine rotor, while gearless drive train or direct drive has a slowly rotating electric generator directly connected to the rotor. A drive train with moderate speed generator is an example of a hybrid solution between geared and gearless drive train, where a simpler one-stage gearbox is used to increase the speed of rotation by a factor 5-10 (175, 176).

In the early period of development of the wind industry, a geared concept wind turbine was more interesting to manufactures (175, 177) due to lower cost. Several successful demonstrations of direct drive turbines between 1980–1990 contributed to the development of direct drive turbines(177, 178). One of the main arguments for a direct drive turbine is simplification of mechanical aspects of the drive train, which could lead to an increase in reliability, but at the higher cost of the drive train (177, 179).

Reported gearbox failures in turbines with power rating $\leq$3MW are accounting for approximately 3% of all faults causing turbines to stop (43, 180). Down time of a turbine (when a turbine is not in operation) caused by a gearbox failures is usually very long (10+ days). Lost income from down time until the fault is repaired can be significant. Thus, the lost income from down time coupled with the cost of gearbox fault (repair of broken or installation of new) makes a geared drive train potentially a

very expensive concept. Serviceability and maintenance issues are even more profound for offshore sites where turbines can be inaccessible for a couple of months (bad winter weather conditions) (41).

A.3 Offshore wind development scenarios

The installed offshore wind capacity, illustrated in Fig.A.7 was first significantly increased around the year 2000. With 626 turbines installed by the end of 2008, offshore had a 1.5 GW capacity which corresponds to 2.2% of the total wind capacity (181).

To fulfill the EU-27 goal of 20% renewable energy penetration(163), a share of 120 GW is expected to be installed offshore, due to higher wind power density at sea and a high population density in coastal areas of the member states. Comparison between the forecast from the European Wind Energy Association (EWEA) and developed offshore capacity is illustrated in Fig.A.7, where cumulative offshore capacity is planned to be increased by two orders of magnetite in 2030 according to a Pure Power scenario (182).

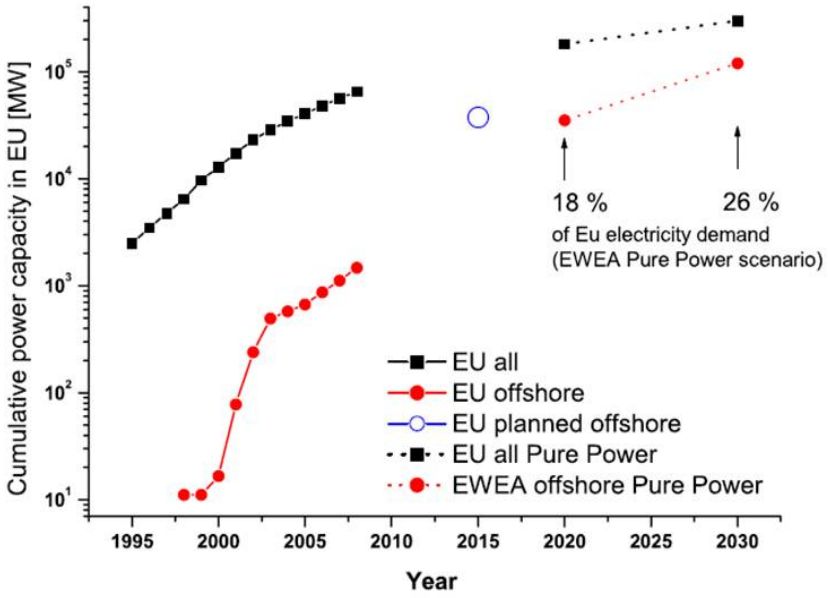

Figure A.7: - Cumulative installed wind power capacity in Europe for both total (offshore and onshore) and only offshore wind is presented. Wind capacity projections for 2020 and 2030 according to EWEA which is based on European goal of a 20% energy supply from renewable sources by 2020 (181) is included. Source:(182), Reproduced from:(41)

The most common offshore wind turbine used in farms was a 2.3 MW turbine (181) and the largest farm was 166 MW (183) where several larger projects are in development (181). The size of the turbines in wind farms under construction is expected to be between 3.0 and 5.0 MW (41). A further increase of the turbine size is expected for offshore wind turbines, because the turbine price accounts for half of the wind farm installation cost. The foundation, grid connections and installation are other major contributors to the cost of offshore. Thus, an optimal offshore wind turbine size will depend on the local wind and water conditions of the installation site. Preliminary analysis in the UPWIND project indicates that 8-10 MW offshore turbines will be desirable(184). The same study has predicted the possibility of a 20MW turbine which is seen as an upper limit of feasibility. An equivalent to an order of 12000 10MW turbines placed in North Sea (41) would be needed to fulfill the EU offshore targets illustrated in the Fig.A.7.

A.3.1 Cost of offshore wind

Growth of the offshore wind sector is driven by an economical aspect. Consequently, offshore development so far had to be subsidized by national development strategies of EU-27 member states. However, the offshore wind would need to become commercially comparable to a cost of energy from other renewable sources. The installation price of offshore wind power is expected to be approximately 1300–1500 EURO/kW (estimates based on cumulative experience from $\leq$1.5 MW turbines (180, 181)) where with 120 GW predicted capacity, the offshore market would be an order of 180 billion EURO. The share of 30% – 50% of total cost need to be allocated to the wind turbines. Installation, foundation and grid connection can account for 50% – 70% of the total cost. These cost estimates do not include scaling of turbine size. Consequently, it must be stated that (185, 186) the share of each contributor to the total cost of an offshore wind capacity will not scale the same way with an increase of turbine power rating. It is expected that for larger turbines, foundation and installation costs will constitute a smaller part of total cost which will ultimately result in reduction of cost of offshore wind energy (184). This trend can be observed in existing data, where reduction from 1500 EURO/kW to 1130 EURO/kW for specific cost of offshore wind installation was observed in two projects. The turbine size was increased from 0.55MW in 1997 Bockstigen-Valar, Baltic, Sweeden to 2MW in 2000 Middlegrunden (180). In general,

offshore experience is limited (turbines of similar ratings) and thus it is very difficult to predict the trend of the cost evolution with a scale of turbines.

In contrast to the offshore wind, the onshore market is considered to be quite mature and the size of the onshore turbines is not expected to increase above 2–3 MW size due to transportation limitations. The installation price of onshore turbines is expected to be 600–700 EURO/kW (estimates based on $\leq$1.5 MW turbine cumulative experience(181)) and the future market is of the same order as the offshore market prediction above. However, it should be noted that wind farm erection (licensing and permits acquisition) is expected to become increasingly difficult with growing population and increasing real estate values. This may result in a cost analysis which favors larger sizes of onshore turbines as well, decreasing the number of turbines per area of land.

A.4 An HTS direct drive - Motivation and challenges

An ideal offshore turbine would have a 20 year life and would have no maintenance requirements. The drive concept closest to an ideal drive with respect to maintenance requirements and reliability is the gearless drive. The extra cost needed for an expensive direct drive generator could be matched with the combination of savings due to higher efficiency of drive train and lower maintenance cost, which for offshore has particular weight. However, a direct drive generator will be very large compared to a geared drive train, since electric machines scale with the rated torque (this will be derived in the next Chapter). The observed tendency of wind turbine scaling, derived in Sec.A.2 and illustrated in the Fig.A.5, shows that turbine torque will scale with $\sim (P_T)^{1.5}$. Consequently, since machines scale with a rated torque, the size of direct drive generators will have the same trend.

Several preliminary studies have been performed comparing a number of drives with conventional machines, including DD(176, 179, 187, 188) where power size were extrapolated to 10 MW wind turbines class. Standing out from other alternatives, a Multibrid concept (single stage gearbox and medium speed generator) and a Direct Drive concept have set themselves apart as the most promising so far. Both concepts have been employed in large turbines, where the 5 MW Multibrid turbine with permanent magnet

synchronous generator is designed by Areva (189) and 7.5 MW DD turbine with wound field synchronous generator is designed by Enercon (190).

Details about superconducting machine design and characteristics of superconducting machines are presented in Ch.3. One of the prominent characteristics of superconducting machines is superior power density compared to a conventional machine, which is expected to be $1.5-3$ times higher(3, 4, 5). Therefore, if a superconducting machine is employed as a wind turbine generator, scaling of a gearless drive train becomes technically easier and potentially commercially superior (which depends on cost and maturity of HTS technology). An additional value of a superconducting DD wind turbine is that the power density of superconducting machines can be optimized by modifying the value of magnetic field in the machine. This stems from the fact that none of the fundamental constraints present in conventional machine technology are present in superconducting machine design.

The technology development road map for offshore wind scale up seems to rely on permanent magnet (PM) machines in either DD concept of the Multibird concept (189, 190). PM machines are highly reliable and efficient and in many ways are an ideal fit for a DD generator for offshore wind turbine (191). However, high Rare Earth (RE) dependence of PM and specific volume of PM per [Nm] of rated torque are biggest weaknesses of PM drive trains. Cost of PM material is in steady increase, where high quality $NdFeB$ magnets are sold at ∼100 EURO/kg (48) and this trend is expected to continue. For the torque found in a large offshore DD wind turbine, usage of PM material can be 500 kg/MW – 1000 kg/MW (41, 175) which for a 10 MW turbine would add up to m_{NdFeB} in the range between 6 tons – 10 tones. Thereby, active material for 10 MW DD PMSM turbine would be above $1{\times}10^6$EURO.

Material analysis of 2G HTS tape used in this project shows that only 0.5% – 1% of the volume of 2G HTS tape contains RE. With MgB_2 superconductor, a machine design would not require any RE. To compare content of RE used in PMSM DD and HTS DD, a preliminary study of a 10 MW HTS wind turbine generator presented as a boundary case reported a L_{10MW} ∼1500 km length of HTS wire required for 10 MW (41). This value is highly overestimated. A length of 300 km – 400 km is more realistic estimates (192). Therefore, with 40 EURO/m for the cost of 2G HTS, the active material of 10 MW DD HTS-SM would be 10–$15{\times}10^6$ EURO which is an order of magnitude higher

compared to the PM DD alternative. However, the mass of superconductor layer used in 300 km of HTS can be expressed

$$m_{YBCO}^{10MW} = 5 \cdot 10^3[\frac{kg}{m^3}] \times (300 \cdot 10^3[m] \times 1.2 \cdot 10^{-6}[m] \times 5 \cdot 10^{-3}[m]) = 9[kg] \quad \text{(A.6)}$$

where ρ_{YBCO}=5·10^3 kg/m^3 (48) is density of YBCO and $v_{YBCO} = a \times b \times L_{10MW}$= 1.8·10^{-3} m^3. In this case study, the RE usage will be 1.8 kg (where the yttrium part would be 1.7 kg). Three orders of magnitude lower RE requirements for a 10 MW turbines with HTS (2G) compared to PM is a very encouraging finding. Consequently, it can be concluded that the HTS drive train concept possesses a higher degree of freedom with regards to the design of power density allowing much higher wind turbine ratings and potentially very low requirement of RE elements. This is very likely to be a major benefit of drive trains based on HTS technology since 12000 of 10 MW turbines would require 60×10^3 tons of NdFeB magnets. For comparison, the production of neodymium and dysprosium in the world today comes almost entirely from China. In the year 2010, China had the total mine production of 134×10^3 tones of the RE where the export quota was 39×10^3 tones (48). Therefore, the concern exists with regards to the available of RE (neodymium and dysprosium) and if the Chinese for wind energy increase from 12 GW in 2009 to 100 GW in 2020 come through, the concern will become even more severe.

Appendix B

Details about HTS coils

The data regarding coil dimensioned and lengths of the selections were derived from the IV room temperature. The dimensions of coil are presented in the Fig.B.1

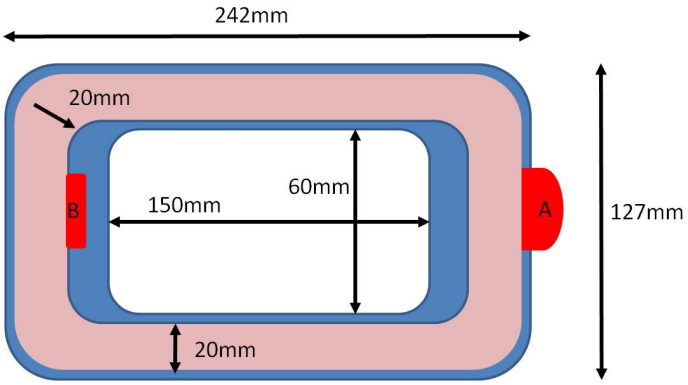

Figure B.1: -

B.1 The coil *Coili#2* – warm test

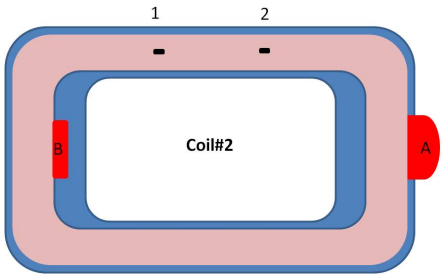

Figure B.2: *Coil#2* -

I=300mA				
Section			Section	Length (m)
	Voltage	Resistance	I=	0,30A
A-B	0,2660	0,8867	Coil	25,4000
1-2	0,0002	0,0007	Short	0,0200
B-1	0,1266	0,4220	Inner	12,0674
A-2	0,1396	0,4652	Outer	13,3064
I=400mA				
			Section	Length (m)
	Voltage	Resistance	I=	0,40A
A-B	0,3525	0,8813	Coil	25,4000
1-2	0,0003	0,0007	Short	0,0199
B-1	0,1678	0,4194	Inner	12,0690
A-2	0,1849	0,4623	Outer	13,3051

Table B.1: *Coili#2* – warm test

B.2 The coil *Coili#3* – warm test

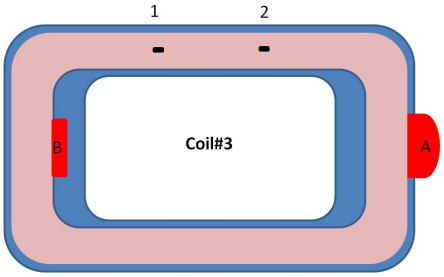

Figure B.3: *Coil#3* -

I=300mA				
Section			Section	Length (m)
	Voltage	Resistance	I=	0,30A
A-B	0,2791	0,9303	Coil	28,8000
1-2	0,0003	0,0010	Short	0,0304
B-1	0,1606	0,5353	Inner	16,5399
A-2	0,1187	0,3956	Outer	12,2173
I=400mA				
			Section	Length (m)
	Voltage	Resistance	I=	0,40A
A-B	0,3725	0,9311	Coil	28,8000
1-2	0,0004	0,0010	Short	0,0301
B-1	0,2144	0,5360	Inner	16,5471
A-2	0,1585	0,3962	Outer	12,2237

Table B.2: *Coili#3* – warm test

B.3 The coil *Coili#5* – warm test

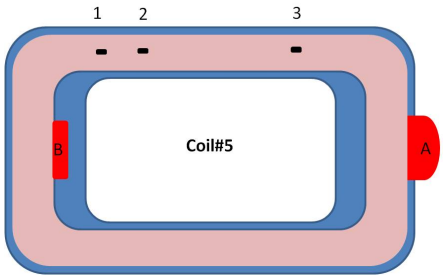

Figure B.4: *Coil#5* -

I=300mA				
Section			Section	Length (m)
	Voltage	Resistance	I=	0,30A
A-B	0,2472	0,8241	Coil	25,0000
3-2	0,0006	0,0021	Short	0,0626
1-2	0,0008	0,0027	Short	0,0814
3-1	0,0002	0,0006	Short	0,0190
B-1	0,1307	0,4357	Inner	13,2179
A-2	0,1157	0,3857	Outer	11,7016
I=400mA				
			Section	Length (m)
	Voltage	Resistance	I=	0,40A
A-B	0,3343	0,8357	Coil	25,0000
3-2	0,0008	0,0021	Short	0,0628
1-2	0,0011	0,0027	Short	0,0815
3-1	0,0003	0,0006	Short	0,0192
B-1	0,1788	0,4469	Inner	13,3691
A-2	0,1565	0,3912	Outer	11,7037

Table B.3: *Coili#5* – warm test

B.4 The coil *Coili#6* – warm test

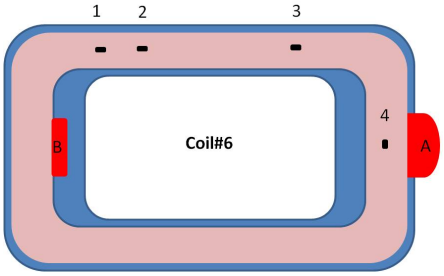

Figure B.5: *Coil#6* -

I=300mA				
Section			Section	Length (m)
	Voltage	Resistance	I=	0,30A
A-B	0,32159	1,0720	Coil	31,6500
A-1	0,161043	0,5368	Outer	15,8494
B-4	0,161782	0,5393	Inner	15,9221
4-1	0,001397	0,0047	Short	0,1375
3-2	0,0005807	0,0019	Short	0,0572
3-1	0,0007957	0,0027	Short	0,0783
2-4	0,001171	0,0039	Short	0,1152
I=400mA				
			Section	Length (m)
	Voltage	Resistance	I=	0,40A
A-B	0,423365	1,0584	Coil	31,6500
A-1	0,21205	0,5301	Outer	15,8525
B-4	0,213096	0,5327	Inner	15,9307
4-1	0,001838	0,0046	Short	0,1374
3-2	0,0007646	0,0019	Short	0,0572
3-1	0,0010487	0,0026	Short	0,0784
2-4	0,001544	0,0039	Short	0,1154

Table B.4: *Coili#6* – warm test

B.5 The coil *Coili#7* – warm test

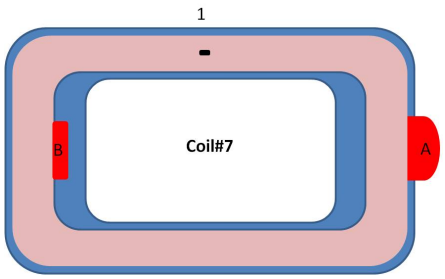

Figure B.6: *Coil#7* -

I=200mA				
Section			Section	Length (m)
	Voltage	Resistance	I=	0,20A
A-B	0,75430	3,772	Coil	70.0
A-1	0,37650	1.880	Outer	35,0
B-1	0,37850	1.895	Inner	35.0

Table B.5: *Coili#7* – warm test

B.6 The coil *Coili#8* – warm test

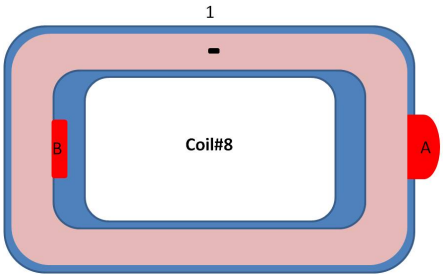

Figure B.7: *Coil#8* -

I=200mA				
Section			Section	Length (m)
	Voltage	Resistance	I=	0,20A
A-B	0,700	3,50	Coil	70.0
A-1	0,355	1.775	Outer	35,0
B-1	0,345	1.755	Inner	35.0

Table B.6: *Coili#8* – warm test

Appendix C

Extended - HTS machines

C.1 An air gap armature winding

If an increase in air gap flux density of a machine is a target due to an increase in power density, heavily saturated teeth will become a problem very fast as most of the conventional designs operate at saturation point (193). First, the loss (hysteretic and eddy current loss) in the teeth will scale with an increase in magnetic flux density which will result in higher energy dissipation very close to armature winding, hence the cooling of the armature conductors will degrade (194). Secondly, as the teeth start to saturate their permeability and thus their effectiveness decrease and consequently, the machine will have a larger effective air gap (195). Instead, in this configuration an air gap armature winding design could have an advantage(193).

An air gap winding, as the name suggests, consists of armature conductors separated by insulating nonmagnetic spacers. Comparative illustration of air gap and conventional winding is found in Fig.C.1. Conductors could be impregnated with resin into a solid armature drum and fixed to the back steel core via pins and bolts (196). An air gap stator was suggested for a turbo generator design (193, 197) in the 1980's arguing considerable material saving and advancement in generator performance. Improvements of an air gap armature winding are:

- Reduction of dissipation caused by ferromagnetic teeth(198)
- Additional space for armature winding(65, 193) i.e. higher electric loading of armature (A_s from 3.1)

- Flux density can be increased above 1 T (63, 193)
- Reduction of required electric insulation for the armature winding (193, 199)

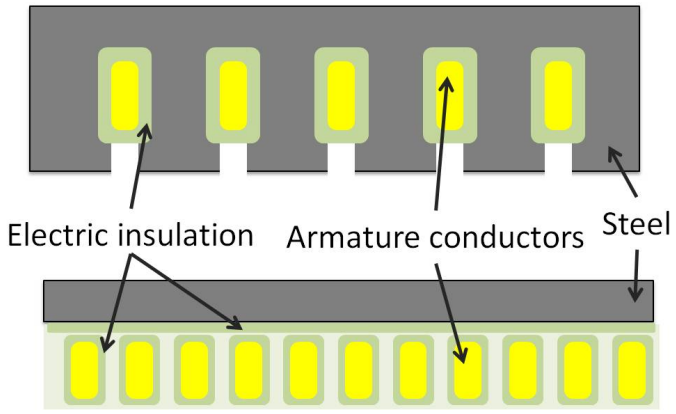

Figure C.1: Comparative illustration of air gap and conventional winding - The upper illustration shows a conventional configuration where insulated armature conductors are placed in slots of stator laminates. The lower illustration presents an air gap winding where conductors are placed in the air gap space next to each other.

Nevertheless, two major concerns regarding the air gap windings must not be forgotten. The armature conductors are now experiencing full linkage flux (alternating). If no measures are taken and armature is wound from solid copper wire, significant loss in the armature would be caused by a skin effect. Hence, an armature winding will need to be wound with Litz wires(194).

Even more pressing issues of an air gap armature are thermal and mechanical considerations. Cooling conditions in such a winding will be degraded(65) since steel teeth have acted as a heat sink and the absence of them will hinder heat conduction from winding conductors. In conventional machines Lorentz forces will only in small part act on the windings in normal operation where a larger part will act on steel teeth (200). In the case of an air gap armature, much larger forces are acting on the conductors in both radial and tangential direction(193). Accordingly, an armature winding drum would need to be designed to sustain these high forces, which can be challenging especially in high torque machines.

C.2 Current sheet approximation

Fig.C.3 illustrates the angular distribution of Ampere-turns of HTS winding. Coils carrying current are represented with angular segments defined with angles θ_1 and θ_2 in Fig.C.2. The HTS turns density n_ρ expressed in $[turns/m^2]$ is considered constant. Expansion of the Ampere-turn distribution into a Fourier series $A_{(\theta)}\,[A/m] = \sum A^{\nu}_{sheet} \cdot sin\,(p\nu\theta)$ results in C.1 and C.2 for the amplitude of each harmonic of the current sheet. The sheet radius, illustrated in Fig.3.8, is derived as $r_{sheet} = 0.5(r_2 + r_{r_1})$.

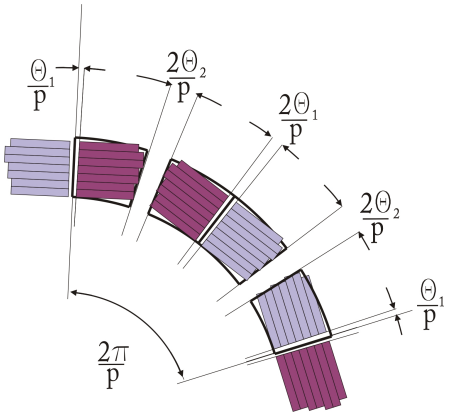

Figure C.2: An illustration of HTS coils in multi pole field winding - HTS field winding is supplied with current where dark purple color is assigned to one direction of current and light purple to opposite direction of current flow. The angles θ_1 and θ_2 are defining the coil filling factor as indicated in the figure where a pair of poles spans $2\pi/p$.

$$A^{\nu}_{sheet} = \frac{I_{sheet}}{r_{sheet}} \frac{1}{\pi} \int_{-\pi}^{\pi} \int_{r_1}^{r_2} n_{\rho_{(r,\theta)}} \cdot sin\,(\nu p\theta) \cdot r d\theta dr = \tag{C.1}$$

$$= \frac{I_{sheet}}{r_{sheet}} \frac{2p}{\pi} n_\rho \frac{{r_2}^2 - {r_1}^2}{2} \underbrace{\left(\left[\frac{-cos\,(\nu p\theta)}{\nu p} \right]_{\left(\frac{\theta_1}{p}\right)}^{\left(\frac{\pi}{2p} - \frac{\theta_2}{p}\right)} + \left[\frac{-cos\,(\nu p\theta)}{\nu p} \right]_{\left(\frac{\pi}{2p} + \frac{\theta_2}{p}\right)}^{\left(\frac{\pi}{p} - \frac{\theta_1}{p}\right)} \right)}_{k_{A\nu}/p} =$$

$$= \frac{n_\rho I_{sheet}}{\pi r_{sheet}} \left({r_2}^2 - {r_1}^2\right) k_{A\nu} \tag{C.2}$$

where $k_{A\nu}$ can be interpreted as the winding coefficient for the HTS rotor winding. The radii r_2 and r_1 are the outer and the inner radii of the HTS ring (red ring on Fig.3.8) while I_{sheet} is the current of the HTS winding.

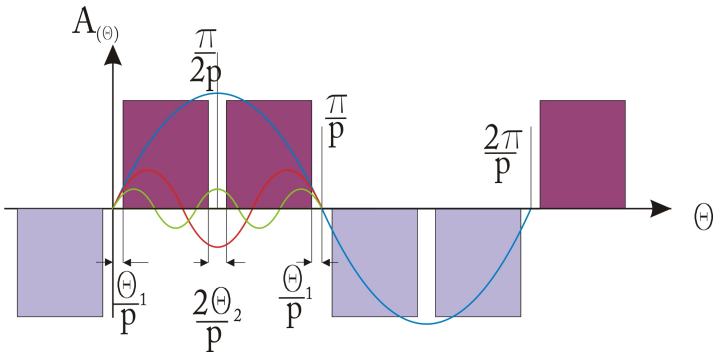

Figure C.3: A current sheet approximation of an HTS field winding - Electric sheet $A_{(\theta)}$, defined by Ampere-turns of HTS coils and angles θ_1 and θ_2. Current orientation corresponds to the Fig.C.2.

Appendix D

Technical drawings

D.1 The SUPERWIND assembly

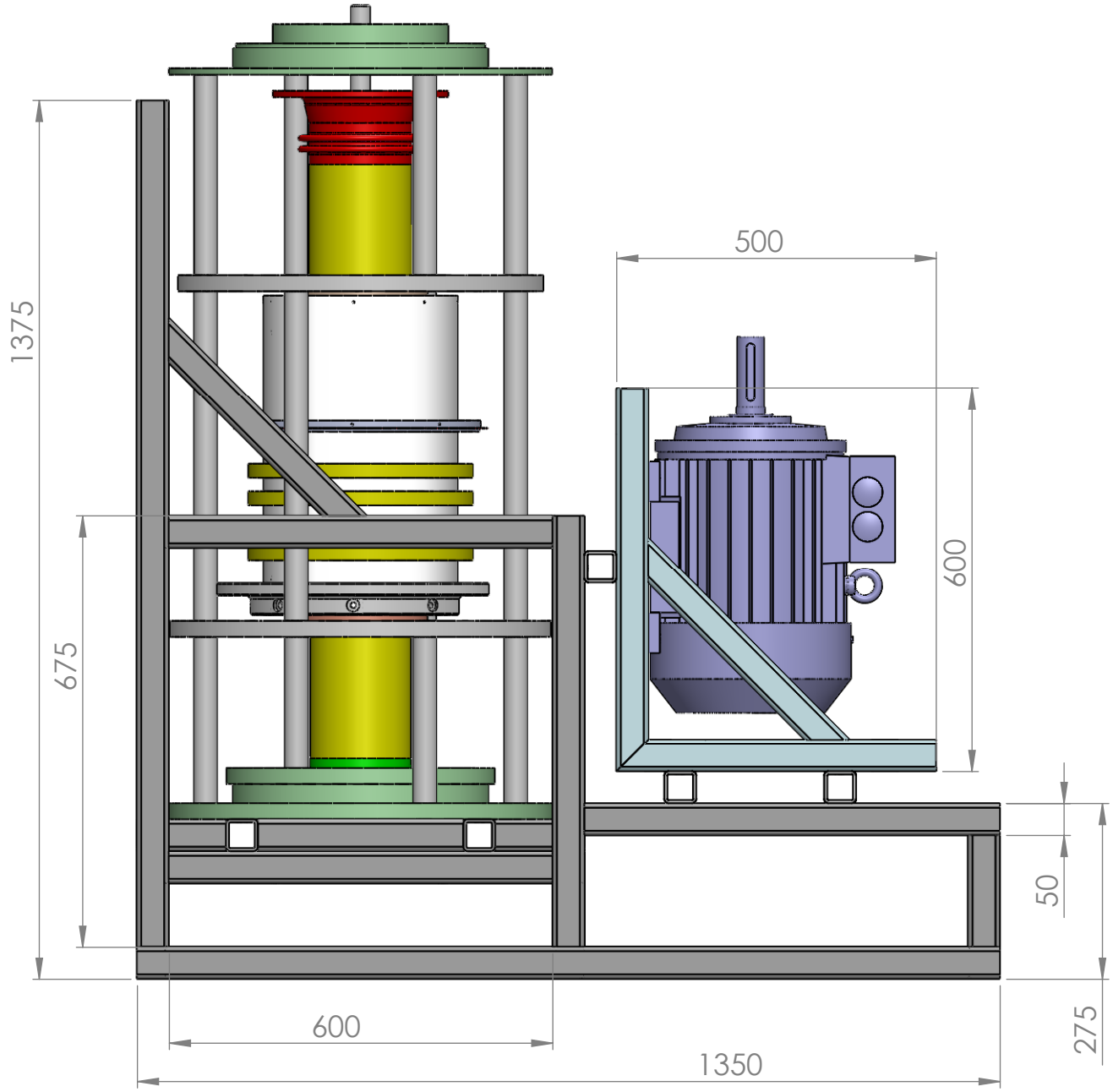

UNLESS OTHERWISE SPECIFIED: DIMENSIONS ARE IN MILLIMETERS SURFACE FINISH: TOLERANCES: LINEAR: ANGULAR:	FINISH:	DEBUR AND BREAK SHARP EDGES	DO NOT SCALE DRAWING	REVISION	

	NAME	SIGNATURE	DATE	TITLE:
DRAWN				
CHK'D				
APPV'D				
MFG				
Q.A				

MATERIAL:	DWG NO.		A4
WEIGHT:	SCALE:1:10	SHEET 1 OF 1	

SolidWorks Student Edition.
For Academic Use Only.

assembly.ver04_ver2

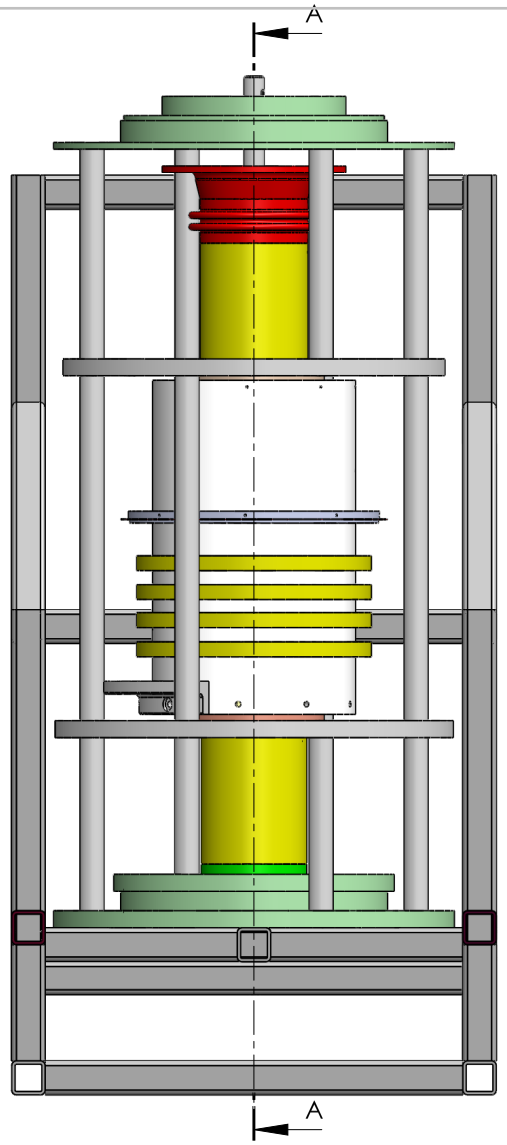

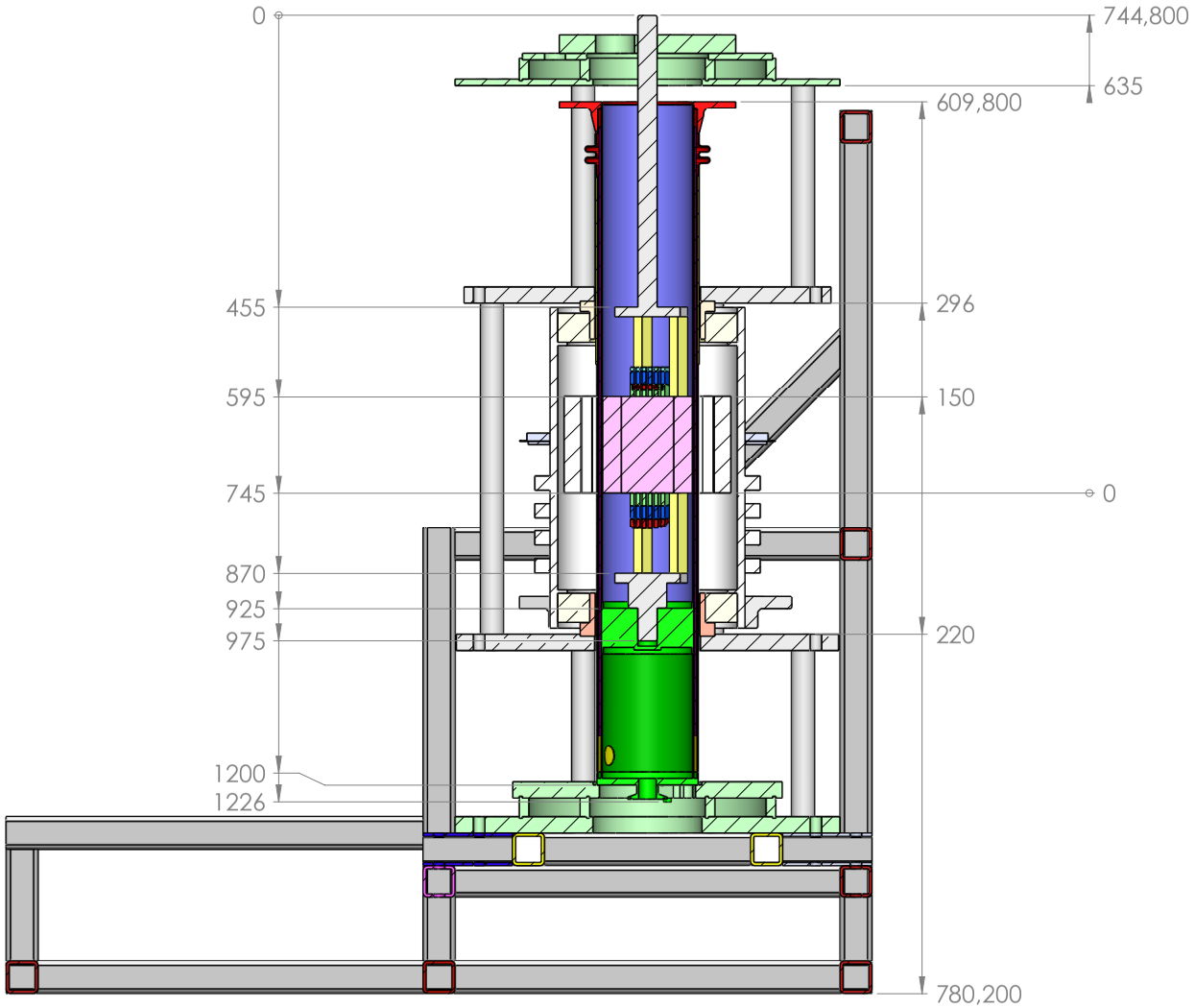

SECTION A-A

UNLESS OTHERWISE SPECIFIED: DIMENSIONS ARE IN MILLIMETERS SURFACE FINISH: TOLERANCES: LINEAR: ANGULAR:		FINISH:			DEBUR AND BREAK SHARP EDGES		DO NOT SCALE DRAWING	REVISION
	NAME	SIGNATURE	DATE				TITLE:	
DRAWN								
CHK'D								
APPV'D								
MFG								
Q.A				MATERIAL:			DWG NO.	A3
							SUPERWIND ver04_ver3	
				WEIGHT:			SCALE:1:8	SHEET 1 OF 1

SolidWorks Student Edition.
For Academic Use Only.

D.2 The cryostat assembly

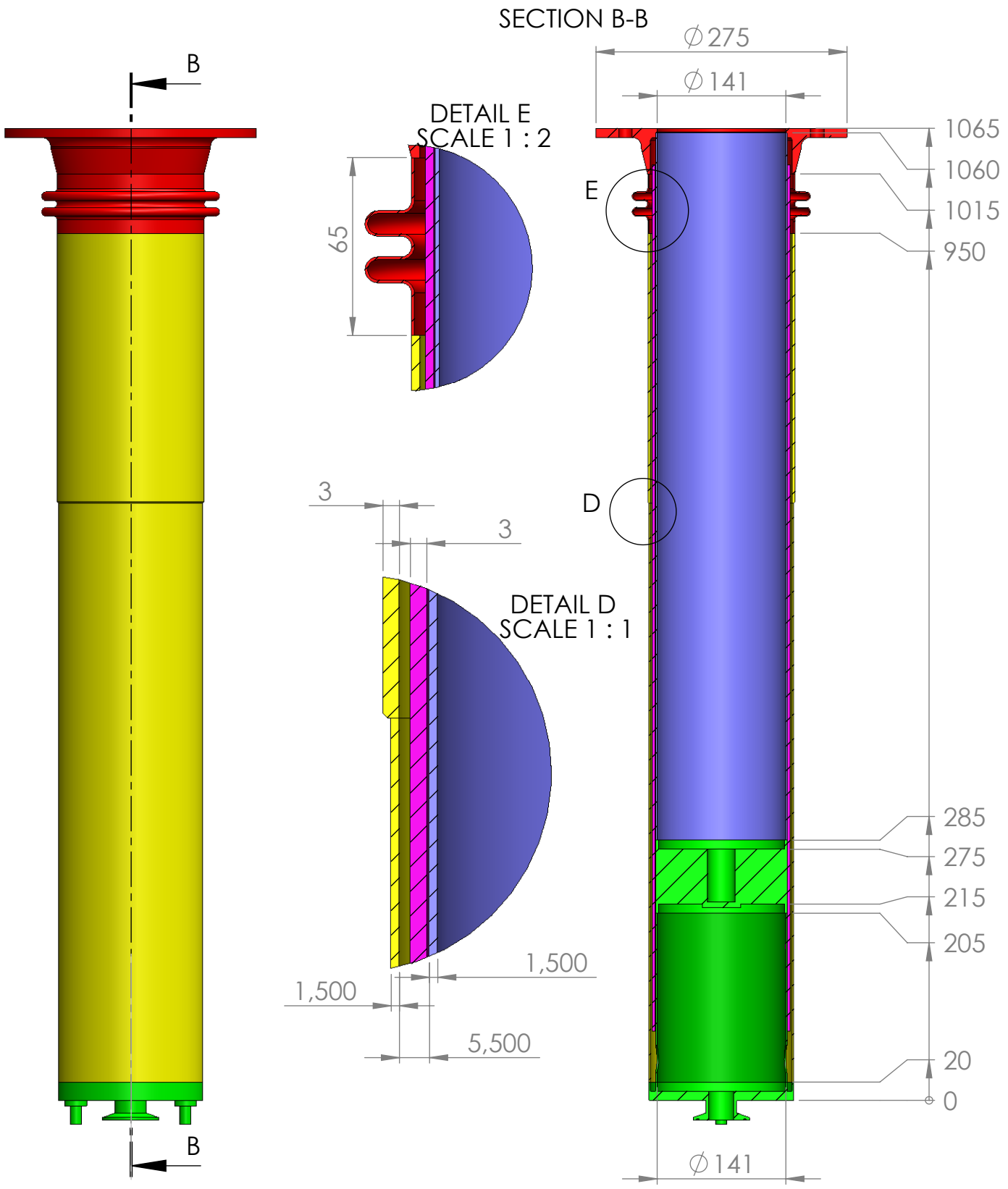

UNLESS OTHERWISE SPECIFIED: DIMENSIONS ARE IN MILLIMETERS SURFACE FINISH: TOLERANCES: LINEAR: ANGULAR:			FINISH:			DEBUR AND BREAK SHARP EDGES	DO NOT SCALE DRAWING	REVISION
	NAME	SIGNATURE	DATE				TITLE:	
DRAWN								
CHK'D								
APPV'D								
MFG								
Q.A				MATERIAL			DWG. NO. SUPERWIND_ver04_ver4-Cryo	A4
				WEIGHT:			SCALE:1:6	SHEET 1 OF 1

SolidWorks Student Edition.
For Academic Use Only.

D.3 The armature assembly

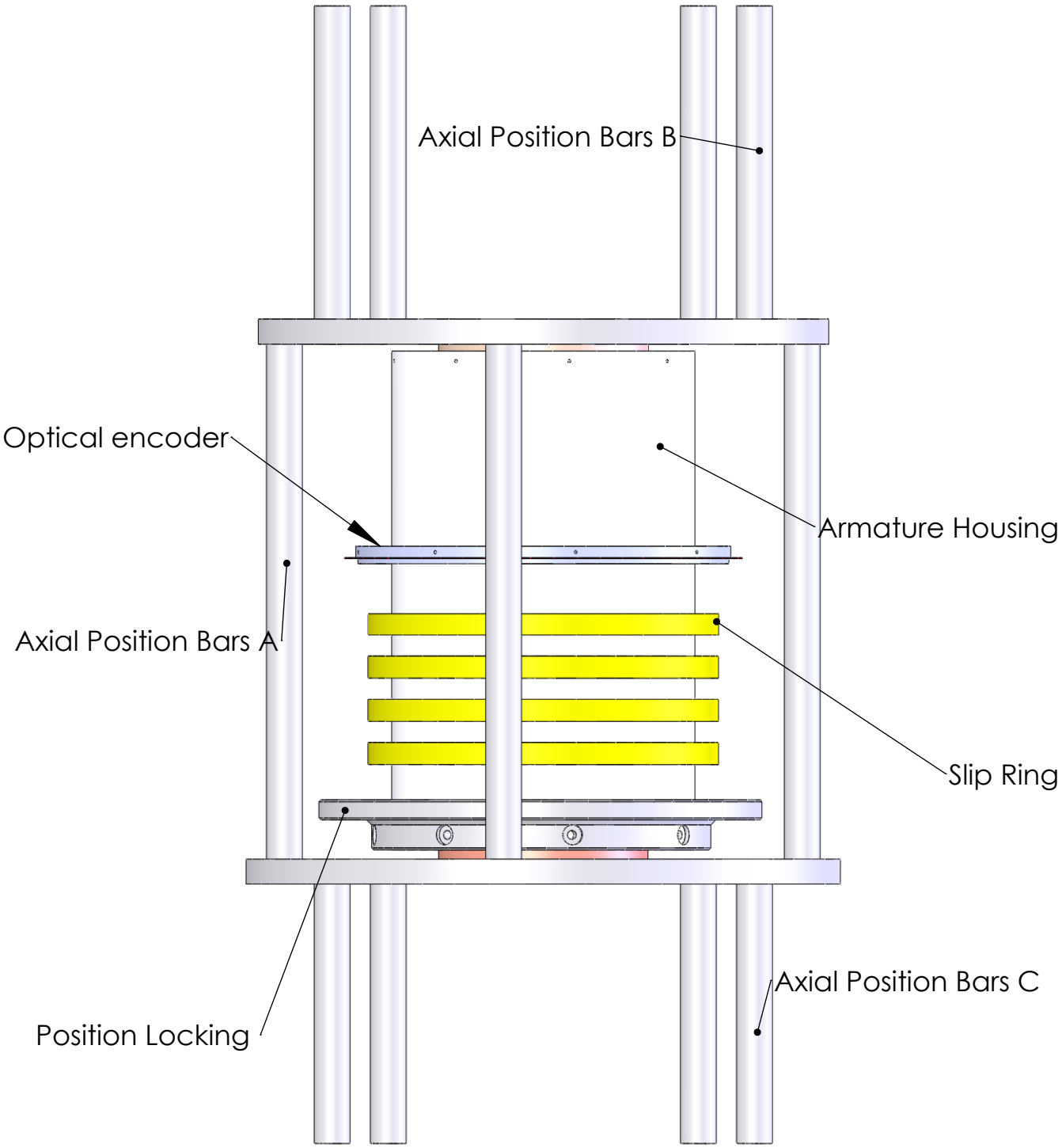

UNLESS OTHERWISE SPECIFIED: DIMENSIONS ARE IN MILLIMETERS SURFACE FINISH: TOLERANCES: LINEAR: ANGULAR:		FINISH:		DEBUR AND BREAK SHARP EDGES		DO NOT SCALE DRAWING	REVISION
	NAME	SIGNATURE	DATE			TITLE:	
DRAWN							
CHK'D							
APPV'D							
MFG							
Q.A				MATERIAL		DWG. NO.	A4
						The armature assembly	
				WEIGHT:		SCALE:1:6	SHEET 1 OF 1

SolidWorks Student Edition.
For Academic Use Only

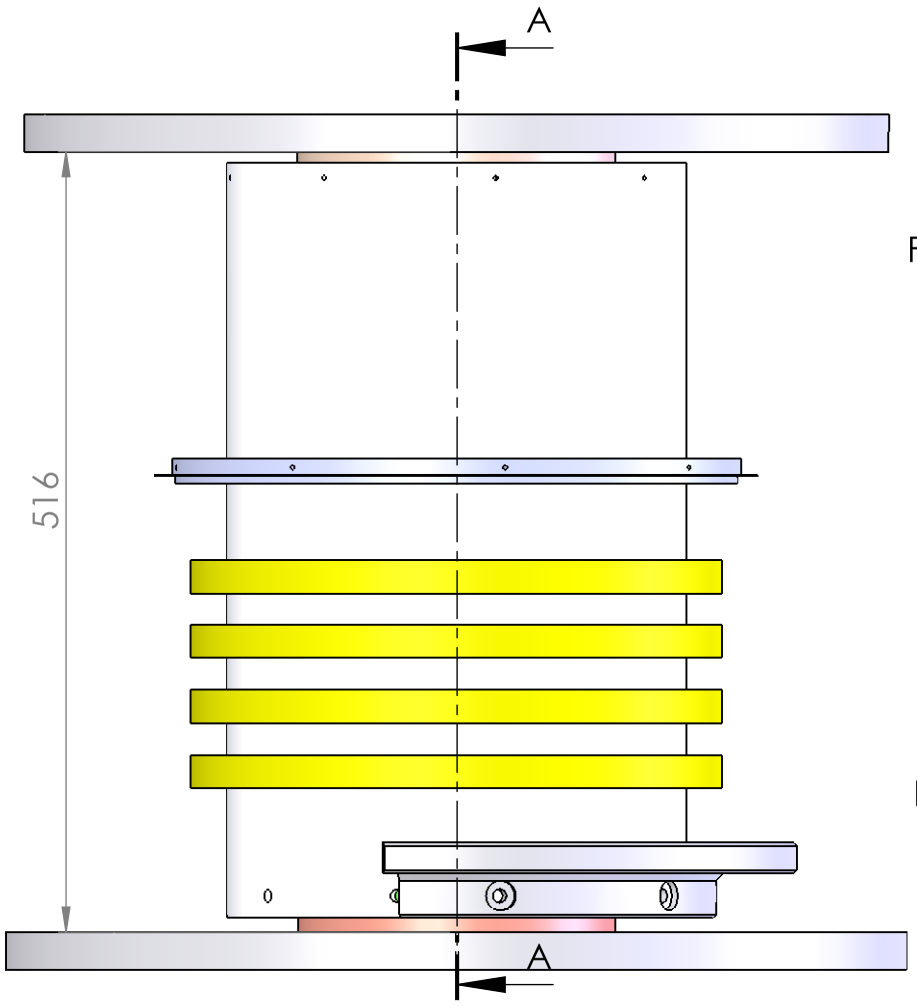

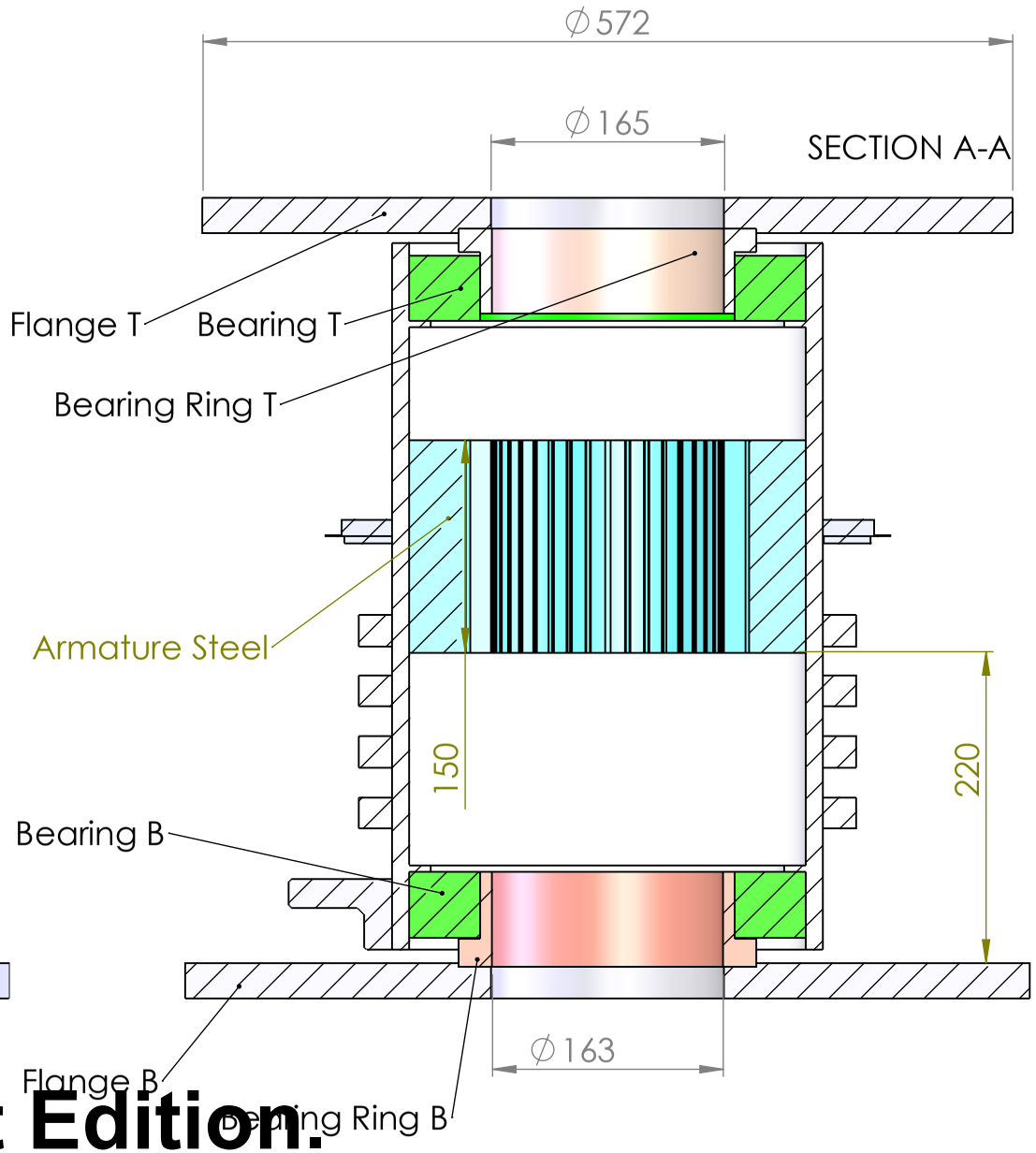

SolidWorks Student Edition.
For Academic Use Only.

Armature

A4

WEIGHT:

SCALE:1:5

SHEET 1 OF 1

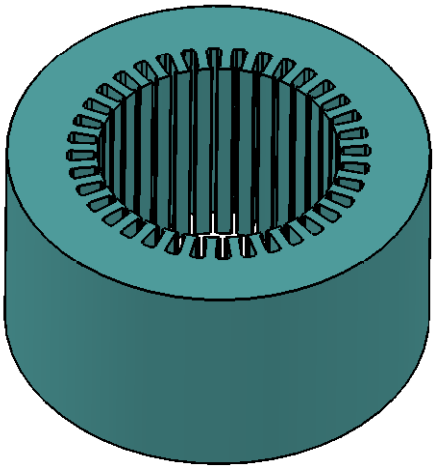

DETAIL A
SCALE 2 : 1

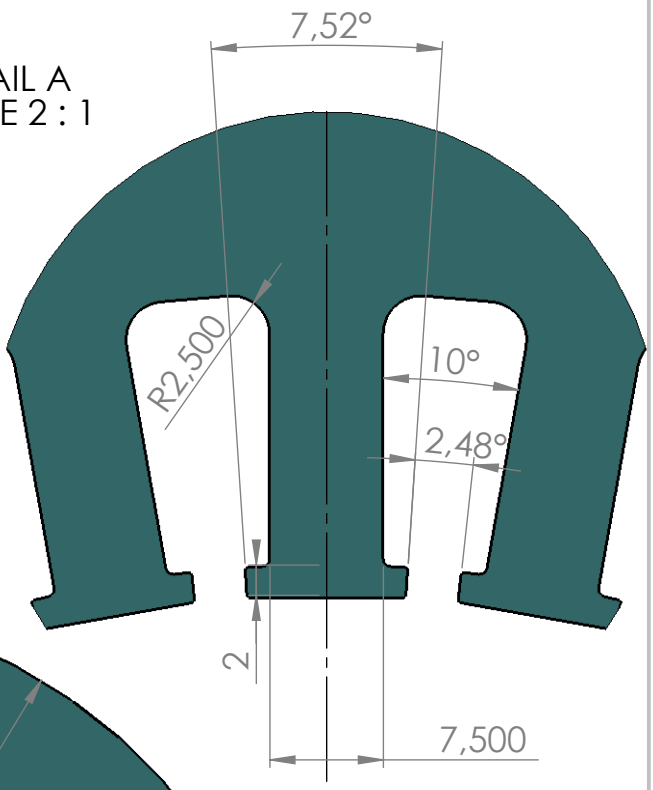

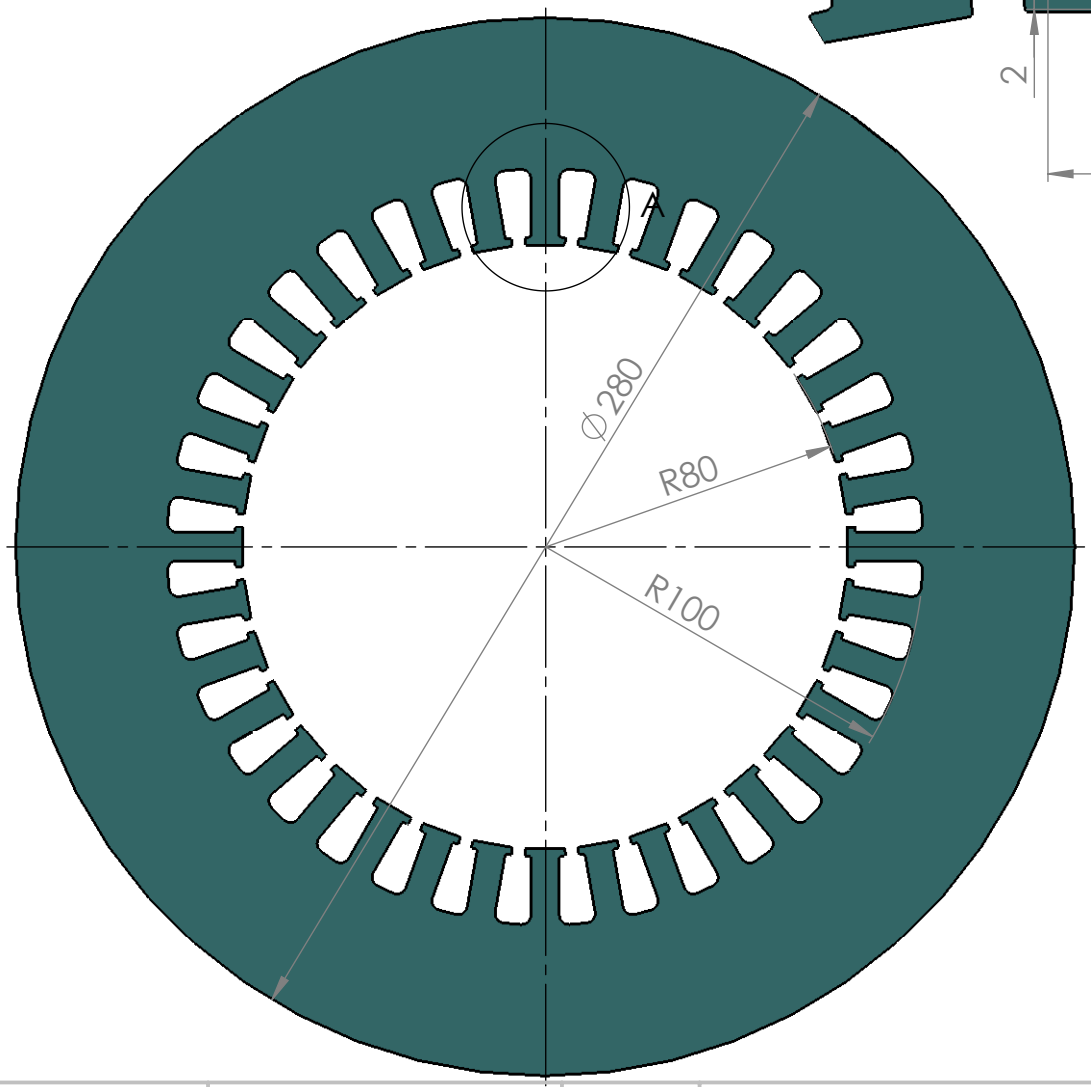

UNLESS OTHERWISE SPECIFIED: DIMENSIONS ARE IN MILLIMETERS SURFACE FINISH: TOLERANCES: LINEAR: ANGULAR:	FINISH:	DEBUR AND BREAK SHARP EDGES	DO NOT SCALE DRAWING	REVISION	
	NAME	SIGNATURE	DATE	TITLE:	
DRAWN					
CHK'D					
APPV'D					
MFG					
Q.A				DWG NO.	A4
			WEIGHT:	SCALE:1:5	SHEET 1 OF 1

SolidWorks Student Edition.
For Academic Use Only.

ArmatureSteel

D.4 The HTS field winding assembly

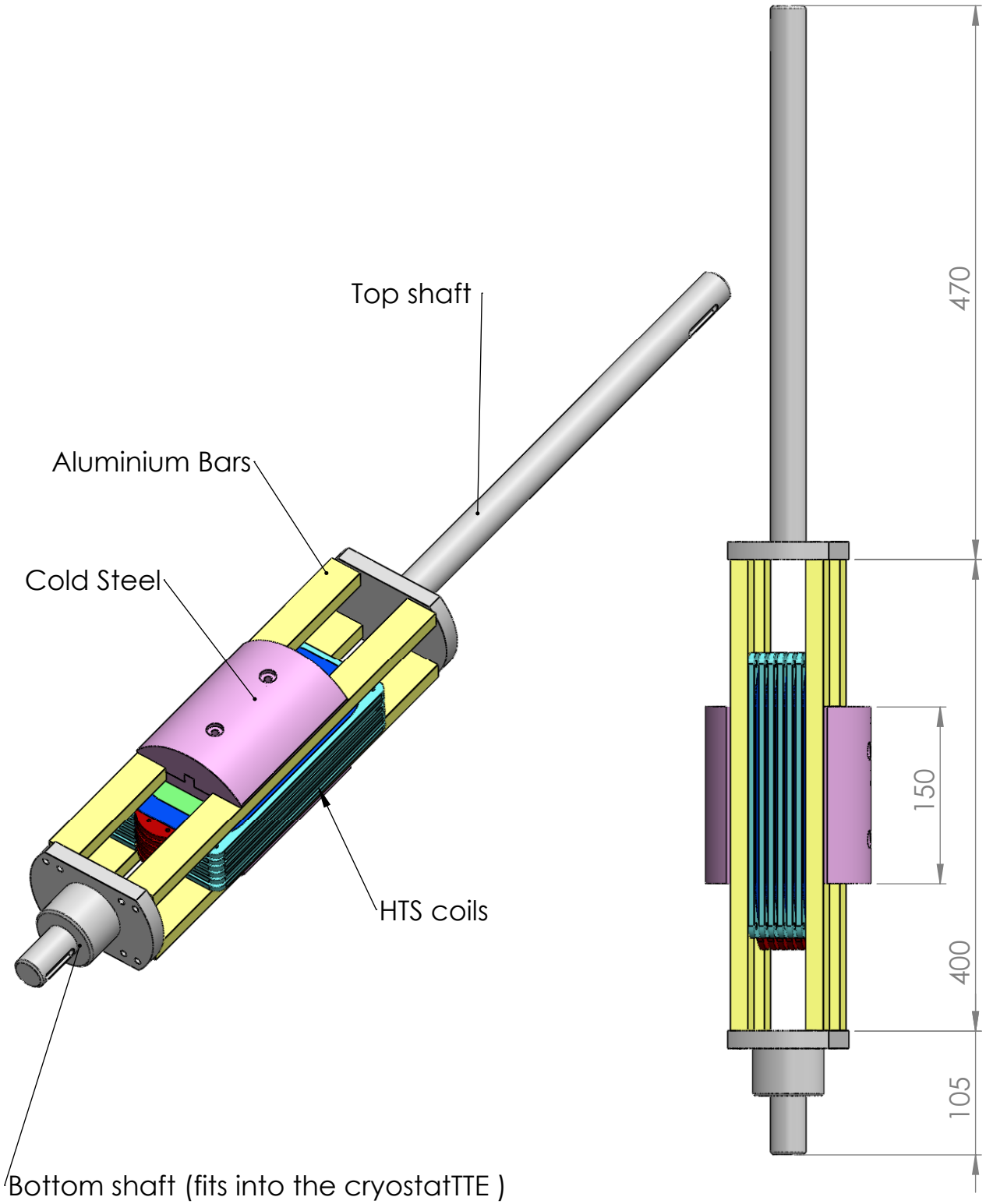

UNLESS OTHERWISE SPECIFIED: DIMENSIONS ARE IN MILLIMETERS SURFACE FINISH: TOLERANCES: LINEAR: ANGULAR:		FINISH:		DEBUR AND BREAK SHARP EDGES		DO NOT SCALE DRAWING	REVISION
	NAME	SIGNATURE	DATE			TITLE:	
DRAWN							
CHK'D							
APPV'D							
MFG							
Q.A				MATERIAL		DWG. NO.	A4
						The HTS field winding	
				WEIGHT:		SCALE:1:5	SHEET 1 OF 1

SolidWorks Student Edition.
For Academic Use Only.

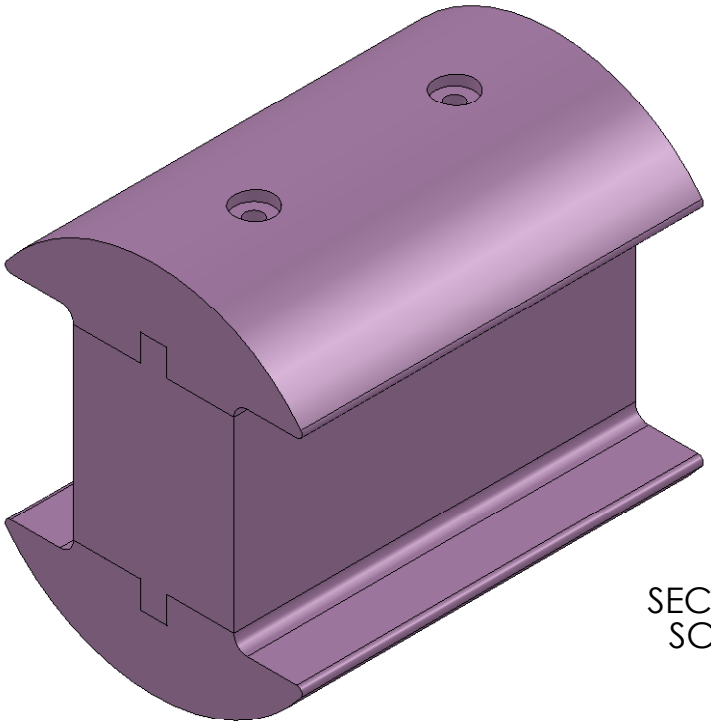

SECTION A-A
SCALE 1 : 2

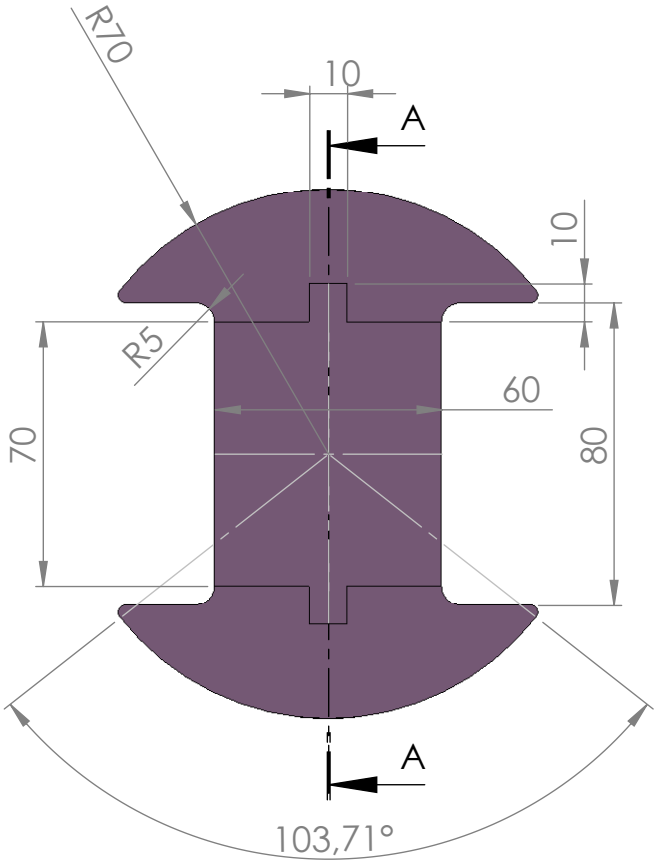

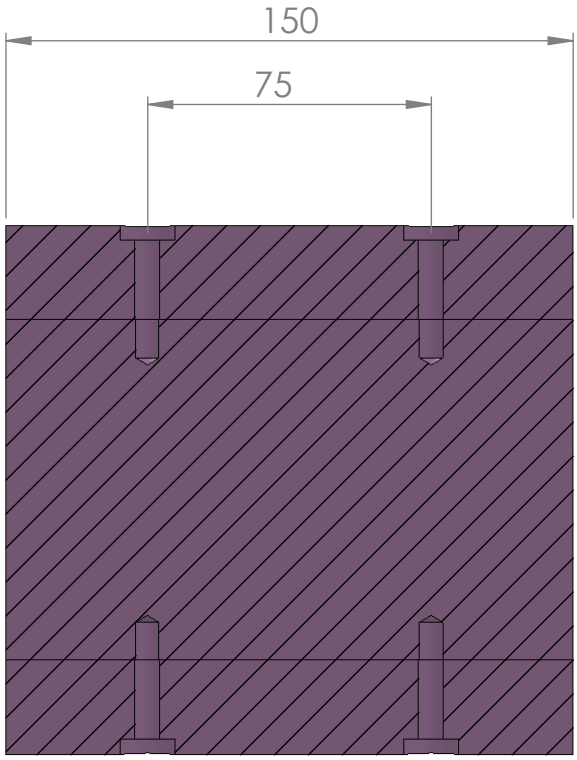

UNLESS OTHERWISE SPECIFIED: DIMENSIONS ARE IN MILLIMETERS SURFACE FINISH: TOLERANCES: LINEAR: ANGULAR:		FINISH:		DEBUR AND BREAK SHARP EDGES		DO NOT SCALE DRAWING		REVISION
	NAME	SIGNATURE	DATE			TITLE:		
DRAWN								
CHK'D								
APPV'D								
MFG								
Q.A				MATERIAL		DWG NO.		A4
				WEIGHT:		SCALE:1:1	SHEET 1 OF 1	

SolidWorks Student Edition.
For Academic Use Only.

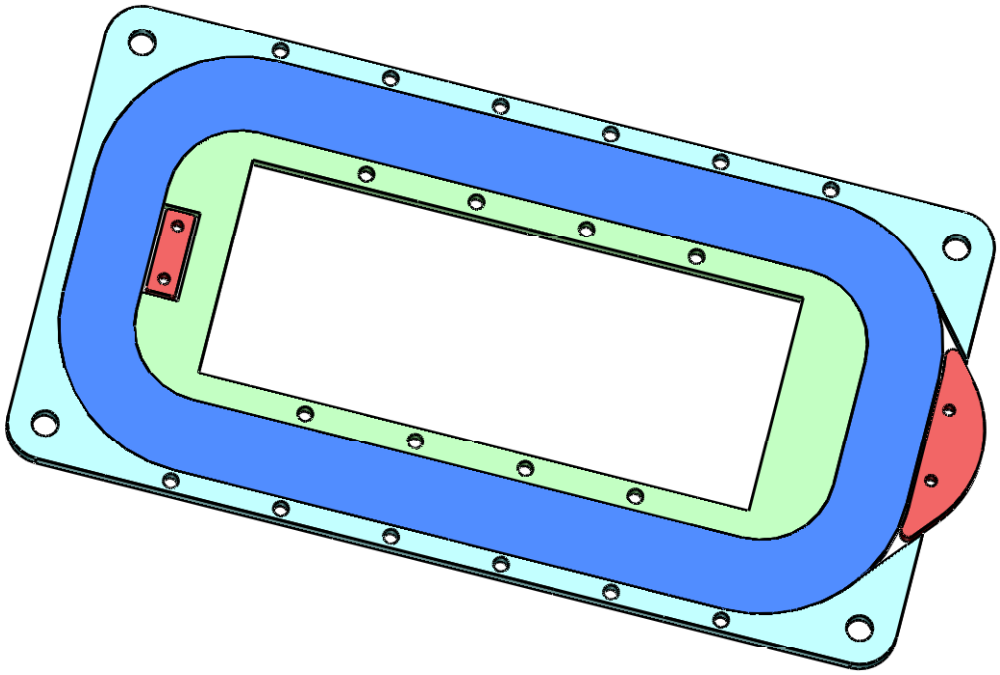

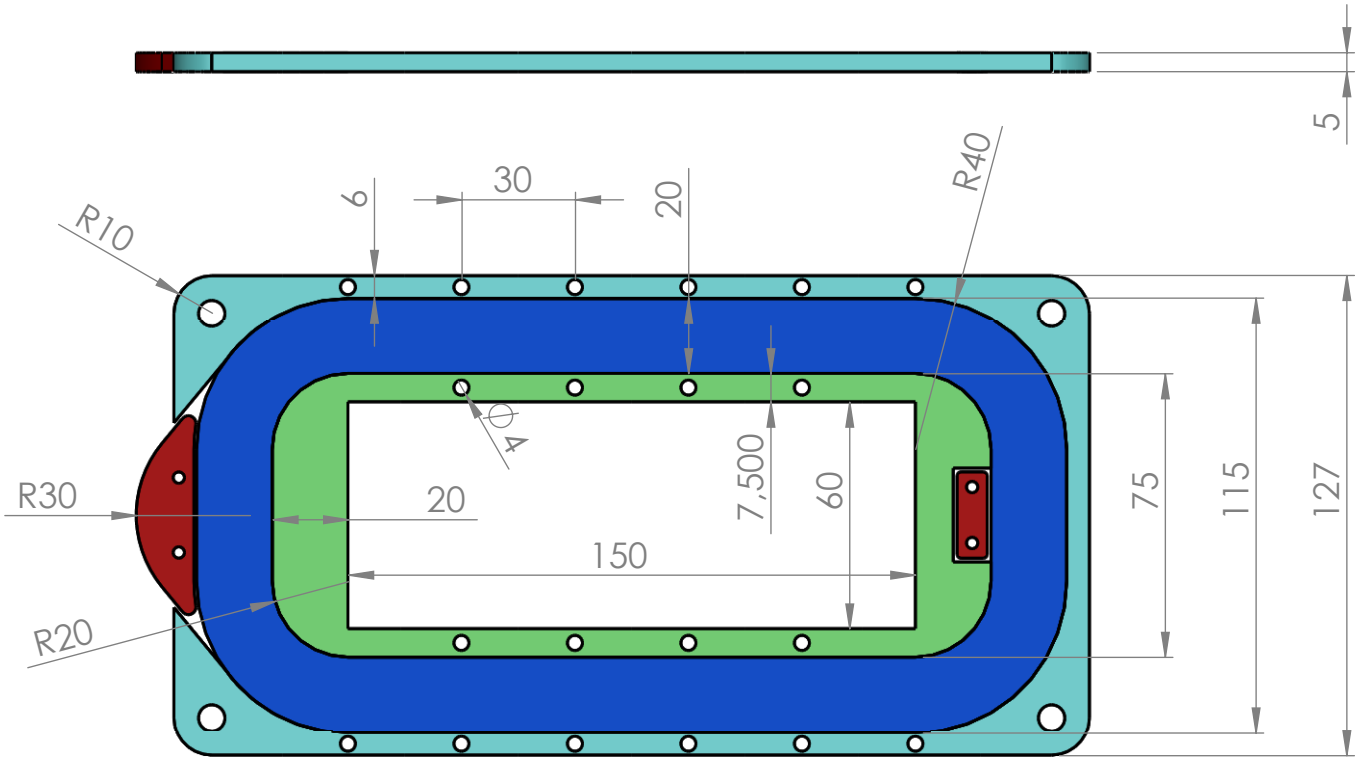

UNLESS OTHERWISE SPECIFIED: DIMENSIONS ARE IN MILLIMETERS SURFACE FINISH: TOLERANCES: LINEAR: ANGULAR:		FINISH:		DEBUR AND BREAK SHARP EDGES		DO NOT SCALE DRAWING	REVISION
	NAME	SIGNATURE	DATE			TITLE:	
DRAWN							
CHK'D							
APPV'D							
MFG							
Q.A				MATERIAL		DWG NO. Body Asmb	A4
				WEIGHT:		SCALE:1:5	SHEET 1 OF 1

SolidWorks Student Edition.
For Academic Use Only

Appendix E

Appendix 3: Induction machine nameplate data

PROTOKOL O TYPOVÉ ZKOUŠCE ASYNCHRONNÍHO MOTORU
Test certificate of induction motor - Typenprotokoll des Asynchronmotors

Test No...Probe Nr. : 24354-A

Typ...Type : **14BG 183-2AA60-Z**	Serial-No: **12645501**	spec.: 180000
22 kW	**400 / 690** V; D / Y	**40,5 / 23,5** A	**2945** min^{-1}	**50** Hz
S1	IP55	Isol. F	40 °C	IM B3	145 kg

ODPOR vinutí - studený ... Winding resistance - cold ... Wicklungswiderstand - kalt

R_{f20} = 0,37801 Ω

R_{isol} > 50 MΩ (500 V)

Svorky...Terminals...Klemmen :	U - V	U - W	V - W
ϑ = 23,1 °C .... **R** (Ω) :	**0,255**	**0,2552**	**0,255**

M_N = 71,3 Nm / **U = 400 V; D** — **MĚŘENÍ PŘI ZATÍŽENÍ** ..... Load test ..... Messung bei der Belastung

		1.	2.	3.	4.	5.	6.
P_{in}	(W)	24084	24082			18038	
P	(W)	22002	22000	22000	22000	16500	**22000**
I	(A)	40,8	40,8	40,8	40,8	31,9	**40,5**
f	(Hz)	50,01	50	50	50	50	**50**
OTÁČKY Speed...Drehzahl	(min^{-1})	2944	2943	2943	2943	2956	**2945**
η	(%)	91,4	91,4	91,3	91,4	91,5	**91,4**
cos φ	(-)	0,851	0,851			0,816	**0,86**
M_{ST}/M_N • M_A/M_N	(-)	2,31	2,31				**2,5**
I_{ST}/I_N • I_A/I_N	(-)	6,76	6,76				**7,0**
M_{MAX}/M_N • M_K/M_N	(-)	3,28	3,28				**3,4**
SKLUZ Slip...Schlupf	(%)	1,89	1,89			1,46	**1,83**
VINUTÍ - Δϑ Winding...Wicklung	30s (K)	75,1	75,1	EN 60034-2 Tref = 95°C	CEMEP Tref = 90,1°C	CEMEP Tref = 90,1°C	**80**
KOSTRA - Δϑ Frame...Gehäuse	(K)	29,5	29,5				
$ϑ_a$	(°C)	16,2	16,2				
DOBA Time...Dauer	(min)	180					
ODPOR vinutí - teplý Resistance - warm Widerstand - warm	(Ω)	0,32250 0,322573 0,32232	0,32249 0,32256 0,32231	... U - V ... U - W ... V - W	R_{isol} > 50 MΩ		

1. **MĚŘENÍ**
   - Measuring
   - Messung
2. **PŘEPOČET na P_N**
   - Corrected for P_N
   - Korrektur auf P_N
3. **PŘEPOČET na T_{REF} podle EN 60034-2**
   - Corrected for T_{REF} acc. to EN 60034-2
   - Korrektur auf T_{REF} nach EN 60034-2
4. **PŘEPOČET na T_{REF} podle CEMEP**
   - Corrected for T_{REF} acc. to CEMEP
   - Korrektur auf T_{REF} nach CEMEP
5. **MĚŘENÍ při 75% P_N**
   - Measuring at 75% P_N
   - Messung bei 75% P_N
6. **ZARUČENO**
   - Guaranteed
   - Garantierwert

MĚŘENÍ NAPRÁZDNO...No-load test...Leerlaufmessung

Napětí Voltage Spannung	Proud Current Strom	Příkon Power input Leistungaufn.	Účiník Power factor Leistungsfaktor
400 V;D	**15,5 A**	**823 W**	**0,076**

MĚŘENÍ NAKRÁTKO .... Locked rotor test .... Kurzschlussmessung

Napětí Voltage Spannung	Proud Current Strom	Moment Torque Moment	Příkon Power input Leistungaufn.	Účiník Power factor Leistungsfaktor
400 V;D	**273,6 A**	**164,9 Nm**	**100388 W**	**0,53**

ZÁVITOVÁ ZKOUŠKA
Coil test .... Windungsprobe
130% U_N - 3 min.

ZKOUŠKA MECH. ODOLNOSTI
High-speed test .... Schleuderprobe
120% n_N - 2 min.

ZKOUŠKA VÝDRŽNÝM NAPĚTÍM
High-potencial test .... Wicklungsprüfung
2380 V - 1 min.

ZKOUŠKY VYHOVUJÍ ... EN 60034-1
Tests conform to the... - Prüfungen entsprechen dem...

CEMEP EFF 2

Pozn.-Note / Bemerkung: Nullserie / 5a

zak.: 10126455
LIAZ : 29892/20

20. 6. 2000
Date...Datum

Quality Assurance...Qualitätssicherung

Podpis : **Ing. Polách**
Signature...Unterschrift

Frenštát p.R., Czech Republic

Appendix F

Extended - Experimental results

F.1 $E_{Coil\#3}$ for Arr1 Locked Armature experiment

For the HTS field winding in Arr1, the electric field profile for the case when I_{coil}=45A and I_{coil}=50A are presented in Fig.F.1 and Fig.F.2. By comparing these with the Fig.5.16 and Fig.5.17, the Arr1 can be identified as the configuration of the field winding with slightly better performance, since the coil $Coil\#3$ shows somewhat better performance for all angles and all armature currents. This can be explained with the proximity of $Coil\#3$ to the pole shoe in Arr1 which serves as a flux diverted, similar to the concept explained in (201, 202).

However, Arr1 also contains $Coil\#5$ which has the same tendency as $Coil\#3$ but with somewhat higher current capacity. For armature reaction of 20A and at ϕ=90°, the critical current of $Coil\#5$ would be 50A. This means not only that $Coil\#3$ has low I_c but also that I_c of $Coil\#5$ is not far away. On the other hand, in Arr2 none of the other coils is close to its critical current for even 55A, where $Coil\#3$ is far above its I_c. Consequently, Arr2 has higher potential (although not utilized) MMF and if $Coil\#3$ is to be substituted with one more 2G coil similar to $Coil\#6$, Arr2 would be the one with superior performance.

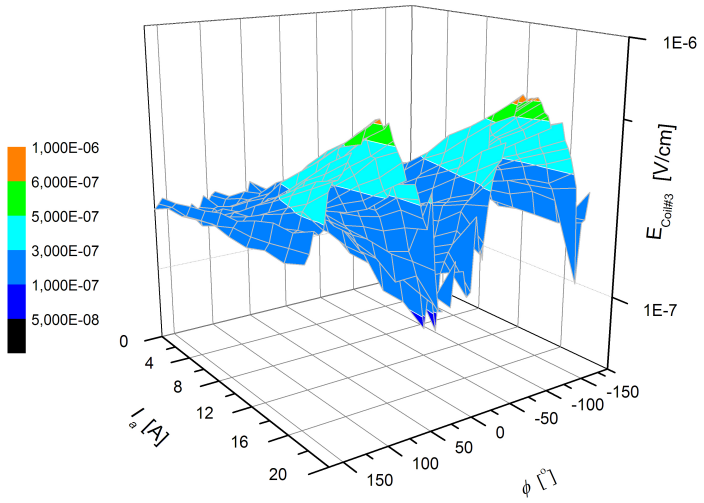

Figure F.1: *Coil#3* **in Arr1 with** I_{coil}**=45 A** - he HTS field winding in Arr1 is connected in serial connection and is supplied with I_{coil}=45 A. The armature reaction, I_a, with values from 0 A – 18 A is at the X axis and the span of 360° of the ϕ at Y axis.

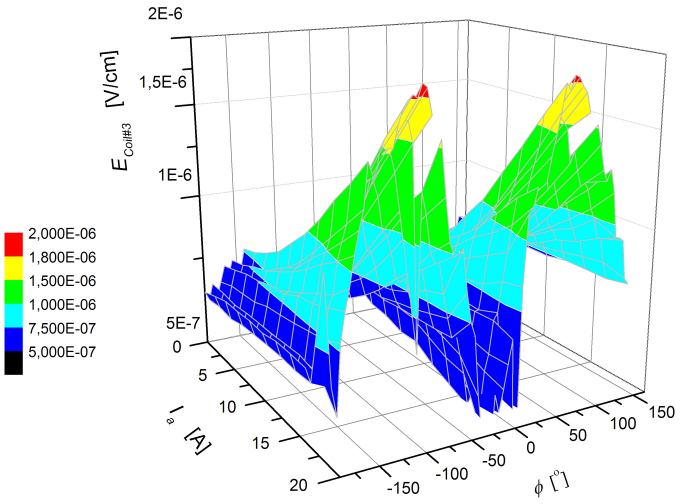

Figure F.2: *Coil#3* **in Arr1 with** I_{coil}**=50 A** - he HTS field winding in Arr1 is connected in serial connection and is supplied with I_{coil}=50 A. The armature reaction, I_a, with values from 0 A – 18 A is at the X axis and the span of 360° of the ϕ at Y axis.

Appendix G

Appendix 5: Published and submitted papers

G.1 Paper: Design study of 10 kW superconducting generator for wind turbine applications

Presented at Applied Superconductivity Conference (ASC) 2010. The article is peer reviewed. The article is published and available online at IEEE Xplore.

Design Study of 10 kW Superconducting Generator for Wind Turbine Applications

A. B. Abrahamsen, N. Mijatovic, E. Seiler, M. P. Sørensen, M. Koch, P. B. Nørgård, N. F. Pedersen, C. Træholt, N. H. Andersen, and J. Østergård

***Abstract*—We have performed a design study of a 10 kW superconducting slow rotating generator suitable for demonstration in a small scale wind turbine, where the drive train only consists of the turbine blades connected directly to the generator. The flux density in the superconducting rotor is chosen as B = 1 Tesla to be similar to the performance of permanent magnets and to represent a layout, which can be scaled up in future off-shore wind turbines. The proposed generator is a 8 pole synchronous machine based on race-track coils of high temperature superconducting tapes and an air cored copper stator enclosed in an iron shield.**

***Index Terms*—Superconductivity, synchronous generator, wind turbines.**

I. Introduction

THE challenges of future energy demand and the possible global warming due to fossil fuel consumption have increased the interest of large-scale use of wind turbines for electricity production. Most present turbines are operated on-shore, but the interference with the residents and higher wind speeds at sea is the motivation for building off-shore wind farms. A major fraction of the cost of off-shore farms is due to the foundations of the turbines, the grid connection and maintenance. Thus there is an incentive to place large turbines at sea and power ratings of 10 MW are desirable in 10 years. A superconducting generator might be advantageous for 10 MW turbines, because the weight and volume can be reduced compared to a conventional generator and thereby simplifying the turbine design. The gearbox of present turbines can also be omitted by utilizing a multi-pole generator which is driven directly by the turbine rotor. We have done a design study of a 10 kW direct driven multi-pole superconducting generator, which can be installed in a small wind turbine and used to evaluate the robustness of the superconducting technology in a wind turbine environment, before the generator is scaled up by 3 orders of magnitude to the large scale turbines.

Manuscript received August 26, 2008. First published June 05, 2009; current version published July 15, 2009. This work was supported in part by the Technical University of Denmark under the globalization funded project superwind.dk

A. B. Abrahamsen, E. Seiler, and N. H. Andersen are with the Materials Research Division, Risø National Laboratory for Sustainable Energy, Technical University of Denmark, DK-4000 Roskilde, Denmark (e-mail: asab@risoe.dtu.dk; eugen.seiler@risoe.dk; niels.hessel@risoe.dk).

N. Mijatovic, M. Koch, N. F. Pedersen, C. Træholt, and J. Østergård are with the Department of Electrical Engineering, Technical University of Denmark, DK-2800 Lyngby, Denmark (e-mail: nm@elektro.dtu.dk; mk@oersted.dtu.dk; nfp@oersted.dtu.dk; ctr@oersted.dtu.dk; joe@oersted.dtu.dk).

M. P. Sørensen is with the Department of Mathematics, Technical University of Denmark, DK-2800 Lyngby, Denmark (e-mail: M.P.Soerensen@mat.dtu.dk).

P. B. Nørgård is with the Wind Energy Division, Risø National Laboratory for sustainable energy, Technical University of Denmark, DK-4000 Roskilde, Denmark (e-mail: joe@oersted.dtu.dk).

Digital Object Identifier 10.1109/TASC.2009.2017697

II. Small Scale Wind Turbines

Small wind turbines are commercially available and a wind turbine from Gaia-Wind [1] is operated at Risø -DTU [2]. It is a stall regulated turbine with a conventional drive train consisting of a gearbox and a fast rotating asynchronous generator with a power rating of 11 kW. This technology represents the first generation of drive trains, but direct driven synchronous generators based on permanent magnets such as $\mathrm{Nd_2Fe_{14}B}$ have recently been introduced even in small scale turbines [3]. A superconducting direct driven synchronous generator will represent a third generation of drive trains for wind turbines, since superconducting coils are expected to provide magnetic flux densities exceeding the operation flux densities of the permanent magnets. The specifications of a superconducting generator for a small scale wind turbine are outlined according to the properties of the Gaia wind turbine. A wind turbine converts the kinetic energy of the wind into electric energy and the power of the wind P_{wind} is ideally given by [4]

$$P_{wind} = \frac{1}{2}\rho v_0^3 A_{rotor} C_P \tag{1}$$

where ρ is the density of the air, v_0 is the average wind speed, $A_{rotor} = \pi R_{rotor}^2$ is the rotor area swept by the blades with a length of R_{rotor} and C_P is the power coefficient, which is determined by the aerodynamic properties of the rotor and is related to the number of blades, the shape of the blade and the blade angle with respect to the incoming wind. The power coefficient determines the fraction of the available kinetic energy, which is transformed into torque on the turbine shaft. It is often given as function of the ratio λ between the blade tip speed v_T and the wind speed v_0

$$\lambda = \frac{v_T}{v_0} = \frac{R_{rotor}\omega}{v_0} \tag{2}$$

where Ω is the angular speed related to the rotor frequency by $\Omega = 2\pi f_{rotor}$.

The available wind power and the power curve of the Gaia turbine is shown on Fig. 1 as function of the average wind speed v_0. The C_P curve has been plotted by assuming a constant rotation speed of 56 Revolutions Per Minute (rpm) and $R_{rotor} = 6.5\,\mathrm{m}$. It is seen that the nominal 11 kW power production is first reached when the wind speed exceeds the nominal wind speed of $v_0 = 9.5\,\mathrm{m/s}$. The Gaia wind turbine illustrate how the stall

1051-8223/$25.00 © 2009 IEEE

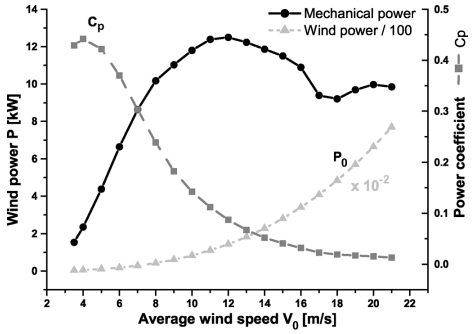

Fig. 1. Mechanical power curve P_{wind} of a small wind turbine as function the average wind speed when operated at a constant rotation speed of 56 rpm [2]. The wind power $P_0 = (1/2)\rho v_0^3 A_{rotor}$ available at the rotor is scaled by a factor 10^{-2} and is shown as well as the power coefficient C_P of the 2 blade rotor. A maximum of the available mechanical power $P_{wind} = P_0 C_P$ of the rotor is seen at intermediate wind speed due to the stall limitation of C_P.

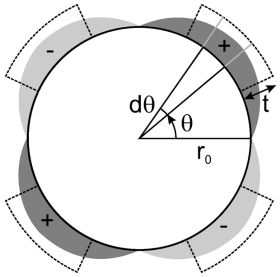

Fig. 2. Sinusoidal and box representation of turn distribution of rotor or stator winding of a 4 pole machine. The + and − sign refer to a current direction in and out of the paper. The turn distribution is assumed to be $n(\theta) = n_0 \sin(p\theta)$ where p is the number of pole pairs and n_0 is the turn density per circumference. Thus the equivalent sheet current is $I(\theta) = n(\theta)i$, where i is the current of each wire.

regulation is obtained by the aerodynamic properties of the rotor and the rotation speed is fixed by the frequency of the electricity grid down scaled by the conversion factor of the gearbox. The available space in the nacelle is approximately a diameter of $D_{nacelle} = 0.8$ m and a length of $L = 1.0$ m. Large turbines today are pitch regulated by controlling the blade angle with respect to the incoming wind direction, whereby different power curves can be chosen. Additionally it becomes more common to decouple the generator frequency from the grid frequency by passing all the power of the turbine through power electronics consisting of two back-to-back coupled AC/DC converters. The generator of such a system can be of the synchronous type with the rotation speed controlled by the power electronics and this is also assumed to be the case for future superconducting wind turbine generators.

III. Analytical Generator Model

We will use the analytical description of an air-cored synchronous machine [5], [6] to determine the properties of a slow rotating generator suitable for a gearless drive train of the Gaia turbine. The problem is only considered in the two dimensional rotation plane of the cylindrical machine, whereby the magnetic flux density distribution $\mathbf{B}(\theta, \mathbf{r})$ can be determined from the axial component of the vector potential. A simple representation of the rotor and stator coils is obtained by introducing a sinusoidal turn distribution

$$\frac{d}{dl} n(\theta) = n_0 \sin(p\theta) \tag{3}$$

where θ is the angle around the machine circumference as shown in Fig. 2, p is the number of pole pairs and n_0 is the maximum winding density per circumference segment $dl = r_0 d\theta$. Thus $n(\theta)$ gives the winding distribution, where the thickness of the winding layer is varying as a sinus function and the sheet current distribution is obtained by multiplying by the current i in each wire, $I(\theta) = n(\theta)i$. However the sinusoidal turn distribution is often realized by a box distribution as illustrated on Fig. 2 and the prefactor of (3) is given by the first harmonic obtained from the Fourier transform of the box function.

The box function is specified as

$$n_b(\theta) = \begin{cases} n_{b0}, & \left|\frac{\pi}{2p} - \theta\right| < \delta\theta_b \\ -n_{b0}, & \left|-\frac{\pi}{2p} - \theta\right| < \delta\theta_b \end{cases} \tag{4}$$

where $\delta\theta$ is half of the opening angle of the box region. By assuming a constant winding density per area n_A then one can obtain the wire density per circumference segment $dl = r_0 d\theta$ from

$$n_{b0} = \frac{\int_{r_0}^{r_0+t} n_A r dr \, d\theta}{r_0 \, d\theta} = \frac{n_A t(t + 2r_0)}{2r_0} \tag{5}$$

where t is the winding layer thickness and r_0 is the radius of the winding support.

The Fourier coefficients b_k of the series representation $n(\theta) = \sum_{k=1}^{\infty} b_k \sin((k\pi\theta/\theta_{max}))$ with $\theta_{max} = \pi/p$ then becomes

$$b_k = \frac{1}{\theta_{max}} \int_{-\theta_{max}}^{\theta_{max}} n_b(\theta) \sin\left(\frac{k\pi\theta}{\theta_{max}}\right) d\theta \tag{6}$$

Thus the first harmonic $(k = 1)$ of the box function becomes

$$b_1 = \frac{4}{\pi} n_{b0} \sin(p\delta\theta_b) = \frac{4}{\pi} n_{b0} k_w \tag{7}$$

where k_w is called the fundamental harmonic winding factor [5]. The sheet current distribution then becomes

$$\frac{d}{dl} i(\theta) = b_1 i \sin(p\theta) = A \sin(p\theta) \tag{8}$$

where A is the sheet current density in the unit $[A/m]$

$$A = b_1 i = \frac{4}{\pi} n_{b0} k_w i \tag{9}$$

A. Magnetic Flux Distribution

The flux distribution at r caused by the turn distribution (3) at r_0 and enclosed by an iron shield at r_{S2} has been derived analytically in [5]

$$\left.\begin{matrix} B_r \\ B_\theta \end{matrix}\right\} = \frac{\mu_0 A}{2}\left(\frac{r_0}{r}\right)^{p+1}\left[1+\eta\lambda_s\left(\frac{r}{r_{S2}}\right)^{2p}\right]\left\{\begin{matrix}\cos(p\theta)\\ \sin(p\theta)\end{matrix}\right. \quad (10)$$

where μ_0 is the vacuum permeability and the square bracket is the enhancement factor due to the iron shield. The factor $\eta\lambda_s$ ranges between 0 and 1 in case of a fully saturated and infinitely permeable iron shield.

B. Machine Power

The output power of a synchronous machine consisting of a rotor and 3 stator turn distributions given by (3) at a radius r_R and r_S can now be calculated as

$$P = \frac{\pi^2}{\sqrt{2}} k_w B_{S0} A_s D^2 L_{gen} n_s \quad (11)$$

where B_{S0} is the peak radial flux density at the stator winding at r_S [6]. A_S is the sheet current of the 3-phase stator windings and $A_S = (3/2)A$ when the wire current i is an alternating current with root mean square amplitude i_{rms}. The stator diameter $D = 2r_S$ has been introduced, the effective length of the generator is L_{gen} and the rotation speed n_s is in [revolutions s^{-1}]. Thus the output power of a 10 kW machine consisting of a superconducting rotor and Cu stator inclosed in an iron shield can now be calculated from a box representation of the windings. We are aiming for a rotor field at the stator radius of the order $B_{S0} \sim 1$ T to match the magnetic flux density obtained by permanent magnets. The generator must fit into the nacelle giving a diameter $D = 0.56$ m and length of $L_{gen} = 0.4$ m. Finally a rotation speed of $n_s = 56\ \mathrm{rpm}/60\ \mathrm{s\ min^{-1}} = 0.93\ \mathrm{s^{-1}}$ results in a stator sheet current density $A_S = 1.2\cdot 10^4\ \mathrm{Am^{-1}}$. The physical realization of such a machine is proposed below.

IV. Generator Layout

The coil geometry of a superconducting generator is restricted by the mechanical properties of the used superconducting wire and in the case of the ceramic high temperature superconductors (HTS) one can not bend the flat wires, which are often called tapes, on a diameter less than the critical bending diameter D_{cb}. Typical bending diameters of HTS tapes are $D_{cb,BiSCCO} = 50{-}70$ mm for the $Bi_2Sr_2Ca_2Cu_3O_{10+x}$ (Bi2223) tapes and $D_{cb,YBCO} = 25{-}35$ mm for $YBa_2Cu_3O_{6+x}$ (YBCO) coated conductors. The tape thickness $t_{tape} = 0.30{-}0.32$ mm is typical including 100 μm plastic insulation wrapped around the wire. The width of the tape is typically $w_{tape} = 4.3{-}4.5$ mm again including insulation. Thus the winding density of HTS tapes is typically, $n_A = 7.3\cdot 10^5\ \mathrm{m^{-2}}$. Coils of HTS tape is often winded in the form of a double pan-cake coil with an inner diameter larger than the critical bending diameter D_{cb} and a thickness equal to $2w_{tape}$.

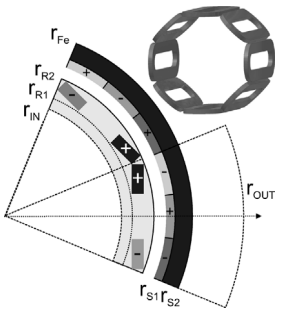

Fig. 3. Layout of 8 pole synchronous generator. The inner support structure spans from r_{in} and to the rotor between r_{R1} and r_{R2}. The stator windings of the 3-phases are spanned between r_{S1} and r_{S2}. An iron shield expands until r_{Fe} and the outer radius of the turbine nacelle is r_{out}. Inset: 3D representation of superconducting race-track rotor coils made of double pan-cake windings.

TABLE I
Generator Dimensions

Rotor	Stator
$r_{in} = 0.200$ m	$r_{S1} = 0.270$ m
$r_{R1} = 0.215$ m	$r_{S2} = 0.290$ m
$r_{R2} = 0.250$ m	$r_{Fe} = 0.320$ m

The superconducting rotor coils are based on the race-track geometry, where the strait section is assumed to be the effective length of the machine, $L_{gen} = 0.4$ m, and the inner opening of the coil is determined by the bending diameter of the HTS tapes $l_{air} = 0.08\ \mathrm{m} > D_{cb}$ as illustrated on Fig. 3. The frequency f of the generator voltage and current is related to the synchronous rotation speed ω and the number of pole pairs p in the generator $f = p\Omega/2\pi = 3.7$ Hz. Fig. 3 shows the 8 pole rotor coil geometry with each pole produced by a race-track coil consisting of two double pan-cakes. The thickness and width of the coil is $t_c = 2.0$ cm and $w_c = 5.0$ cm respectively. The positions of the rotor and stator windings are given in Table I, but the box representation of the rotor is assumed to span $r_{Rbox} = 0.223{-}0.243$ m and the opening angle is $\delta\theta_b = (\pi/2p)(2/3)$.

V. Results and Discussion

The load line of the rotor coils is determined from the field and temperature dependent critical current $I_C(H,T)$ of different tapes [7]–[9] by calculating the resulting flux density in the rotor coil from (10) when the $I_C(H,T)$ at a certain field $\mu_0 H_0$ is inserted in the expression for the sheet current A given by (9). If the flux density produced by the coil exceeds the flux density used to determine the I_C then superconductivity is suppressed. Fig. 4 shows the maximum flux density along the θ direction in the rotor coil as function of the field used to determine I_C and the critical region is at the left of the dashed line. The θ component corresponds to the magnetic flux density perpendicular to the tape surface and will result in the lowest I_C due to the anisotropy of the critical current [10]. A safety margin of 50-80% of I_C must be applied to lower the probability of quenches of the rotor coils.

From Fig. 4 it is seen that the coated conductors will have a $B_{max} = 0.5{-}0.8$ Tesla corresponding to an $I_C = 50{-}120$ A

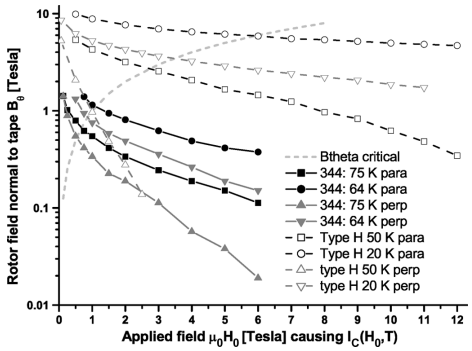

Fig. 4. Tangential magnetic flux density B_θ at the rotor winding given by (10) when inserting the field depend critical current $I_C(H_0, T)$ of different tapes into the expression for the rotor sheet current (9) (344 and Type H refer to coated conductors from American Superductor and Bi-2223 tapes from Sumitomo respectively). The dashed line indicates the critical load line when the flux density of the coil exceeds the flux density specified by the critical current. Thus the operational load line of the rotor must be below the critical load line by a sufficient safety margin.

at $T = 75$ K and $T = 64$ K respectively. The large anisotropy of the Bi-2223 pinning properties makes operation at $T = 77$ K impossible due to the complete suppression of superconductivity when a magnetic flux component perpendicular to the tape is present. Thus a maximum flux density at the conductor of $B_{max} = 1{-}3$ T is possible with $I_C = 100{-}550$ A at $T = 50$ K and $T = 20$ K respectively. An operational engineering critical current of $J_e = 1.1 \cdot 10^4$ Acm^{-2} is assumed to fulfil the safety margin and this will correspond to a wire current of $I = 150$ A. The corresponding sheet current (9) becomes $A_R = 2.5 \cdot 10^6$ Am^{-1} and the maximum flux densities at the rotor coil and stator is predicted from (10) to become $|B|_{rotor,max} = 1.79$ T and $|B|_{stator,max} = 0.96$ T. Finite element calculation of the layout shown on Fig. 3 have confirmed the predicted flux densities and shows that the analytical box winding description is a good approximation of realistic superconducting coils.

A. Stator Properties

The current of one stator phase winding I_S can be determined by choosing a base voltage of $U_S = 400\,\mathrm{V}/\sqrt{3} = 231$ V

$$P_{phase} = U_s I_s \Rightarrow I_s = \frac{P_{phase}}{U_s} = \frac{10\,\mathrm{kW}/3}{231\,\mathrm{V}} = 14.4\,\mathrm{A} \quad (12)$$

By assuming a stator winding made of square copper wire with area $A_{Cu} = 5.3$ mm^2 then one can determine the wire area density needed to obtain a sufficient stator sheet current A_S. First A_S is calculated from the rotor flux density found in the previous section and the output power given by (11)

$$A_s = \frac{\sqrt{2}}{\pi^2} \frac{P}{k_w B_{S0} D^2 L_{gen} n_s} = 1.5 \cdot 10^4\,\mathrm{Am}^{-1} \quad (13)$$

TABLE II
LENGTH AND WEIGHT OF GENERATOR COMPONENTS

Part	Length[m]	Weight [kg]
Rotor wire	7539	89 - 93
Rotor former	L = 0.66 m	73
Stator wire	2149	102
Iron	R = 0.29 → 0.32 m & L = 0.4 m	181

The stator wire density is then determined from (5), (7) and (9) applied to the stator geometry

$$n_{A,S} = \frac{\pi}{2} \frac{\frac{2}{3} A_s r_{S1}}{t(t + 2r_{S1}) k_{w,S} I_s} = 1.0 \cdot 10^5\,\mathrm{windings\,m}^{-2} \quad (14)$$

which correspond to approximately 20% of the stator area for epoxy. The resistance of the stator is estimated to be $R_S = 4.06\,\Omega$ which will give a stator loss of $P_{Cu} = R_S I_S^2 = 842$ W and a stator efficiency of 0.92.

B. Wire Length and Generator Weight

The estimated length of the wires needed for the generator is shown in Table II. The weight has been estimated by assuming that the density of the HTC superconductor tapes is either equivalent to a 70/30 ratio of silver and Bi2223 or to pure nickel representing the coated conductors. Additionally the weight of the rotor support is estimated from the density of glass fiber. It is seen that the choice of a high rotor flux density comes at the price of a larger amount of superconductor in the rotor than copper in the stator. Thus from an economical point of view it would be desirable to replace some superconductor by Cu in the stator, but the present design is focused on demonstrating a superconducting coil layout, which can be scaled up to larger power ratings in future off-shore turbines. It is interesting to note that the total weight of Table II is $W_{total} = 449$ kg, which must be compared to 300 kg of gearbox and generator in the Gaia turbine. An increase of the drive train weight is often seen when changing to direct drive, but it is expected that the superconducting machines will become lighter than the conventional at high power ratings [11].

VI. CONCLUSION

We have shown a possible design of a direct driven 10 kW superconducting 8 pole synchronous generator based on 7.5 km of high temperature superconductor tape and that this generator might be demonstrated in a small scale wind turbine. An optimization of the generator is needed as a next step as well as the design of a cryogenic cooling system. The operation temperature will be determined by the trade off between higher engineering critical current density J_e at low temperatures and the power loss of the cooling system. However tapes with higher J_e would be needed if the operation temperature should be increased up to $T = 50$ K.

REFERENCES

[1] (2008). Gaia-Wind A/S [Online]. Available: www.gaiawind.com

[2] H. Bindner, P. A. C. Rosas, R. Teodorescu, and F. Blaabjerg, "Stand-Alone Version of the 11 kW Gaia Wind Turbine," 2004, ISBN 87-550-3376-8, Risø report: risø-R-1480 (EN).

[3] Aircon GmbH & Co., Web-page [Online]. Available: www.aircon-international.com

[4] T. Burton, D. Sharpe, N. Jenkins, and E. Bossanyi, *Wind Energy Handbook*. New York: Wiley, 2001, ISBN 0471489972.

[5] A. Hughes and T. J. E. Miller, "Analysis of fields and inductances in air-cored and iron-cored synchronous machines.," *Proc. IEE*, vol. 124, no. 2, pp. 121–126, 1977.

[6] T. J. E. Miller and A. Hughes, "Comparative design and performance of air-cored and iron-cored synchronous machines," *Proc. IEE*, vol. 124, no. 2, pp. 127–132, 1977.

[7] M. W. Rupich, U. Shoops, D. T. Verebelyi, and C. L. H. Thieme *et al.*, "The development of second generation HTS wire at American Superconductors," *IEEE Trans. Appl. Supercond.*, vol. 17, no. 2, pp. 3379–3382, Mar. 2007.

[8] N. Ayai, M. Kikuchi, K. Yamazaki, and S. Kobayashi *et al.*, "The Bi-2223 superconducting wires with 200A-class critical current," *IEEE Trans. Appl. Supercond.*, vol. 17, no. 2, pp. 3075–3078, Mar. 2007.

[9] (2007). Sumitomo Electric. [Online]. Available: www.sei.co.jp/super/hts_e/index.html

[10] R. Foltyn, L. Civale, L. MacManus-Driscoll, X. Jia, B. Maiorov, H. Wang, and M. Maley, "Materials science challenges for high-temperature superconducting wire," *Nature Materials*, vol. 6, p. 631, 2007.

[11] S. S. Kalsi, K. Weeber, H. Takesue, C. Lewis, H. W. Neumueller, and R. D. Blaugher, "Development status of rotating machines employing superconducting field windings," *Proc, IEEE*, vol. 92, no. 10, pp. 1688–1695, Oct. 2004.

G.2 Paper: Superconducting wind turbine generators

Presented as invited talk at European Conference on Applied Superconductivity (EUCAS) 2009. The article is peer reviewed. The article is published and available online at Superconductor Science and Technology.

Supercond. Sci. Technol. **23** (2010) 034019 (8pp) doi:10.1088/0953-2048/23/3/034019

Superconducting wind turbine generators

A B Abrahamsen[1], N Mijatovic[2], E Seiler[1], T Zirngibl[1], C Træholt[2], P B Nørgård[3], N F Pedersen[2], N H Andersen[1] and J Østergård[2]

[1] Materials Research Division, Risø-DTU, Frederiksborgvej 399, 4000 Roskilde, Denmark
[2] Department of Electrical Engineering, Technical University of Denmark, DK-2800 Lyngby, Denmark
[3] Wind Energy Division, Risø-DTU, Frederiksborgvej 399, 4000 Roskilde, Denmark

E-mail: asab@risoe.dtu.dk

Received 16 September 2009, in final form 1 November 2009
Published 22 February 2010
Online at stacks.iop.org/SUST/23/034019

Abstract
We have examined the potential of 10 MW superconducting direct drive generators to enter the European offshore wind power market and estimated that the production of about 1200 superconducting turbines until 2030 would correspond to 10% of the EU offshore market. The expected properties of future offshore turbines of 8 and 10 MW have been determined from an up-scaling of an existing 5 MW turbine and the necessary properties of the superconducting drive train are discussed. We have found that the absence of the gear box is the main benefit and the reduced weight and size is secondary. However, the main challenge of the superconducting direct drive technology is to prove that the reliability is superior to the alternative drive trains based on gearboxes or permanent magnets. A strategy of successive testing of superconducting direct drive trains in real wind turbines of 10 kW, 100 kW, 1 MW and 10 MW is suggested to secure the accumulation of reliability experience. Finally, the quantities of high temperature superconducting tape needed for a 10 kW and an extreme high field 10 MW generator are found to be 7.5 km and 1500 km, respectively. A more realistic estimate is 200–300 km of tape per 10 MW generator and it is concluded that the present production capacity of coated conductors must be increased by a factor of 36 by 2020, resulting in a ten times lower price of the tape in order to reach a realistic price level for the superconducting drive train.

(Some figures in this article are in colour only in the electronic version)

1. Introduction

There are many indications that our dependency on fossil fuels must be addressed in the next few decades in order to formulate solutions to problems such as lack of resources and the impact on the climate. In this context there have been many political discussions on how to regulate the release of CO_2, with agreements such as the Kyoto protocol. The reduction of the CO_2 emissions recommended by the Intergovernmental Panel of Climate Change (ICPP) is rather high and of the order 50–80% by the year 2050. In a European perspective a target of 20% greenhouse gas reduction by 2020 compared to the 1990 level, 20% of energy demand supplied by renewable sources and a 20% reduction of the energy consumption have been decided among the member states as an initial step towards addressing the climate challenge. Wind power is considered as one of the main technologies to deliver the renewable energy for Europe and the European Wind Energy Association has formulated scenarios that predict a need for 300 GW of installed wind power by 2030 [1]. A share of 120 GW is expected to be installed offshore, because the population density in the coast areas of the member states of the European Union (EU) is relatively high and offshore installation will cause less interference with the habitants. It is interesting to compare the predictions from the European Wind Energy Association (EWEA) with the development of the offshore capacity, as shown in figure 1. The offshore capacity was first significantly increased around the year 2000 and the 626 turbines installed by the end of 2008 had a 1.5 GW capacity, corresponding to 2.2% of the total capacity [2]. The working horse of the present offshore wind farms is a 2.3 MW turbine and the largest farm is 166 MW. However, the turbine size of the wind farms under construction will have an average size between 3.0 and 3.6 MW and a significant number of 5 MW turbines will be installed. A further increase of the turbine size is expected, because the turbine price is only about half of the wind farm installation price with foundations and grid connections being the other major costs. Thus the optimal

 © 2010 IOP Publishing Ltd Printed in the UK

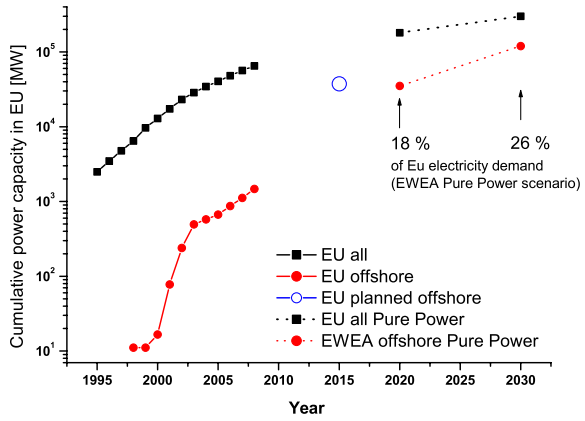

Figure 1. Total and offshore wind power capacity of Europe and also the capacity that will be needed to fulfil the European goal of having a 20% energy supply from renewable sources by 2020. The capacity has been reproduced from the European Wind Energy Association (EWEA) statistics [2] and the Pure Power scenario [1].
(This figure is in colour in the electronic version only)

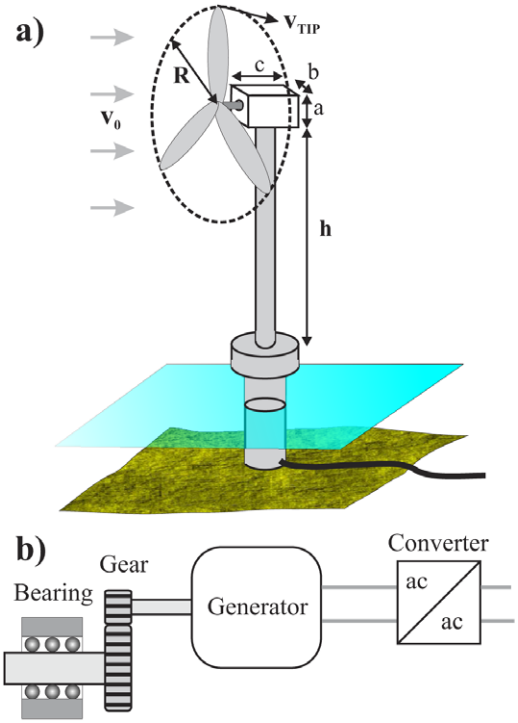

Figure 2. (a) Offshore turbine with a rotor blade radius of R, a nacelle size given by a, b and c, and tower height h. The turbine is shown on a static foundation and is connected to an offshore transformer station by the underwater cable. (b) The main components of the drive train are bearings holding the turbine shaft, a gear box, a generator and a frequency converter for connection to the electricity grid of a wind farm.

offshore wind turbine size will depend on the local wind and water conditions of the installation site and preliminary analysis in the UPWIND project indicate that 10 MW offshore turbines will probably be desirable [4]. The number of 10 MW turbines needed to fulfil the EU offshore target is then of the order 12 000 and with a 1 km distance between the turbines an area of 110 km × 110 km would be needed in the North Sea. The installation price of offshore wind power is expected to be approximately 1300–1500 Euro kW^{-1} and the up-coming offshore market would be of the order 180 billion euros [1]. In contrast to the above analysis, the onshore market is considered to be quite mature and the size of the onshore turbines is not expected to increase above the present 3–3.6 MW size due to transportation limitations. The installation price of onshore turbines is expected to be 600–700 Euro kW^{-1} and the future market is of the same order as the offshore market prediction above.

From a superconducting point of view it should be asked whether superconducting technology can provide technical solutions to the up-scaled offshore turbines, which will lower the production price of the electricity over the 20 year lifetime of the entire wind farm. The advantages of the superconducting drive train are a high torque and the mechanical simplification in the form of the direct drive, where the turbine blades are connected directly to the generator without a gearbox. This simplification is envisioned to increase the reliability to a level that will match the demand of the offshore application [5]. The high magnetic field strength produced by superconducting coils is expected to provide a more lightweight and compact design of the direct drive than can be done with copper coils, permanent magnets and magnetic iron [6]. At present, the superconducting generators are not expected to have an impact on the onshore turbines due to the limited size growth, but if the solution can be made economically and technically feasible in the offshore sector then they might eventually also be used onshore [5].

This paper is organized to give an introduction to basic wind turbine physics and present a turbine scaling from 1.3 to 10 MW. The properties of a suitable superconducting generator for the 10 MW power range are discussed and a 10 kW demonstration generator, which can be tested in a small wind turbine, is suggested as the starting point before the generator size is scaled up in successive steps to 100 kW, 1 MW and then 10 MW. Finally the challenges of providing a sufficient supply of superconducting tape at a reasonable price will be discussed.

2. Offshore wind turbines

Figure 2(a) shows the layout of a typical three bladed offshore turbine with rotor radius R given by the blade length, a nacelle size given by the lengths a, b and c, and a tower height h on top of an offshore foundation with an underwater grid connection. The average velocity of the wind passing the rotor plane is v_0 and the velocity of the tip of the blade is v_{TIP}. The kinetic energy of the incoming wind provides a power of [3]

$$P_W = \tfrac{1}{2}\rho\pi R^2 v_0^3 \quad (1)$$

where $\rho = 1.225\ kg\ m^{-3}$ is the mass density of the air at $T \sim 15\,^{\circ}C$. A fraction given by the power coefficient $C_P(\lambda, \beta)$ of P_W is converted into mechanical power by the aerodynamic properties of the rotor plane, which are characterized by the ratio λ between the incoming wind velocity v_0 and the tip speed of the blade and by the pitch angle β of the blade with respect to the rotor plane. Pitching of the blades is used to smoothen

the fluctuating wind loads and to halt the turbine in case of strong winds. The power coefficient C_P has a maximum when changing λ because the extraction of the kinetic energy depends on the change of the wind velocity before and after the rotor plane. If the blades are at a stand still all the wind is passing the rotor plane without interaction and if the blades are rotating very fast then the rotor plane will appear as a solid disk deflecting all the wind around the rotor plane. The mechanical power P_T of the rotor shaft then becomes

$$P_T = P_W C_P(\lambda, \beta) \tag{2}$$

$$\lambda = \frac{v_{tip}}{v_0} = \frac{R\omega}{v_0} \tag{3}$$

where ω is the rotation speed of the turbine blades.

Figure 2(b) shows the components of the drive train, which is converting the kinetic energy of the rotor into electricity. It consists of bearings holding the turbine shaft, a gear box for increasing the rotational speed of the subsequent generator, which is connected to the electricity grid through a power electronics frequency converter. The frequency converter makes it possible to decouple the generator and grid frequency, and also to improve the fault ride through capabilities imposed by the system operator of the grid.

2.1. Challenges of offshore wind turbines

The rough environment at sea is increasing the need for tougher and most importantly more reliable technology than is needed for onshore turbines. It is therefore believed that the offshore turbines developed in the future will be based on technologies different from the onshore turbines, and that innovative but expensive technologies will be introduced if they enable total cost minimization. The cost minimization of offshore wind power involves many aspects as listed below.

Planning. Design wind farm and get authorization to build, which might take several years.

Installation. Cost C will scale with the number of turbines N and farm components:

$$C_I \sim \sum^{N}(C_{I\,\text{turbine}} + C_{I\,\text{foundation}} + C_{I\,\text{connection}}) + 1(C_{I\,\text{transformer}} + C_{I\,\text{cable}}).$$

Operation and maintenance. Income I and cost C will scale with the number of turbines during the 20 year lifetime

$$I_O \sim \sum^{N} \int (I_{\text{turbine}})\,\mathrm{d}t$$

$$C_{OM} \sim \int \left[\sum^{N}(C_{\text{turbine}} + C_{\text{foundation}} + C_{\text{connection}}) + 1(C_{\text{transformer}} + C_{\text{cable}}) \right] \mathrm{d}t.$$

Decommissioning/repowering. This will be a cost if everything has to be removed after 20 years or an income if the foundations can be sold and new turbines are installed.

The cost optimization of the entire wind farm is a complicated problem and interdependencies of the separate cost functions must be known not only for the turbines themselves, but also for the rest of the components such as the foundations and connecting cables. This task is undertaken in the present EU project UPWIND [7] and it would be interesting to examine the possible impact of a superconducting generator in the future. The simple economical model presented above illustrates that reliability of the turbine is a major concern when operating offshore farms, because a failure might stop the electricity production and thereby the income I_O for a considerable time until the weather conditions permit a major repair, which in itself adds to the maintenance cost. The worst case scenario is a major failure at the beginning of the winter period and no access to the turbine until the winter storms are gone. Since most of the energy production of a turbine is done during this period it also means a large loss of income.

Historically the drive trains have given huge problems in the offshore turbines, with bearing and gearbox failures as the major challenges [8]. Until recently most turbines were built with a drive train consisting of a three stage gearbox with a gearing ratio of approximately 1:100 and a fast rotating double fed induction generator with the stator connected directly to the net. Limited speed regulation can be done by controlling the current of the rotor using power electronics [9]. However, a number of alternative drive trains have been suggested with the focus on simplifying or eliminating the gearbox [10]. From figure 2 it is seen that the consequence of removing the gearbox would be the need of a generator with a torque matching the turbine rotor and which operates at a much lower rotation speed. A drawback of the higher torque of the alternative generators is often a larger weight and price. Before the different drive train solutions are compared with the superconducting drive train then an estimate of the needed shaft torque will be given for turbines approaching the 10 MW power range.

2.2. Up-scaling of future offshore turbines

The description of the turbine physics in section 2.1 can be used to predict the properties of turbines exceeding the present power limit of 5 MW. The following scaling is inspired by a similar scaling study by Li *et al* [11] of the Multibrid 5 MW wind turbine, which is characterized by the ideal power curve shown in figure 3. It is seen that the turbine is first started above the cut-in velocity and that the maximum power production is reached at the ideal rated wind velocity v_{RI}. The turbine is stopped and secured against detrimental loads above wind velocities given by v_{cut}. Turbines in the 5 MW class such as the Multibrid M5000 and the UPWIND reference turbine identical to a RePower 5M turbine are regulated by keeping the power coefficient C_P at the maximum $C_{P\,max}$ of the rotor and at the optimal tip-speed ratio $\lambda = \lambda_{opt}$ whenever the incoming wind velocity is $v_{in} < v_0 < v_{RI}$ [13]. The power coefficient is then decreased by pitching the blade angle when $v_{RI} < v_0$ and a constant shaft power is obtained by pitch regulation. Practical power curves are often smoother and one can define the ideal v_{RI} corresponding to an ideal v^3 scaling and an experimental

Table 1. Scaling of wind turbine properties as a function of the rated power.

	a	b	c	d	Predicted	
Rated power P_N (MW)	1.3	2.0	3.0	5.0	8.0	10.0
Shaft power P_T (MW)[e]	1.40	2.16	3.24	5.40	8.64	10.80
Rated wind velocity v_R (m s^{-1})	13.5	15.0	15.0	12.0	12.0	12.0
Rated ideal wind velocity v_{RI} (m s^{-1})	11.7	11.4	12.0	12.0	12.0	12.0
Tip-speed-ratio $\lambda(v_R)$	4.57	4.70	5.05	7.48	7.48	7.48
Rotor diameter $2R$ (m)	61.6	79.5	90.1	116.4	147.2	164.6
Tip speed v_{TIP} (m s^{-1})	61.7	70.5	75.8	89.8	89.8	89.8
Rotation speed ω_R (rad s^{-1})	2.00	1.77	1.68	1.54	1.22	1.09
Rotation speed $\omega_{R,rpm}$ (rpm)	19.1	17.0	16.1	14.8	11.7	10.4
Shaft torque τ_T (10^6 N m)	0.70	1.22	1.93	3.50	7.08	9.90
Hub height h (m)	55.8	64.7	70.1	83.2	98.6	107.3
Annual Energy Production AEP (GWh)				24.2	39.0	48.8
Max $AEP_{100\%}$ (GWh)				43.8	70.1	87.6

[a] Siemens SWT1.3-62. [b] Vestas V80-2.0 MW.
[c] Vestas V90-3.0 MW. [d] Multibrid M5000.
[e] Assuming $C_{P\,max} = 0.48$ and a drive train loss of 8%.

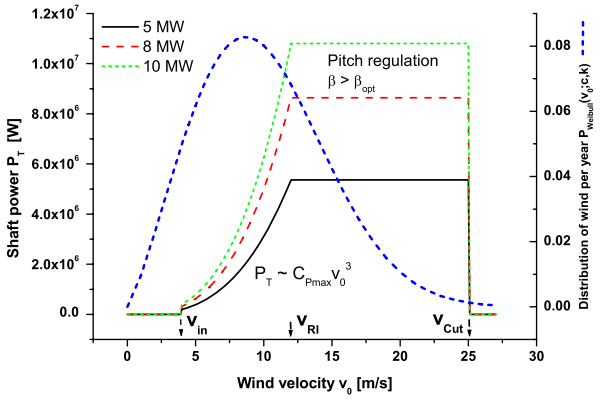

Figure 3. Ideal power curve of the Multibrid M5000 turbine (5 MW), which has cut-in, ideal rated and cut out wind velocities of v_{in}, v_{RI} and v_{cut}, respectively. The maximum power coefficient of the rotor is $C_{P\,max} = 0.48$ and the optimal tip ratio is $\lambda_{opt} = 7.48$ [11]. The shaft power is obtained at the maximum of the power coefficient below the rated wind velocity by regulating the rotational speed and the power is given by $P_T = \frac{1}{2}\rho C_{P\,max}\pi R^2 v_0^3$. The rotor blades are pitch regulated by changing β in $C_P(\lambda, \beta)$ for wind velocities above v_R whereby the shaft power is kept constant [12]. Additional power curves for turbines up-scaled to 8 and 10 MW are also shown as well as the annual Weibull distribution of the wind resources measured at 100 m height at the Fino 1 mast 50 km off the coast of northern Germany. The energy production of the turbine is obtained by integrating the product of the power curve and the Weibull distribution.

rated v_R where the measured power curve reaches a maximum. From equation (2) it is possible to determine the size of the rotor by

$$R = \sqrt{\frac{2(1+\varepsilon)P_N}{\rho C_{P\,max}\pi v_{RI}^3}} \tag{4}$$

where the shaft power $P_T = (1+\varepsilon)P_N$ includes a loss factor of the drive train ($\varepsilon \sim 8\%$ [11]). The tip-speed ratio at rated wind velocities v_R can now be determined from

$$\lambda(v_R) = \frac{v_{TIP}}{v_R} = \frac{R\omega_R}{v_R}. \tag{5}$$

The rated wind velocity $v_R = 12$ m s^{-1} and the rated rotation speed $\omega_R = 14.8$ rpm are obtained from the Multibrid M5000 specifications [12]. By inserting the $C_{P\,max} = 0.48$ and $\lambda(v_R) = \lambda_{opt} = 7.48$ from [11, 12] then a rotor diameter of $2R = 116.4$ m is obtained and is in good agreement with the physical size. The scaling of the Multibrid turbine to higher power ratings can now be done by assuming that the ideal rated wind velocity v_{RI} is the same, and that the maximum power coefficient and the tip-speed ratio are also the same. The consequence of these criteria is that the rotor area is used as efficiently as possible, since $C_P = 0.48$ is close to the practical possible maximum. Additionally the rotation speed must be lowered for larger turbines to limit the tip speed, which will keep the mechanical loads at the blade tip constant. This strategy represents a conservative up-scaling approach and the alternative to allow a faster rotation speed will need reenforcement of the rotor blades to handle the extra loads. It should be said that the construction of such long rotor blades will need substantial development effort, but it is considered possible from a materials point of view. Table 1 contains the properties of a scaled version of an 8 and a 10 MW turbine as well as the estimated shaft torque, which must be provided by the drive train. The hub height is determined as $h = R + 25$ m, since well behaved wind conditions are obtained approximately 25 m above the sea surface. Table 1 also contains information about typical turbines in the power range 1.3–3.0 MW. The up-scaling of the UPWIND 5 MW reference turbine resembling the RePower 5M turbine [13] gives numbers qualitatively the same as presented in table 1. The annual energy production of the scaled turbines has been estimated by integrating the product of the power curve of the turbines and the annual wind distribution quantified by the Weibull distribution

$$P_{Weibull}(v_0; c, k) = \frac{k}{c}\left(\frac{v_0}{c}\right)^{k-1}\exp\left(-\left(\frac{v_0}{c}\right)^k\right) \tag{6}$$

where v_0 is the wind velocity, c is the scale parameter and k is the shape parameter [14]. The annual energy production (AEP)

is then given by

$$\mathrm{AEP} = C_1 \int \frac{P_T(v_0)}{1+\varepsilon} P_{\mathrm{Weibull}}(v_0; c, k)\, \mathrm{d}v_0 \qquad (7)$$

where the loss ε in the drive train has been included and the unit of AEP is watt hour (Wh) if $C_1 = 8760$ h year^{-1}. The Weibull distribution used for the AEP estimates is the measured distribution at 100 m above sea level from the German Fino 1 offshore wind mast giving $c = 11.25$ m s^{-1} and $k = 2.25$ [15]. Table 1 constitutes a solid starting point for discussing the properties demanded by a superconducting drive train in 5–10 MW wind turbines, but additionally it also contains an estimate of the possible income over the lifetime of the turbine. This will of course depend heavily on the electricity price and on the possible feed in tariff, which will make the income predictable.

3. The superconducting drive train

Superconducting (SC) machines were developed after the successful fabrication of the low temperature superconducting (LTS) NbTi metal alloy wires, but the operation was complicated by the need to cool with liquid helium because of the low critical temperature $T_C = 9.8$ K [6, 16]. SC machines were revisited after the discovery in 1986 of the ceramic high temperature superconductors (HTS) with T_Cs up to 110 K and large SC machines up to 36 MW were constructed from the first generation (1G) of HTS tapes made of $Bi_2Sr_2Ca_2Cu_3O_{10+x}$ (Bi-2223) ceramic powder embedded in a silver matrix [17]. The price of the silver was, however, setting a limit to the minimum price of the 1G tape and the second generation (2G) HTS coated conductor tape based on $YBa_2Cu_3O_{6+x}$ (YBCO) deposited on cheap materials such as Ni or steel was developed. Both the 1G and 2G tapes are commercially available and the price of the 2G tape is expected to decrease as the production is scaled up [18–21]. The MgB_2 superconductor with a $T_C = 39$ K was discovered in 2001 and is now also available as wires [22, 23]. The main focus of the HTS superconducting machines has previously been on electrical propulsion motors for military and cruise ships [6], but the interest in wind turbine application has increased during the last five years [24–27].

3.1. Specification of properties

From the turbine size scaling it is seen that the superconducting drive train must comply with the following demands.

- Provide the shaft torque listed in table 1.
- Provide active damping of dynamic loads (blade and tower oscillations).
- Reasonable size <4 m for road transport due to bridges. No limit at sea.
- Reasonable weight to reduce dynamic loads on the rest of the structure.
- Reasonable efficiency with a loss factor ε of 8% or better [11].
- Reasonable interface to power electronics.
- Well proven reliability over 20 years and maintenance only required at 1–2 year intervals.
- Small impact on the reliability of other components such as the rotor and bearings.
- A lower price than the alternative drive trains.

The last point must be seen from the wind farm point of view as formulated earlier and the weight and the reliability in particular can cause a major cost reduction.

3.2. Torque and generator geometry

The torque τ provided by an electrical machine is generally proportional to the magnetic field strength B_r produced by the rotor at the stator wires carrying a current I_S on a cylinder of radius R and length L

$$\tau \sim B_r I_S R^2 L. \qquad (8)$$

One can classify the generators of the wind turbine drive trains by the technology used to produce the magnetic field in the rotor. The first generation, exemplified by the low torque asynchronous double fed induction generator, is based on copper windings and magnetic steel to shape the field. However, the field strength is limited by the saturation magnetization of the steel and the copper coils get hot due to the Joule heating, $P = RI^2$, dictated by the resistance of the rotor winding. One can overcome the Joule heating by introducing permanent magnets to produce the rotor field, whereby the mechanical design can be simplified considerably. The drawbacks are, however, a higher material cost and still a limitation of the field strength when all the magnetic moment of the Fe atoms of $Nd_2Fe_{14}B$ are aligned. Superconducting tapes can carry a DC current I in a magnetic field with a very small electric field E along the tape, because the superconducting flux lines pushed into the tape are prevented from moving due to the presence of pinning sites on the nanometer scale inside the material. However, if the current in the tape approaches the critical current I_C provided by the pinning sites then a gradual increase of flux movement is seen and the electric field is well described by the empirical power law

$$E = E_0 \left(\frac{I}{I_C(\mathbf{B}, T)} \right)^{n(\mathbf{B},T)} \qquad (9)$$

where the critical current $I_C(\mathbf{B}, T)$ depends on temperature, the direction and magnitude of the applied field $\mathbf{B}$ and is defined as giving an electric field of $E_0 = 10^{-4}$ V m^{-1} in a specific tape. The exponent of the power law quantifies how abrupt the transition out of the superconducting phase appears and it will also depend on the applied field and the temperature. The power dissipation of the superconducting tape per unit length at $I/I_C = 0.8$ is then given by $P_S = EI$ and is of the order 1.5×10^{-5} W m^{-1} for Bi-2223 values of $n = 28$ and $I_C = 100$ A at $T = 77$ K and $B = 0$ T [21]. Thus superconducting coils can produce rotor magnetic fields of several tesla provided that the support material has sufficient strength to hold the tapes and that a cooling device can keep the superconductors far below the critical temperature inside a cryostat. The term first, second and third generation drive train based, respectively, on steel/copper, permanent magnets and superconducting coils was introduced by Hill and Grieve [25].

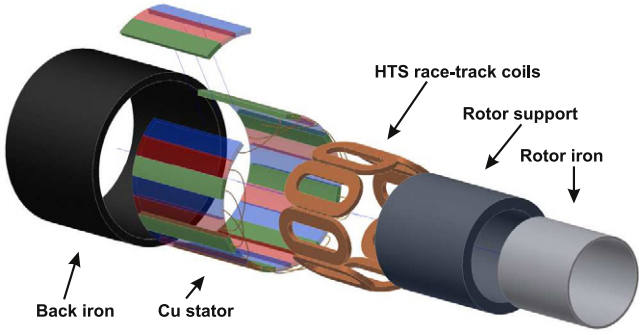

Figure 4. Generator layout extruded along the rotation axis. The stator back iron (left) is holding the three phase stator Cu winding. Superconducting racetrack coils are mounted on the rotor support structure which is holding an inner steel tube (right) to confine the magnetic flux between the rotor and the stator.

The stator is usually made of copper windings sitting at room temperature, because superconductors exposed to time varying magnetic fields and currents will suffer an AC loss orders of magnitude higher than the DC losses due to hysteretic movement of flux lines and due to coupling currents in the tape. The resulting loss at low temperature has to be removed by the cooling device, which usually has a quite low efficiency of the order 10^{-2} at $T = 35$ K. Thus only the DC cold losses are low enough to prevent the cooling device in contributing more than about 1% to the total drive train loss.

The geometry of superconducting generators will depend on the operational magnetic field strength B_r compared to the saturation field strength of the magnet steel present inside the generator. A generator with B_r lower than the saturation limit can be quite similar to the conventional machine where magnetic teeth in both the rotor and stator are used to shape the magnetic flux path. The effect of the steel is, however, diminished above the saturation limit and severe hysteretic losses in the steel would result. Thus the steel inside the rotor and the stator must be removed when designing superconducting generators operating at field strengths above the saturation limit of the steel. Steel can still be present as long as it is not saturated. The superconducting generator is operated as a synchronous machine, because the magnetic field of the stator will rotate synchronously with the superconducting rotor coils, which ideally then experience a field constant in time and therefore only suffer from DC losses. Figure 4 shows the layout of an air-cored superconducting synchronous generator, which consists of the outer back iron enclosing the air-cored stator made of copper bars fixed by a non-magnetic support material. Superconducting tapes have been wound into race track coils, which are mounted on a non-magnetic support tube. The support tube is also transmitting the torque from the generator to the shaft and it might have an inner steel tube to confine the magnetic flux between the rotor and the stator.

The superconducting drive train for wind turbines was discussed in 2005 as part of the Japanese activities on superconducting machines. Maki *et al* have suggested a 1800 rpm machine, which would be lighter and more efficient [24]. A UK based project on HTS wind energy systems was also initiated in 2005 with Converteam as project leaders and with the goal to make a market entry of a 8 MW and 12 rpm direct drive generator by 2011 [25]. In 2007 American Superconductor initiated a joint research venture with TECO-Westinghouse with the goal to develop a 10 MW and 11 rpm direct drive generator [27]. Later Converteam and Zenergy formed a joint venture in HTS technology with Zenergy as the supplier of HTS coils for the HTS generator developed by Converteam. Both the Converteam and American Superconductor generators are of the air-cored type, where as Maki has found the conventional type to be the most feasible in the form of a 20 pole salient pole machine [26].

4. 10 kW demonstration project

The authors of this paper are working on the Superwind project started in 2007 at the Technical University of Denmark (DTU) and the goal of the project is to investigate the challenges of constructing 10 MW direct drive superconducting generators for wind turbines [28]. The main activities are focused on establishing new methods for producing cheap coated conductors, possible constructions of superconducting generators and the integration of these into large wind turbines. The first part of this paper reflects the consideration of the integration. The discussions with the wind power researchers in Risø-DTU resulted in a strategy of gradual growth of the generator with real demonstration in wind turbines starting with a power range of 10 kW, 100 kW, 1 MW and finally 10 MW. It was concluded that the possible weight and size reduction for the 10 MW superconducting machine was clearly interesting to the wind turbine community, but it will be competing with alternative drive trains based on gearboxes [11]. The major challenge will be to obtain reliability experience, which can document that the possible benefits of a superconducting drive train are not compromised by failures and the superconducting drive trains are making more money than the alternatives. A 11 kW Gaia wind turbine installed at the Risø-DTU test site was chosen as the first end-application and a design study of the eight pole synchronous air-cored superconducting direct drive generator shown in figure 4 was conducted [29]. The active length of the generator was $L = 0.4$ m, the outer diameter was $D = 0.64$ m and the air gap field strength was $B_r = 1.0$ T created by having $I = 150$ A in 4 mm wide tapes with $B_{max} = 1.8$ T. It was concluded that it would be possible to build such a machine operated at $T = 20$–50 K, but the needed length of wire was estimated to be $L_{wire} = 7.5$ km. With a wire price for coated conductors of the order $P_{CC} = 60$ Euro m^{-1} and for Bi-2223 tapes $P_{Bi2223} = 15$ Euro m^{-1} it was then too much for the superwind budget but a lab-scale test generator holding racetrack coils cooled in liquid nitrogen is now under construction.

5. HTS tape consumption for a 10 MW generator

The challenges of constructing a 10 MW direct drive generator providing the torque specified in table 1 are illustrated by the

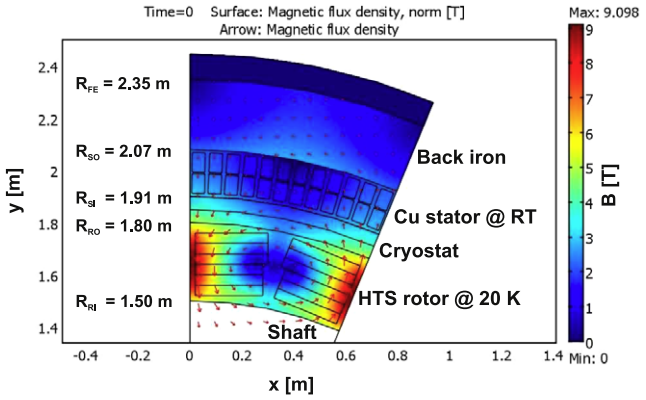

Figure 5. Magnetic field distribution of a 10 MW direct drive 16 pole air-cored synchronous generator providing a torque of 9.7 MN m.

Table 2. Properties of an extreme 10 MW generator example.

Rated power P_N (MW)	10
Poles	16
Diameter D_{gen} (m)	4.7
Length L_{gen} (m)	1.15
Rotation speed $\omega_{\text{R,rpm}}$ (rpm)	10
Shaft torque τ_T (10^6 N m)	9.7
Mass superconductor m_{sc} (ton)	22
Mass Cu m_{Cu} (ton)	14
Mass Fe m_{Fe} (ton)	32
Mass glass fiber m_{GF} (ton)	20
Mass total (ton)	88
Length of SC (km)	1450
Current density J_e (A m^{-2})	6.3×10^7
Temperature T (K)	20
Maximum field B_{max} (T)	9.1

16 pole machine example in figure 5. It shows an air-cored rotor made of HTS tapes wound into pancake coils stacked on top of each other and supported by glass fiber. A cryostat of thickness 10 cm is expected in between the rotor and the air-cored stator enclosed by magnetic steel. The cryostat is expected to provide an environment where the superconducting tapes can be operating at $T = 20$ K. The current in the tape is assumed to be $I = 75$ A and with a cross sectional area of $A_{\text{tape}} = 4\text{ mm} \times 0.3\text{ mm} = 1.2 \times 10^{-6}$ m^2, including insulation, one will have an engineering current density of $J_e = 6.3 \times 10^7$ A m^{-2}. COMSOL has been used to calculate the two-dimensional (2D) field distribution assuming a homogeneous J_e in the coil and from figure 5 it is seen that the maximum field at the conductors will then be $B_{\text{max}} = 9.1$ T and that the field strength at the stator is of the order 3 T. The above example represents an extreme machine where the superconducting coils are producing a very high magnetic field, whereby the amount of copper in the stator becomes small. It is, however, uncertain whether such a high field can be supported by the rotor support structure. The extreme machine has an outer diameter of $D = 4.7$ m, a length of $L = 1.15$ m and a mass of $m = 87$ tons, as shown in table 2. A tape length of $L_{\text{tape}} = 1450$ km would be needed and would cost about $P \sim 87$ MEuro for a coated conductor and $P \sim 22$ MEuro for Bi-2223 tape. It should be stressed that the above extreme machine does not represent an optimized generator and the needed tape length can be reduced considerably by increasing the amount of iron in the machine as well as lowering the magnetic field strength. American Superconductor stated a target weight of 180 tons using 180 km of wire in 2007 [25], whereas the latest press releases reveal a target weight of 110 tons. The tape consumption will therefore be of the order 200–300 km and much lower than the extreme machine above. The main conclusion from the generator example above is that several hundreds up to a thousand kilometers of tape will be needed to build the lightweight machines.

6. Discussion

The analysis of the potential European market for offshore wind turbines gives a rough estimate of how many superconducting generators could be introduced. By assuming that the superconducting turbines will constitute about 10% of the EU offshore market then there is a need to build about 1200 generators before 2030. This 10% of the market could actually be the future turbines mounted on floating foundations in the deep water part of the North Sea. These turbines will be swinging due to the water waves and a lightweight drive train will be essential. If it is also assumed that a superconducting generator will first be ready in 2020, then the annual production would need to be 120 generators per year with a consumption of 36 000 km of superconducting tape per year. This production capacity is a factor of 36 bigger than the current capacity, estimated to be 1000 km year^{-1} [30, 31]. Thus the wind turbine community will not consider the superconducting drive train as a realistic alternative before a roadmap for up-scaling of the production capacity is available. Secondly, the price estimate of a one 10 MW generator is $P = 300\text{ km} \times 60\text{ Euro m}^{-1} = 18$ MEuro, which exceeds the expected installation cost of 15 MEuro for the turbine, foundation and cables. This calls for a tenfold price reduction of the tape, which is probably realistic if the up-scaling of the coated conductor to mass production can be done. The Converteam/Zenergy group has just recently published a discussion of the benefits of the superconducting drive train and estimated that it will be more cost effective than permanent magnet direct drives above 5 MW [32].

One final and quite important point is to calculate the volume and mass of the 1 μm thick layer of the active YBCO material in the 10 MW generator

$$V_{\text{YBCO}} = 4 \times 10^{-3}\text{ m} \times 1 \times 10^{-6}\text{ m} \times 300 \times 10^3\text{ m} = 1.2 \times 10^{-3}\text{ m}^3 \quad (10)$$

$$m_{\text{YBCO}} = \rho_{\text{YBCO}} V_{\text{YBCO}} = 5 \times 10^3\text{ kg m}^{-3} \times 1.2 \times 10^{-3}\text{ m}^3 = 6\text{ kg} \quad (11)$$

which should be compared to $m_{\text{NdBFe}} = 0.7$ ton and $m_{\text{NdBFe}} = 7.0$ ton for the multibrid hybrid drive train scaled to 10 MW and the full permanent magnet direct drive train, respectively [11]. Thus the superconducting drive trains use three orders of magnitude less active material, which will most likely become a great advantage in the future.

7. Conclusion

The future offshore wind turbine market of Europe has been examined and the properties of an up-scaled 10 MW wind turbine suitable as the end-application of a superconducting direct drive train have been determined. It is concluded that the weight and size advantages of a 10 MW superconducting drive train are important, but the main challenge will be to prove that the superconducting drive train has a higher reliability than the alternatives. This has resulted in a recommendation of demonstrating superconducting direct drive trains in real wind turbines first from the 10 kW power range and gradually increasing the power rating to 100 kW, 1 MW and then 10 MW in order to obtain reliability experience from a system point of view. It is estimated that the current production capacity of coated conductor tapes must be increased by a factor 36 by 2020 to cover 10% of the EU offshore wind market by 2030. The tape price must also be decreased by a factor of ten for the cost of the superconducting drive train to become realistic. Finally it is shown that if the YBCO layer is considered as the only active material then the consumption is three orders of magnitude lower in weight than that of the permanent magnet direct drive train.

Acknowledgments

The funding of the Superwind.dk project from the Globalization grant of the Technical University of Denmark (DTU) is acknowledged as well as the valuable discussions with Sten Tronæs Frandsen at Risø-DTU.

References

[1] Zervos A and Kjaer C 2008 Pure power: wind energy scenarios up to 2030 *European Wind Energy Association Report* www.ewea.org
[2] Offshore statistics 2007 and 2008 *European Wind Energy Association Report* www.ewea.org
[3] Burton T, Sharpe D, Jenkins N and Bossanyi E 2001 *Wind Energy Handbook* (New York: Wiley) ISBN 0471489972
[4] Frandsen S T 2009 private communication (coordinator of the FP6 UPWIND project)
[5] Fichaux N and Wilkes J 2009 Oceans of opportunities *European Wind Energy Association Report* www.ewea.org
[6] Kalsi S S, Weeber K, Takesue H, Lewis C, Neumueller H W and Blaugher R D 2004 Development status of rotating machines employing superconducting field windings *Proc. IEEE* **92** 1688
[7] UPWIND *FP6 EU Program on Upscaling of Wind Turbines* www.upwind.eu
[8] Westwood A 2007 Siemens at full throttle *Renew. Energy Focus* **8** 28
[9] Hansen A D and Hansen L H 2007 Wind turbine concept market penetration over 10 years (1995–2004) *Wind Energy* **10** 81
[10] Poore R and Lettenmaier T 2002 Alternative design study report: WindPACT advanced wind turbine drive train designs study *National Renewable Energy Laboratory Report* NREL/SR-500-33196
[11] Li H, Chen Z and Polinder H 2009 Optimization of multibrid permanent-magnet wind generator systems *IEEE Trans. Energy. Convers.* **24** 82
[12] Areva Multibrid web-site *M5000 Specifications* www.multibrid.com
[13] Bossanyi E, Witcher D and Mercer T 2009 Controller for 5 MW reference turbine *UPWIND Report* 11593/BR/04 www.upwind.eu workpackage 5 on control
[14] Kiss P and Janosi I M 2008 Comprehensive empirical analysis of ERA-40 surface wind speed distribution over Europe *Energy Convers. Manag.* **49** 2142
[15] Berge E, Byrkjedal Ø, Ydersbond Y and Kindler D 2009 Modelling of offshore wind resources. Comparison of a mesoscale model and measurements from FINO 1 and North Sea oil rigs. EWEC 2009 contribution www.norsewind.eu/public/publications.html
[16] Akita S 2002 Special issue on superconducting generator in Japan *Cryogenics* **42** 149
[17] Barnes P N, Sumption M D and Rhoads G L 2005 Review of high power density superconducting generators: present state and prospects for incorporating YBCO windings *Cryogenics* **45** 670–86
[18] Sumitomo www.sumitomoelectricusa.com/scripts/products/scc/
[19] SuperPower www.superpower-inc.com
[20] American Superconductors www.amsc.com
[21] Bruker Energy & Supercon Technologies www.bruker-est.com
[22] Columbus Superconductors SpA www.columbussuperconductors.com
[23] Hyper Tech Research Inc. www.hypertechresearch.com
[24] Maki N, Takao T, Fuchino S, Hiwasa H, Hirakawa M, Okumura K, Asada M and Takahashi R 2005 Study of practical applications of HTS synchronous machines *IEEE Trans. Appl. Supercond.* **15** 2166
[25] DBU Conference 2007 *Technical and Economical Impact of Superconductors on Wind and Hydro Power (Osnabrück)*
[26] Maki N 2008 Design study of high-temperature superconducting generators for wind power systems *J. Phys.: Conf. Ser.* **97** 012155
[27] Matthews J N A 2009 Superconductors to boost wind power *Phys. Today* (April) 25–6
[28] Superwind Project web-site www.superwind.dk
[29] Abrahamsen A B, Mijatovic N, Seiler E, Sørensen M P, Koch M, Nørgard P B, Pedersen N F, Træholt C, Andersen N H and Østergard J 2009 Design study of 10 kW superconducting generator for wind turbine applications *IEEE Trans. Appl. Supercond.* **19** 1678–82
[30] Li X *et al* 2009 The development of second generation HTS wire at american superconductor *IEEE Trans. Appl. Supercond.* **19** 3231
[31] Selvamanickam V *et al* 2009 High performance 2G wires: from R and D to pilot-scale manufacturing *IEEE Trans. Appl. Supercond.* **19** 3225
[32] Lesser M and Müller J 2009 Superconductor technology generating the future of offshore wind power *Renewable Energy World Conference and Exhibition (Colonge)*

G.3 Paper: Superconducting generators for wind turbines: design considerations

Presented at European Conference on Applied Superconductivity (EUCAS) 2009. The article is peer reviewed. The article is published and available online at Journal of Physics: Conference Series.

IOPscience iopscience.iop.org

Home Search Collections Journals About Contact us My IOPscience

Superconducting generators for wind turbines: Design considerations

This article has been downloaded from IOPscience. Please scroll down to see the full text article.

2010 J. Phys.: Conf. Ser. 234 032038

(http://iopscience.iop.org/1742-6596/234/3/032038)

View the table of contents for this issue, or go to the journal homepage for more

Download details:
IP Address: 192.38.67.112
The article was downloaded on 23/11/2011 at 08:54

Please note that terms and conditions apply.

Journal of Physics: Conference Series **234** (2010) 032038 doi:10.1088/1742-6596/234/3/032038

Superconducting generators for wind turbines: design considerations

N Mijatovic[1], A B Abrahamsen[2], C Træholt[1], E Seiler[2], M Henriksen[1], V M Rodriguez-Zermeno[3], N F Pedersen[1]

[1] Department of Electrical Engineering, Technical University of Denmark, Elektrovej 325, Lyngby 2800, DK

E-mail: [1] nm@elektro.dtu,dk

[2] Risø National Laboratory- DTU, P.O. Box 49, DK-4000 Roskilde, Denmark

[3] Department of Mathematics, Technical University of Denmark, Lyngby 2800, DK

Abstract. The harmonic content of high temperature superconductors (HTS) field winding in air-core high temperature superconducting synchronous machine (HTS SM) has been addressed in order to investigate tendency of HTS SM towards mechanical oscillation and additional loss caused by higher flux harmonic. Both analytical expressions for flux distribution and current sheet distribution have been derived and analyzed. The two main contributors to the AC loss of HTS rotor winding are also identified and their influence addressed on general level.

1. Introduction

The electrical machine's output power to volume ratio, as shown in Eq.1, is proportional to revolution speed n_s, rotor produced magnetic flux density B_{rotor}, stator electrical loading (stator's magnetomotive force along its circumference) A_{stator}, diameter of the stator winding D and length of the machine L.

$$P = \frac{\pi^2}{\sqrt{2}} k_w B_s A_{stator}^{3ph} D^2 L n_s \Longrightarrow \frac{P}{n_s} = T = (2\sqrt{2}\pi k_w) B_s A_{stator}^{3ph} V \tag{1}$$

From Eq.1 it is obvious that the torque is volume dependent since D^2L presents machine's volume. For conventional Synchronous Machines (SM), Induction Machines (IM) and Permanent Magnet (PM) SM machine product $B_{rotor}A_{stator}$ is limited. Saturation of steel in rotor and stator or properties of PM [1] are limiting the air gap flux density on $1.5T$-$2.2T$. Current capacity of the stator and rotor winding is set by maximal tolerable temperature increase caused by Joule dissipation. Maximal stator electrical loading is reported to be $350kA/m$ [2,3]. Thus in practice, the torque to volume ratio is constant for all electrical machines. On the other hand, from Eq.1 the power of the machine for a given torque can be increased by rising its operational speed. Consequently, using the gearbox together with the electrical machine (also referred as a drive) and adjusting machine's product ($T \times n_s = const.$) to a lower torque - higher speed, is often very useful and justified, resulting in a lighter drive. Nevertheless, the gearbox as a solution is bound to low and mid-torque application and has significant influence on overall efficiency and maintenance requirements of the drive.

© 2010 IOP Publishing Ltd

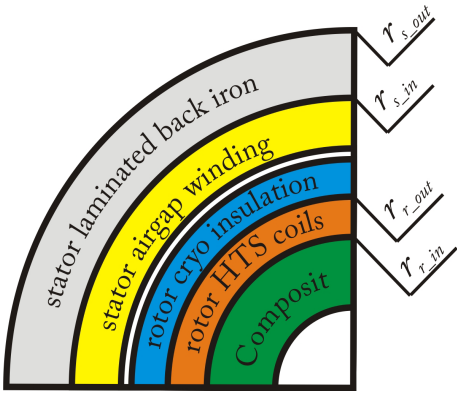

Figure 1. Illustration of the generic cross section of the HTS SM with main generator parts: stator back iron - gray, stator three phase air-gap winding - yellow, rotor's cryostat - blue, HTS rotor winding - orange, rotor's composite support - dark green

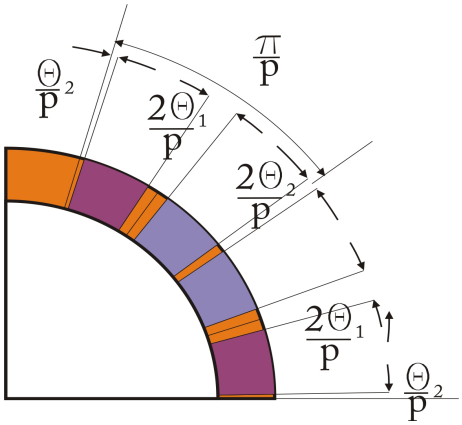

Figure 2. Illustration of the angular sector of the HTS winding. The sector of $\pi/(2p)$ angle corresponds to the one pole pair of the machine, while the angles θ_1 and θ_2 are determining the space in the middle of the coil and the space between two neighboring coils, respectively.

Wind turbine (WT) producers have in the past preferred the choice of geared drive with high speed generator. Still, rapid development of wind industry, especially aimed at offshore WT farms and WT up to $10MVA$ is favoring direct drive (DD) generators in WT due to low maintenances and robustness towards torque transients. The conventional DD generator for powers and speeds of present WT would need higher torque (and volume) ≈60 times compared to the high speed generator in geared drive. This volume expansion can be easily calculated from the Eq.1 if we assume for speed of high speed generator $\omega_{GBgen} \approx 1500rpm$ and speed of WT $\omega_{DDgen} \approx 25rpm$. Obviously, in order to introduce DD generators in WT for high power range, the machine technology requires improvements of torque to volume ratio (T/V). High Temperature Superconductors (HTS) SM have become very interesting to researchers and industries enabling the machines with very high torque densities $T/V[Nm/m^3]$. By increasing the current densities up to 100 times (and steadily rising) higher than cupper, HTS SM is aiming to redesign the electrical machines, making conventional machine's design obsolete. With power ratings from $100kVA$ up to $5MVA$, the wind power industry is one where these advances would open new horizons for gearless WT and units up to $10MVA$, suitable for distant offshore wind farms.

One of the main ways how the HTS SM can offer advance of the DD train's T/V is by increasing the excitation (rotors) magnetic field. According to the Eq.1, if the field is increased twofold, the volume of such machine would be half of the conventional machine, both rated with same torque. As the flux of HTS winding is much larger than in conventional machine, control of space harmonic of HTS winding as one of the main sources of mechanical vibrations, increased losses in the machine and induced harmonics of stator's voltage and current are essential for ensuring good performance of machine. Actually, since HTS is produced as a rather stiff tape, especially for applications where mechanical properties are crucial to provide the necessary strength and protection for the brittle superconductor, only the simple geometry coils (racetrack coils) can be constructed with present HTS technology. Having these constraints for designing excitation winding for the SM can create a reservation towards the flux spatial distribution of such winding and its harmonic contents. The study of the HTS SM electromagnetic parameters and impact of construction factors and constraints on machine's flux distribution and harmonic content have been performed in Sec.2.1, Sec.2.2.

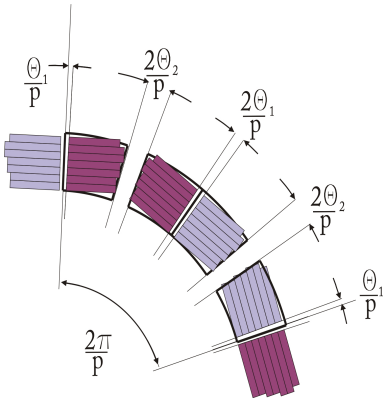

Figure 3. Illustration of current fed HTS coils of the HTS winding with corresponding angles.

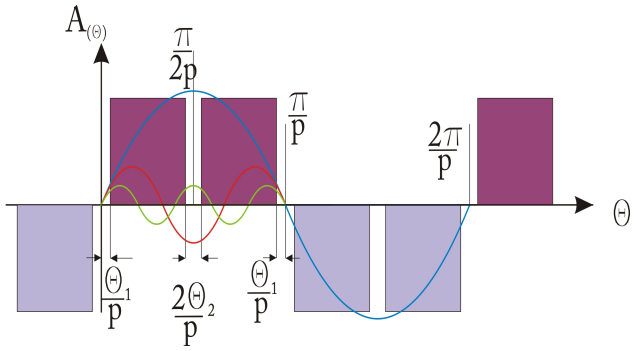

Figure 4. Illustration of rotor's electrical loading $A_{(\theta)}$ for 1/(p) of circumference, defined by the ampere turns of HTS coils and angles θ_1 and θ_2. The current orientation is corresponding to the Fig.3.

HTS is a novel material in electrical machines and one of main concerns is the HTS losses which needs to be addressed. Other loss mechanisms in machine as eddy currents, iron loss, Jules loss, skin effect etc. will not be focus of this study. The two main contributors to the AC losses in HTS have been identified: pulse with modulation (PWM) caused by power electronics high frequency (HF) switching and wind turbine load changes caused by stochastic wind speed changes. The AC loss of HTS is function of the flux perturbations and we have evaluated amplitude of these oscillations in the case of air-core HTS SM wind turbine generator. The DC energy loss in HTS in HTS SM is also shown to be minor, using expected values of machine parameters.

2. HTS SM design layout

HTS SM are promising to double the torque densities $T/V[Nm/m^3]$ compared to conventional SM (double fed and PM), and doing so mainly by increasing the rotor excitation field above $2T$. As rotor magnetic parts become saturated on higher fields, substituting rotor iron with nonmagnetic composite materials will provide necessary mechanical support and additionally contribute to lighter machine design. It is reported in [2, 3] that high magnetomotive force (MMF) available with the HTS rotor winding would saturate the conventional slotted stator. With that respect, air gap stator winding, suggested by [2, 3] for turbo-generators, would be more suitable to SM with HTS rotor. Cross section of such configuration is illustrated on Fig.1.

The necessary low temperature cooling system for HTS-SM (in the range $20[K] - 80[K]$) presents additional complexity to the machine system. Even so, with steady development of no maintenance or low-level maintenance industrial cryocoolers (like pulse-tube [4]) and growing HTS power applications (cable, FCL, SMES), it is believed that such cooling system can have the necessary reliability with minimum maintenance in due time and with the 'off the shelf' application strategy [5]. Depending of HTS design operating temperature, the cooling system and its performance will differ. Nevertheless, for this study it is assumed that in order to keep the rotor thermally well insulated, the thickness of the cryostat can be estimated to $50[mm]$ for temperatures between $50[K]$-$80[K]$, and to 100 $[mm]$ between $20[K]$-$50[K]$ where besides vacuum and ML insulation the chamber with LN_2 is desirable as a pre-cooling step. The pre cooling with LN_2 will increase cooling efficiency and lower cool-down time and price of it [6] but may also increases cooling system complexity and machine's air gap. Thus, the tradeoff is necessary.

2.1. Analytical approximation of flux density of HTS SM

Absence of iron in rotor and air gap stator winding are making traditional approach of machine analysis inapplicable [7, 8]. Assumption that the mutual flux between rotor and stator can be derived from calculation of magnetic permeance of overall magnetic circuit and machine's MMF, in the air-core machine is flawed, mainly due to the fact that flux is not only radial across the air gap as in conventional machine. This presents obstacle in analysis of such machines since calculation of the electro-magnetic parameters is bound to the FEM modeling and derivation of spatial distribution of magnetic flux. While the exact values can be derived only using FEM analysis on specific generator geometry, analytical formulation of magnetic flux distribution for arbitrary machine geometry would be very useful for identification of inductances and flux density of air cored machines.

A convenient way of deriving analytical expression for the spatial flux distribution is to use the vector potential A_z formulation of Maxwell equations as done by [7, 8] and applied to arbitrary geometry. The Eq.2 present the radial magnetic flux density distribution of arbitrary current sheet enclosed by the stator back iron. In formulation of problem, authors have assumed infinitely thin current sheet at radius r_{sheet} with harmonic current distribution along the circumference $A_{(\theta)} = A_{sheet} sin(p\theta)$. Derivation of $A_{(\theta)}$ for general case of HTS winding will be presented in Sec.2.2.1. Neglecting saturation and 'end effects' and for $r_{sheet} < r < r_{s_{in}}$, the radial flux distribution can be expressed as Eq.2 [7,8]

$$B^{\nu}_{(r,\theta)} = \frac{\mu_0}{2} A^{\nu}_{sheet} \cdot \underbrace{\left[\frac{r_{sheet}}{r}\right]^{(\nu p+1)} \left(1 + \eta_s \lambda_s \left[\frac{r_{sheet}}{r_{s_{in}}}\right]^{2p\nu}\right)}_{K^{\nu}_{(r,p)}} \cdot cos\left(\nu p\theta\right) = \frac{\mu_0}{2} A^{\nu}_{sheet} K^{\nu}_{(r,p)} \cdot cos\left(\nu p\theta\right) \tag{2}$$

where μ_0, μ_s are magnetic permeability of vacuum and relative permeability of stator back iron, respectively, ν-harmonic order, p-number of poles pairs, A_{sheet} is electrical loading of the current sheet (see Sec.2.2.1) at its radius r_{sheet} and $r_{s_{in}}$ and $r_{s_{out}}$ are inner and outer radius of the stator back iron. The influence of the stator back iron on flux density of the rotor current sheet is seen throughout the parameters λ_s and η_s, defined by the Eq.3.

$$\lambda_s = \frac{\mu_s - 1}{\mu_s + 1}; \qquad \eta_s = \left[1 - \left(\frac{r_{s_{in}}}{r_{s_{out}}}\right)^{2p\nu}\right] / \left[1 - \lambda_s^2 \left(\frac{r_{s_{in}}}{r_{s_{out}}}\right)^{2p\nu}\right] \tag{3}$$

Interesting fact to illustrate is nature of synchronous inductances of air-cored machines. The tendency of inductances in full air core machine (no iron) and conventional machine (very narrow air gaps), where g is radial air gap between stator iron and rotor iron, would go as [7,8]

$$\frac{L_{(conv)}}{L_{(air)}} = 2\frac{(1 + ((r_{s_{in}} - g)/r_{s_{in}})^{2p})}{(1 - ((r_{s_{in}} - g)/r_{s_{in}})^{2p})} \tag{4}$$

If the air gap, g, is aspiring towards small values (few mm), ratio of inductances in Eq.4 can be as big as 100 [7,8]. Now, the value for the inductance of conventional machines (small air-gap machines) is $\approx 1.5 p.u$ and if we take for the ratio of the air cored machine and conventional inductances value of 100, the air core design would yield only $\approx 0.015 [p.u.]$. In the case of HTS SM, since the back iron is present, the ratio of inductances will be smaller but even so it is expected to be 2 to 20 times lower than inductance in conventional machine. From electrical side of characterization of electrical machines, the very low value of synchronous inductances is the biggest difference between conventional and air cored HTS SM suited for WT.

2.2. Consideration of the HTS coils and field winding
In order to investigate the flux distribution of the simple HTS rotor, as general as possible, the space current sheet approximation for the proposed HTS rotor layout must be established first.

2.2.1. Current sheet approximation of HTS rotor winding The Fig.4 is illustrating the angular distribution of ampere-turns along the sheet circumference. In the radial cross section of the machine, HTS windings can be presented by a ring with constant turns density n_ρ, shown on the Fig.1 with a orange color. Current fed coils (light and dark purple color on Fig.2) or angular segments of orange ring are defined by the angles θ_1 and θ_2. Fig.3 is illustrating the corresponding angles between the ring presentation and actual stacks of racetrack coils for two pole pitch rotor segment ($2\pi/p$).

The HTS turns density n_ρ expressed in $turns/m^2$ of the rotor's cross section, is considered constant in the coil angular segments. Expansion of the ampere turns distribution into Fourier series $A_{(\theta)}\,[A/m] = \sum A^\nu_{sheet} \cdot sin\,(p\nu\theta)$ would yield Eq.5 and Eq.6 as expression for the amplitude of each harmonic of the current sheet, where the $r_{sheet} = 0.5(r_{r_{out}} + r_{r_{in}})$.

$$A^\nu_{sheet} = \frac{I_{sheet}}{r_{sheet}} \frac{1}{\pi} \int_{-\pi}^{\pi} \int_{r_{r_{in}}}^{r_{r_{out}}} n_{\rho_{(r,\theta)}} \cdot sin\,(\nu p\theta) \cdot r d\theta dr = \tag{5}$$

$$= \frac{I_{sheet}}{r_{sheet}} \frac{2p}{\pi} n_\rho \frac{{r_{r_{out}}}^2 - {r_{r_{in}}}^2}{2} \underbrace{\left(\left[\frac{-cos\,(\nu p\theta)}{\nu p} \right]_{\left(\frac{\theta_1}{p}\right)}^{\left(\frac{\pi}{2p} - \frac{\theta_2}{p}\right)} + \left[\frac{-cos\,(\nu p\theta)}{\nu p} \right]_{\left(\frac{\pi}{2p} + \frac{\theta_2}{p}\right)}^{\left(\frac{\pi}{p} - \frac{\theta_1}{p}\right)} \right)}_{k_{A\nu}/p} =$$

$$= \frac{n_\rho I_{sheet}}{\pi r_{sheet}} \left({r_{r_{out}}}^2 - {r_{r_{in}}}^2 \right) k_{A\nu} \tag{6}$$

where $k_{A\nu}$ can be interpreted as the winding coefficient for HTS rotor winding, $r_{r_{out}}$ and $r_{r_{in}}$ are outer and inner diameter of HTS ring (orange ring on Fig.1) and I_{sheet} would be current of the HTS winding. The $n_{\rho_{(r,\theta)}}$ is spatial distribution of HTS conductors in radial cross section.

2.2.2. Harmonic content of HTS winding All radii will be normalize to the radius of current sheet r_{sheet}. The normalization of radial dimension of machine is desirable in order elevate the discussion on more general level. For example, if r_{sheet} is the base value ($1p.u.$), all radial dimensions (calculated as r/r_{base} and expressed in $p.u.$) will lie in few percentage of the base value. If the rotor winding is at radius of $1.5m$, cryostat is $100mm$ and stator iron $r_{s_{in}}$=$2.1m$, the radii from interest would be in the range $1.067pu - 1.4pu$, expressed in relative units and would corresponds to the space between outer radius of rotor's cryostat and inner radius of the stator back iron.

- The dependence of $K^\nu_{(r,p)}$ from Eq.2 and amplification of the flux spatial harmonics inherited from current sheet harmonics can be observed on Fig.5. The tendency of the main flux harmonic is illustrated in the inset figure on Fig.5 while varying p and normalized r. All higher harmonics are referred to its main and the black plane is plotted as a indicator to 5% of higher harmonics content.

The flux harmonics content are decreasing approximately as $r^{-(\nu p+1)}$. It can be observed that ν harmonic is falling with increasing radius and number of poles faster than the first harmonic and for a factor $r^{(1-p\nu)}$. Hence, the content of flux spatial harmonics is decreasing with increasing number of poles, favoring the high pole machines and with increasing r distance from excitation

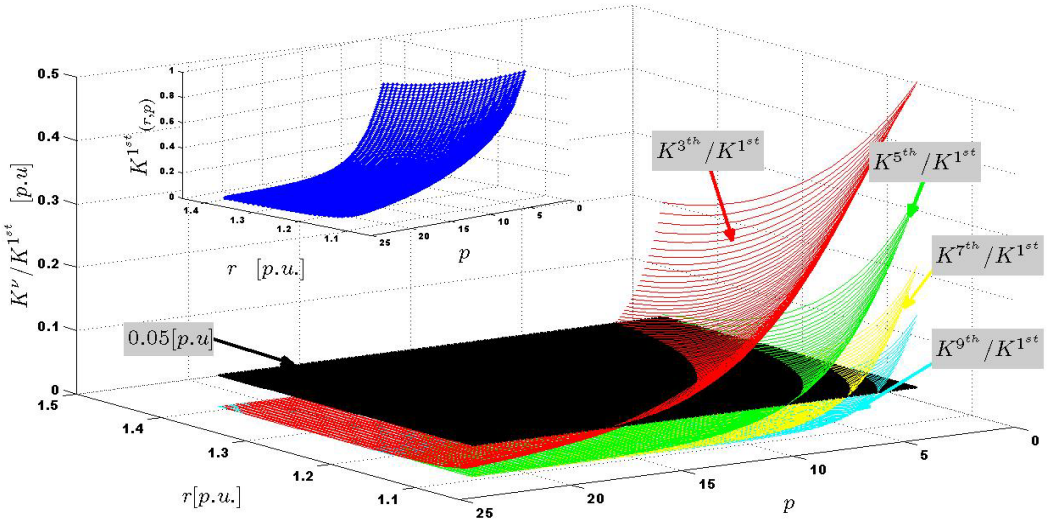

Figure 5. Dependence of rotor's flux higher harmonics referred to its first harmonic, calculated as a ratio of $K^{\nu=3,5,7}/K^{1^{st}}$ from Eq.2, from (r,p), illustrating the tendency for harmonics content of rotor's flux for different numbers of poles and stator radial position. The $0.05pu$ of the main flux harmonic is presented with black plain. Inset: Illustration of the tendency of the first harmonic of rotor's flux in the air core machine, seen throughout the $K^{1^{st}}$, while varying the normalized radial and number of poles.

sheet, favoring machines with low synchronous inductance.

It is also noteworthy to state that for fixed value of A_{sheet}, the main flux harmonic is decreasing as $\approx r^{-p}$, as illustrated in inset figure on Fig.5.

- Concerning the HTS current sheet and harmonic content of rotor MMF, if the available space for the HTS coil is known ($r_{r_{in}}$ and $r_{r_{out}}$), the sector angles θ_1 and θ_2 (between 0 and $\frac{\pi}{4}$) are having significant influence on current sheet harmonics. The k_A^{ν} from Eq.6, if referred to its first k_A^{1st}, would be the measure of the sheet harmonics (ν harmonic as a % of first harmonic). We can observe the first harmonic of HTS current sheet, k_A^{1st} and tendency of higher harmonics referred to k_A^{1st} on Fig.6 where the 20% is marked with black plane. For the $\theta_1 \approx 30[deg]$ and $\theta_2 \approx 5[deg]$, lower order harmonics are less than 20% of the main harmonic. Thus, it is prudent to set the coils sector angles on these values. By doing so, the lower order spatial harmonics (3^{rd} and so on) of the current sheet and flux they make will be lowest. Higher order harmonics of current sheet and the flux they create will be attenuated more than for lower harmonics as concluded previously. Thus, construction parameters of HTS winding have significant influence on flux distortion and should be adjusted accordingly.

As the result of previous analysis, the overall harmonic content in the rotor's flux, donated by $k_A^{\nu} \cdot K^{\nu}$ from Eq.2 and Eq.6, can be adjusted by stator and rotor winding radii and HTS winding angles θ_1, θ_2 to negligible values. The black planes in Fig.5 and Fig.6 are presenting 5% from the main flux harmonic and 20% from the main current sheet harmonic, respectably. Values for $k_A^{\nu} \cdot K^{\nu}$ from planes would yield high harmonic with amplitude of 1% of the main harmonic.

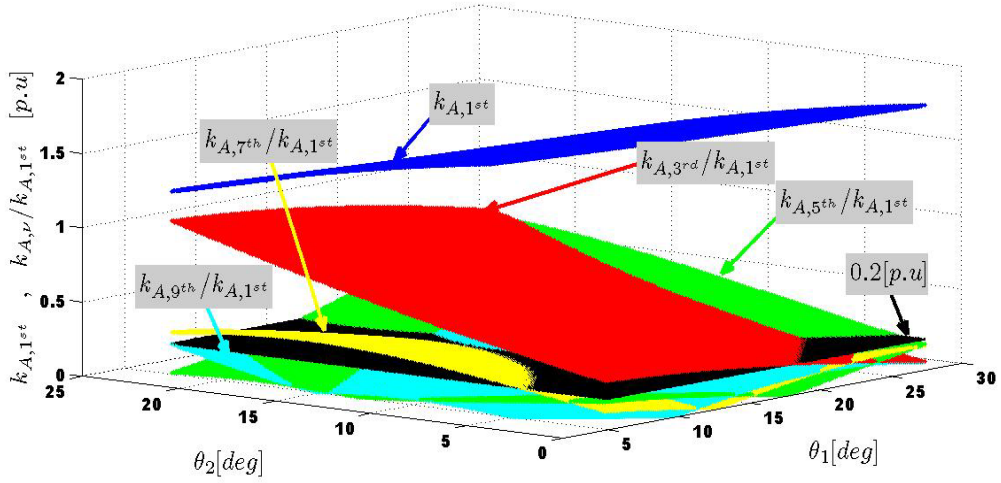

Figure 6. Illustration of the rotor's current sheet first harmonic in the air core machine, seen throughout of $k_A^{1^{st}}$, while varying the angles (θ_1, θ_2) and dependence of $k_A^{\nu=3,5,7}/k_A^{1^{st}}$ from (θ_1, θ_2) as a measure of sheet harmonic content. The $0.2pu$ of the main harmonic is presented with black plain.

3. The HTS SM for wind power application

With power ratings up to $4[MVA]$ and the rotation speed $20[rpm]$, today's WT with the gearbox (GB) and IM have been the more favorable option by wind turbine producers. This is mainly due to the smaller weight and cost of the high speed generator and gearbox compared to the direct driven (DD) generator [9]. GB equipped WT units have been very successful on the 'on shore' market, yet inherent maintenance requirements for GB and call for larger units (up to 10MVA) is one of the main technical issues and the reason for unexploited offshore wind potential. One of the biggest challenges of DD WT generator is its size and weight. As previously said the HTS can generate high magnetic field and with it increase the T/V of electrical machines significantly and hence the motivation towards DD HTS SM wind turbine generator.

3.1. Topologies of the drive train

As it is well established in WT by now, the variable speed DD WT will have a full power frequency converter (voltage source /current source or more advanced topology) as an interface between WT generator and the power grid ensuring variable speed operation. As power electronic and PWM will be unavoidable to achieve full control of the HTS generator, it is crucial to predict the behavior of such machine under WT like conditions. The losses in HTS rotor which are amplified by the cooling efficiency of rotor cryogenic cooling (ranging from 50 up to 1000 [6] for temperatures ranging in $80[K]$ to $20[K]$), will be function of WT operation conditions. We will address the biggest two contributors to AC loss of HTS in wind turbine generator.

4. Contributors to energy loss in HTS

Thermal load of the cooling system (cryocoolers) of HTS SM would be the heat load thru the insulation and heat load generated by HTS, both DC and AC. To be able to estimate energy loss we have to know how to characterize the HTS. The electro-magnetic behavior of all superconductors can be described with the Power low shown in Eq. 7 and used to derive voltage

of the tape/coil.

$$E_{(L)} = E_0(\frac{I}{I_{c(B,\alpha,T)}})^{n_{(B,\alpha,T)}} \tag{7}$$

The $I_c(B,\alpha,T)$ is HTS critical current and it is a local tape attribute. It depends from intensity of magnetic flux density, B, the angle between B vector and wide face of the tape, α, and local temperature (accounting for thermal gradients in coils). The I is the electrical current of HTS and $n_{(B,\alpha,T)}$ is a measure of the transition abruptness between superconducting and normal state and is a also local tape attribute. The $n_{(B,\alpha,T)}$ has tendency to decrease logarithmically with increasing B and/or T [10]. The E_0 is the voltage seen when the tape is carrying critical current and the value of $10^{-4}[V/m]$ is wildly used.

4.1. DC energy loss in HTS winding

The energy loss of the HTS winding is seen as a DC voltage drop (generated by the movement of unpinned flux vortices) along tape and across the HTS field winding when loaded with DC current. The voltage of HTS coil, shown in Eq.8 would be line integral of the Power low along the tape's length.

$$U = \int_0^L E_{(L)} dL \tag{8}$$

The DC loss is calculated as a product of tape's current and tape's voltage drop. For the time constant electrical and magnetic loading of the HTS winding, the expressions for the power losses can be written as Eq.9

$$P = \int_0^L I \cdot E_{(L)} dL \tag{9}$$

Since I_c and n are both functions of flux distribution, the equations Eq.9 requires FEM simulations in order to derive exact voltage along the HTS. It is much more desirable to have high I/I_c which is minimizing amount of expensive HTS but usually some parts of the HTS coils are experiencing higher flux and are very close to I_c while other parts are in much lower flux and have higher I_c. Thus, for the purpose of this discussion we can define average I_c and n as averages values for one coil. If the average ratio I/I_c is relatively low (0.5), and assuming the average $n = 15$, the power dissipation due to this loss will be minimal i.e. the voltage drop along a km of tape would be $10^{-4}[V/m](0.5)^{15} \times 1000[m] \approx 3 \cdot 10^{-6} V/km$. Under hypothesizes that $10MVA$ generator for WT would need $500km$ of standard $4mm$ HTS tape, operating at $20K$ and carrying $50A$, the approximate amount for static losses would be $500[km] \times 50A \times 3 \cdot 10^{-6} V/km \approx 0.075W$ at low temperature. Multiplying that loss with cooling efficiency (10^3 for T$\approx$20K) would result in $\approx 100[W]$ at room temperature what is negligible value compared with $10MVA$.

4.2. The contributors to AC loss in HTS winding

The AC loss of HTS windings would result from high frequency ($1[kHz] - 5[kHz]$) field modulation caused by PWM flux and WT torque fluctuation caused by stochastic wind speed profiles (WT operating frequency is in the range $0.1Hz - 1Hz$). This loss depends primarily of the magnetic and electric loading of HTS and the intensity and frequency of oscillations. The HTS coils current ripple [11] can also have the big influence on power loss, I_c and n value but due to the large self inductance of HTS winding, it is expected that excitation system can maintain HTS current very smooth (negligible ripple).

To address the wind caused torque fluctuations, we can calculate the armature reaction using the value for synchronous reactance of HTS SM. The intensity of the flux perturbations due to the wind load oscillations will be proportional to the stator current change, donated with $\Delta I_{(d)_{wind}}$. For the value of L_d of the HTS SM, referring to the Sec.2.1, we can assume 0.1 $p.u$

since that is 15 times lower value than for conventional inductance. The simplified dq model of SM without rotor dumper circuits [12], is shown in Eq.10

$$\begin{bmatrix} u_d \\ u_q \\ u_f \end{bmatrix} = \begin{bmatrix} -Ri_d + \frac{d}{dt}\Psi_d - \omega\Psi_q \\ -Ri_q + \frac{d}{dt}\Psi_q + \omega\Psi_d \\ R_f i_f + \frac{d}{dt}\Psi_f \end{bmatrix} ; \begin{bmatrix} \Psi_d \\ \Psi_q \\ \Psi_f \end{bmatrix} = \begin{bmatrix} -(L_{ad} + L_l)i_d + L_{ad}i_f \\ -(L_{aq} + L_l)i_q \\ L_{ff}i_f - L_{ad}i_d \end{bmatrix} \tag{10}$$

where the $L_{ad/aq}$, L_l and $L_{d/q} = L_l + L_{ad/aq}$ are the mutual, leakage and self inductances of the dq stator representation and L_{ff} is the self inductance of the field winding (all referred to the stator). The $u_{d/q/f}$, $i_{d/q/f}$ and $\psi_{d/q/f}$ are presenting voltages, currents and fluxes of d and q axis of stator and field winding, respectively. The resistance of the stator is donated with R. The measure of the stator's magnetic influence on the rotor is the $L_{ad/aq}$ and can be seen in Eq.10.

The mutual inductance $L_{ad/aq}$ will be smaller than synchronous inductance $L_{d/q}$. This means that for current change of 1 pu (from no load to full load), the maximum flux perturbation at the rotor HTS would be less the 10% of main flux, accounting for a stator leakage flux. Thus, it can be argued that with a lower value for the $L_{d/q}$, the rotor - stator magnetic coupling is weaker and with it the losses of HTS, caused by change of stator current. It is noteworthy at this point to remind that such tendency goes together with the increasing ratio of $[T/V]$, both favoring high values for rotor flux density. As the WT torque oscillations (unsteady wind speeds, blades effects - 3P, etc) would be a portion of rated torque and reciprocal to the its frequency [13], the $\Delta I_{(d)_{wind}}$ will also be a portion of rated current. It is realistic to assume that stator current will behave similar to $I_d = 0.75[p.u.] + 0.25[p.u.]sin(p\omega_{load}t)$, where $\Delta I_{(d)_{wind}} \approx 0.5p.u.$. Thus, flux perturbation due to the wind load change can be estimated with mutual flux perturbation calculated with $L_{ad/aq} \cdot \Delta I_{(d)_{wind}} < 0.1 \cdot 0.5$.

The HF PWM magnetic field ripples, and its effect on HTS excitation winding, are caused by armature current on PWM frequency. Again using the $L_{ad/aq}$, we can estimate the amplitude of armature ripple. Let us assume the non excited steady state, i.e $[u_d, u_q] = [0, 1]p.u.$, $i_f = 0p.u.$, where the dq frame is rotating with $\omega_{pwm} = 500p.u. - 2000p.u.$. The base speed is $p\omega_{WT}$. By assuming 10 pole generator and WT revolution $1Hz$, the $p\omega_{WT}$ would be $5Hz$. If the PWM frequency is in the range $2.5 \cdot 10^3 - 10 \cdot 10^3 Hz$ the ω_{pwm} will be in the range $500p.u. - 2000p.u.$. If we neglect the R_s, from Eq.10 the armature current will be

$$i_d = \frac{u_d}{\omega_{pwm} L_d} \Rightarrow \Psi_{f\,pwm} = L_{ad}\frac{1[p.u]}{500[p.u]L_d} < 0.002 \tag{11}$$

and associated HF flux perturbations will have less than 0.2% of main harmonic. It is recommended to use additional rotor circuit (dumpers) to effectively screen out HF armature flux and thus minimize the AC loss of HTS. Yet, in the case of HTS SM suited for WT with imperative on low weight of machine and with it low synchronous inductance too (the T/V increase is going together with lowering L_{ad}), the additional rotor circuit will decrease the transient and sub transient parameters of machine far lower than already low synchronous inductance. The additional complexity of cryostat, energy loss and transient parameters of machine all need to be optimized if the rotor dumper circuits are to be used to minimize HTS AC loss due to the armature flux oscillations.

Returning to the rotor winding and the HTS tapes, the intensity of the magnetic flux oscillations caused by armature current, in the case of slow changing wind load ($f_{load} < 10^{-1}[Hz]$ [13]) and for a realistic values for inductances, $L_d = L_l + L_{ad} = 0.025[p.u.] + 0.075[p.u.]$ of the air core HTS SM and mentioned WT load oscillation, $\Delta I_{(d)_{wind}}$, the amplitude of oscillation of armature reaction will be $L_{ad}\Delta I_{(d)_{wind}} = 0.075 \cdot 0.5$. Thus, for having the flux density at rotor HTS winding for example $8T$, the wind load change would cause 3.75% flux oscillation,

i.e. $300mT$.

In order to calculate HTS loss, the tapes parameters $I_{c(B,\alpha,T)}$ and $n_{(B,\alpha,T)}$ must be obtain experimentally and since the AC power loss will depend from local distribution of magnetic field and current density in HTS, it can not be discussed on generally level. The influence of the ratio I/I_c and expected flux perturbations, derived in this article, on AC loss of HTS will be part of the future work.

5. Conclusion

This paper has briefly shown the nature of improving the output capabilities (T/V) of electrical machines. The content of higher harmonics in the spatial flux distribution was derived proving that when using the HTS with all its mechanical constraints as a rotor field winding, the amount of harmonics can be minimal. Also, we have addressed two main contributors to AC loss of HTS and using realistic values for HTS SM parameters, we have estimated the extent of their influence. It is noticed that when increasing the machine's flux density (resulting in the tendency towards the low $L_{d/q}$ SM and increasing the (T/V)), the HTS winding will be less susceptible to stator flux distortions and will have lower AC loss.

6. Acknowledgments

This work is a part Ph.D project and part of the Superwind.dk project enabled by globalization funds.

References

[1] E P Furlani 2001 *Permanent Magnet & Electromechanical Devices: Materials, Analysis, and Applications (Electromagnetism)* (Academic Press)
[2] E Davies 1971 *IEE Proceedings* **118** 529–535
[3] E Spooner 1973 *IEE Proceedings* **120** 1507–1518
[4] Z H Gan, et al 2009 *ScienceDirect Cryogenics* **49** 198–201
[5] J Frauenhofer, J Grundmann, G Klaus, W Nick 2007 *IEEE Transactions on Applied Superconductivity* **17** 1568–1570
[6] T M Flynn 2005 *Cryogenic engineering* (CRC Press)
[7] A Hughes, T Miller 1977 *IEE Proceedings* **124** 121–126
[8] T Miller, A Hughes 1977 *IEE Proceedings* **124** 127–132
[9] L H Hansen et al 2001 *Conceptual survey of Generators and power electronics for wind turbines* (RISØ National Laboratory)
[10] E Martinez, et al 2007 *IEEE Transactions on Applied Superconductivity* **17** 2738–2741
[11] L F Goodrich, J D Splett 2007 *IEEE Transactions on Applied Superconductivity* **17** 2603–2606
[12] P Kundur 1994 *Power System Stability and Control* (McGraw Hill)
[13] T Burton, D Sharpe, N Jenkins, E Bossanyi 2001 *Wind energy handbook* (Wiley Press)

G.4 Paper: Coil Optimization for High Temperature Superconductor Machines

Presented at Applied Superconductivity Conference (ASC) 2010. The article is peer reviewed. The article is published and available online at IEEE Xplore.

Coil Optimization for High Temperature Superconductor Machines

N. Mijatovic, *Student Member, IEEE*, B. B. Jensen, *Member, IEEE*, A. B. Abrahamsen, V. M. R. Zermeno, C. Træholt, and N. F. Pedersen

***Abstract*—This paper presents topology optimization of HTS racetrack coils for large HTS synchronous machines. The topology optimization is used to acquire optimal coil designs for the excitation system of 3 T HTS machines. Several tapes are evaluated and the optimization results are discussed.**

The optimization algorithm is formulated to minimize the cost for the coils wound with one type of HTS as well as multiple HTS types. It could also be used to minimize other parameters, e.g. space required for the coils. The results are inherently highly dependent on the HTS properties, which at 20 K seem to be in favor of the 1 G tape. The maximal HTS savings achieved allowing multiple current supplies in the excitation system are investigated and estimated to be in the range of 50% for highly nonlinear J-B dependence HTS tapes.

***Index Terms*—HTS coil optimization, HTS machines, topology optimization.**

I. Introduction

HIGH temperature superconducting (HTS) applications are currently limited to a few main areas, such as advance medical diagnostics tools (MRI and NMR) and high energy particle research (accelerators). Large scale HTS applications have been thoroughly demonstrated in the energy sector, e.g. HTS cables, Superconducting Magnetic Energy Storage and HTS machines. Yet their commercialization is still limited by the cost of the HTS materials.

Optimization of the superconducting devices is crucial in order to make them competitive in a free market. At present the two main HTS candidates suitable for industrial applications are first generation (1 G) BSCCO and second generation (2 G) Coated Conductors. The price and performance of the HTS conductors depend strongly on the type of HTS material including: magnetic field dependent critical current density $J_c(B)$, manufacturing procedures, availability and quantity.

Manuscript received August 03, 2010; accepted November 14, 2010. Date of publication December 30, 2010; date of current version May 27, 2011. This work was supported in part by the Technical University of Denmark under the globalization funded Project Superwind.dk.

N. Mijatovic, B. B. Jensen, N. F. Pedersen, and C. Træholt are with the Department of Electrical Engineering, Technical University of Denmark, Lyngby DK-2800, Denmark (e-mail: nm@elektro.dtu.dk; bbj@elektro.dtu.dk; nfp@elektro.dtu.dk; ctr@elektro.dtu.dk).

A. B. Abrahamsen is with the Materials Research Division, Risø National Laboratory for Sustainable Energy, Technical University of Denmark, Roskilde DK-4000, Denmark (e-mail: asab@risoe.dtu.dk).

V. M. R. Zermeno is with the Department of Mathematics, Technical University of Denmark, Lyngby DK-2800, Denmark (e-mail: V.Zermeno@mat.dtu.dk).

Color versions of one or more of the figures in this paper are available online at http://ieeexplore.ieee.org.

Digital Object Identifier 10.1109/TASC.2010.2094171

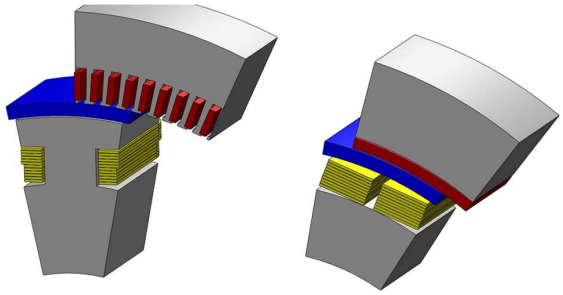

Fig. 1. Conceptual design of one pole-section for salient (left) and non-salient (right) synchronous machines with conventional and air-gap armature windings respectively. The magnetic steel is gray, the armature winding is dark red, the thermal insulation (vacuum chamber, spacers, radiation shield) is blue, and the space for the HTS coils is yellow.

The HTS price is usually the dominating factor of any system employing HTS. Optimization of the HTS usage and cost is therefore one of the main tasks of any superconducting system's designer. In the case of the electrical machines, many designs have been optimized for different applications ranging from air industry to utility companies [1]–[3].

We have employed the constrained Finite Element topology optimization in order to obtain improved HTS coil designs. Doing so it is possible to minimize the amount of HTS needed and hence the cost of HTS, or even to pinpoint a combination of HTS tapes with different properties in order to minimize the cost of the HTS machine.

II. Methodology

First the model of the HTS machine will be discussed, in order to formulate the topology optimization problem for the HTS coils in a machine. After that, details of the design of the HTS coils, HTS tapes, and most important constraints for the HTS coils will be reviewed. Finally, the formulation, implementation, and results of the topology optimization are described.

A. HTS Machine Design

Recommended HTS machine designs vary depending on the application that the machine is intended for. The common characteristic for all HTS machines, and one of their main benefits, is the power density which could be significantly larger than in conventional machines [4].

The two main designs, which the HTS synchronous machines are gravitating towards, are salient pole machines with conventional armature windings and non-salient multi-pole machines with air-gap armature windings [4], [5]. Both designs are shown and described in the Fig. 1.

1051-8223/$26.00 © 2010 IEEE

The magnetic field is established by the HTS excitation winding. A cryostat for thermal insulation between the armature windings at room temperature and the HTS excitation windings at cryogenic temperatures is necessary. Given that the radial thickness of the cryostat is crucial for the machine design and directly responsible for the increase in required MMF, it is important to have a good estimate of the cryostat thickness necessary for operational temperatures between 20 K and 80 K.

The choice of material for the cryostat could be stainless steel (SS) or composite materials. The advantage of SS is the ease of manufacturing, and the advantage of the composite material is zero eddy current losses. The conduction and radiation heat transfer need to be suppressed with a vacuum chamber and multilayer insulation (MLI). The heat transfer through the mechanical and electrical connections also needs to be minimized. It could be assumed that for temperatures above 60 K a cryostat thickness of 20 mm can be achieved and for temperatures between 20 K and 60 K a cryostat thickness of 50 mm is necessary, due to the additional MLI and tighter heat inflow restriction because of lower cooling efficiency at lower temperatures.

Armature designs for HTS machines have been and still are a topic of a debate. Some arguments in favor of the air-gap armature design are removal of teeth saturation and higher armature current loadings. The advantages of air-gap armature windings have not yet been proven commercially and it was reported [6] that the air-gap armature winding involves several challenges, which still needed to be addressed e.g. cooling, mechanical integrity, assembly, and eddy current loss. However, if the trend for development of the compact machines continues, the air-gap armature winding's inherent advantages over conventional slotted armature windings will make the air-gap armature a more favorable choice.

It is also possible to draw some electromagnetic parallels between air-gap and conventional armature windings in slots. Having slotted configuration windings allows very small electromagnetic air gaps, but it also effectively decreases the radial flux path surface of the armature steel. This is taken in to account in conventional analytical machine design by the Carter coefficient, which modifies the effective air-gap to account for the effects of the iron teeth and slots dimensions. Bearing this in mind the model in Fig. 2 can also be used to analyse conventional slotted armatures by altering the inner radius of the stator steel according to the Carter coefficient.

B. HTS Coil Design

HTS tapes, both 1 G and 2 G, are manufactured as a thin tapes (0.1 mm–0.4 mm) of different widths (where 5 mm is the most common) [7]–[9]. In order to estimate the impact of very high engineering current densities in the HTS 2 G tapes, it is assumed that coated insulation is applied. This yields cross sectional areas of only 1 mm^2 for insulated tapes which allows compact coil designs. This tape would correspond to the most expensive tape and it is currently available in limited lengths. Extended tape lengths are currently only available for the 1 G tapes, which adds additional constrains on large scale applications.

Due to the mechanical limitations, the preferred coil layout for the HTS tapes is racetrack coils. Commercially available HTS tape can also be purchased in insulated form (usually Kapton of Glass-Fiber tape insulated) or the tape could be insulated by the coil manufacture. The insulation of the HTS tape can have large impacts on the compactness of the HTS structures.

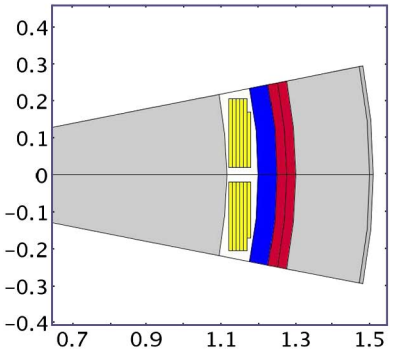

Fig. 2. Simplified model of a synchronous HTS machine with air-gap winding. The magnetic steel is gray, armature winding is dark red, thermal insulation (vacuum chamber, spacers, radiation shields) is blue and space for HTS coils is yellow. The units of x and y axes are [m].

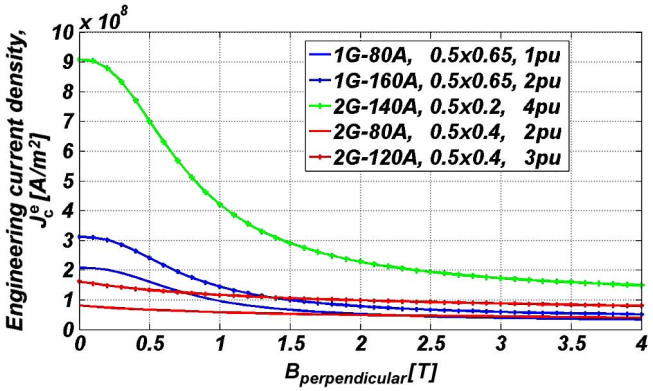

Fig. 3. Estimated engineering current density for 1 G and 2 G tapes at 20 K. The legend shows the HTS type, the critical current at 77 K in the self field, the estimated dimensions of the cross section of the insulated HTS tapes in [mm], and the estimated price of the tape all normalized to the price of 1 G–80 A. The insulation of the tapes is assumed to be 0.3 mm for glass fiber and 0.15 mm for coated insulation.

The HTS' magnetic dependence of its engineering critical current, i.e. $J_c^e - B$ data, is not standardized and is highly dependent on several parameters. In order to compare different types of HTS tapes, the data from published material [6]–[9] is used in this study together with estimated price ratios for the HTS tapes, Fig. 3.

It is also assumed that the price of the same type of HTS tapes scales linearly with the current rating. All HTS prices are normalized to 1 G-80 A, hence having the 1 G–80 A BSCCO tapes as a base value. The HTS 2 G tapes are more expensive at present but it is predicted that they could become cheaper than 1 G tapes.

C. Machine Electromagnetic Model

The model geometry of the conceptual machine used for the coil topology optimization is shown on Fig. 2. The 16 pole machine is non-salient and can be analysed with an air-gap armature winding or a slotted armature winding (simplified with the Carter coefficient). The FE model is reduced to one pole section

using electromagnetic periodicity. The magnetic fields are calculated in steady state using the vector potential formulation of Maxwell's equations. The ferromagnetic steel used in the model for both cold and room temperature magnetic parts is the silicon steel M800-50.

The optimization space domain corresponds to the six double pancake coils. Each double pancake coil was presented with one rectangle of width of 10 mm.

D. Coil Magnetic Anisotropy

An important feature of HTS machines, which needs to be taken in to account, is the high sensitivity of the HTS current carrying capacity in magnetic fields. The prevailing impact on the critical current of the HTS tapes is the perpendicular direction of the magnetic flux to the wide side of the HTS tape. In the machine a single HTS tape is not in a homogenous field but rather, the gradients of the magnetic field can be very large over the entire HTS coil. However, critical currents of HTS tapes are usually derived by the 'short piece' experiment in different fields and field directions, where the field in the experiment is homogenous.

In the model, the perpendicular component of the flux density $\hat{B}_{\perp}^{[p,j]}(x)$ for tape p, is averaged over tape p width, w_{tape}, as shown in (1).

$$\hat{B}_{\perp}^{[p,j]}(x) = \frac{1}{w_{tape}} \int_{0}^{w_{tape}} {}^{j}opt \cdot |B_{\perp}(x,y)|\, dy \tag{1}$$

The ${}^{j}opt$ represents the optimization variable which corresponds to the one type of HTS and $|B_{\perp}(x,y)|$ is the absolute value of the perpendicular component of the magnetic flux density. The peak perpendicular flux density, $B^{j}_{\max\perp}$, experienced by coils made from the j HTS material, can be found by searching for a maximum of the perpendicular flux density experienced by each tape calculated in (1), over the entire optimization domain Ω_{coils}, like in (2).

$$B^{j}_{\max\perp} = \overset{\Omega_{coils}}{MAX}\left(\hat{B}_{\perp}^{[p,j]}(x)\right) \tag{2}$$

At this point we need to consider the excitation strategy. The conventional excitation strategy for a synchronous machine implies one excitation system and one excitation current. Yet it might be wise to allow more excitation currents in the case of HTS machines, assuming that the complication in the excitation system does not cancel out potential savings in HTS material. In this model that feature is investigated and compared with the case of having only one current supply.

The total spatial current distribution $J(x,y)$ with more than one excitation current supply, is calculated as the sum of all the coil current density contributions, as shown in the (3). The J_{cj} is the critical current density for the j type of HTS tape where the ${}^{j}opt(x,y)$ is the optimization variable which controls the spatial distribution of the j type HTS in the coil domain. An additional scalar variable is tied to each HTS type, K_j, scaling current density of that coil from the value defined by the critical current density $J_c(B)$

$$J(x,y) = \sum_{j} {}^{j}opt(x,y) \cdot K_j \cdot J_{cj}\left(B^{j}_{\max\perp}\right) \tag{3}$$

The K_j coefficient is assumed to be fixed to 0.8 in the case of single HTS type employed, thus making sure the electrical loading of the HTS is 80% of the critical loading. In the case of different HTS types, the K_j should also be an optimization variable with values bounded between 0.4 and 0.8.

If one excitation current is allowed, (4) defines the maximal safe supply current.

$$I_{field} = \underset{j}{MIN}\left(K_j \cdot J_{cj}\left(B^{j}_{\max\perp}\right) \cdot {}^{j}A_{tape}\right) \tag{4}$$

Since the different tapes have different cross sections ${}^{j}A_{tape}$, the engineering current densities need to be scaled in order to correspond to I_{field}. The total spatial distribution of the coil domain in this case is formulated in (5).

$$J(x,y) = \sum_{j} {}^{j}opt(x,y) \cdot \frac{I_{field}}{{}^{j}A_{tape}} \tag{5}$$

E. Optimization Formulation

Topology optimization is used in structural studies to ensure minimum material usage and cost, and increased robustness of the structure, especially in an application where over sizing caries high cost penalty (airplane industry) [10].

The objective function, which in COMSOL [11] implementation is minimized by default, will have several terms in the formulation of the optimization problem. The form of the generalized objective function, which is minimized is shown in (6).

$$\min\ Objectiv = \sum_{k=1}^{3} obj_k \tag{6}$$

where obj_k are contributions to the objective function.

The optimization variables, ${}^{j}opt(x,y)$, are defined in the 2D space which corresponds to the space intended for the HTS coils. The idea is to allow the optimization algorithm to control the spatial distribution of the HTS tapes. All optimization variables are constrained between zero and one with (7) and (8).

$$0 \le {}^{j}opt(x,y) \le 1 \tag{7}$$

$$\sum_{j} {}^{j}opt(x,y) \le 1 \tag{8}$$

If the optimization variable is one, current carrying HTS will be present at those coordinates and if it is zero, no HTS tape will be present. Additionally the sum of all the optimization variables at a specific coordinate need to be less than or equal to one, which corresponds to the statement that the same space can have only one tape.

However, since it is not possible to constrain the optimization variables in COMSOL to only binary values, the first term of the objective function, obj_1, needs to penalize all values between zero and one, which is done with (9).

$$obj_1 = \sum_{j}\left(c_{obj1} \int_{\Omega_{coils}} \left[a_{obj1} - \left({}^{j}opt - b_{obj1}\right)^2\right] d\Omega_{coils}\right) \tag{9}$$

where the adjusting constants a_{obj1}, b_{obj1} and c_{obj1} are set to 0.25, 0.5 and 100 respectively, in order to allow this term to have significant effect to the value of the objective function.

$$obj_2 = \left(a_{obj2} \left(B_{r,peak}^{design} - \underbrace{2 \int_{-\pi/2}^{\pi/2} B_r \cos(\theta) d\theta_{armature}}_{firstharmonic} \right) \right)^2 \tag{10}$$

The second term of the objective function, obj_2, shown in (10) is to make sure that the fundamental harmonic of the radial air-gap flux density, B_r, is maintained closely to the desired design value, $B_{r,peak}^{design}$. Thus, the $obj2$ will have the dominating effect on the objective function as long as the air-gap flux is far from the desired value. The constant a_{obj2} controls how dominant this term is in the final objective function and in this implementation its value is set to 5.

The final term of the objective function is the price contributions of each HTS which is calculated using (11).

$$obj_3 = \sum_j \left(\int_{\Omega_{coil}} {}^j opt \cdot \frac{C_j}{{}^j A_{tape}} \cdot d\Omega_{coil} \right) \tag{11}$$

where the price of each tape is C_j.

III. Results

In order to compare the coil optimization results of the generator design shown in the Fig. 2, the price of the optimized coil topology made from a single type of HTS material (both 1 G and 2 G) is compared.

The limiting factor during simulations, especially for the case of multiple tape coils, was a built-in optimization algorithm in COMSOL, which searches only for local minimum [10]. Thus it is very important to keep in mind that the solution, which is a local minimum is highly dependent on the initial conditions. This requires a good initial estimate of which tape should be in which portion of the coil.

1) Single Tape Coils: An optimization example is done on the 16 pole air-gap stator machine. For the machine design input the flux density was set to 3 T with an HTS operating temperature of 20 K.

The optimization results for the 16 pole machine in Fig. 2 are shown in Fig. 4. In the case where the coils consist of a single HTS, the coils made from 2 G 120 A tape (with a relative price of 3 pu), had a price of 54×10^3 pu, as compared to the coils made from 1 G 180 A tape (with a relative price of 2 pu) where the price was only 18×10^3 pu. The price difference between 1 G and 2 G is a factor of three which is in line with expectations, since 1 G tapes have more current capacity between 2 T and 3 T and are 50% cheaper, according to Fig. 3. The coils from ultra thin 2 G 140 A tape would result in a price of 63×10^3 pu. However, the cost impact of the coil space reduction is not taken into account here. This could have a significant impact on the overall price of the machine as it could result in a reduced effective air-gap and hence a lower required value of ampere-turns

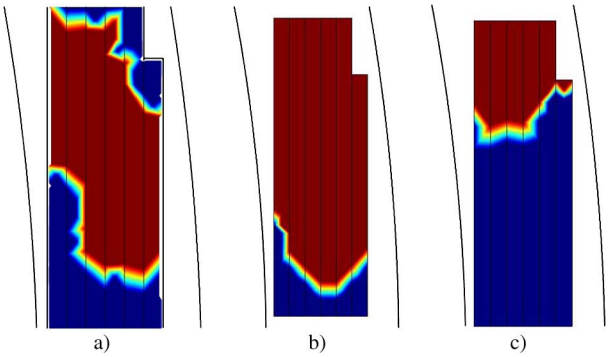

Fig. 4. Optimization results for HTS coils with single HTS type at 20 K. The results are shown only for the upper side of the coils, since the current distribution is symmetrical to the x axis. The dark red is the HTS active domain and the dark blue empty space. (a) 1G-180A-2pu; (b) 2G-120A-3pu; (c) 2G-140A-4pu.

for a given air-gap fluxes density. The lowest grading 1 G 100 A and 2 G 80 A tapes were unable to produce the required 3 T with the allowed coil space.

The optimization results show that the 1 G-180 A tape is most advantageous at 20 K. It has the lowest price and degree of magnetic anisotropy. The results for the ultrathin 2 G-140 A tape are interesting, with a very compact coil of similar price to the 2 G-120 A tape. This tape requires further analysis which allows for the potential benefits of the compact coil to be taken into account.

2) Multiple Excitation Currents: In order to investigate the potential savings in HTS material by allowing multiple excitation currents, we have examined the extreme case were each tape has its own current supply, which should yield the lowest amount of HTS needed to achieve 3 T. This means that each tape operates with its own maximal safe J defined by $J_c(B)$. It is not realistic that each tape would have its own current supply, but it is realistic to imagine that the HTS area was divided into sections with a few separate current supplies.

The optimization was carried out with the same tapes as in the single excitation current case. The optimization resulted in the following price for 1 G–180 A, 2 G–120 A and 2 G–140 A respectively: 12×10^3 pu, 25×10^3 pu and 26×10^3 pu.

The optimization has confirmed the potential for significant HTS savings if multiple current supplies are allowed. The tapes with higher degree of nonlinearity in $J_c - B$, as 2 G at 20 K, have potential savings exceeding 50%. Such savings are less for the 1 G tapes and are in the order of 30% at 20 K.

IV. Conclusion

In this article an optimization algorithm for HTS coils in electrical machines is presented. We have estimated the price ratios of three commercially available types of HTS and used it to derive the price ratios for excitation coils of multi-pole HTS machines. The results were clearly in favor of 1 G tape at 20 K, due to its lower cost and higher current capacity. Promising results were achieved with ultra thin 2 G tape, which require further investigation. Additionally, the article discusses the potential HTS savings of using multiple excitation supplies. Future work will focus on optimal design of coils with two and more types of tapes with one or more current supplies.

REFERENCES

[1] M. H. Ali, W. Bin, and R. A. Dougal, "An overview of SMES applications in power and energy systems," *IEEE Trans. Sustainable Energy*, vol. 1-1, pp. 38–47, Mar. 18, 2010.

[2] J. Cho *et al.*, "Design and experimental results of a 3 phase 30 m HTS power cable," *IEEE Trans. Applied Superconductivity*, vol. 16, no. 2, pp. 1602–1605, June 2006.

[3] S. S. Klasi, "Advances in synchronous machines employing high temperature superconductors (HTS)," in *IEEE Int. Conf. Electric Machines and Drives Conference 2003-IEMDC'03*, vol. 1, pp. 24–28.

[4] G. Klaus, "Design challenges and benefits of HTS synchronous machines," in *IEEE General Meeting 2007*, June 2007, pp. 1–8.

[5] P. J. Masson and C. A. Luongo, "HTS machines for applications in all-electric aircraft," in *IEEE General Meeting 2007*, June 2007, pp. 1–6.

[6] E. J. Davies, "Airgap winding for large turbogenerators," in *Proc. of the Institution of Electrical Engineers*, 1971, vol. 118-3.4, pp. 529–535.

[7] [Online]. Available: http://www.superpower-inc.com/content/technical-documents

[8] [Online]. Available: http://global-sei.com/super/hts_e/index.html

[9] [Online]. Available: http://www.amsc.com/products/htswire/

[10] M. P. Bendsøe, N. Olhoff, and O. Sigmund, "Recent developments in the commercial implementation of topology optimization," in *IUTAM Symp. on Topological Design Optimization of Structures, Machines and Materials*, 2006, vol. 137, pp. 239–248.

[11] *"Comsol Multiphysic 4.0a—Optimization Module, Software Manual,"* 2010.

G.5 Paper: Feasibility study of 5 MW superconducting wind turbine generator

Author's personal copy

Physica C 471 (2011) 1464–1469

Contents lists available at ScienceDirect

Physica C

journal homepage: www.elsevier.com/locate/physc

Feasibility study of 5 MW superconducting wind turbine generator

A.B. Abrahamsen [a,*], B.B. Jensen [b], E. Seiler [d], N. Mijatovic [b], V.M. Rodriguez-Zermeno [c], N.H. Andersen [a], J. Østergård [b]

[a] Materials Research Division, Risø DTU, Technical University of Denmark, Frederiksborgvej 399, Roskilde, Denmark
[b] Department of Electrical Engineering, Technical University of Denmark, Lyngby, Denmark
[c] Department of Mathematics, Technical University of Denmark, Lyngby, Denmark
[d] Institute of Electrical Engineering, Slovak Academy of Sciences, Bratislava, Slovakia

ARTICLE INFO

Article history:
Available online 13 May 2011

Keywords:
Superconducting generator
Offshore wind turbine
Race track coils

ABSTRACT

The feasibility of installing a direct drive superconducting generator in the 5 MW reference offshore wind turbine of the National Renewable Energy Laboratory (NREL) has been examined. The engineering current densities J_e obtained in a series of race track coils have been combined with magnetization measurements to estimate the properties of suitable field coils for a synchronous generator, which is more light weight than the conventional used combination of a gear box and a fast rotating generator. An analytical model and finite element simulations have been used to estimate the active mass of generators with varying number of poles. A 24 pole machine with an outer diameter of 4.2 m and active length and mass of 1.2 m and 34 tons is suggested possible, if a J_e = 300 A/mm^2 can be obtained in B = 4 T pointing to an operation temperature around 40 K.

© 2011 Elsevier B.V. All rights reserved.

1. Introduction

The urge for the development of offshore wind power in Europe has increased due to member state policies on fossil fuel independency by 2050 in order to reduce global warming and to secure energy supplies. Offshore wind power is an emerging technology with only 2.1 GW installed capacity in EU by the end of 2009, which should be compared to 76.2 GW and 156.5 GW of total installed capacity in EU and world wide respectively [1,2]. The EU offshore capacity must be expanded by two orders of magnitude by 2030 in order to supply 20% of the electricity demand from renewable sources [3]. Effort is now made to increase the size of offshore turbines and to improve the reliability by introducing mechanically simplified drive trains, such as direct drive generators based on permanent magnets [4].

The EU offshore capacity is provided by 830 turbines with an average size of 2.9 MW, but a small number of 5 MW offshore turbines have been in operation since 2009 with a distribution of 14 REpower 5M and 6 Areva Multibrid M5000 [4]. The REpower 5M turbine is based on a conventional drive train with a three stage gearbox and a generator rotating at 1500 revolutions per minutes (rpm), whereas the Multibrid turbine has a hybrid drive train with a single stage gearbox and a slow rotating generator at 150 rpm. The Repower turbine was developed as part of a research project and it is often referred to as the NREL reference turbine, since public informations about the properties are available [5].

We have previously examined the challenges of introducing a superconducting direct drive generator in future 10 MW offshore wind turbines and indicated that the price of coated conductors must be reduced by an order of magnitude before the 2030 target installation price of 1.5 MEuro/MW can be reached [6]. Secondly the reliability of a superconducting direct drive generator must be proven and in this paper we will examine the possibility of a demonstration installation in a turbine resembling the NREL reference turbine. In this context it is interesting to mention that the present offshore installation price is in the range of 3.4–3.6 MEuro/MW [7,8]. This price increased to 4–5 MEuro/MW for the present 5 MW installations and indicates a reasonable price for a superconducting direct drive demonstration.

This paper is organized by a presentation of the engineering current density J_e of a series of race track coils constructed within the Superwind project at DTU [9]. The temperature and field scaling of J_e as determined by magnetization measurements is used as input for determination of the properties of a synchronous generator suitable for the NREL reference turbine. An analytic generator model based on reluctance circuit analysis is introduced and compared to finite element simulations. Finally the active material of the superconducting generators is determined as function of the pole number and the feasibility is discussed.

* Corresponding author. Tel.: +45 46774741; fax: +45 46775758.
E-mail address: asab@risoe.dtu.dk (A.B. Abrahamsen).

0921-4534/$ - see front matter © 2011 Elsevier B.V. All rights reserved.
doi:10.1016/j.physc.2011.05.217

Author's personal copy

2. Superconducting race track coils

A number of race track coils have been constructed and tested as part of the Superwind project at DTU in order to demonstrate the feasibility of using high temperature superconducting tapes in rotor coils of synchronous generators suitable for wind turbines [9]. A coil design which can hold both Bi-2223(denoted first generation tape 1G) and coated conductor tapes (denoted second generation 2G) was developed. The design is based on an inner frame of 316 stainless steel onto which a superconducting tape and a glass fiber (GF) tape are wound. A copper block is soldered onto the beginning of the tape prior to winding and serves as one of the current contacts and another copper block is soldered to the end of the tape to provide the outer current contact as shown on Fig. 1. Thin copper wires are soldered onto the tape during the winding in order to allow voltage measurement directly across sections of the superconducting tapes and the wires are connected to a circuit board sitting on an outer 316 stainless steel frame, which also provides the mechanical support of the coil. The coils are vacuum impregnated by epoxy in a stainless steel form after the assembly and cured in air. Excess epoxy was mechanically cracked off from the coils, which were treated with epoxy release agents before assembling. Fig. 1 shows one of the coils, which allows a 20 mm thick winding of tape. The purpose of the coils is to stack them onto the iron rotor piece of a two pole test machine under construction at DTU.

The properties of the tapes used in the coils are summarized in Table 1 as well as the engineering current density J_e

$$J_e = \frac{I_C}{(t_{tape} + t_{insulation})w_{tape}} \quad (1)$$

defined as the critical current I_C of the tape divided by the sum of the tape t_{tape} and the insulation $t_{insulation}$ thickness multiplied by the width of the tape w_{tape}. Two types of Bi-2223 tapes from American Superconductors based on brass and steel reinforcement have been investigated using the glass fiber tape insulation technique in the winding of coil no. 1 and nos. 2–5 respectively. This method was also used for coil no. 6 holding a 2G $YBa_2Cu_3O_{6+x}$ coated conductor from American superconductor. Coated conductor tape of type 4050 from Superpower has been insulated by a thin layer of epoxy adding only 60 μm to the tape thickness and this is planned for the winding of coil no. 7 [11]. Estimates of the critical current of the coils have been obtained from 3D finite element simulations of the field distribution by assuming a homogenous current density in the entire cross section of the coil winding. The maximum field component

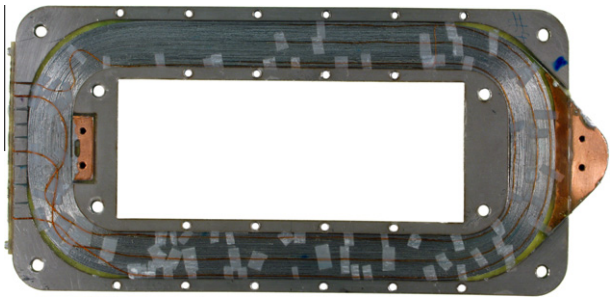

Fig. 1. Racetrack coil based on a winding of 5 mm wide high temperature superconducting tape. Electrical contact is provided by copper block at the two ends of the winding and thin copper wires are soldered onto the tape, whereby 4 point voltage measurements can be performed on selected sections of the tape. The inner and outer frame is made of 316 stainless steel and provides mechanical support for the coil. A circuit board is mounted on the left hand side of the steel frame for connection of voltage probe wires. The square hole of 150 mm × 60 mm in the middle can be fitted around an iron core of a test machine under construction at DTU.

Table 1
The properties of the high temperature superconducting tapes used in the Risø-DTU race track coil are listed in the first part of the table, whereas the predicted and obtained coil properties are shown below. 1G and 2G refers to Bi-2223 and coated conductor tapes respectively. *Expected values since winding of coil no. 7 is planned.

Coil no	1	2–5	6	7
Tape	1G Brass	1G Steel	2G 348C	2G 4050
Width (mm)	4.3	4.3	4.8	4.2
Thickness (mm)	0.39	0.28	0.22	0.10
I_C (77K, sf) (A)	150	145	95	125
Insulation	GF tape	GF tape	GF tape	Epoxy
Thickness (mm)	0.10	0.10	0.10	0.06
J_e (77K, sf) (A/mm^2)	68.8	88.7	61.8	186.0
No. turns	31	48–51	57	125*
Tape length (m)	16.3	25.4–28.8	31.6	69.1*
$I_{C,coil}$ 77 K (A)	76.7	82.9–83.5	69.4	–
n_{coil} 77 K	14.1	14.4–15.6	41.9	–

normal to the tape surface was evaluated and compared to the field dependent critical current of the used tapes. This field component is along the c-axis of the textured HTC material in the tape and it is usually causing the smallest critical current. The Current–Voltage (IU) curves of the tapes were measured in liquid nitrogen at $T = 77$ K using an Agilent 34420A nano voltmeter connected to voltage probe copper wires soldered onto the tape surface with a 15–20 mm spacing. A HP6031A power supply was used to increase the current from $I = 0 - 120$ A controlled by a Labview program also collecting the voltage across the tape. A magnetic field of $B = 0 - 1$ T was applied perpendicular to the tape surface using an electromagnet [10].

The IU curves all showed a power law behavior

$$U = E_0 \cdot l\left(\frac{I}{I_C(\mathbf{B}, T)}\right)^{n(\mathbf{B},T)} \quad (2)$$

where I is the transport current of the tape, $I_C(\mathbf{B}, T)$ is the critical current causing a voltage drop of $U = E_0 \cdot l$ and $n(\mathbf{B}, T)$ is the exponent of the power law quantifying how abrupt the transition from the superconducting to the resistive state will be. The choice of $E_0 = 10^{-6}$ V/cm was used as criteria for defining the critical current, where l is the distance between the voltage taps. The IU curves of the coils of Table 1 were obtained by measuring the voltage across the beginning and end copper wires of the coil immersed in liquid nitrogen as the current was increased in the setup also used for the tape measurements. Fig. 2 shows the IU curves of coil no. 1 based on 1G-brass tape and the 1G-steel tape is represented by the coils 2 and 3, which are similar to coils 4 and 5 (not shown). The two IU curves of coil 6 based on AmSC 348 tape are first showing a quench of the coil and the subsequent measurement confirming that the coil was not damaged by the quench. A critical current criteria of $U_0 = E_0 \cdot l$, where l is the length of the tape in the coil was applied and the IU curves in Fig. 2 have been normalized by the length of tape in the coil. The critical current and n-values of the coils at $T = 77$ K are listed in Table 1. The demonstrated engineering current density of the demonstration coils will be used to extrapolate the properties of larger race track coils operating in higher field and at lower temperatures.

3. Temperature and magnetic field scaling of critical current

The in-field pinning properties of the coated conductor tapes of the coils have been investigated in applied fields up to 16 T using a vibrating sample magnetometer (VSM) from Cryogenic Limited [12]. Pieces of tapes with identical width and length were mounted in straws using Kapton tape and inserted into the VSM with the applied field normal to the tape surface and parallel to the c-axis of

Author's personal copy

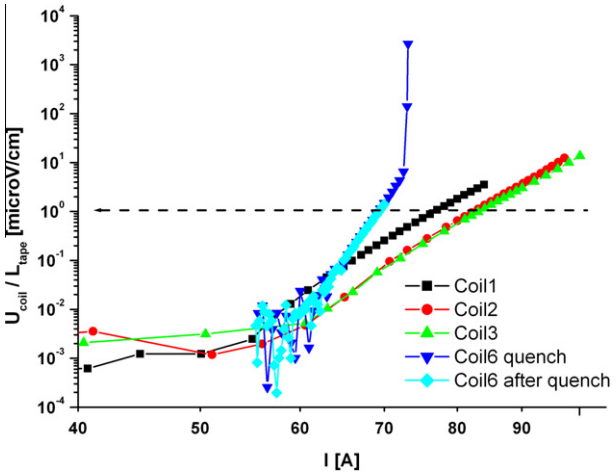

Fig. 2. *IU* curves of race track coil no. 1 (American Superconductor Bi-2223-Brass tape), coil nos. 2 and 3 (American Superconductor Bi-2223-Steel) and coil no. 6 (American superconductor coated conductor 348C) immersed in liquid nitrogen at $T = 77$ K. The two *IU* curves of coil no. 6 are showing a quench at $I = 73$ A and the following measurement confirming no damage during the quench. The noise level of the measurements of coil no. 6 is similar to the other coils and is not shown for clarity.

the $YBa_2Cu_3O_{6+x}$ superconductor. Magnetization curves were obtained by cooling the samples below the critical temperature $T_C \sim 93$ K in zero applied field and then sweeping the applied field $\mu_0 H = 0 \rightarrow 16 \rightarrow -16 \rightarrow 16 \rightarrow 0$ T. Subsequent magnetization curves were obtained by decreasing the temperature after the applied field was ramped to zero. The opening of the hysteresis curves Δm was determined as the difference between the $\mu_0 H = 16 \rightarrow -16$T and $\mu_0 H = -16 \rightarrow 16$ T part of the curves. Figs. 3 and 4 are showing the hysteresis opening scaled by the value at $T = 77$ K and zero applied field as function of applied field and at different temperatures. From the simple Bean model it is known that the magnetization hysteresis Δm will be proportional to the critical current density J_C of a superconductor, $\Delta m \propto J_C$. Similar relations are also found for thin film solution [13]. Thus the critical current $I_C(B, T)$ of the tapes scaled to the critical current $I_C(\textit{self field}, 77\text{ K})$ provided by the tape manufacturers can be assumed to scale like the hysteresis scaling shown in Figs. 3 and 4. This temperature scaling will be used to estimate the current density of coils suitable for a wind turbine generator.

4. NREL reference turbine and generator model

The properties of the drive train of the NREL/REpower wind turbine are summarized in Table 2 and it should be noted that the weight of the gearbox and the generator is 80 tons. One could ask if a 80 tons superconducting direct drive generator could replace the conventional drive train, but the competition from $Nd_2Fe_{14}B$ permanent magnet based direct drive generators as installed in the recent Siemens SWT 3.0-101 turbine will call for a further weight reduction [16]. A target of 40 tons of active mass will be used in the following analysis, but a target price of the drive trains must first be estimated. A target installation cost of 2 MEuro/MW in 2020 will be assumed and this gives a drive train price estimate of $P_{DT} = 2$ MEuro/MW·5 MW·1/3·1/2 = 1.65 MEuro, since the turbine fraction of the cost is often 1/3 and the drive train fraction is 1/2. Using the density of the superconductor/insulation composite deduced from Table 1 and an target price of 8 Euro/m in 2020 then one can estimate a maximum allowed volume of superconductor to be used. This would correspond to 228 km of AmSC 348C or 206 km of Superpower tape resulting in a weight of 2061 kg or 706 kg respectively. We will focus the analysis on a radial synchronous machine with a superconducting field winding and an stator winding without iron teeth at room temperature as has been demonstrated for large scale systems [17,18].

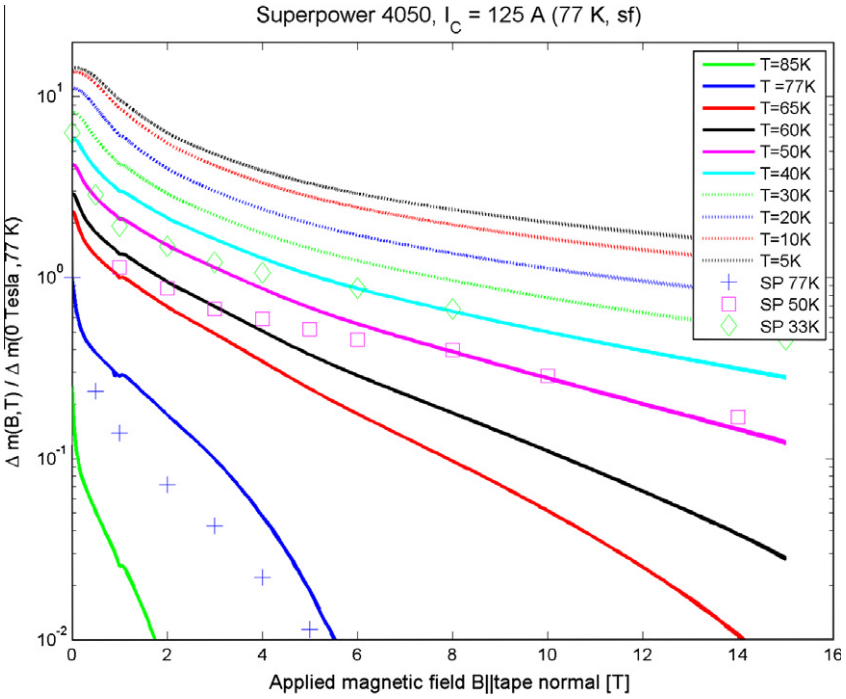

Fig. 3. Scaling of magnetization hysteresis $\Delta m(B, T)/\Delta m(0\text{ T}, 77\text{ K})$ of Superpower 4050 tape. A simple description of the pinning in superconductors like formulated in the Bean model will result in a proportionality between the magnetization hysteresis $\Delta m(B, T)$ and the critical current density J_C, $\Delta m(B, T) \propto J_C$. Thus one can in principle use the magnetization hysteresis to obtain information about the in-field performance of the tape by applying the scaling factor to the critical current of a tape obtained in a transport measurement. The markers are showing the publicly available in-field performance of a standard SP4050 tape with a $I_C = 80$ A (self field, 77 K) [14]. The discrepancy is believed to be caused by the fact that the tape studied here has an $I_C = 125$ A (self field, 77 K), which is expected also to result in a better in-field performance.

Author's personal copy

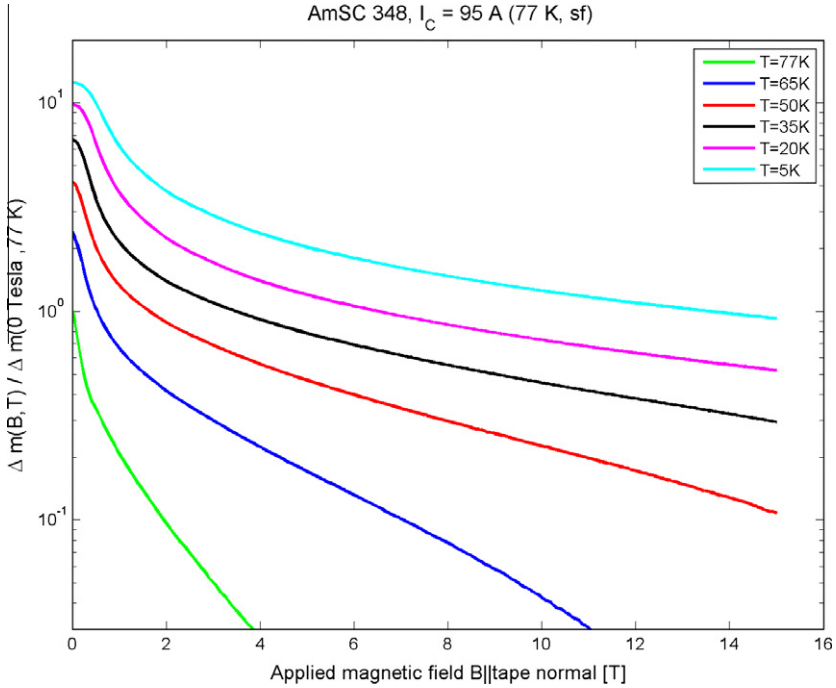

Fig. 4. Scaling of magnetization hysteresis of American Superconductor 348 C tape observed on top of the ferromagnetic response of the Ni–W based substrate of the tape.

Table 2
Drive train properties of the NREL/REpower wind turbine [5,15]

Power (MW)	5
Rotation speed (rpm)	12.1
Gearbox size $W \times H \times L$ (m)	$4.6 \times 3.0 \times 4.1$
Gearbox weight (tons)	63
Generator size $W \times H \times L$ (m)	$2.2 \times 2.2 \times 4.0$
Generator weight (tons)	17
Nacelle Size $W \times H \times L$ (m)	$6.0 \times 6.0 \times 18$
Nacelle weight (tons)	265

Alternatives based on bulk superconductors [19] or fully superconducting machines [20] have not been investigated, since the magnetization method of the bulk superconductor and low AC loss superconducting wires or tapes for a superconducting stator are still under development. A cryostat of 4 cm thickness on each side of the superconductor field winding is assumed and the outer diameter of the machine is fixed at $D_{out} = 4.2$ m in order to make the generator fit into the nacelle.

An analytical model based on a lumped reluctance circuit has been used to estimate air gap flux of a multipole machine as shown on Fig. 5a. The circuit on Fig. 5b describes the flux linkage between the two sides of a superconducting field winding by introducing reluctances related to the radial direction $R_{i,r}$ and to the circumferential direction $R_{i,c}$ of the active layers i of the machine. The reluctance reflects both the geometry of the machine and also the magnetic properties of the material specified by the relative permeability μ_r

$$R_{i,r} = \frac{1}{\mu_{r,i}\mu_0}\frac{l_{r,i}}{A_{r,i}} \tag{3}$$

where μ_0 is the vacuum permeability, l_r is the length of the flux path in the radial direction and A_r is the area which the flux passes through. Using Kirchhoff's circuit law on the reluctance loops a matrix relation between the magneto motive force F_{sc} of the superconductor and the flux ϕ_i in the loops is obtained

$$\begin{pmatrix} 0 \\ 0 \\ F_{sc} \\ 0 \\ 0 \\ 0 \end{pmatrix} = \begin{pmatrix} R_{11} & R_{12} & 0 & 0 & 0 & 0 \\ R_{21} & R_{22} & R_{23} & 0 & 0 & 0 \\ 0 & R_{32} & R_{33} & R_{34} & 0 & 0 \\ 0 & 0 & R_{43} & R_{44} & R_{45} & 0 \\ 0 & 0 & 0 & R_{54} & R_{55} & R_{56} \\ 0 & 0 & 0 & 0 & R_{65} & R_{66} \end{pmatrix} \begin{pmatrix} \phi_1 \\ \phi_2 \\ \phi_3 \\ \phi_4 \\ \phi_5 \\ \phi_6 \end{pmatrix} \tag{4}$$

The terms $R_{x,y}$ contain the reluctance sums linking the fluxes, ex. $R_{32} = -R_{si,c}$, $R_{33} = 2R_{si2,r} + 2R_{so1,r} + R_{si,c} + R_{so,c}$ and $R_{34} = -R_{so,c}$. By inverting Eq. (4) one can obtain the airgap flux of the pole and by assuming a sinusoidal angular variation one can deduce the maximum flux density B_0 in the airgap

$$\phi_3 = \int B_0 \cos(p\theta) r d\theta L \tag{5}$$

where p is the pole number and L is the active length of the machine. Similarly by assuming a sinusoidal current distribution of the 3-phase stator $I_S = \sqrt{2}A_S \cos(p(\theta - \psi))$ one can estimate the torque of the machine by

$$T = \sqrt{2}B_0 A_s V \cos(p\psi) \tag{6}$$

where A_s is the electric loading in [A/m] and $V = \pi r^2 L$ is the volume of the machine given by the airgap radius r and the active length L. The power is then $P = T\omega$, where ω is the angular rotation speed.

The analytical model was used to obtain the dimensions and hence the active mass of the machines, as the number of poles was varied. The output power was kept at 5 MW while the sum of the iron losses and the copper losses were maintained at 5% of the input power; the electric loading of the stator was kept at 90 kA/m; the airgap flux density at 2.4 T; and the core flux density was kept below 2.5 T. The finite element program Magnet from Infolytica was used to verify the magnetic field distribution as shown on Fig. 5c in the case of a 24 pole generator. The analytical model results were within 2–10% of the FE simulations. Fig. 6 shows the usage of active materials for the machines with a $J_e = 70$ A/mm^2 and a $J_e = 300$ A/mm^2 as obtained for the AmSC coil no. 6 and as expected for the Superpower coil no. 7 when the temperature is

Author's personal copy

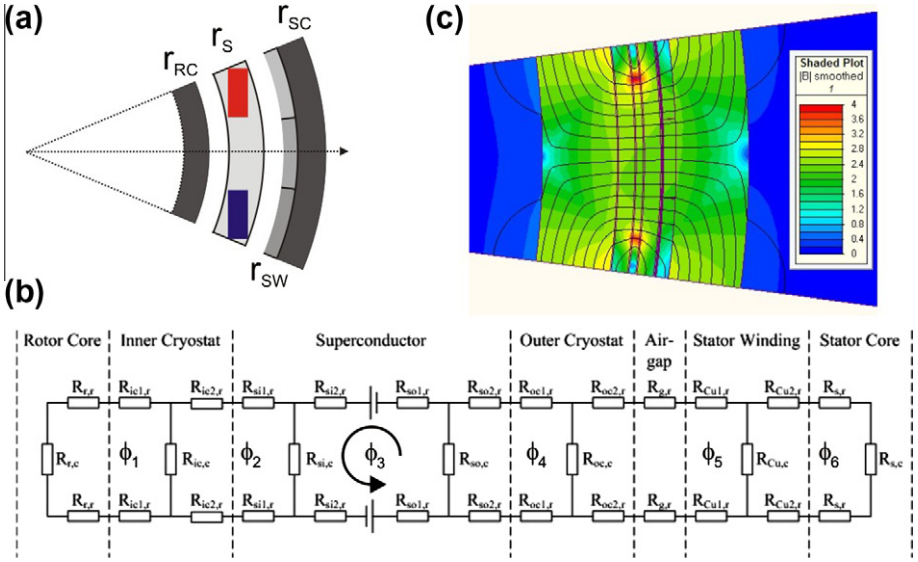

Fig. 5. (a) Layout of generator with $R_{RC1,2}$ denoting the inner and outer radius of the rotor iron core back, $R_{S1,2}$ denoted the superconducting field winding, $R_{SW1,2}$ the 3 phase stator winding and $R_{SC1,2}$ the stator core back iron. (b) A reluctance circuit representation of generator topology. (c) Finite element simulation of field distribution in a 24 pole machine.

lowered to $T = 30$ K and $T = 40$ K respectively. The operation temperature is deduced from Figs. 4 and 3 by identifying when the scaling factor is 1.13 for the AmSC tape and 1.61 for the Superpower tape at $B = 4$ T, which is the maximum flux density on the superconductors as seen on Fig. 5c. The finite element simulations showed that although the peak flux density in the iron was 2.5 T, the iron losses were very small (below 10 kW in all the cases). This is because the frequency was very low, e.g. 2.4 Hz for a 24 pole machine rotating at 12 rpm, and the iron losses depend heavily on the frequency. As the iron was heavily saturated where the peak flux density occurred, some flux would penetrate through the iron and come into the ambient air surrounding the iron. The magnitude of the flux density outside the iron core was investigated and found to be reduced to below 0.1 T at a distance of half a pole pitch, i.e. 250 mm outside the iron core the peak flux density was 0.07 T in the 24 pole machine. This was deemed acceptable by the authors, because the application is a wind turbine with free ambient air surrounding the machine.

5. Discussion

The general trend of Fig. 6 is that the amount of superconductor increases with the number of poles, but the usage of iron for both the rotor and stator can be decreased and thereby reduces the total weight of the generator. In the case of $J_e = 70$ A/mm^2 it is seen that the total target weight is first fulfilled for a 24 pole machine, but this would need about 5 tons of 2G AmSC tape, which is more than twice the allowed limit. One could stay within the usage limit of the tape by choosing a 8 pole machine, but then the total active mass is 90 tons. This indicates that a higher J_e is needed and this could be obtained by applying the epoxy insulation technique or to replace the GF tape with a thinner material. Additionally it should be said that using a wider tape would also increase the effective J_e, since the present tape has a soldering region at the edges of 0.4 mm/ 4.9 mm = 8%. Finally one could consider to decrease the operation temperature further, but this would also increase the complexity of the cryogenic design. In the case of $J_e = 300$ A/mm^2 the active weight target is fulfilled for a 20 or higher pole number machine and the usage of tape is within the price target, which would also allow funding for the cooling system and cryostat. Such a 24 pole machine does seem interesting because

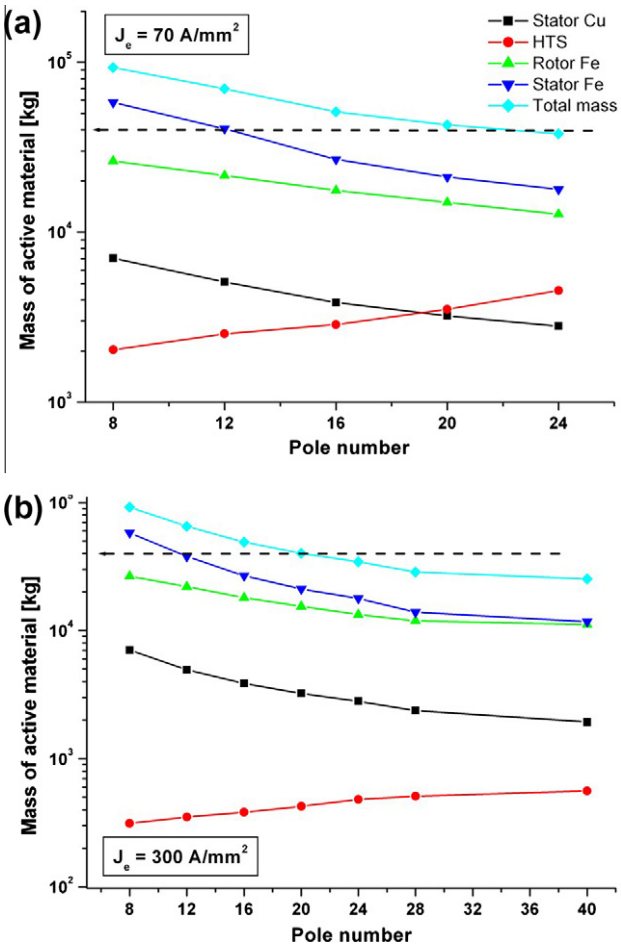

Fig. 6. Active material usage as function of pole number for a 5 MW direct drive superconducting generator with a 2.4 T airgap flux density and with a engineering current density of the superconducting winding corresponding to (a) $J_e = 70$ A/mm^2 and (b) $J_e = 300$ A/mm^2. The horizontal line indicate the design criteria of a total active mass of 40 tons.

Author's personal copy

the dimensions are down to a 4.2 m diameter and an active length of 1.2 m, which should allow for a large reduction of the nacelle size and thereby further weight reductions of the support structure. From this analysis it seems that the thin substrate of the Superpower tape is a great advantage combined with a thin insulation layer, but it does remain to be proved that sufficient quench protection can be applied to the coils.

6. Conclusion

A series of race-track coils holding 16–32 m of Bi-2223 and coated conductor high temperature superconducting tapes have been constructed and magnetization measurements have been performed on the tapes to estimate the applied field and temperature scaling of the engineering current density J_e. This was used as input for model calculations of the usage of active material in a direct drive synchronous radial multipole generator suitable for installation in the 5 MW offshore reference wind turbine described by NREL. It is concluded that a $J_e = 70$ A/mm^2 at $B = 4$ T and $T = 30$ K when using an AmSC tape is too low to both fulfilling a weight reduction target below 40 tons of active material and also a price target of 8 Euro/m. By increasing $J_e = 300$ A/mm^2 at $B = 4.0$ T and $T = 40$ K when using a Superpower tape it is indicated that both the weight and price targets can be fulfilled resulting in $D = 4.2$ m and active length and mass of 1.2 m and 34 tons respectively. Further studies on cryogenic design and quench protection are needed to confirm the feasibility of such a generator.

Acknowledgements

We would like to acknowledge the globalization initiative of DTU for the funding of the Superwind project and EDFA for funding studies of coated conductor properties in high magnetic field. Danfysik A/S for the insulation of the Superpower tape and Ultera A/S for providing the 1G brass tape. One of the authors (VMRZ) acknowledges financial support from: Technical University of Denmark, The Research School of the Danish Center for Applied Mathematics and Mechanics, Vestas Wind Systems and SEP-Mexico.

References

[1] European Wind Energy Association(EWEA) Report, "The European Offshore Wind Industry key Trends and Statistics 2009, January 2010. <www.ewea.org>.
[2] S. Sawyer, A. Zervos, "Global Wind 2009 Report, Global Wind Energy Council, March 2010. <www.gwec.net>.
[3] P. Capros, L. Mantzos, N. Tasios, A. De Vita, N. Kouvaritakis, ISBN 978-92-79-16191-9, 2010.
[4] P. Gardner, A. Garrad, L.F. Hansen, P. Jamieson, C. Morgan, F. Murray, A. Tindal, J. Ignacio Cruz, L. Arribas, Nicholas Fichaux, ISBN 9781844077106, EarthScan, March 2009.
[5] J. Jonkman, S. Butterfield, W. Musial, G. Scott, Technical Report NREL/TP-500-38060, February 2009.
[6] A.B. Abrahamsen, N. Mijatovic, E. Seiler, T. Zirngibl, C. Træholt, P.B. Nørgård, N.F. Pedersen, N.H. Andersen, J. Østergård, Supercond. Sci. Technol. 23 (2010) 034019.
[7] Thanet Offshore Wind Farm. <www.vattenfall.co.uk/en/thanet-offshore-wind-farm.htm>.
[8] Anholt Offshore Wind Farm. <www.dongenergy.com>.
[9] Superwind Project. <www.superwind.dk>.
[10] Arepoc s.r.o. <www.arepoc.sk>.
[11] Epoxy Insulation Done by Danfysik A/S. <www.danfysik.com>.
[12] Cryogenic Limited. <www.cryogenic.co.uk>.
[13] E.H. Brandt, Rep. Prog. Phys. 58 (1995) 1465.
[14] D.W. Hazelton, V. Selvamanickam, Proc. IEEE 97 (2009) 1831.
[15] REpower Systems AG Webpage. <www.repower.de>.
[16] Siemens SWT3.0-101 Specifications. <www.energy.siemens.com>.
[17] S.S. Kalsi, K. Weeber, H. Takesue, C. Lewis, H.-W. Neumueller, R.D. Blaugher, Proc. IEEE 92 (10) (2004) 1688.
[18] P.N. Barnes, M.D. Sumption, G.L. Rhoads, Cryogenics 45 (2005) 670686.
[19] Y. Jiang, R. Pei, Z. Hong, J. Song, F. Fang, T.A. Coombs, Supercond. Sci. Technol. 20 (2007) 585591.
[20] Q. Jiang, M. Majoros, Z. Hong, A.M. Campbell, T.A. Coombs, Supercond. Sci. Technol. 19 (2006) 11641168.

G.6 Paper: Towards faster FEM simulation of thin film superconductors: a multiscale approach

Presented at Applied Superconductivity Conference (ASC) 2010. The article is peer reviewed. The article is published and available online at IEEE Xplore.

Towards Faster FEM Simulation of Thin Film Superconductors: A Multiscale Approach

V. M. Rodriguez-Zermeno, N. Mijatovic, *Student Member, IEEE*, C. Træholt, T. Zirngibl, E. Seiler, A. B. Abrahamsen, N. F. Pedersen, and M. P. Sørensen

***Abstract*—This work presents a method to simulate the electromagnetic properties of superconductors with high aspect ratio such as the commercially available second generation superconducting YBCO tapes. The method is based on a multiscale representation for both thickness and width of the superconducting domains. A couple of test cases were successfully simulated and further investigations were made by means of structured (mapped) meshes. Here, large aspect ratio elements were used to simulate thin material layers with a reduced number of elements. Hence, more complex geometries can be studied at considerable lower computational time. Several test cases were simulated including transport current, externally applied magnetic field and a combination of both. The results are in good agreement with recently published numerical simulations. The computational time to solve the present multiscale approach in 2D is estimated as two orders of magnitude faster than other 2D methods.**

***Index Terms*—AC losses, finite element methods, high temperature superconductors, superconducting coils.**

I. Introduction

THE large aspect ratio of 2G superconducting tapes is a matter of concern for the numerical simulation of its electromagnetic properties [1], [2]. Meshing of thin layers using elements with aspect ratio close to unity puts a big constrain in the number of degrees of freedom to be solved for. In the particular case of 2G superconducting wires, the layers have aspect ratios in the order of $10^3 \sim 10^4$. Therefore, simulation of systems involving several conductors proves to be a rather cumbersome task.

So far, several methods have been proposed to overcome this burden: use of 1D approaches that neglect the thickness of the superconducting layer [1] and implementation of geometries with a lower aspect ratio along with scaled current density values [2], among others. However, the problem persists as the aforementioned methods are either based upon extrapolation of calculations for lower aspect ratio domains; or do not provide very accurate results for the case where low transport currents and small separation among multiple conductors.

The large aspect ratio of the thin film conductors makes clear that the superconducting material is located in a multiscale domain: thickness and width are in different spatial scales. Here, we present a way to simulate superconductors in a timely effective manner. The simulation is based on previously published models [3], [4] and an existing implementation using COMSOL [5]. The use of this multiscale approach allows creating custom made applications rapidly and with ease.

II. Governing Equations

Following a formulation originally proposed in [4], the magnetic field strength is calculated by solving:

$$\nabla \times (\rho \nabla \times H) = -\mu \frac{\partial H}{\partial t}, \tag{1}$$

where μ is the permeability; the resistivity ρ is a constant for normal conductors but for superconductors it is given by the following power law:

$$\rho = \frac{E_c}{J_c} \left(\frac{|J|}{J_c} \right)^{n-1}, \tag{2}$$

here the current density $J = \nabla \times H$; E_c is the electric field strength of $1\ \mu\mathrm{V/cm}$ obtained when the current density reaches the critical current density J_c and n characterizes how abruptly the transition from the superconducting to normal state is taking place.

To impose an explicit transport current in each of several conductors, integral constraints are used, so that the total electric current can be arbitrarily specified by means of a function of time. In this case, Neumann boundary conditions were used. For the case when an external magnetic field was applied, appropriate Dirichlet boundary conditions were selected.

III. Structured (Mapped) Meshes

Traditional meshing techniques use elements with aspect ratio close to unity to discretize a domain [6]. Their use in thin layers (either normal or superconducting) poses a significant drawback. This is due to the fact that the number of elements increases heavily with the growing aspect ratio of the layer. As a result, the number of degrees of freedom is augmented and so is the computing time. This has important consequences for the simulation of second generation superconducting tapes since the aspect ratio of the superconducting layer in such conductors can be as high as 10^4.

Manuscript received August 18, 2010; accepted October 31, 2010. Date of publication December 17, 2010; date of current version May 27, 2011. This work was supported in part by the Technical University of Denmark, The Research School of the Danish Center for Applied Mathematics and Mechanics, Vestas Wind Systems and SEP-Mexico.

V. M. Rodriguez-Zermeno and M. P. Sørensen are with the Department of Mathematics, Technical University of Denmark, Kgs. Lyngby 2800, Denmark (e-mail: V.Zermeno@mat.dtu.dk).

N. Mijatovic, C. Træholt, and N. F. Pedersen, are with the Department of Electrical Engineering, Technical University of Denmark Kgs. Lyngby 2800, Denmark.

A. B. Abrahamsen, T. Zirngibl and E. Seiler are with Risø National Laboratory for Sustainable Energy, Materials Research Division, Technical University of Denmark, Roskilde, Denmark.

Color versions of one or more of the figures in this paper are available online at http://ieeexplore.ieee.org.

Digital Object Identifier 10.1109/TASC.2010.2091388

1051-8223/$26.00 © 2010 IEEE

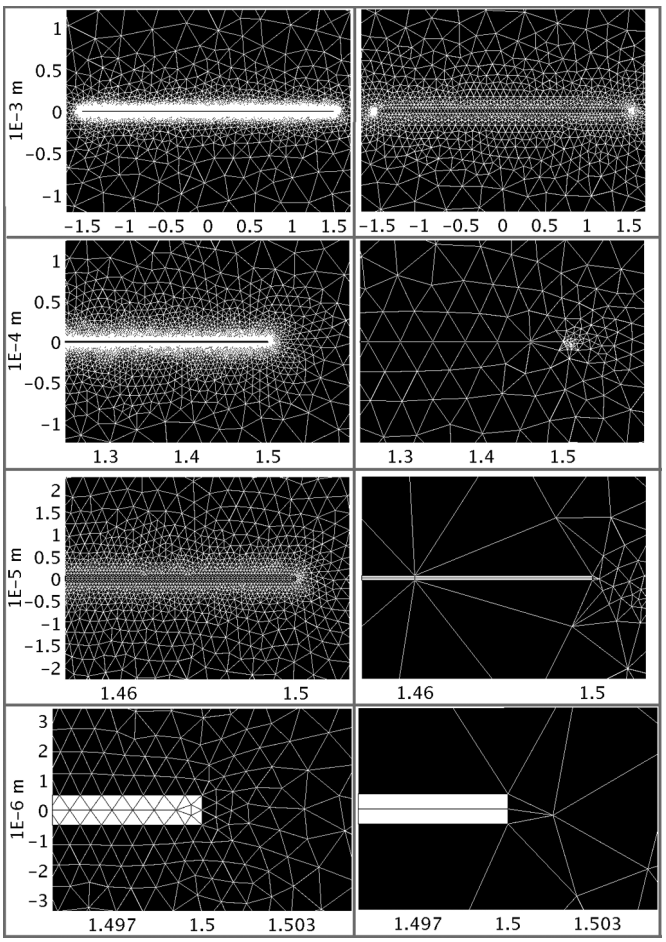

Fig. 1. Consecutive zoom of the mesh in and around a superconducting strip of 3 mm by 1 μm. The horizontal scale is in mm in all subfigures. Left column: using free meshes 17150 elements were needed to discretize the superconducting region. Right column: using mapped meshes only 150 were necessary for the same purpose.

The big scale difference in the conductor width/thickness can be dealt with by means of a multiscale mesh. The aspect ratio of such mesh elements should, up to some degree, resemble the conductor's own aspect ratio. In this work, aspect ratios in excess of 100 provided good results, but the optimal aspect ratio for the mesh elements was not investigated.

Structured (mapped) meshes were implemented in all thin layers, allowing for 75 elements for the width and 2 (or 4) for the thickness of each layer. Therefore, mesh element aspect ratios of 80 (or 160) were obtained. Fig. 1 shows a comparison of both free and structured meshing approaches.

IV. Results

A. Validation

To test the proposed meshing technique, the cases of transport current and applied external field exposed in [1] were considered. AC losses were calculated for a superconducting strip of 3 mm of width and thickness of 1 μm. J_c and n were assigned values of 10^{10} A/m^2 and 25 respectively. For the air (or vacuum) surrounding the conductor, a finite resistivity of 1 $\Omega\cdot$m was used. The relative permeability was assumed to be equal to unity. All transport currents and externally applied fields were

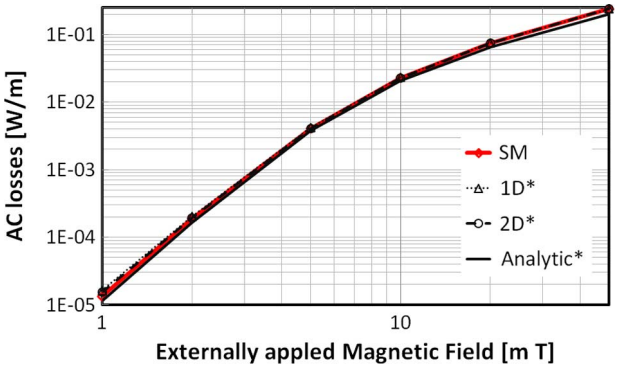

Fig. 2. Comparison of calculated AC losses for different values of externally applied AC Magnetic Field. The SM label corresponds to our calculations and the labels with the symbol $*$ to published results in [1].

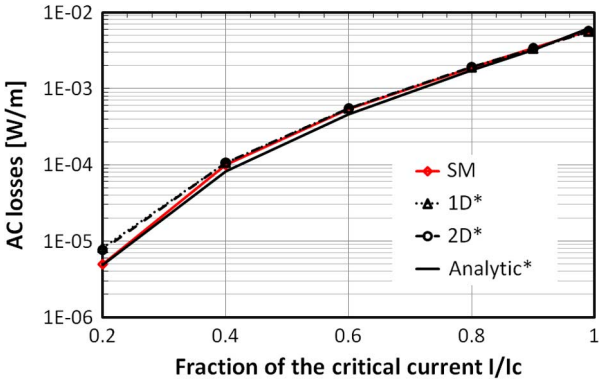

Fig. 3. Comparison of calculated AC losses for different values of AC transport current. The SM label corresponds to our calculations and the labels with the symbol $*$ to published results in [1].

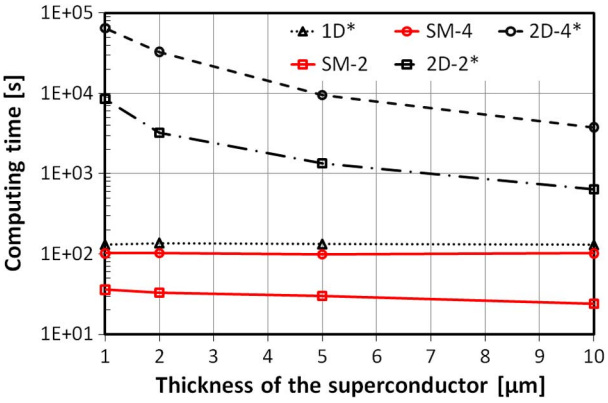

Fig. 4. Computing time for a full cycle at 50 Hz. The SM-2 and SM-4 curves refer to our calculation with 2 or 4 elements across the thickness, respectively. The labels with the symbol $*$ correspond to results published in [1].

sinusoidal signals with frequency of 50 Hz. The comparison of the calculated values is shown in Figs. 2 and 3.

Note that for both considered cases, the numerical results are in good agreement with the previously published numerical computations. Comparison of the computing time for the same publication [1] with our calculations is shown in Fig. 4.

It is relevant to point out that the use of mapped meshes allowed for calculations to be performed 2 to 3 orders of magnitude faster than with regular free meshing for a full 2-D simu-

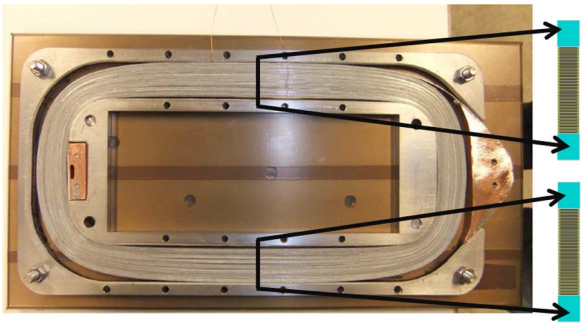

Fig. 5. Left: Racetrack coil from the Superwind project [7]. The coil consists of 57 turns of the commercially available Copper Laminated Amperium Wire from American Superconductors [8]. Right: geometrical representation used to model the cross section of the coil.

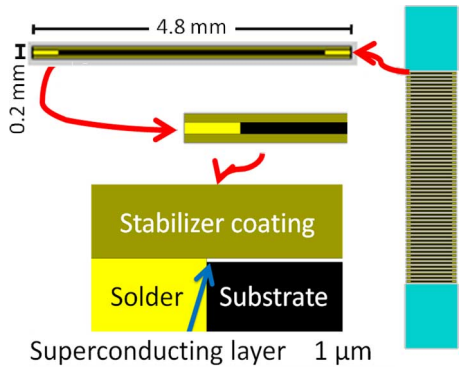

Fig. 6. Model of the coil used for simulations. Left: Wire structure including all layers in true aspect ratios. Each tape is an accurate reproduction of the commercially available Copper Laminated Amperium Wire from American Superconductors [8]. Right: cross section of the racetrack coil.

lation. Furthermore, calculations using mapped meshes with 2 and 4 elements used across the thickness were up to five times faster than the reported computing time for the 1D formulation proposed in [1].

B. Calculation of the Magnetic Field of a Racetrack Coil

To illustrate the potential of the method, the magnetic field produced by a racetrack coil of the Superwind project [7] was simulated. The coil is composed of 57 turns of the commercially available Copper Laminated Amperium Wire from American Superconductors [8]. Fig. 5 shows the actual architecture of the coil along with its corresponding modeled cross section.

Fig. 6 shows the model geometry used to perform simulations. The true thickness of the 1 μm superconducting layer is taken into account. For simplicity and taking advantage of the symmetry, only one quarter of the cross section of the coil was simulated. An AC current of $I = 65.8$ A, assuming a critical current value $I_c = 95$ A, at 50 Hz was evaluated for a tape with a n-value of 21 and a critical current density of J_c of 2.375×10^{10} A/m^2. The simulation of a whole AC cycle was done under 6 hours using a single processor solver (UMFPACK).

Values for the resistivity of the hardened copper coating (6 nOhm$\cdot$m), solder (30 nOhm$\cdot$m) and substrate (65 nOhm$\cdot$m) were obtained from [9] assuming an operating temperature of 77 K. The Magnetic Field Intensity for the whole cross section of the coil at a peak current value of 65.8 A is presented in Fig. 7. Also, the Magnetic Field Intensity at different phase values is shown in Fig. 8. For simplicity in comparison, only one quarter of the cross section is presented.

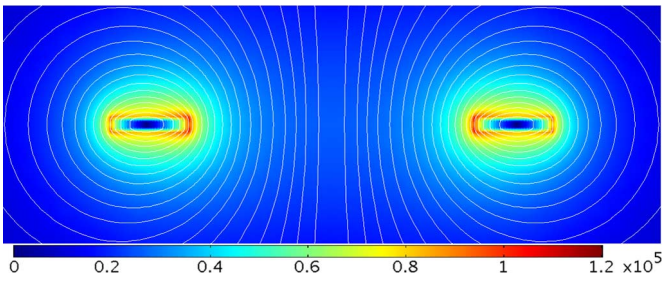

Fig. 7. Magnetic Field Intensity [A/m] for the cross section of the coil at peak current value. The stream lines show the magnetic field lines. For simplicity the geometric features were removed.

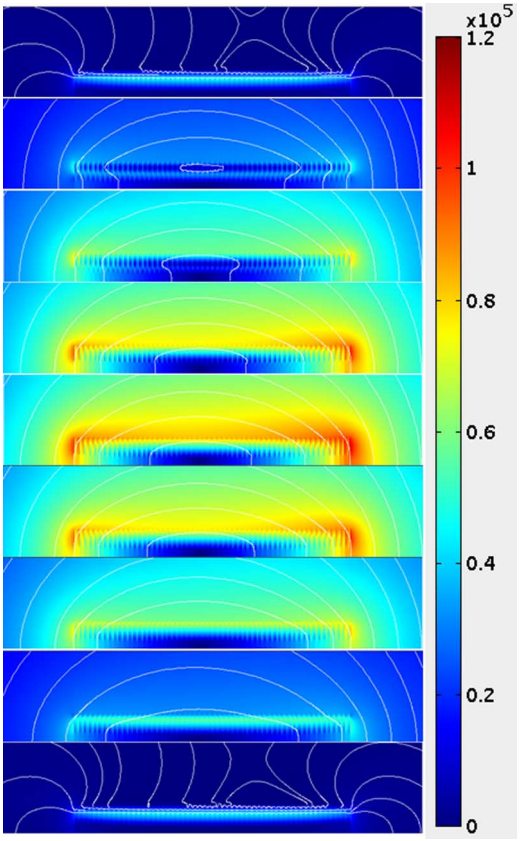

Fig. 8. Magnetic field intensity [A/m] at different phase values (from top to bottom, from π to 2π in $\pi/8$ increments. The stream lines show the magnetic field lines. The geometric features were removed for clarity.

C. Calculation of AC Losses

AC losses were calculated for the previously mentioned Racetrack coil from the Superwind project [7]. Two approaches were followed, one assuming a constant value for $J_c = 2.375° \times 10^{10}$ A/m^2 and the other with the following empiric $J_c(B)$ dependence: $J_c = 1/(a + bB_{||})$, where $B_{||}$ is the component of the magnetic field parallel to the c-axis, $a = 0.0104$ A^{-1} and $b = 0.043$ A^{-1}T^{-1}. This relation was found experimentally testing the Copper Laminated Amperium

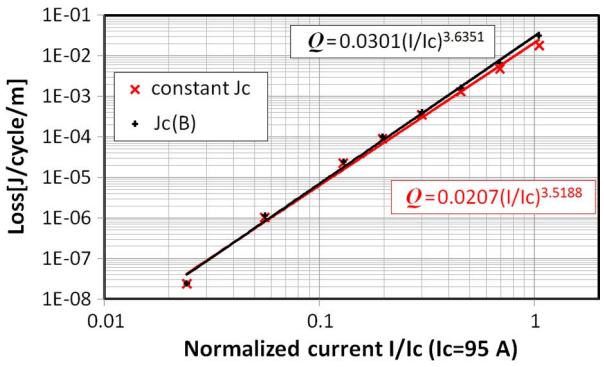

Fig. 9. Simulated AC losses Q at different values of $\mathrm{I/I_c}$.

Wire from American Superconductors [8] used to wind the coil (data not shown).

The calculated values for the AC losses Q (in J/cycle/m) are reported in Fig. 9. A power fit for both sets of data is also shown. Note that although both approaches with $\mathrm{J_c}$ being constant and as dependent on the magnetic field present a similar behavior, the losses assuming $\mathrm{J_c}$ as a constant are lower.

V. Discussion

Use of mapped meshes with large aspect ratio elements allowed simulating the electromagnetic properties of superconducting materials in thin geometries faster than when using free meshes without compromising accuracy in the calculation of AC losses. Both transport and applied field cases were presented here. In the case of a single conductor, computational time was reduced by more than 2 orders of magnitude. Even though other electromagnetic formulations could be implemented, given enough validation, use of mapped meshes could be implemented to reduce the time to solution.

Although the aspect ratio values of 80 and 160 for the mesh elements used in this work provided accurate results consistent with previously published data, further studies upon finding an optimal mesh distribution are yet to be performed.

Whereas it could be argued that the computing time is similar to the one using integral equations for a single conductor, the 2D formulation with mapped meshes allows for simulating several conductors in arbitrary arrangements in one single equation, making the interaction among them natural and reducing the programming time.

Calculation of AC-losses was performed well under 6 hours for a real application racetrack coil conformed of 57 tapes. The obtained dependence of the AC loss on the current has been fitted by a power law as shown on Fig. 9. Exponents in the range 3.5–3.6 have been obtained and are in qualitative agreement with the analytical expression of an elliptical conductor [10].

Additional hysteretic losses should be expected from the magnetic substrate, which are not considered in this work. Future work will include such effects as well as comparison with experimental data.

VI. Conclusions

It has been shown how the use of mapped meshes allows simulating complex and fairly large coated conductor problems with ease and within manageable time. This permits to think about optimization or simulations of further applications like large magnets or superconducting motors and generators in the near future.

References

[1] R. Brambilla, F. Grilli, L. Martini, and F. Sirois, "Integral equations for the current density in thin conductors and their solution by the finite element method," *Supercond. Sci. Technol.*, vol. 21, no. 10, pp. 105 008-1–105 008-8, Jul. 2008.

[2] K. P. Thakur, M. P. Staines, L. S. Lakshmi, and N. J. Long, "Numerical computation of AC losses and flux profiles in high-aspect-ratio superconducting strips in perpendicular AC magnetic field," *IEEE Trans. Appl. Supercond.*, vol. 19, no. 6, pp. 3770–3778, Dec. 2009.

[3] K. Kajikawa, T. Hayashi, R. Yoshida, M. Iwakuma, and K. Funaki, "Numerical evaluation of AC losses in HTS wires with 2D FEM formulated by self magnetic field," *IEEE Trans. Appl. Supercond.*, vol. 13, no. 2, Jun. 2003.

[4] R. Brambilla, F. Grilli, and L. Martini, "Development of an edge-element model for AC loss computation of high-temperature superconductors," *Supercond. Sci. Technol.*, vol. 20, pp. 16–24, 2007.

[5] COMSOL Multiphysics, "Superconductive wire," 2008 [Online]. Available: http://www.comsol.com/showroom/documentation/model/689/superconducting_wire_sbs.pdf

[6] P. M. Knupp, "Remarks on mesh quality," in *45th AIAA Aerospace Sc. Meeting Exhibit*, Reno, NV, Jan. 7–10, 2007.

[7] E. Seiler *et al.*, "AC loss in superconducting wires operating in a wind turbine like generator," *J. Physics: Conf. Series*, vol. 234, p. 032051, 2010.

[8] American Superconductor, "Amperium wire: Copper laminated," 2010 [Online]. Available: http://www.amsc.com/products/amperiumwire/copper.html

[9] K. Nam, C. Lee, D. K. Park, T. K. Ko, and B.-Y. Seok, "Thermal and electrical analysis of coated conductor under AC over-current," *IEEE Trans. Appl. Supercond.*, vol. 17, no. 2, pp. 1923–1926, Jun. 2007.

[10] W. T. Norris, "Calculation of hysteresis losses in hard superconductors carrying ac: Isolated conductors and edges of thin sheets," *J. Phys. D: Appl. Phys.*, vol. 3, p. 489, 1970.

G.7 Paper: High Temperature Superconductor Machine Prototype

Presented at International Conference on Electrical Machines and Systems (ICEMS) 2011. The article is not peer reviewed. The article is published and available online at IEEE Xplore.

High Temperature Superconductor Machine Prototype

Nenad Mijatovic[1], Bogi B. Jensen[1], Chresten Træholt[1], Asger B. Abrahamsen[2], Victor Manuel Rodriguez-Zermeno[3], Niels F. Petersen[3], Mogens Henriksen[1], Eugen Seiler[2,4], Niels H. Andersen[2], Jacob Østergård[1]
[1] Department of Electrical Engineering, Technical University of Denmark, Denmark
[2] Materials Research Division, Risø DTU, Technical University of Denmark, Denmark
[3] Department of Mathematics, Technical University of Denmark, Denmark
[4] Institute of Electrical Engineering, Slovak Academy of Sciences, Slovakia
E-mail: nm@elektro.dtu.dk, bbj@elektro.dtu.dk

Abstract — A versatile testing platform for a High Temperature Superconductor (HTS) machine has been constructed. The stationary HTS field winding can carry up to 10 coils and it is operated at a temperature of 77K. The rotating armature is at room temperature.

Test results and performance for the HTS field winding comprising four coils wound with two types of HTS tapes are shown and discussed. The field winding produces up to 0.62T in the 10mm air gap which constitutes 78% of the armature design value. Recommendations for the field winding operation are proposed and verified, which resulted in an increase of available magneto-motive force of the field winding up to 25%.

I. Introduction and Motivation

A. Superconductivity and electrical machines

Prospects of Low Temperature Superconductors (LTS) as a field winding in synchronous machines seemed promising in the early 60's. Several parties [1] aimed to improve utility size generator units (20MVA-70MVA) but due to lack of funding the projects were terminated. The root of the problem with the application of LTS was the low temperature cooling system. Ensuring less than 1K thermal margin at liquid helium temperature (4.2K) in the entire lifetime of the machine proved to be too complex and the potential gains of LTS large current capacity were not commercially feasible [1].

Discovery of High Temperature Superconductors (HTS) in the 1980's was welcomed by the industry as its application seemed less complex compared to the LTS (HTS is in the superconducting state for temperatures as high as 100K). A number of pilot projects, mainly industrial efforts, have successfully applied HTS to electrical machines. Only few HTS machine projects [2] have chosen higher temperature range (64K-77K) while others have employed midrange cryogenics temperatures (30-50K) for operating temperature, mainly because the current capacity of HTS at lower temperatures is higher.

B. Power density

The output power [3] for radial flux electrical machines can be expressed as (1),

Manuscript received July 10th, 2011. The project Superwind (www.superwind.dk) is funded in part from the Globalization grant of the Technical University of Denmark (DTU) funds.

$$P_{\max} = \sqrt{2} A_s \hat{B}_g \underbrace{\pi R^2 L}_{Volume} \omega = T_{\max} \omega \tag{1}$$

where the A_s[A/m] is armature electric loading, B_g[T] air gap flux density, R[m] and L[m] radius and axial length of the air gap, ω[rad/s] angular speed and T_{max}[Nm] is electromagnetic torque of the machine.

Constraints imposed to the torque density of electrical machines are rooted in thermal limits of the conductor insulation and magnetic saturation of the electric steels. Because of this, the electric loading and air gap flux density are limited and hence high values of output torque of an electrical machine will cause an increase of the volume of the machine.

The Magneto Motive Force (MMF) from the field winding in an HTS machine is not limited by thermal limits and thus high values of MMF can be employed in such machines. This leads to higher values of B_g resulting not only in a higher torque density but also in better efficiency, because the electric loading can be decreased, and transient performance, because of the low machine reactance [3].

C. Wind industry

As the direct drive concept is gaining popularity in the offshore wind turbine industry [4], technical limits of large direct drive wind turbine generators could prove to be a barrier for an up scaling of wind turbines to 10MW and above.

The project Superwind is aiming to assess the status and feasibility of HTS machines as an alternative to conventional geared and direct drive wind turbine generators.

D. High Temperature Superconductors

The superconducting state is limited by three parameters, temperature, T, magnetic flux density, B, and current density, J, of the material. Superconductivity exists only if the superconductor operating point parameters, (T,B,J), are lower than the critical values, (T_c,B_c,J_c). The nonlinear relation between current and voltage of the superconductor, the so called IV curve, is one of the ways HTS materials can be characterized. The IV relation of superconductors describes a power law dependence between the electric field E and the current density J as

$$E[V/m] = E_0 \left(\frac{J}{J_c(B,T)} \right)^{n(B,T)} \tag{2}$$

where J_c is a critical current density and n is a measure of how abruptly the superconductor transition from the non-resistive to the resistive state will take place. Both J_c and n are functions of temperature and magnetic flux density. E_0 is a constant that defines the electric field across the superconductor when the current density is identical to the critical current density. The value of 1μV/cm is most commonly used [4].

The HTS conductors most attractive for power applications are bismuth based copper oxide tape with T_c~110K [5], also called 1G or BSCCO, and yttrium based copper oxide coated tapes with T_c~93K [5] also called 2G or YBCO. Magnesium diboride with T_c=39K is also looking promising [5].

II. SUPERWIND PROTOTYPING PLATFORM

The setup, illustrated in Fig.1, consists of a conventional armature winding which is rotating around a stationary cryostat. The cryostat contains the HTS coils in a low temperature chamber filled with liquid nitrogen (LN_2). The setup is also equipped with a custom made torque and speed measurement system and an armature position locking system. The HTS field winding is supplied with dc power supplies controlled via a PC running the LabView software.

During the design process, a modular approach to the setup was of vital importance. It was important to design the HTS machine where any modification of the field winding, like interchanging the HTS coils with different sets of coils or changes in internal coil connections or in a sensing system, etc. could be done fast and in an easy manner.

To accommodate HTS coils, a custom cryostat had to be designed. At this stage the cryostat is operated as an open LN_2 bath ensuring 77K as operating temperature of the HTS field winding. However, it is possible to design a flange for the cryostat and thus have cooling in the closed cycle of LN_2 which would allow temperatures down to 64K.

A. Armature winding

A three phase two pole armature with distributed windings was adopted from a 690V, 22kW, 50Hz induction machine and custom fitted to a metal cylinder which acts as a structural housing (see Fig. 2.). The design employs a rotating armature winding in order to avoid challenges with the low temperature rotating parts. Accordingly, four slip rings are mounted on the outer armature bore. The armature winding is driven by an induction machine (IM) drive controlled by a frequency converter and coupled to the IM drive via a belt transmission. The speed can be adjusted from 0 to 400rpm (limit imposed by the choice of bearings used in the armature housing).

The geometry of the armature steel and windings have been inspected and illustrated in the Fig. 2. The armature steel stack of M800-50A silicon steel has an axial length of 150mm and an inner diameter of 160mm. The three phase single layer winding is distributed over 36 slots with 18 series conductors per slot.

B. Cryostat design

The cooling system and thermal insulation are integral and very important parts of an HTS machine. The choice to use the LN_2 temperature range, i.e. from 64K -77K, was made in part to simplify the cooling system requirements but also to challenge the HTS performance since the current and magnetic field capabilities of HTS is degrading with increasing temperature.

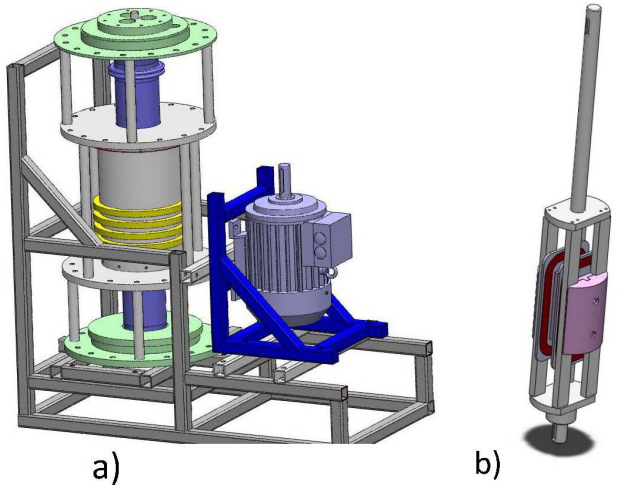

Fig.1. a) 3D CAD model of the Superwind setup. The armature winding is rotating around the HTS field winding which is enclosed inside an open top LN_2 cryostat. An induction motor and a belt connection(not shown) are used to rotate the armature windings. b) 3D CAD model of the assembled HTS field winding. The HTS field winding is lowered to the LN_2 chamber from the top of the cryostat.

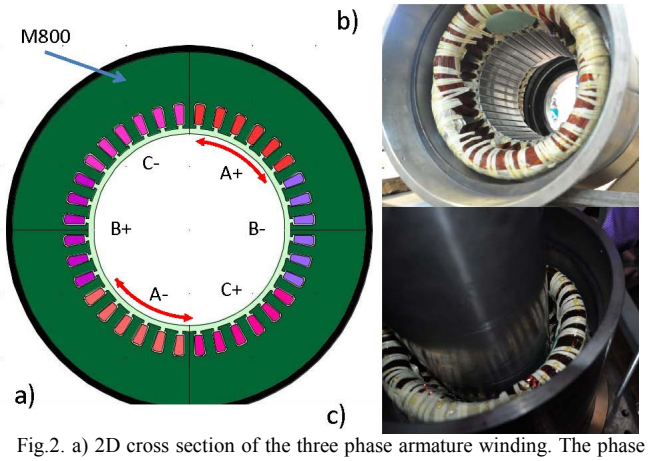

Fig.2. a) 2D cross section of the three phase armature winding. The phase belts are indentified as A, B and C. b) The armature winding enclosed in the steel housing during the construction phase. c) The armature winding with the cryostat in the centre. The mechanical clearance between the cryostat and the armature is 1mm while the effective magnetic air gap is 10mm.

1) Design details

The axis of the cryostat and the three phase winding is vertical (see Fig. 3.). This allows open system cooling via LN_2 evaporation. Design constraints for the outer diameter of the cryostat, the integral thickness of the cryostat in the radial direction, the mechanical clearance between the outer wall and the rotating armature, the inner wall, and the HTS winding are all set to be 158mm, 9mm, 1mm and 0.5mm, respectively. No strict constraint has been put on the axial length of the cryostat. The resulting magnetic air gap between the rotating armature winding and the stationary field winding is 10mm.

Two 316L stainless steel (SS) sheets of 1.5mm thickness have been pressed rolled and welded into two cylinders with an outer diameter of 158mm and 143mm respectively. The space in between the inner and outer wall contains Multi Layer Insulation (MLI) and is evacuated to a high vacuum (in the range of 10^{-5} mbar).

A thermal contraction of material has large implications for the design of an HTS machine. The thermal expansion coefficient for SS is approximately 0.2%. This means that the cold wall of the cryostat will shrink up to 3mm in the axial direction and 0.3mm in the radial direction when cooled from 300K to 77K. A carefully designed corrugated bellow, illustrated in the Fig. 3, is needed to accommodate this difference between outer and inner walls.

One of the curtail elements in an HTS machine design is a Torque Transfer Element (TTE). As the name suggests, this element ensures mechanical coupling between a stationary support and a field winding. A TTE needs to have minimal heat transfer through itself while withstanding a full rated torque.

The design input for the maximal torque of the TTE is 250Nm. The 316L SS was chosen as material because it offers advantages in manufacturing and cost (important for eventual scale up) compared to the composites. The TTE is fashioned as a cylinder with 72mm for an outer radius and with wall 1.5mm thick, as illustrated in Fig. 3. Such a TTE would cause approximately four times less heat transferred then if the TTE is a simple shaft with same axial length and same torque ability. This is illustrated in the Table. 1, where the heat transferred for a cylinder and a shaft are compared.

2) *Thermal consideration for the cryostat*

a) Conduction heat transfer

The heat through the wall is determined by the thermal conductivity of the material used (SS in our case), K and its dimensions with respect to the heat transfer direction. This can be expressed by (3),

$$Q_{cond} = \frac{A}{L}\int_{T_1}^{T_2} K(T)dT \tag{3}$$

where A is the cross section area of the wall, L is the distance from the warm side of the wall where the temperature is T_2 = 300K to the surface of the LN_2, where T_1 = 77K (or 64K). The cross section area A, the length of the TTE and the inner walls of the cryostat (top and bottom) L, the integral of thermal conductivity for T_2 = 300K and T_1 = 77K (64K) and conduction heat transferred, Q_{cond}, are presented in Table. 1.

a) Radiation heat transfer

A radiation shield has been employed to limit the radiation heat transfer. Ten layers of CoolCut 2NW MLI are wrapped three times around the outer side of the inner wall of the cryostat and tied with a SS wire and a low emissivity aluminum adhesive tape. Each layer of aluminum in the MLI is 12µm thick and is coated on a 0.13mm polyester substrate [6]. With MLI, the heat transferred by radiation can be neglected as Table.1 confirms, where the heat due to radiation transfer has been calculated for the case with and without MLI.

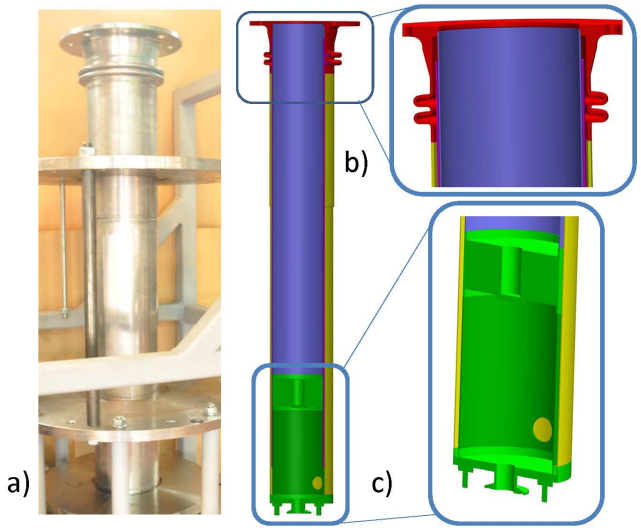

Fig. 3. a)Cryostat, 1.15m high, is placed in the machine frame. b) Cross section of 3D CAD model of the cryostat with corrugation part (red) emphasized. Corrugation is placed at the warm wall of the cryostat to accommodate thermal expansion/compression of the inner wall of the cryostat due to a temperature change.c) Cross section of 3D CAD model of the cryostat with emphasized Torque Transfer Element (TTE) (green). The TTE is positioned at the bottom of the cryostat just below the LN_2 chamber. The HTS field winding shaft will lock into the hole on top of the TTE when the HTS field winding is lowered down into LN_2 chamber.

TABLE I
CONDUCTION AND RADIATION HEAT TRANSFER FOR THE CRYOSTAT

	Section	A [m^2]	L [m]	$\int K(T)dT$ [W/m]	Q_{cond} [W]
Conduction	Top	6.7 10-4	0.115	2720 @77K	15.9(16.6)
	TTE	6.7 10-4	0.195	2850 @64K	9.35(9.8)
	Shaft*	2.8 10-3	0.115		66.9 (70.0)
Radiation	Section	A[m^2]	L [m]	Q(No MLI)[W]	Q(MLI) [W]
	Top	0.06	0.115	< 0.41	-
	Mid	0.37	0.745	2.57	0.08
	TTE	0.097	0.195	< 0.67	-

*Heat transferred by conduction for the Shaft is highly overestimated for the case when the cryostat is operated in the open bath mode. This number is included to illustrate the statement that the TTE shaped as a shaft would cause 4 times higher heat transfer rate then if the TTE is a cylinder (same as Top part-conduction in Table. 1).

The thermal performance of the cryostat was validated with an LN_2 boil-off experiment. The LN_2 evaporation test was performed where 11 liters of the LN_2 have evaporated over 45 hours. This results in the average heat load for the cryostat (conduction and radiation included) of 10.5W.

C. *HTS field winding*

The HTS coils, illustrated in Fig. 4 assembled into an HTS field winding, are impregnated with epoxy and are designed to fit onto coil holders made from SS.

Depending on the type of HTS tape, insulation employed,

cooling requirements, etc., the number of turns for the different coils varies. The HTS tape is soldered to copper terminals at either end of the coils (see Fig. 5). More details about the coils can be found in [7].

Completed coils are presented in the Table. 2. All coils have access to a four point voltage measurement across the coil as well as several sections (one or more) in the middle of the winding. The measurement points are accessible on a printed board mounted on the frame (see Fig.5.) of the coil. This allows evaluation of the difference in performance of the outer and the inner part of the coils (turns are not exposed to the same magnetic field).

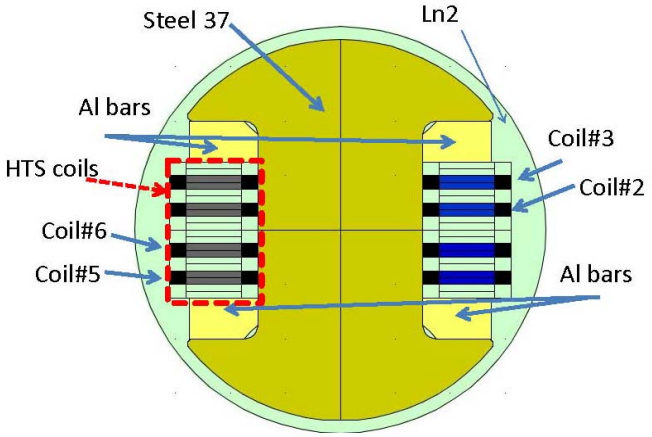

Fig.4. 2D cross section of the HTS field winding with the HTS coils. The arrangement of the coils is the same for all results of this paper.. The space allocated for the HTS coils can accommodate maximum 10 coils, each 5mm thick. The coils are placed between four aluminum bars (yellow) acting as a mechanical support structure – coil housing. Steel 37, the field winding steel (light green) is fixed by screwing the pole shoe into the steel body and thus exerting the pressure on the aluminum bars.

III. Experiments and Results

The design of an HTS machine is governed by the performance of the HTS coils. First the amount of MMF the HTS coils can provide needs to be determined. An integral voltage drop over the entire length of the HTS tape in a coil, or an average voltage of an HTS coil per length, can be expressed with (4)

$$U_{coil}[V/m] = \frac{1}{L_{coil}} \int_o^{L_{coil}} E_0 \left(\frac{I}{I_c(|B|)} \right)^{n(|B|)} dl \qquad (4)$$

where L_{coil} is the length of the HTS tape in the coil winning and I_c is the critical current of the HTS coil. The I_c determined from the coil voltage could lead to the overestimates in the current ratting of the HTS coil, especially if the flux distribution across the HTS coil contains large gradients. In that case closer investigation of I_c for each section of the HTS coil is necessary.

The IV curve for each of the coils (only one at the time is carrying current) are plotted in the Fig.6 when the coils have been installed in the machine as shown in the Fig.4. The I_c derived from these IV curves is the maximal current capacity of each coil in self produced leakage flux. In the next test, the HTS coils have been connected in a serial connection.

TABLE II
COILS CONSTRUCTED FOR TESTING IN SUPERWIND SETUP

Coil ID	L_{coil} [cm]	Number of Turns	HTS Type**	Insulation
Coil#2	2540	48	AMS-1G	Glass-Fiber
Coil#3	2880	51	AMS-1G	Glass-Fiber
Coil#5	2500	46	AMS-1G	Glass-Fiber
Coil#6	3165	56	AMS348C-2G	Glass-Fiber
Coil#7*	>7000	>100	SP4050-2G	Epoxy
Coil#8*	>7000	>100	SP4050-2G	Epoxy

* to be tested

** AMS-1G is BSCCO wire from American Superconductor, AMS348C-2G is YBCO coated conductor 348C from American Superconductor and SP4050-2G is YBCO coated conductor from Super Power Inc.

Fig. 5. a) Preview of one of the HTS coils constructed for the Superwind setup. The HTS tape is impregnated in epoxy in between SS frames. The coil terminals are made from copper blokes. They are located on the outer frame (right) and on the inner frame (left) in the end winding area of the HTS coil. The access to the 4 point measurement, the hall probes and the temperature sensors are located on the outer frame of the coil (left). Twisted pairs of wires have been soldered to the HTS tape during the winding procedure (at the beginning, end and middle of the winding).b) The HTS field winding during assembly. Two HTS coils, aluminum holders, Steel 37 pole shoe, current leads can be seen on the rotor as illustrated in Fig. 1b.

The first HTS coil with the coil voltage, U_{coil}, equal to the critical voltage of the coil, $L_{coil}E_0$, will determine the total MMF of the HTS field winding. This can be expressed with (5).

$$MAX\left(\frac{U^i_{coil}}{L^i_{coil}}\right)\Big|_{i=coil\#2-coil\#6} < E_0 \qquad (5)$$

The recorded IV curves are plotted in the Fig. 7. The coil limiting the MMF is Coil#3. This is expected as the position of Coil#3 and Coil#5 (also close to the critical voltage) is unfavorable, i.e. these coils will experience most of the stray flux because they are closest to the pole shoes. The

distribution of the flux density the HTS coils are experiencing is shown in the Fig. 8 and confirms the conclusion from IV tests.

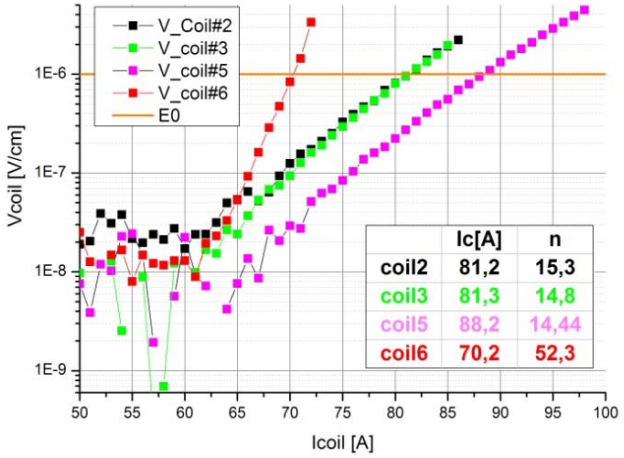

Fig.6. The IV curves for Coil#2, Coil#3, Coil#5, Coil#6 when only that coil is carrying current. The power law fit was preformed and I_c and n values are listed in the inset table for each of the coils using the 1μV/cm critical voltage criteria.

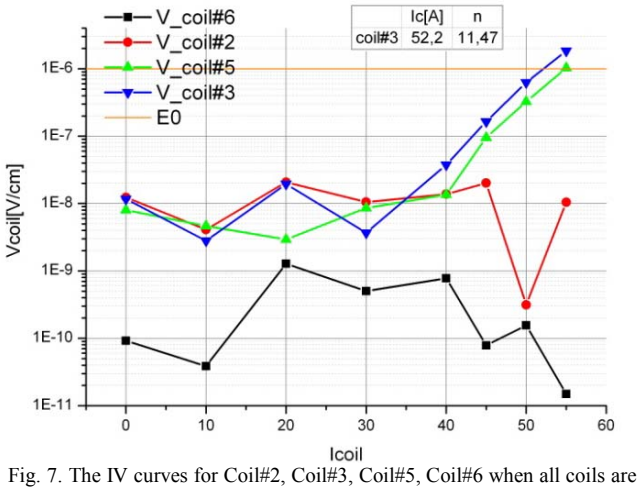

Fig. 7. The IV curves for Coil#2, Coil#3, Coil#5, Coil#6 when all coils are carrying the same current. The power law fit was performed for the IV curve of Coil#3 and I_c and n values have been extracted using the 1μV/cm critical voltage criteria.

The reduction of the current capacity of Coil#3 when the HTS field winding is connected in series and when the coils are supplied individually one at the time is substantial (from 81.3A to 52.2A). This is also expected due to the higher magnetic field the coil is exposed to and high sensitivity of 1G HTS to the magnetic field. Going one step further by analyzing the voltages of the coil sections, it is possible to see that the outer section of Coil#3 is the one adding to the total coil voltage slightly more than inner part of the coil. Using FE simulation we have estimated (see Fig. 8.) that the HTS tapes are exposed to the maximal magnetic flux density of ~200mT for Coil#3 and Coil#5 and less then 100mT for Coil#2 and Coil#6 when the coils are carrying 50A.

It is clear from Fig. 7 that the two other coils, namely Coil#2 and Coil#6 could carry higher current. Many optimization approaches have been reported in the literature on how to maximize the magnetization current and thus the magnetic flux of the HTS magnets.

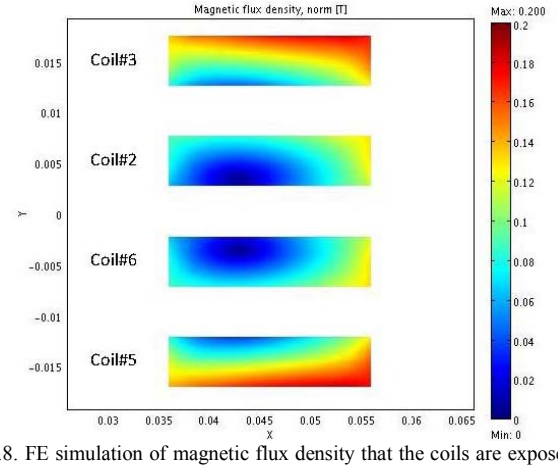

Fig.8. FE simulation of magnetic flux density that the coils are exposed to when the coils are carrying 50A. The superconducting properties are not included in the FE model.

Most of these have dealt with the shape and position of the coil itself [8], while others have employed flux shields around the coils [9]. If the HTS coils in the HTS winding are allowed to carry different currents, i.e. multiple current supplies are used, it has been reported [10] that the same MMF can be achieved with substantially lower amount of HTS tape. With four HP dc power supplies connected to the HTS coils, each coil has an independent current supply and thus (5) can become(6).

$$\forall\left(\frac{U^{i}_{coil}}{I^{i}_{coil}}\right)\Big|_{i=coil\#2-coil\#6} < E_0 \tag{6}$$

The current limit for Coil#3 is I_c=52A. Any additional increase in the current of any of the other coils would cause exponential voltage increase of Coil#3 due to the increase of the leakage flux. Setting the current of Coil#3 to 45A allows an increase in the flux density Coil#3 is exposed to and thus increases in the total MMF.

To demonstrate the potential of the multiple power supplies, two sets of the coil currents have been found to satisfy the condition expressed with (6) and are illustrated in the Fig. 9. Having the coils carrying currents close to their individual I_c, the total MMF of the HTS field winding was increased by 25% and 12% compared to the serial connected HTS coils with 45A and 50A, respectively. This can also be seen in the higher induced No Load voltage in Fig.10.

If the price of the HTS tape is taken into account, the multiple current supplies approach can be effective in the reduction of the amount of HTS conductor, especially for large machines. Yet, the analysis of its impact on the cost of the whole system needs to be evaluated where factors like complexity increase, cost for additional power supplies, optimal coil-current arrangement, increased heat load to the cooling system due to the higher number of current leads, etc.

should be taken into account.

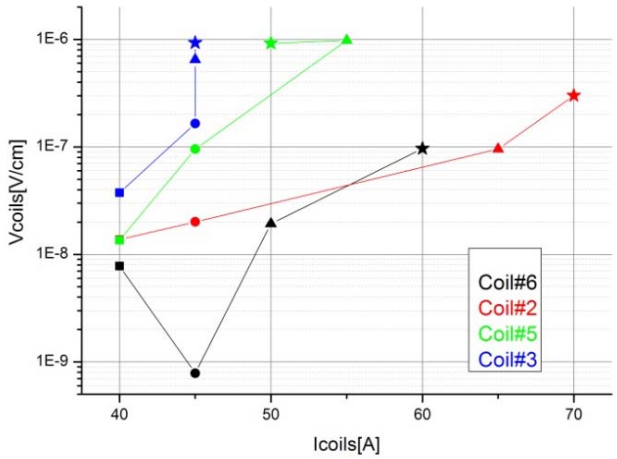

Fig. 9. The trace of the voltages of the coils with four power supplies is shown. Coil currents in the plot are: square - [Coil#2-40A; Coil#3-40A; Coil#5-40A; Coil#6-40A], circle - [Coil#2-45A; Coil#3-45A; Coil#5-45A; Coil#6-45A], triangle - [Coil#2-65A; Coil#3-45A; Coil#5-55A; Coil#6-50A] star - [Coil#2-70A; Coil#3-45A; Coil#5-50A; Coil#6-60A].

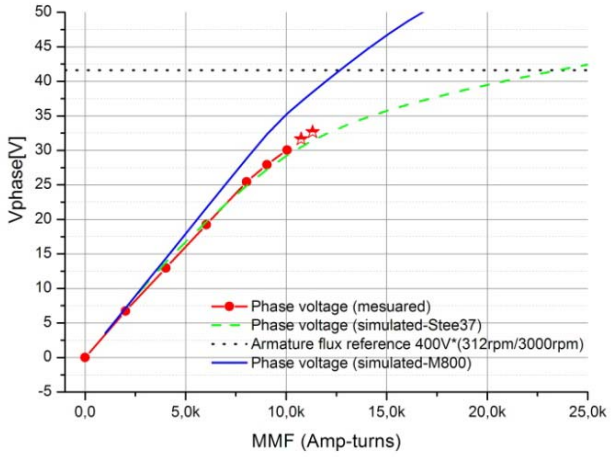

Fig.10. No Load phase voltage for 4 HTS coils at 312rpm. Star markers are used in the case when the coils have carried different currents (multi currents supplied to coils). Constant voltage dotted line is illustrating 400V/3000rpm level for the test speed, 312rpm, as a reference value for the air gap flux. Solid blue and dashed green lines are representing simulation estimates for No-Load voltage induced if M800 and Stee37 steel are used in HTS iron, respectively.

The No-Load voltage was measured in the No-Load test conducted at several speeds and validated via 2D FE simulation, respectively. The simulated results for the induced voltage are in the good agreement with measured data. Both measured and simulated results are presented in the Fig. 10.

The magnitude of the induced voltage is a direct indicator of the flux linkage in the machine. With the four HTS coils operated at the 77K the maximal induced phase voltage is 32.6V at the speed of 312rpm when the multiple supplies to the HTS coils have been used. It is estimated that the HTS field winding generated approximately 78% of the design value for the flux of the armature winding (i.e. 400V phase voltage at 3000rpm).

This corresponds to the peak flux density of 0.62T in the 10mm air gap. The lower value of induced voltage in the phase winding is a consequence of the poor magnetic permeability of the steel Stee37. If the high permeability steel is used instead (for example, M800), both the flux linkage and the HTS current capacity could be boosted. The armature design flux reference of 400V/3000rpm could be reached with the same four HTS coils because the high permeability steel would also decrease the leakage flux coils are exposed to. Future studies will focus on the performance of the HTS coils in the HTS machine under load.

IV. Conclusion

A testing platform for a HTS machine has been constructed and several HTS coils have been tested. The testing platform is operated at 77K and can test up to 10 coils. The experimental results have confirmed the importance of the flux distribution the HTS coils are exposed to through a series of measured IV curves. The multiple supply currents to the HTS coils in HTS field winding are proposed as a way to increase the MMF of the HTS field winding up to 25%.

Acknowledgment

The authors would like to acknowledge the support and contribution provided by the Center for Electric Technology (CET), Risø DTU and RUAG Space.

References

[1] S.S Kalsi, K. Weeber, H. Takesue, C. Lewis, H.W Neumueller, R.D Blaugher, "Development status of rotating machines employing superconducting field windings ", *Proceedings of the IEEE,* Vol. 92. No.10, pp. 1688 – 1704, October 2004

[2] Paul N. Barnes, Michael D. Sumption, Gregory L. Rhoads "Review of high power density superconducting generators: Present state and prospects for incorporating YBCO windings", *Cryogenics*, Vol. 45, No. 10-11, pp. 670-671, 2005.

[3] T.J.E. Miller and A. Hughes, "Analysis of fields and inductances in air-cored and iron-cored synchronous machines," *IEE Proceedings*, Vol. 124, No. 2, pp. 121-126, February 1977.

[4] Abrahamsen A, Mijatovic N, Seiler E, Zirngibl T, Træholt C, Nørgård P, Pedersen N, Andersen N and Østergaard J, "Superconducting wind turbine generators," *Superconductor Science and Technology*, Vol. 23, April 2010.

[5] Lynn, J and Allen, P, *High temperature superconductivity,* Springer, 1990.

[6] http://www.ruag.com/Space/Products

[7] Abrahamsen B A, Jensen B B, Seiler E, Mijatovic N, Rodriguez-Zermenoc V M, Andersen H N and Østergaard J, "Feasibility study of 5 MW Superconducting wind turbine generator" *Physica C* , Vol. 23, April 2010.

[8] Fukui S, Ohsugi K, Nishijyo T, Ogawa J, Oka T, Yamaguchi M, Sato T, Furuse M, Takao T, Tsukamoto O, "Study on Optimal Design of High Temperature Superconducting Coil Based on AC Loss Minimization ", *IEEE Transactions on Applied Superconductivity,* Vol. 18. No.2, pp. 762-765, 2008

[9] Al-Mosawi M K, Goddard K, Beduz C and Y. Yang, "Coreless HTS Synchronous Generator Operating at Liquid Nitrogen Temperatures ", *IEEE Transactions on Applied Superconductivity,* Vol. 18. No.2, pp. 762-765, 2008

[10] Mijatovic N; Jensen BB; Abrahamsen AB; Zermeno, VMR; Traeholt C. and Pedersen, NF, "Coil Optimization for High Temperature Superconductor Machines", *IEEE Transactions on Applied Superconductivity,* Vol. 21. No.3, pp. 1136 – 1140

G.8 Paper: An HTS machine laboratory prototype

Presented at European Conference on Applied Superconductivity (EUCAS-ISEC-ICMC) 2011. The article is submitted for peer review.

Available online at www.sciencedirect.com
ScienceDirect
Physics Procedia 00 (2011) 1–6
Physics Procedia
www.elsevier.com/locate/procedia

Superconductivity Centennial Conference

An HTS machine laboratory prototype

N.Mijatovic, B.B.Jensen, C.Træholta[a], A.B.Abrahamsen[b], V.M.R. Zermeno, N.F. Pedersen[c]

[a]*Department of Electrical Engineering, Technical University of Denmark, 2800 Lyngby, DK*
[b]*Materials Research Division, National Laboratory for Sustainable Energy, RIS - DTU, 4000 Roskilde, DK*
[c]*Departments of Mathematics, Technical University of Denmark, 2800 Lyngby, DK*

Abstract

This paper describes Superwind HTS machine laboratory setup which is a small scale HTS machine designed and build as a part of the efforts to identify and tackle some of the challenges the HTS machine design may face. One of the challenges of HTS machines is a Torque Transfer Element (TTE) which is in this design integral part of the cryostat. The discussion of the requirements for the TTE supported with a simple case study comparing a shaft and a cylinder as candidates for TTE are presented. The discussion resulted with a cylinder as a TTE design rated for a 250Nm and with more then 10 times lower heat conduction compared to a shaft. The HTS machine was successfully cooled to 77K and tests have been performed. The IV curves of the HTS field winding employing 6 HTS coils indicate that two of the coils had been damaged. The maximal value of the torque during experiments of 78Nm was recorded. Loaded with 33%, the TTE performed well and showed sufficient margin for future experiments.

© 2011 Published by Elsevier Ltd. Selection and/or peer-review under responsibility of Horst Rogalla and Peter Kes.

Keywords: Keywords: HTS machine \ Torque Transfer Element \ HTS coils

1. Introduction

The torque of the wind turbine scales as P/ω, where the P is power and ω is speed of the turbine. Due to the tip speed limitation, the speed needs to decrease with increasing power rating[1]. For a direct drive concept where a generator will need to have same rated torque as the turbine, the wind generator is a large machine [2],[3]. An HTS machine can increase the torque density of the electrical machine and serve as an alternative to a large conventional generator[4].

As a part of the efforts to identify and address some of the challenges the design of an HTS machine may face, we have designed and constructed the HTS machine laboratory prototype. This paper contains the description of the setup and the reasoning behind some of the choices made in the design.

2. Superwind An HTS machine laboratory prototype

The Superwind setup, illustrated in the Fig.1a, is a synchronous machine with an HTS field winding and a conventional armature winding. It consists of a room temperature armature which rotates around stationary HTS field winding placed inside of a stationary cryostat. The low temperature chamber of the cryostat is

filled with liquid nitrogen (LN_2), where cooling of the HTS field winding to the $77K$ was performed by evaporation of the LN_2 on the atmospheric pressure. The HTS field winding is supplied from dc power supplies controlled via a PC running the LabView software.

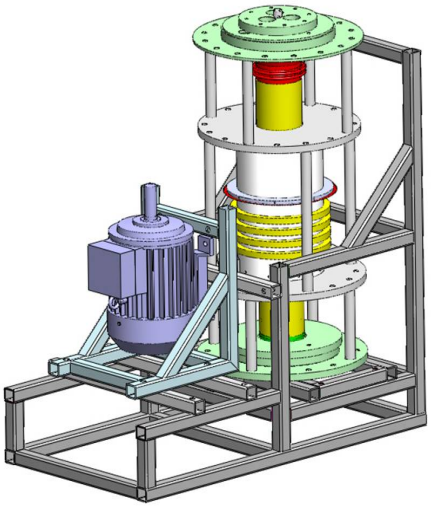

(a) Superwind HTS machine

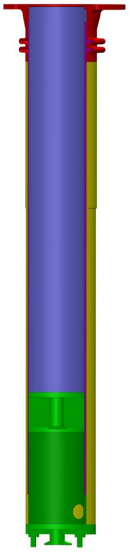

(b) Superwind cryostat

Fig. 1: **(a) Superwind setup-** The conventional armature winding is rotating around the HTS field winding which is enclosed inside an open top LN_2 cryostat. The armature is driven by the belt coupled induction motor controlled by the frequency converter. The HTS field winding is lowered to the LN_2 chamber from the top of the cryostat. **(b) Cross section of the cryostat-** The cross section of 3D CAD model of the cryostat is shown. The low temperature chamber is colored blue, the thermal expansion compensator red, and Torque Transfer Element (TTE) green.

2.1. The armature winding

A three phase two pole armature with distributed windings was adopted from a high speed 690V, 22kW, 50Hz induction machine. The armature winding is connected in a Y connection where all terminals are accessible through 4 slip rings mounted on the metal bore the armature was placed in. The speed of the armature can be adjusted from 0 to 400rpm. The armature steel stack of $M800-50A$ silicon steel has an axial length of 150mm and a bore diameter of 160mm where the three phase single layer winding is distributed over 36 slots with 108 turns in each of the phase windings.

2.2. The Cryostat

To allow open system cooling via $LN2$ evaporation, the orientation of the cryostat and the three phase winding is vertical. Two $316L$ stainless steel (SS) sheets of $1.5mm$ thickness have been pressed rolled and welded into two cylinders with an outer diameter of 158mm and 143mm respectively. The space in between the inner and outer wall contains 30 layers of Multi Layer Insulation (MLI) and was afterwards evacuated to the high vacuum (in the range of 10^{-5}mbar).

A corrugated bellow was placed on the top of the cryostat outer wall to accommodate deformation due to the thermal stress between outer and inner walls of the cryostat. This cryostat has integrated Torque Transfer Element (TTE) placed at the bottom of the cryostat. As the name suggests, this element ensures mechanical coupling between a stationary support and a field winding and is rated for 250Nm including safety factors.

Design constraints for the outer diameter of the cryostat, the integral thickness of the cryostat in the radial direction, the mechanical clearance between the outer wall and the rotating armature, the inner wall, and the HTS winding are all set to be 158mm, 9mm, 1mm and 0.5mm, respectively. No strict constraint

has been defined for the axial length of the cryostat. The resulting magnetic air gap between the rotating armature winding and the stationary HTS field winding is 10mm.

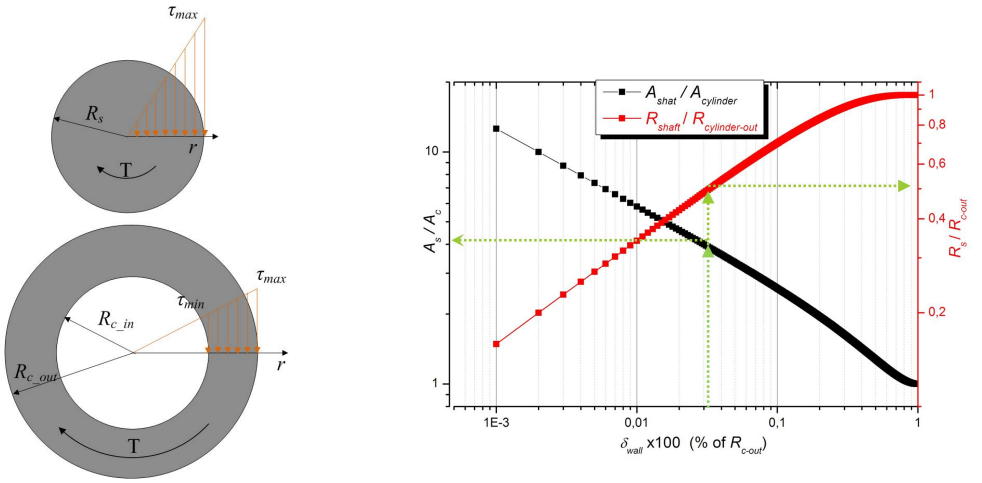

(a) TTE case study

(b) Ratio of the radii and cross sections for the shaft and the cylinder

Fig. 2: **(a) TTE candidates exposed to the torque T-** The stress distribution in the TTE for the case TTE is a shaft or a cylinder. The maximum stress will occur at the largest radius. **(b) Ratio of radii and cross sections for shaft and cylinder-** The derived ratio of the cross sections of the shaft and cylinder with the same maximum sheer stress in the material when exposed to the same torque, as a function of the wall thickens of the cylinder normalized to the outer radius of the cylinder is presented with the black trace. The red trace defines the ratio of the radii of the shaft over cylinder as a function of the wall thickness of the cylinder normalized to the outer radius when both are equally strong (same torque capability). Thus, the shaft with the same mechanical capability to transfer the torque as for example the cylinder with the radius (outer) of 1m and wall thickness of 3cm (which is 3% of the outer radius) would need to have radius of 0.5m. This is indicated with the green dashed line going from 3% for the horizontal axis and reading the value for the red trace on the right axis. To compare now the heat conduction of these two, the value of the black trace for the 0.03 is found on the left axis for the black trace. The conclusion is that the cylinder would have ≈ 4 time lower heat conduction. In the case of the TTE integrated in Superwind cryostat design, the wall thickness is 0.1%.

2.3. The Torque Transfer Element-TTE

A Torque Transfer Element (TTE) is a structural element in superconducting machines with two main functions. Primary, it creates mechanical coupling between an HTS field winding and the 'world' (depending of the design, the 'world' can be a shaft, a housing or something else) with rated load capability corresponding to the maximum machine torque. Secondly, a TTE should also thermally insulate cold HTS from warm 'world'. Thermal insulation and mechanical strength as objectives in the design are contradictory as most of the materials with good mechanical properties are very often excellent thermal conductors.

Simple analysis of the TTE performance will be carried out by comparing the performance of a shaft and a cylinder. Due to the vertical orientation only torsion is considered as a mechanical load and no bending moments are included. When exposed to the torsion torque, T, the stress distribution in the material is a linear function of the distance from the axis around which the torsion torque acts[5]. The largest sheer stress, τ_{max}, will always occur at the largest radius. This is illustrated in Fig.2a for the shaft and the cylinder where R_s, R_{c-out}, R_{c-in} and $\delta_{wall} = R_{c-out} - R_{c-in}$ are radius of the shaft, outer and inner radii of the cylinder and thickness of the wall of the cylinder. The connection between the torsion torque, T and maximum sheer stress in the material τ_{max} is expressed with

$$T = \int rdF = \int r\tau dA = \int r \underbrace{\frac{r}{R}\tau_{max}}_{\tau} dA = \frac{\tau_{max}}{R} \int r^2 dA \longrightarrow J\frac{\tau_{max}}{R} \tag{1}$$

where J is a polar moment of inertia of the particular cross section of interest. To compare these two configurations for the TTE with the dimensions of R_s for a shaft radius and R_{c-out} and R_{c-in} for a outer and

inner cylinder radius, respectively, both TTE will need to have same torque capability. The relationship between dimensions of the shaft and cylinder, if both are equally strong (same torque and same τ_{max}) is derived using (1) and can be expressed as

$$T_s = T_c \rightarrow J_s \frac{\tau_{max}}{R_s} = J_c \frac{\tau_{max}}{R_{c-out}} \rightarrow R_s = \sqrt[3]{\frac{R_{c-out}^4 - (R_{c-out} - \delta_{wall})^4}{R_{c-out}}} \tag{2}$$

where the $J_s = 0.5\pi R_s^4$ and $J_c = 0.5\pi(R_{c-out}^4 - R_{c-in}^4)$ was used. From (2) we can notice that for the one R_s, there are a number of pairs of $(R_{c-out}, \delta_{wall})$ which will satisfy (2). It is possible thus to define the ratio of the radii of these two as a function of a wall thickness of the cylinder, where for each wall thickness this ratio will be fully defined. If the wall thickness of the cylinder is normalized to the outer radius of the cylinder, the ratio is defined with (3).

$$\frac{R_s}{R_{c-out}} = \frac{\left(\frac{R_{c-out}^4 - (R_{c-out} - \delta_{wall})^4}{R_{c-out}}\right)^{1/3}}{R_{c-out}} = \left(1 - (1 - \delta_{\%wall})^4\right)^{1/3} \tag{3}$$

Now, let's compare the heat conduction trough these two by defining the ratio of the cross sectional areas. The ratio of the cross sections is expressed by (4) and is also a function of the cylinder wall thickness.

$$\frac{Q_s}{Q_c} \rightarrow \frac{A_s}{A_c} = \frac{\pi R_s^2}{\pi(R_{c-out}^2 - (R_{c-out} - \delta_{wall})^2)} = \frac{(\frac{R_{c-out}^4 - (R_{c-out} - \delta_{wall})^4}{R_{c-out}})^{2/3}}{R_{c-out}^2 - (R_{c-out} - \delta_{wall})^2} = \frac{\sqrt[3]{(1 - (1 - \delta_{\%wall})^4)^2}}{1 - (1 - \delta_{\%wall})^2} \tag{4}$$

Both (3) and (4) have been plotted at the Fig.2b. From this figure it is clear that the larger radius of the cylinder will require thinner wall thickness for a same torque and that it will also result with the TTE with smaller cross section. This analysis implies that not only the cylinder has the potential to decrease the conductive heat transfer compared to the shaft in the role as a TTE, but also it will require less material and thus be lighter too.

2.4. The HTS winding

Fig.3a illustrates the HTS field winding and its main parts. The space allocated for the HTS coils can accommodate maximum 8 single HTS coils, each 5*mm* thick. All coils are placed between 4 aluminum bars which are screwed into the top and bottom shaft. The aluminum bars are acting as housing for the HTS coils and the cold steel providing all the mechanical support for the HTS field winding.

The position of the coils can be adjusted with a spacer placed in between the coils in the HTS field winding. The coil stack is fixed together with four treads and 8 nuts placed in each corner of the coil. To utilize the versatility of the HTS field winding, each coil can have separate leads. The current leads are led to the screw terminal where connections can be altered without interfering with the coil arrangement itself. Maximum flexibility of the experimental setup is achieved if the each of the current lead is brought outside of the cryostat.

2.4.1. The HTS coil design

All HTS coils, illustrated in Fig.3b, have uniform design which as a consequence allows evaluation of the coils on the basis of engineering current density achieved by each coil. In this way not only that an HTS conductor is tested in various conditions but also the coil design and manufacturing procedure is tested as well. The factors like electrical insulation of HTS and mechanical support do impact the engineering current density of a coil and should be included in the analysis. The coils are impregnated with epoxy and are designed to fit onto a coil frames made from 316L stainless steel. The HTS tape is soldered to copper terminals at both ends of the coils. More details about the coils can be found in [6]. Depending on the type of HTS tape, insulation employed, cooling requirements, etc., the number of turns for the different coils varies.

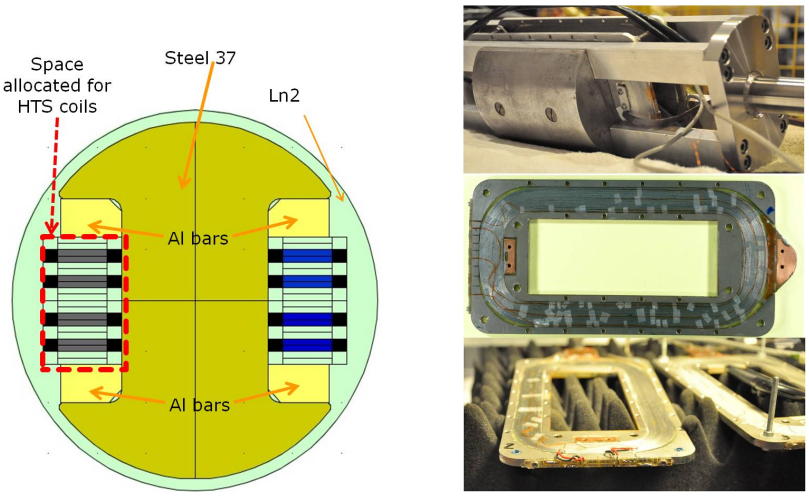

(a) The HTS filed winding (b) The HTS coils

Fig. 3: **(a)-**2D cross section of the HTS field winding with the HTS coils. **(b)-** The HTS field winding and HTS coils

All coils have access to a four point voltage measurement across the coil as well as several sections (one or more) in the middle of the winding. The measurement points are accessible on a printed board mounted on the frame of the coil. This allows evaluation of the potential difference in the performance of the outer and the inner part of the coils (turns are not exposed to the same magnetic field).

3. Experimental results

The individual IV curves for each of the HTS coils are presented in the Fig.4a. The power fit have been performed according to the expression

$$E_{coil} = \frac{V_{coil}}{L_{coil}} = \frac{1}{L_{coil}} \int_0^{L_{coil}} E_0 \left(\frac{I}{I_c} \right)^n \tag{5}$$

where E_{coil} and V_{coil} are the average electric field along the length of the HTS tape and voltage of the coil as measured, respectively. The L_{coil} is a length of the HTS tape in the coil while I_c, n are critical current and transition coefficient of the coil. The $E_0 = 1\mu$ V/cm is the criteria used for the electric field in the HTS tape when current in superconductor is equal to a critical current. It is important to keep in mind that the I_c determined from the coil voltage could lead to overestimates in the current rating of the HTS coil, especially if the flux distribution across the HTS coil contains large gradients and because of that the condition (5) should be used with caution when deriving the I_c of the coil.

Looking at the Fig.4a, we can observe that coils *Coil*#2, *Coil*#3, *Coil*#5 and *Coil*#6 do have critical currents > 60A which is expected. As the coils are mounted on the cold steel (steel 37 in the Fig.3a) and the magnetic field created by the individual coil cannot saturate the cold steel, the flux conditions are favorable for the coils as most of the flux is located in the steel and the stray flux is mostly parallel to the HTS tapes. That is the reason why 1*G* coils, namelly *Coil*#2, *Coil*#3 and *Coil*#5 are exhibiting rather high I_c values, 81.3*A*, 81.0*A* and 88.3*A* respectively. The n value is close to 14 for all 1*G* coils. As for the 2*G* coils, *Coil*#6 with the I_c of 72*A* and n value of 46, has performed as expected. Unfortunately, two other 2*G* coils, *Coil*#7 and *Coil*#8, have been damaged during winding procedure which has reduced the I_c of these coils to 12*A* and 30*A* respectively. Since the coils are with defect, the IV curves are showing dominant resistive component with low n value of 2.8 and 3.0, respectively. Further studies have concluded that the delamination of the HTS tape during cool-down was most probable cause of the low I_c of the coil.

For the machine operation, all HTS coils in the field winding had to be connected in serial connection. If this set of coils was used the current would be limited to only 10*A*. Thus the coils *Coil*#7 and *Coil*#8 were

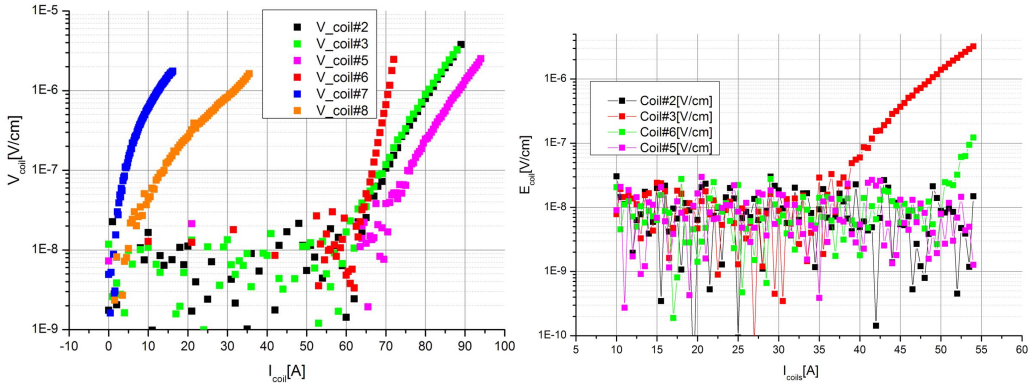

(a) Individual coils (b) Serial connection

Fig. 4: **(a)** - The individual IV curves for *Coil*#2, *Coil*#3, *Coil*#5, *Coil*#6, *Coil*#7, *Coil*#8 are presented. **(b)**The IV curves for the same set of coils connected in serial connection. The coils *Coil*#7, *Coil*#8 have not been included in this test.

not included and IV curve for the HTS field winding with 4 coils connected in series is presented in the Fig.4b. When coils are powered with currents, the coil reaching the I_c of $48A$ first is *Coil*#3. Coils *Coil*#2 and *Coil*#5 are not indicating that they are close to the I_c while *Coil*#6 do exhibit small voltage increase for the currents above $50A$.

During the course of experiments, several machine tests have been performed as well. The value of the No-load phase voltage recorded for the HTS field winding in this configuration has peaked at $30,5V\ RMS$ for the speed of $312rpm$, corresponding to the peak air gap flux density of $0.62T$ which was verified by FE simulation. The highest value of the torque recorded during experiments was during the short circuit tests and the torque peaked at $78Nm$ for the $50A$ in HTS field winding, $30A\ RMS$ armature phase current and at speed $227rpm$.

4. Conclusion

Superwind experimental prototype of a synchronous HTS machine with the HTS field winding was designed, constructed and successfully tested. The setup proved to be highly versatile allowing a number different HTS tapes and field winding concepts to be tested. TTE was identified as one of the crucial elements of any HTS machine (high torque machines) and optimized design was presented which resulted in more than 10 times lower heat input. Finally, the experimental results have confirmed validity of the TTE design by loading it with $\approx 80Nm$. The IV curves of the coils have confirmed that $1G$ HTS coils have performed as expected while the coil design (winding and epoxy curing) of $2G$ HTS coils need to be revised.

References

[1] L. Fingersh, M. Hand, A. Laxson, N. R. E. L. (US), Wind turbine design cost and scaling model, National Renewable Energy Laboratory, 2006.

[2] H. Li, Z. Chen, Optimal direct-drive permanent magnet wind generator systems for different rated wind speeds, in: Power Electronics and Applications, 2007 European Conference on, IEEE, 2007, pp. 1–10.

[3] D. Bang, H. Polinder, G. Shrestha, J. Ferreira, Review of generator systems for direct-drive wind turbines, in: European Wind Energy Conference & Exhibition, Belgium, 2008, pp. 1–11.

[4] A. Abrahamsen, B. Jensen, E. Seiler, N. Mijatovic, V. Rodriguez-Zermeno, N. Andersen, O. J, Feasibility study of 5mw superconducting wind turbine generator, Physica C: Superconductivity (0) (2011) –. doi:10.1016/j.physc.2011.05.217.
URL `http://www.sciencedirect.com/science/article/pii/S0921453411003042`

[5] J. Dewolf, Mechanics Of Materials (In Si Units), McGraw-Hill Education (India) Pvt Ltd, 2004.
URL `http://books.google.com/books?id=OuDQmNkmLYgC`

[6] N. Mijatovic, J. B.B, C. Traeholt, , A. B. Abrahamsen, V. M. Rodriguez-Zermeno, N. F. Pedersen, M. Henriksen, E. Seiler, N. H. Andersen, High temperature superconductor machine prototype, in: part of: International Conference on Electrical Machines and Systems (ISBN:) , 2011, IEEE, International Conference on Electrical Machines and Systems 2011, ICEMS 2011, 2011, Beijing, China.